FABRICATION AND CHARACTERIZATION OF NANOSTRUCTURED HALF METALS AND DILUTED MAGNETIC SEMICONDUCTORS

LI HONGLIANG

NATIONAL UNIVERSITY OF SINGAPORE

2006

FABRICATION AND CHARACTERIZATION OF NANOSTRUCTURED HALF METALS AND DILUTED MAGNETIC SEMICONDUCTORS

LI HONGLIANG

(M. Eng., Tongji University, P. R. China)

A THESIS SUBMITTED

FOR THE DEGREE OF DOCTOR OF PHILOSOPHY

DEPARTMENT OF ELECTRICAL AND COMPUTER ENGINEERING

NATIONAL UNIVERSITY OF SINGAPORE

2006

ACKNOWLEDGEMENTS

First of all, I would like to express my sincere gratitude to my supervisor, A/P Wu Yihong, for his guidance and constant encouragement throughout this project. His invaluable discussions and explanations about the complicated experimental results always let me on the right way in my research work. It is impossible to finish this project without him. I am very impressed for his diligence, scientific research attitude, and acute sense to development trends in the nanospintronic field.

I am grateful to my two co-supervisors, A/P Teo Kie Leong and Dr. Guo Zaibing, for their kind help and valuable advices over the entire course of my Ph.D. project. Specially, Dr. Guo Zaibing gave me great help in the magnetic properties measurements.

I am greatly indebted to Dr. Wang Shijie and Mr. Liu Binghai for the preparation and observation of TEM samples. The TEM results are very important for the publication of my journal papers.

Sincere thanks should also go to all the staffs in nanospin electronics laboratory, data storage institute. They have helped me in one way or another in my studies and daily life. I also want to acknowledge the excellent experimental and study environment provided by both data storage institute and national university of Singapore.

I deeply thank other students in our group for their valuable help in my research work, and their friendship and happy time spent with them throughout four-year studies.

Forever, great heartfelt thanks to my family: my parents, my wife, my daughter, and my relatives for their firm support and everlasting love, which is my impetus to finish four-year Ph.D. studies and optimistically face all kinds of challenges in my life. In particular, my wife has accompanied me almost throughout four-year Ph.D. studies and taken the responsibility alone to look after our lovely daughter.

TABLE OF CONTENTS

ABSTRACT

The performance of existing metal-based spintronic devices is limited primarily by two factors: low polarization of the ferromagnetic materials used to build the devices and inability to control charge motion in metals. The former can be resolved by using suitable half metals and the latter can be overcome if room temperature diluted magnetic semiconductors exist. This work has attempted to grow and characterize two types of potential materials for future spintronic devices: Fe_3O_4 and $Ge_{1-x}Mn_x$. The former is a kind of half metal, while the latter a Ge-based diluted magnetic semiconductor.

The work on Fe_3O_4 was focused on the understanding of electrical transport mechanism across antiphase boundaries through processing the thin film into nanowires and then studying their transport properties. Prior to this work, intensive studies have been carried out on the preparation and characterization of Fe_3O_4 thin films and their application in spin valves and magnetic tunnel junctions. However, the magnetoresistance ratio of Fe_3O_4-based spintronic devices was significantly lower than the value which one would expect if the Fe_3O_4 thin films employed were fully polarized half metals. Through detailed dynamic conductance measurements, we were able to reveal that the poor performance of Fe_3O_4-based spintronic devices obtained so far was mainly caused by the low average polarization due to the existence of randomly distributed antiphase boundaries. We further revealed that the electrical transport mechanism across the antiphase boundaries was dominated by tunnelling,

through detailed studies on nanowires samples. A model was proposed to account for the experimental results.

The work on $Ge_{1-x}Mn_x$ was focused on understanding of the origin of ferromagnetism in this material system. Prior to this work, near or above room temperature ferromagnetism in $Ge_{1-x}Mn_x$ has been reported by several groups. However, the mechanism of ferromagnetic ordering is still controversial. In this study, amorphous $Ge_{1-x}Mn_x$ thin films with or without secondary phases, granular thin films, and δ-doped amorphous thin films have been fabricated and characterized.

The amorphous samples were found to consist of a low-temperature highly ordered spin-glass-like phase and a high-temperature cluster dopant phase. The magnetization of the low-temperature phase was found to be coupled antiferromagnetically with that of the high-temperature phase, leading to the appearance of a negative thermal remanent magnetization. Detailed magnetic and electrical transport measurements revealed that the low-temperature highly ordered spin-glass-like phase consists of both spin-glass-like phase and ferromagnetically ordered regions. The amorphous samples also exhibited a negative magnetoresistance and an anomalous Hall effect at low temperatures.

The samples grown at 300 ^{o}C were found to consist of amorphous $Ge_{1-x}Mn_x$, Ge crystallites, and high T_C secondary phases. These samples were ferromagnetic near or above room temperature and exhibited a positive MR effect. There was no anomalous Hall effect observed in these samples. Electrical transport across the interface between high T_C secondary phases and the host semiconductor matrix was studied in $Ge_{0.88}Mn_{0.12}$ nanowires with different diameters. Although the existence of a Schottky barrier at the nanoparticle / host matrix interfaces and carrier localization at low

temperatures were observed, the transport across the interfaces was of spin-independent nature.

In the δ-doped amorphous $Ge_{1-x}Mn_x$ thin films, it was found that the spacing between magnetic impurities had a strong effect on the magnetic properties. The electrical transport properties and ordering temperature (T^*_C) were found to be closely related to both the Mn concentration and the ratio of Ge and Mn layer thicknesses.

In spite of the large structural differences, one common result observed for these materials was that the T^*_C values were very close to those reported for epitaxially grown samples. This suggested that the so-called Curie temperature reported in literature was not an indicator of global ordering but rather the ordering temperature of magnetic clusters in the $Ge_{1-x}Mn_x$ system.

Some preliminary results were also obtained for a spin valve with amorphous $Ge_{0.67}Mn_{0.33}$ as one of the electrodes. Typical spin-valve-like *M-H* curves were obtained in this structure.

LIST OF TABLES

LIST OF FIGURES

NOMENCLATURE

A	area
B	magentic induction
d	thickness
e	electron charge
E_F	Fermi energy
G	conductance
H	magnetic field strength
H_c	coercivity
I	current
M	magnetization
M_r	remanence
M_s	saturation magentization
n	carrier density
N	number of the electrons
$N(E_F)$	density of state of the electron at the Fermi level
P	spin polarization ratio
R	resistance

R_a	surface roughness
t	time
T	temperature
T_C	Curie temperature
V	voltage
β	bulk spin asymmetry coefficient
γ	interface spin asymmetry coefficient
$\hbar$	reduced plank constant
K_B	Boltzmann constant
Λ_F	mean free path
v_F	Fermi velocity
ρ	resistivity
μ_0	magnetic permeability
χ'	real part of ac susceptibility
χ''	imaginary part of ac susceptibility

ACRONYMS

AFM	atomic force microscope
AFM	antiferromagentic
AHE	anomolous Hall effect
APB	antiphase boundary
BMP	bound magnetic polaron
CIP	current in the plane
CPP	current perpendicular to the plane
CVD	chemical vapor deposition
DMS	diluted magnetic semiconductor
FC	field cooling
FIB	focused ion beam
FM	ferromagnetic
GMR	giant magnetoresisitance
HRTEM	high resolution transmisssion electron micrscope
JMR	junction magnetoresistance
K-cell	Knudsen-cell
MBE	molecular beam epitaxy

MR	magnetoresistance
MTJ	magnetic tunneling junction
NM	nonmagentic
OHE	ordianry Hall effect
PLD	pulsed laser deposition
PM	paramagentic
RBS	Rutherford backscattering spectrometry
RHEED	reflection high energy electron diffraction
RKKY	Ruderman-Kittel-Kasuya-Yoshida
RP	rotary pump
SQUID	superconducting quantum interference device
TEM	transmisssion electron micrscope
TMP	turbo molecular pump
TMR	tunneling magnetoresistance
TRM	thermal remanent magnetization
UHV	ultrahigh vacuum
VSM	vibrating sample magnetometer
XPS	x-ray photoelectron spectroscopy
XRD	x-ray diffraction
ZFC	zero field cooling

LIST OF PUBLICATIONS

Journal papers

1. **Hongliang Li**, Yihong Wu, Zaibing Guo, Ping Luo, and Shijie Wang, "Magnetic and electrical transport properties of $Ge_{1-x}Mn_x$ thin films", J. Appl. Phys. **100**, pp. 103908, 2006.
2. **H. L. Li**, H. T. Lin, Y. H. Wu, T. Liu, Z. L. Zhao, G. C. Han, and T. C. Chong, "Magnetic and electrical transport properties of delta-doped amorphous Ge:Mn magnetic semiconductors", J. Mater. Magn. Mater. **303**, pp. e318-e321, 2006.
3. **Hongliang Li**, Yihong Wu, Tie Liu, Shijie Wang, Zaibing Guo, and Thomas Osipowicz, "Magnetic and transport properties of Ge:Mn granular system", Thin Solid Film **505**, pp. 54-56, 2006.
4. **Hongliang Li**, Yihong Wu, Zaibing Guo, Shijie Wang, Kie Leong Teo, and Teodor Veres, "Effect of antiphase boundaries on electrical transport properties of Fe_3O_4 nanostructures", Appl. Phys. Lett. **86**, pp. 252507, 2005.

Conference papers

5. Yihong Wu, **Hongliang Li**, Tie Liu, Shijie Wang, and Zaibing Guo, "Magnetic and transport properties of Ge:Mn granular system", Materials Research Society (MRS) 2005, Mar. 28-Apr. 1, 2005, San Francisco, CA, USA.

6. **Hongliang Li** and Yihong Wu, "Magnetic and electrical transport Properties of Fe_3O_4 nanostructures", International Magnetics Conference (INTERMAG) 2005, Apr. 4-8, 2005, Nagoya, Japan.
7. **Hongliang Li**, Yihong Wu, Zaibing Guo, and Shijie Wang, "Magnetic and transport properties of Ge:Mn granular system", International Conference on Materials for Advanced Technologies (ICMAT) 2005, Jul. 4-9, 2005, Singapore.
8. Yihong Wu and **Hongliang Li**, "Magnetic properties of amorphous $Ge_{1-x}Mn_x$ thin films", Spintech III, Aug. 1-5, 2005, Awaji Island, Japan.
9. **Hongliang Li**, Hong Tai Lin, Yihong Wu, Tie Liu, Guchang Han, and Tow Chong Chong, "Magnetic and electrical transport properties of delta-doped Ge:Mn magnetic semiconductors", International Symposium on Physics of Magnetic Materials (ISPMM) 2005, Sep. 14-16, 2005, Singapore.
10. **Hongliang Li**, Yihong Wu, Zaibing Guo, and Zeliang Zhao, "Structural, magnetic and transport properties of Ge:Mn thin films", 2nd MRS-S Conference on Advanced Materials, Jan. 18-20, 2006, Singapore.

Other publications

11. Hao Ming Chen, Ru-Shi Liu, **HongLiang Li**, and Hua Chun Zeng, "Generating isotropic superparamagnetic interconnectivity for the two-dimensional organization of nanostructured building blocks", Angew. Chem. Int. Ed. **45**, pp. 2713-2717, 2006.
12. H. H. Long, E. T. Ong, T. Liu, **H. L. Li**, Z. J. Liu, E. P. Li, Y. H. Wu, A. O. Adeyeye, "Micromagnetic simulation of magnetic nanowire with constrictions by FIB", J. Mater. Magn. Mater. **303**, pp. e299-e303, 2006.
13. Y. Z. Peng, T. Liew, T. C. Chong, W. D. Song, **H. L. Li**, and W. Liu, "Growth and characterization of dual-beam pulsed-laser-deposited $Zn_{1-x}Co_xO$ thin films", J. Appl.

Phys. **98**, pp. 114909, 2005.

14. Z. J. Liu, J. T. Li, H. H. Long, H. T. Wang, and **H. L. Li**, "Distribution of slanted write field for perpendicular recording heads with shielded pole", IEEE Trans. Magn, **41**, pp. 2908-2910, 2005.

CHAPTER 1

INTRODUCTION AND LITERATURE SURVEY

1.1 Background

It is well known that an electron has charge, spin, and orbits. Nowadays information processing and communication are mainly based on charge-based Si devices such as diodes and transistors, in which the spin degree of freedom of electrons has been neglected. Moore's law predicated that the number of transistors on a chip would double roughly every 18 months. [1] According to the international roadmap for semiconductors, the minimum feature size will reach 40 nm in 2010; [2] In addition to the size effect, theoretical analyses suggest that thermal dissipation will probably be the ultimate limiter of CMOS scaling and new types of devices based on different operating principles will be required. Among many of the possible candidates, the idea of using spin in electronics, i.e., spintronics, has attracted great attention. [3,4]

Spintronics involves the study of active control and manipulation of spin degree of freedom in materials and devices. [5] As in this case, the information is carried by both the spin and charge degree of freedoms of an electron, it offers opportunities for a new generation of devices combining standard microelectronics with spin-dependent effects. Adding the spin degree of freedom to conventional semiconductor charge-based electronics or using the spin degree of freedom alone will add substantially more capability and performance to electronic products, which has the advantages such as nonvolatility, increased data processing speed, decreased electric power consumption,

and increased integration densities. [4] In comparison with the existing charge-based microelectronics technology, the ability to control and manipulate the dynamics of both charges and spins by external electric, magnetic or optical fields is expected to lead to novel spintronic devices. Spintronics is a very broad field including all types of electronics that make use of both charges and spins. In general, it can be classified into three subgroups: (1) Nanomagnetism, (2) GMR-based electronics or magnetoelectronics and (3) semiconductor-based spintronics. As nanomagnetism is out of the scope of this thesis, we only provide an overview for magnetoelectronics and semiconductor-based spintronics in this chapter.

1.2 Magnetoelectronics

1.2.1. GMR effect and spin-polarized transport

The era of spin electronics began almost exactly from 1988 with the discovery of giant magnetoresistance (GMR) effect by Fert *et al.* [6] and Grünberg *et al.* [7]. GMR effect was observed in artificial multilayer structures composed of alternate ferromagnetic (FM) metal and nonmagnetic (NM) metal layers. The resistivity change is strongly influenced by the relative orientation of the magnetization between the magnetic layers. In GMR multilayers, it was found that FM - NM interfacial scattering played a crucial role in determining the MR ratio. [8] Interfacial scattering is dependent on the bandstructure of FM and NM metals at the Fermi level. If the bandstructure between FM and NM matches one of the spin states, a lower resistance can be obtained; otherwise, a higher resistance will be obtained [see Fig. 1.1]. In principle, the GMR effect is a structural instead of a material property. The GMR effect can be understood with the two-current model proposed by Mott, [9] where the conduction is considered as

the sum of two independent and unequal current channels for spin-up and spin-down electrons. In other words, the current is spin-polarized.

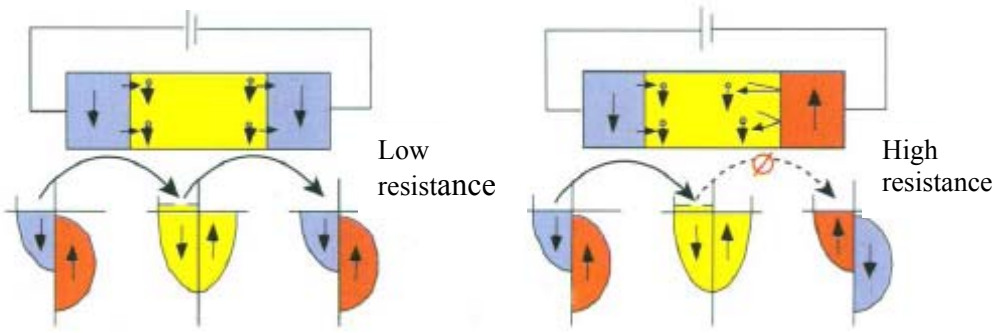

FIG. 1.1 Schematic representation of spin-polarized transport from a ferromagnetic metal, through a nonmagnetic metal, into the second ferromagnetic metal. [After G. A. Prinz, 1998, Ref. 3]

Spin-polarized transport will appear in the materials for which there is an imbalance of the spin population for the spin-up and spin-down electrons at the Fermi level. In the normal metal, there is no imbalance of the spin polarization at the Fermi level, i. e., equal numbers for spin-up and spin-down electrons at the Fermi level. Thus, spin-polarized transport is not expected for them. However, in ferromagnetic metals such as Fe, Co, Ni and their alloys, the imbalance appears. Although the density of states of the spin-up and spin-down electrons are often identical, the states are shifted in energy with respected to each other. The shift leads to an unequal filling of the bands, which is the origin of the net magnetic moment, but it can also cause the spin-up and spin-down carriers at the Fermi level to be unequal in number, character, and mobility. [3] A net spin polarization is produced due to the inequality in charge transport for different spins. The spin-polarization ratio (P) is defined as $P = \frac{N_\uparrow - N_\downarrow}{N_\uparrow + N_\downarrow}$ to show the spin asymmetry

at the Fermi level, where $N_{\uparrow(\downarrow)}$ is the number of the carriers that are in spin-up or spin-down states.

Although very large resistance changes can be obtained in the GMR multilayer structures, they are not suitable for practical device applications. A very high magnetic field (2 T for (Fe30 Å/Cr 9 Å)$_{60}$ structure [6]) has to be applied to achieve the MR effect as the two ferromagnetic layers are magnetically decoupled. The sensor in the spintronic devices requires having a response to a small applied magnetic field. To meet the requirement, several GMR-based devices, including spin valves and magnetic tunnelling junctions (MTJs) have been invented and already been applied to commercial products. In the following sections of 1.2.2 and 1.2.3, we will have a brief review about spin valves and MTJs.

1.2.2. Spin valves

In 1991, Parkin *et al.* [10] invented the spin valve, a GMR-based device, where two ferromagnetic layers are separated by a thin nonmagnetic metal such as Cu or Ru. One of the two magnetic layers is pinned by an antiferromagnetic (AFM) layer, which means that the magnetization in this layer is relatively insensitive to moderate magnetic fields. Therefore, this layer is called “pinned layer”. The other magnetic layer is named as the “free layer”. When applying a relative small magnetic field, the magnetization direction in the “free layer” can be changed easily. Thus, the change in the relative magnetization direction in the two magnetic layers leads to a resistance change. Dependent on the current direction, spin-valves are classified as CIP (current in the plane) and CPP (current perpendicular to the plane). In comparison with CIP spin valves, CPP spin valves are more promising for future device application.

Bass and Pratt [11] obtained the following equation in the case where the spin diffusion length was much larger than the layer thickness for CPP spin valves, which included both the interface and bulk spin-dependent scattering:

$$\Delta RA = \frac{M^2[\beta d_{FM}\rho_{FM}/(1-\beta^2) + 2\gamma AR_{F-N}/(1-\gamma^2)]^2}{R^{AP}} \tag{1.1}$$

$$= \frac{M[\beta d_{FM}\rho_{FM}/(1-\beta^2) + 2\gamma AR_{F-N}/(1-\gamma^2)]^2}{d_{FM}\rho_{FM} + d_N\rho_N/(1-\beta^2) + 2\gamma AR_{F-N}/(1-\gamma^2)}$$

where d_{FM} and d_N are the thicknesses of the ferromagnetic and non-magnetic layers. The bulk spin asymmetry coefficient (β) and interface spin asymmetry coefficient (γ) are defined as:

$$\beta = \frac{\rho_F^{\downarrow} - \rho_F^{\uparrow}}{\rho_F^{\downarrow} + \rho_F^{\uparrow}}, \tag{1.2}$$

$$\gamma = \frac{AR_{F-N}^{\downarrow} - AR_{F-N}^{\uparrow}}{AR_{F-N}^{\downarrow} + AR_{F-N}^{\uparrow}}, \tag{1.3}$$

We can simplify the equation by neglecting the interface scattering,

$$\Delta RA = \frac{\beta^2}{1-\beta^2}\frac{M(d_{FM}\rho_{FM})^2}{d_{FM}\rho_{FM} + d_N\rho_N}, \tag{1.4}$$

Thus, we can find two methods to improve the sensitivity of CPP spin valves: (1) increasing number of layers and get a higher M; (2) increasing value of β. For the ideal case, we can get $\beta = 1$, which means that only spin-up or spin-down electrons are scattered at the Fermi level.

1.2.3 Magnetic tunnelling junctions

Another type of magnetoelectronic device is magnetic tunnelling junctions, where the two ferromagnetic layers are separated by an ultrathin insulating material such as

aluminium oxide (Al_2O_3) or magnesium oxide (MgO) instead of nonmagnetic metals in the spin valves. [12,13] With the switching of magnetization of the two magnetic layers between parallel and antiparallel states, the differences in the tunnelling resistance of the junction are produced and thus the MR effect could be achieved. The electrical conduction in MTJs is based on the spin-dependent tunnelling effect, different from the spin-dependent scattering effect in spin valves. Recently, giant tunnelling magnetoresistance (TMR) of > 350% at room temperature and 575% at 4.2 K were achieved by Parkin *et al.* with MgO (100) barriers. [14]

The tunnelling conductance in MTJs can be calculated using the transfer Hamiltonian approach and the following results can be obtained (15):

$$G^{\uparrow\uparrow}(0) \propto N_1^{\uparrow}(E_F)N_2^{\uparrow}(E_F) + N_1^{\downarrow}(E_F)N_2^{\downarrow}(E_F), \tag{1.5}$$

for the parallel case and

$$G^{\uparrow\downarrow}(0) \propto N_1^{\uparrow}(E_F)N_2^{\downarrow}(E_F) + N_1^{\downarrow}(E_F)N_2^{\uparrow}(E_F), \tag{1.6}$$

for the antiparallel case. Here, $N_1^{\uparrow}(E_F)$ ($N_1^{\downarrow}(E_F)$) and $N_2^{\uparrow}(E_F)$ ($N_2^{\downarrow}(E_F)$) are the density of states at the Fermi level of the majority (minority) electrons of the two electrodes. The junction magnetoresistance (JMR) is given by

$$JMR = \frac{1/G^{\uparrow\downarrow}(0) - 1/G^{\uparrow\uparrow}(0)}{1/G^{\uparrow\downarrow}(0)} = \frac{2P_1P_2}{1+P_1P_2}, \tag{1.7}$$

Here $$P_1 = [N_1^{\uparrow}(E_F) - N_1^{\downarrow}(E_F)]/N_1^{\uparrow}(E_F) + N_1^{\downarrow}(E_F)], \tag{1.8}$$

$$P_2 = [N_2^{\uparrow}(E_F) - N_2^{\downarrow}(E_F)]/N_2^{\uparrow}(E_F) + N_2^{\downarrow}(E_F)], \tag{1.9}$$

This model was proposed by Jullière in 1975. [16] According to equation 1.7, we can obtain the maximum JMR ratio of 100% when $P_1 = P_2 = 1$. This means that only one kind of spin state exists at the Fermi level. Note that, in addition to JMR, TMR is often used in literature, which is defined as

$$TMR = \frac{1/G^{\uparrow\downarrow}(0) - 1/G^{\uparrow\uparrow}(0)}{1/G^{\uparrow\uparrow}(0)} = \frac{2P_1P_2}{1-P_1P_2}. \quad (1.10)$$

It is apparent that TMR is larger than JMR and approaches infinity when $P_1 = P_2 = 1$.

1.2.4 Half-metallic materials and classification

The simple theoretical analysis above suggests that ferromagnetic materials with high spin polarization are crucial to achieve a higher MR ratio in the spintronic devices. Traditional 3*d* ferromagnets such as Fe, Co, Ni and their alloys have a spin polarization of P of only 40% to 50%. Thus, it is necessary to find higher spin-polarized conducting ferromagnetic materials, in ideal case with 100% spin polarization, for which only one spin channel is available at the Fermi surface and all the currents must be carried by these majority spins. This kind of materials is called half metals.

The term of half metal was proposed by de Groot *et al.* on the basis of electronic structure calculations for the Heusler alloy NiMnSb. [17] Only several ferromagnets can satisfy the criterion of half metallicity and their properties are summarized in Table 1.1. In fact, it is difficult to find direct experimental evidence for half metallicity because all the common experimental methods for measuring spin polarization, including photoemission, [18] point-contact magnetoresistance, [19] tunnelling magnetoresistance, [20] Andreev Reflection [21] or tunnelling in a planar superconducting junction (Tedrov-Meservey experiment) [22] are encountered by some degree of experimental difficulty and uncertainty. In general, electronic structure calculation is the best method to identify the half metallicity. [23]

Table 1.1 Some half-metallic materials and their properties

Materials	↑ electrons	↓ electrons	T_C(K)	N↑-N↓	P (%)	Reference
CrO_2	3d-t_{2g}(Cr)	-	396	2	85-100	24-27
Sr_2FeMoO_6		5d-t_{2g}(Mo)	421	4	>85	28,29
$(La_{0.7}Sr_{0.3})MnO_3$	3d-e_g (Mn)	3d-t_{2g} (Mn)	280-380	3.7	72-95	30-35
Fe_3O_4	-	3d-t_{2g}(Fe)	860	4	39-85	36-39
$Tl_2Mn_2O_7$	Mn (t_{2g})	Tl (6s)	120	6	66	40,41
$(Co_{1-x}Fe_x)S_2$	Co (e_g)	-	100	-		42
NiMnSb	-	Ni (e_g)	730	4	58	22,43
Mn_2VAl	Mn (t_{2g})	-	760	2		44
Co_2MnSi	-	-	985	-	54	45,46
Co_2MnGe	-	-	905	-	-	47

There are five kinds of half metals dependent on the electron states of the spin-up and spin-down electrons at the Fermi level, which is summarized as follows:

(1) Only spin-up electrons exist at the Fermi level as shown in Fig. 1.2(a). CrO_2, $(Co_{1-x}Fe_x)S_2$ and half-heusler alloy NiMnSb are some of the materials fall under this category.

(2) Only spin-down electrons exist at the Fermi level as shown in Fig. 1.2(b). Those half metals include Sr_2FeMnO_6 and the heusler alloy $NiMnV_2$.

(3) Only localized electrons exist at the Fermi level as shown in Fig. 1.2(c). As the spin-down electrons are in the localized state, the electron transport is dominant by the thermal assisted hopping. Fe_3O_4 (magnetite) belongs to this kind of half metals.

(4) Both spin-up and spin-down electrons exist at the Fermi level, but only one spin population is localized and the other is delocalized as shown in

Fig. 1.2(d). The current is carried overwhelmingly by electron of a single spin polarization. An example is the manganites $(La_{0.7}A_{0.3})MnO_3$ with A=Ca, Sr,…..

(5) Both spin-up and spin-down electrons exist at the Fermi level, but with different effective masses as shown in Fig. 1.2(e). $Tl_2Mn_2O_7$ is so far the only material which satisfies the criterion, for which the holes are localized and have a larger effective mass than that of electrons.

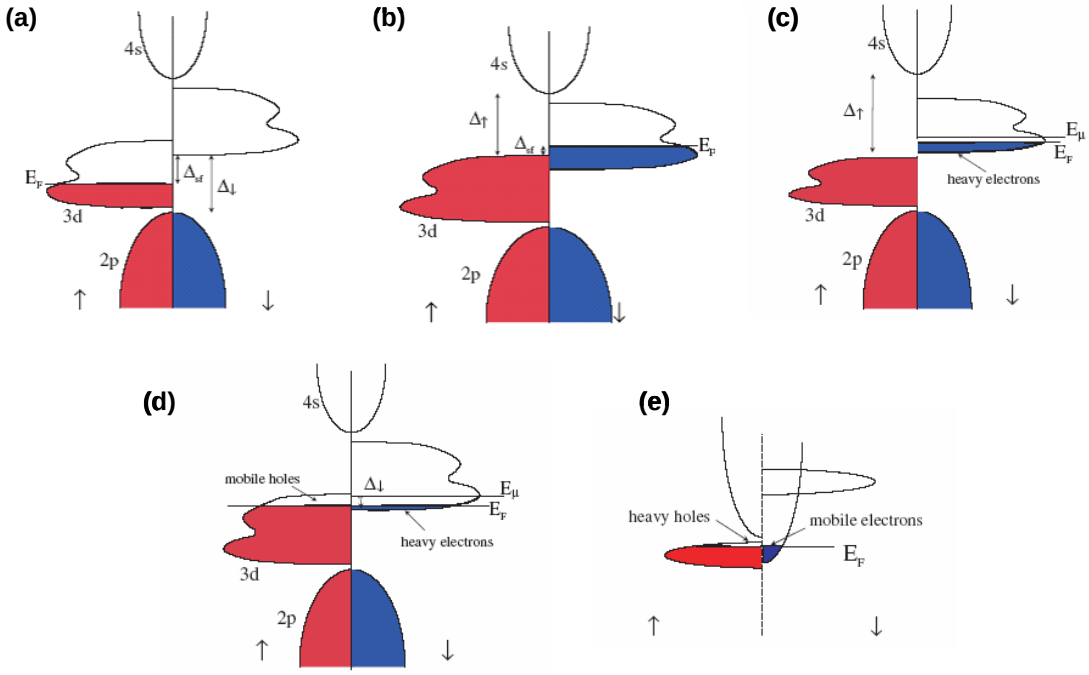

FIG. 1.2 Schematic illustration of the density of states at the Fermi level for different kinds of half metals. [After J. M. D. Coey, 2004, Ref. 23]

A prerequisite to use half metals for practical devices is to have T_C in excess of 500 K. [23] Fe_3O_4 is one of the half metals to meet this requirement, for which T_C is ~ 860 K. Intensive studies have been done on the fabrication and integrating it into GMR-based spintronic devices. However, the MR ratios in Fe_3O_4-based GMR devices were still low, for which the existence of antiphase boundaries may be one of possible

reasons. In this thesis, epitaxially-grown Fe_3O_4 thin films and nanowires were fabricated and the effect of antiphase boundaries on the electrical transport properties was studied to explore the possible reasons for the low MR ratios.

1.3 Semiconductor-based spintronics

1.3.1 Diluted magnetic semiconductors

Although GMR-based spintronic devices have made great progress recently, the lack of the ability in charge control limits their further application. At the same time, the semiconductors used for devices and integrated circuits do not contain the magnetic ions and are nonmagnetic. Very high magnetic fields have to be applied in order to create a useful difference in energy between the spin-up and spin-down electrons. If we can combine the properties of ferromagnetism and semiconductors, some novel magneto-optical and magneto-electrical devices, which can easily be integrated with current semiconductor technology, can be developed. However, difference in crystal structure and chemical bonding make this goal very difficult to be realized. [48, 49] By introducing magnetic elements into nonmagnetic semiconductor matrixes to make them magnetic, a new kind of materials named diluted magnetic semiconductors (DMSs) has been obtained. [50] After successful epitaxial growth of uniform (In, Mn)As films on GaAs substrates in 1989 [51] with partial ferromagnetic order, and ferromagnetic (Ga, Mn)As in 1996 [52] by Ohno group, numerous papers have been published in this research field from both in experiment and theory. Since magnetic properties in DMSs are a function of carrier concentration in the materials, it is possible to have the electrically or optically controlled magnetism through field-gating of transistor or optical excitation to alter the carrier density. Recently, several breakthroughs have been achieved based on InMnAs and GaMnAs, including electrical-field controlled

magnetization, [53] spin injection using GaAsMn, [54] current-induced domain-wall switching, [55] and optical control of magnetization in InMnAs [56].

1.3.2 Classification of diluted magnetic semiconductors

Although great breakthroughs discussed above have been achieved in InMnAs and GaMnAs, their low Curie temperatures limit their practical application into spintronic devices. A theoretical predication by Dietl *et al.* [57] demonstrated that the Curie temperature can be increased above room temperature in some *p*-type semiconductor-based DMSs [see Fig. 1.3]. Owing to the recent intensive studies, new DMSs with near or above room temperature ferromagnetism have been discovered such as Mn-doped $GdGeP_2$, [58] zinc-blende-CrAs, [59] $TiCoO_2$, [60] ZnCoO, [61] and ZnNiO [62]. Table 1.2 lists some milestones in DMSs research.

Figure 1.4 shows different types of DMSs. After the pioneering work on III-V group DMSs, other kinds of DMSs have been fabricated by different groups, which include II-VI, IV-VI, IV, oxides based and others. Some examples of different groups are also shown in Fig. 1.4. DMSs materials should be far more than those listed in this figure. Most of the 3*d* transition metals and 4*f* rare earth metals can be doped into the different semiconductor matrixes, leading to the ferromagnetic behaviour. DMSs with co-doping of different magnetic impurities, such as Ge:(Mn, Co) [63] and ($Mn_{0.03}$, $Co_{0.07}$)$Zn_{0.90}O$ [64], have also been studied.

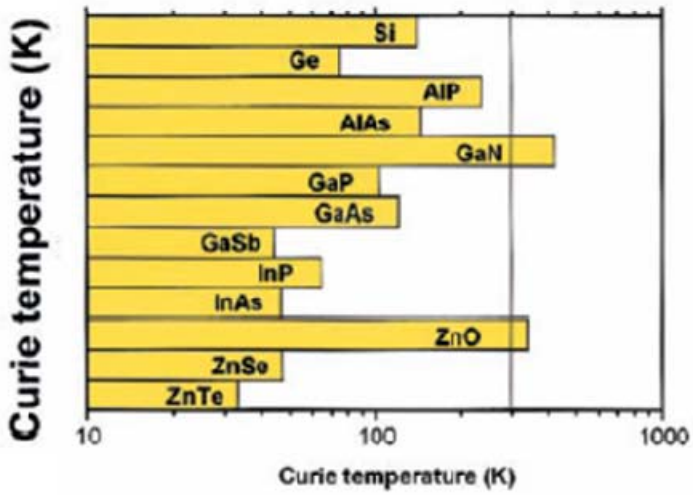

FIG. 1.3 Computed values of the Curie temperature T_C for various *p*-type semiconductors containing 5% of Mn and 3.5×10^{20} holes per cm^3. [After T. Dietl, 2000, Ref. 57]

Table 1.2 The list of some milestones in the DMSs research

Materials	Year	T_C (K)	Reference
InAs: Mn	1989	35	51
GaAs: Mn	1996	110	52
CaB6: la	1999	600	65
TiO_2: Co	2001	400	60
ZnO: Co	2001	Above 300	61
CrAs and CrSb	2001	Above 300	66
GaN: Mn	2001	940	67
Ge: Mn	2002	116	68
(Ga, Mn)P: C	2002	270 K	69
ZnTe: Cr	2003	300 ± 10	70
SnO_2: Co	2003	650	71
Cu_2O: (Co, Al)	2003	> 300	72
HfO_2	2004	> 500	73, 74

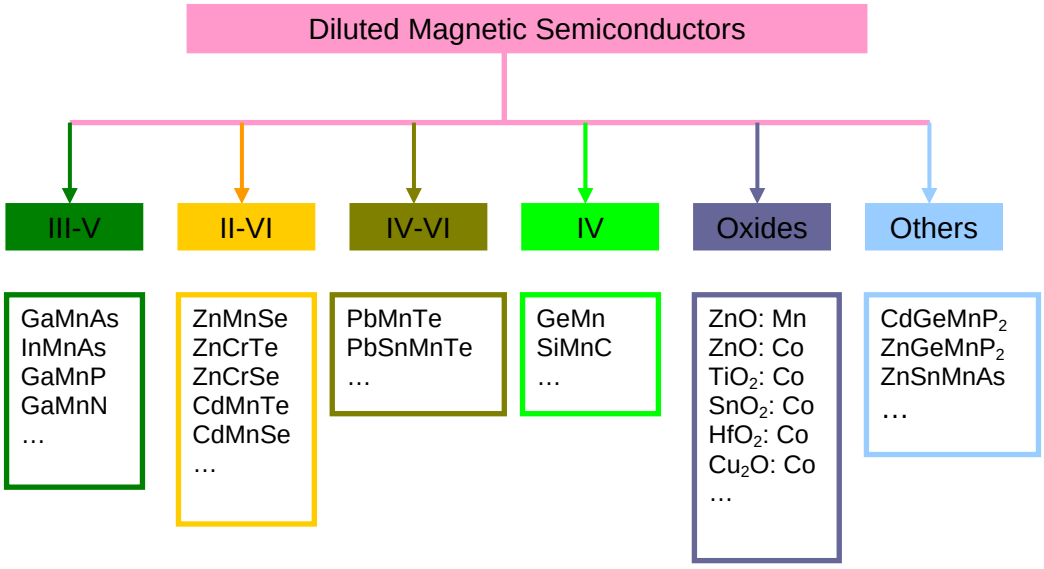

FIG. 1.4 Classification of DMSs materials.

Recently, special attention both in experiment and theory has been given to group-IV $Ge_{1-x}Mn_x$ diluted magnetic semiconductor due to its compatibility with mainstream Si-based electronics. So far, near or above room temperature ferromagnetism in $Ge_{1-x}Mn_x$ has been reported by several groups after the initial report of ferromagnetism in $Ge_{1-x}Mn_x$ [68]. However, various magnetic properties in $Ge_{1-x}Mn_x$ were obtained dependent on preparation methods. The mechanism of the ferromagnetic ordering in $Ge_{1-x}Mn_x$ system still remained controversial. In this thesis, amorphous $Ge_{1-x}Mn_x$ thin films, thin films of coexistence of amorphous $Ge_{1-x}Mn_x$, Ge crystallites, and high T_C secondary phase, granular $Ge_{0.74}Mn_{0.26}$ thin film, and δ-doped amorphous $Ge_{1-x}Mn_x$ thin films have been fabricated and characterized to explore the origin of ferromagnetism in $Ge_{1-x}Mn_x$ system and possible application into spintronic devices.

1.3.3 Ferromagnetism origin in diluted magnetic semiconductors

The origin of ferromagnetism in DMSs has been described by two main theoretical models. The first is based on mean-field theory with the assumption that DMSs are more-or-less random alloys. The second suggests that the magnetic atoms form small clusters or bound magnetic polarons (BMPs) that produce the observed ferromagnetism.

Figure 1.5 shows the schematic illustration of the mechanism of the carrier-mediated ferromagnetism. [75] When Mn substitutes Ga in the GaAs lattice, it acts as an acceptor, providing holes that mediate a ferromagnetic interaction between the local moments in the Mn atoms. Here the Mn atoms provide both the carriers and magnetic moments. At least 2% Mn atoms are necessary to provide a sufficiently high hole density. [75] The spin-spin coupling is assumed to be a long-range interaction, which allows the use of a mean-field approximation. As the direct interaction between Mn atoms is antiferromagnetic, the Curie temperature is a result of competition between the ferromagnetic and antiferromagnetic interactions. For most (II, Mn)VI semiconductors, subtitutional Mn impurities have 2+ valence states. The interaction between these moments is weak, and spin-orientations are random [see Fig. 1.5(a)]. In (III, Mn) V semiconductors, the Mn^{2+} ions can be as acceptors which localized a valence band hole [see Fig. 1.5(b)]. The valence-band spins tend to spread out. If the density of the valence hole is high enough and they are sufficiently to spread out to the whole system, they can mediate the effective interactions between nearly all subtitutional Mn moments and ferromagnetism appears [see Fig. 1.5(c)].

In the BMP model, the carrier concentration is assumed to be much less than the Mn density. The formation of BMPs results from the exchange interaction of localized holes with magnetic impurities. Thus, a BMP consists of a localized hole and some surrounding impurity spins [see Fig. 1.6]. The localized holes (large arrows) produce an

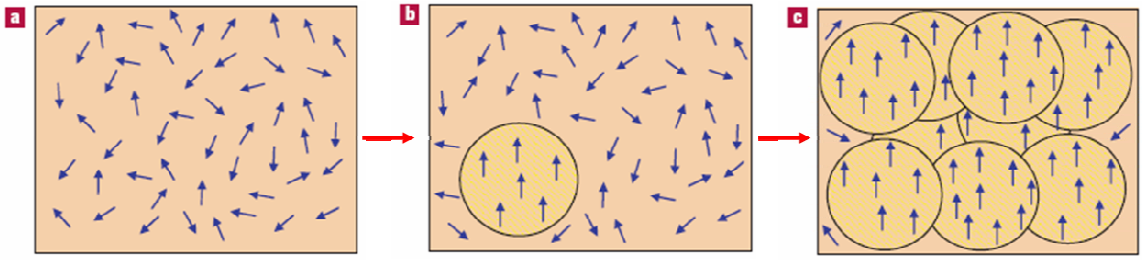

FIG. 1.5 Illustration of the mechanism of the carrier-induced ferromagnetism in diluted magnetic semiconductors. [After A. H. Macdonald, 2005, Ref. 75]

effective field for the impurity spins (small arrows). The energy minimum and the field maximum are achieved in this system when the direction of impurity spins is parallel or antiparallel to the effective field. [76] Although the interaction between holes is antiferromagnetic, the interaction can be ferromagnetic when the concentration of the magnetic impurities is high enough. BMPs begin to form at a certain temperature and their diameter will increase with decreasing temperature and eventually spreads out the whole system at the Curie temperature to produce ferromagnetism.

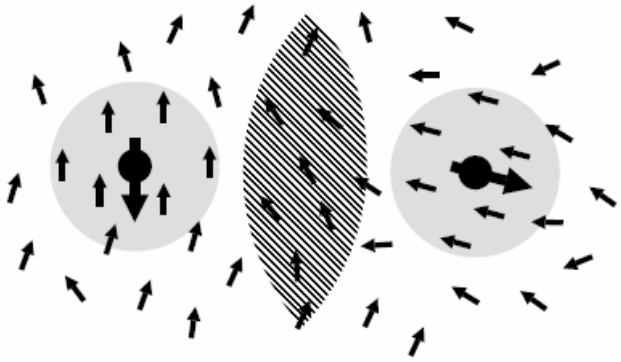

FIG. 1.6 Interaction of two bound magnetic polarons. The polarons are shown with gray circles. Small and large arrows show impurity and hole spins, respectively. [After S. D. Sarma, 2002, Ref. 76]

1.4 Objectives and motivation

In this study, we focused on the fabrication and characterization of two kinds of spintronic materials: Fe_3O_4 and $Ge_{1-x}Mn_x$. The former is a kind of half metal, while the latter is a type of DMS. Both of them have the potential for the application in the spintronic devices, and can be deposited in our two-chamber molecular beam epitaxy (MBE) system.

Epitaxially-grown Fe_3O_4 thin films and nanowires based on the thin films were fabricated. Structure, magnetic, and electrical transport properties were characterized. The effect of antiphase boundaries on the electrical transport properties was studied in detail to explore the possible reasons of the low MR ratios obtained in Fe_3O_4-based GMR devices until now.

Amorphous $Ge_{1-x}Mn_x$ thin films, thin films of coexistence of amorphous $Ge_{1-x}Mn_x$, Ge crystallites, and high T_C secondary phases, granular $Ge_{0.74}Mn_{0.26}$ thin film, and δ-doped amorphous $Ge_{1-x}Mn_x$ thin films were fabricated. Structure, magnetic, and electrical transport properties were characterized. Our studies aimed to answer the following unsettled questions in the $Ge_{1-x}Mn_x$ system: (a) What is the true origin of ferromagnetism? (2) What determines the various characteristic temperatures? (3) What kinds of properties will one obtain if the Mn concentrations can be increased further without the formation of dominative precipitates? (4) What is the role of disorder and carrier localization? (5) What is the spin-dependent transport across the interface between high T_C secondary phases and the host semiconductor matrix? (6) What is the effect of dimension on the spin-dependent transport? (7) How will the spacing between magnetic impurities affect the magnetic properties? (8) What is the possibility of applying it into practical spintronic devices?

1.5 Organization of this thesis

The outline of the thesis is as following:

Chapter 1: Introduction and literature survey

Some background information about spintronics and spintronic devices were introduced. Half metals and DMSs as two kinds of promising material candidates were reviewed, including the classification of different types of materials, recent breakthroughs, and some basic theoretical models. Based on these backgrounds, we stated clearly the objective and motivation of this work, followed by the outline of this thesis.

Chapter 2: Fabrication and characterization of Fe_3O_4 nanostructures

Epitaxially-grown Fe_3O_4 thin films and nanowires based on thin films were fabricated. Structure, magnetic and electrical transport studies were performed with emphasis on the effect of antiphase boundaries on electrical transport properties. A model was proposed to explain the obtained experimental results.

Chapter 3: Magnetic and electrical transport properties of amorphous $Ge_{1-x}Mn_x$ thin films

Amorphous $Ge_{1-x}Mn_x$ thin films ($0.153 < x < 0.42$) were fabricated. Detailed studies on structural, magnetic and electrical properties were carried out. The amorphous system was found to be composed of two phases: the high-temperature "cluster dopant" and the low-temperature highly ordered spin-glass-like phases. The

antiferromagnetic coupling between the two phases was invoked to explain the observed magnetic and electrical transport properties. Although anomalous Hall effect was observed in these amorphous samples, it did not origin from the homogeneous DMS phase.

Chapter 4: Magnetism and electrical transport properties of amorphous $Ge_{1-x}Mn_x$ thin films embedded with Ge crystallites and high T_C secondary phases and granular thin film

Amorphous $Ge_{1-x}Mn_x$ thin films embedded with Ge crystallites and high T_C secondary phases ($1.5\% < x < 56.1\%$) were fabricated. The magnetic properties were dominated by the secondary phases. Structural, magnetic and electrical transport properties of as-grown thin films were discussed. The thin film samples were further processed into nanowires with diameters of 5, 1, and 0.1 μm and their electrical transport properties were studied using the dynamic conductance technique. The work was also extended to the fabrication and characterization of a $Ge_{0.74}Mn_{0.26}$ granular thin film.

Chapter 5: Magnetism and electrical transport of amorphous δ-doped Ge:Mn thin films

Amorphous δ-doped Ge:Mn thin films with varying Ge and Mn layer thicknesses were fabricated. Structural, magnetic and electrical transport properties were discussed. It was found that the T^*_C values were very similar in both epitaxial and amorphous films. This suggests that the so-called Curie temperature reported in literature was not an indicator of global ordering, but rather the ordering temperature of magnetic clusters in the $Ge_{1-x}Mn_x$ system.

Chapter 6: A spin valve with amorphous $Ge_{0.67}Mn_{0.33}$ thin film as one of electrodes

A spin valve with the structure of $Ge_{0.67}Mn_{0.33}$ (30 nm)/Cu (2.4 nm)/NiFe (3 nm)/IrMn (8 nm) was fabricated. Typical spin-valve-like *M-H* curves was obtained with this structure.

Chapter 7: Conclusions and recommendation for future work

Some suggestions for future work were given after summarizing the main results obtained in this work.

References:

1 M. Quirk and J. Serda, Semiconductor manufacturing technology, Upper Saddle River, NJ: Prentice Hall, 2001.

2 G. E Moore, "No exponential is forever", IEEE ISSCC, February 2003

3 G. A. Prinz, "Magnetoelectronics", Science **282**, pp. 1660-1663, 1998.

4 S. A. Wolf, D. D. Awschalom, R. A. Buhrman, J. M. Daughton, S. Von Molnár, M. L. Roukers, A. Y. Chtchelkanova, D. M. Treger, "Spintronics: A Spin-Based Electronics Vision for the Future ", Science **294**, pp. 1488-1495, 2001.

5 I. Žutić, J. Fabian, and S. Das Sarma, "Spintronics: fundamentals and applications", Rev. Mod. Phys. **76**, pp323-410, 2004.

6 M. N. Baibich, J. m. Broto, A. Fert, F. N. Van Dau, and F. Petroff, P. Eitenne, G. Greuzet, A. Friederich, and J. Chazelas," Giant Magnetoresistance of (001)Fe/(001)Cr Magnetic Superlattices", Phys. Rev. Lett. **61**, pp. 2472-2475, 1988.

7 G. Binash, P. Grünberg, F. Saurenbach, and W. Zinn, "Enhanced magnetoresistance in layered magnetic structures with antiferromagnetic interlayer exchange", Phys. Rev. B **39**, pp. 4828-4830, 1989.

8 S. S. P. Parkin, "Origin of enhanced magnetoresistance of magnetic multilayers: Spin-dependent scattering from magnetic interface states", Phys. Rev. Lett. **7**1, pp. 1641-1644, 1993.

9 N. H. Mott, "The resistance and thermoelectric properties of the transition metals", Proc. Roy. Soc. A **153**, pp. 699-717, 1936.

10 B. Dieny, V. S. Speriosu, S. S. P. Parkin, B. A. Gurney, D. R. Wilhoit, and D. Mauri, "Giant magnetoresistive in soft ferromagnetic multilayers", Phys. Rev. B **43**, pp. 1297-1230, 1991.

11 J. Bass and W. P. Pratt Jr., "Current-perpendicular (CPP) magnetoresistance in magnetic metallic multilayers", J. Magn. Magn. Mater. **200**, pp. 274-289, 1999.

12 T. Miyazaki and N. Tezuka, "Giant magnetic tunneling effect in Fe/Al_2O_3/Fe junction", J. Magn. Magn. Mater. **139**, pp. L231-L234, 1995.

13 J. S. Moodera, L. R. Kinder, T. M. Wong, and R. Meservey, "Large magnetoresistance at room temperature in ferromagnetic thin film tunnel junctions", Phys. Rev. Lett. **74**, pp. 3273-3276, 1995.

14 S. S. P. Parkin, C. Kaiser, A. Panchula, P. M. Rice, B. Hughes, M. Samant, and S.-H. Yang, "Giant tunneling magnetoresistance at room temperature with MgO (100) tunnel barriers", Nat. Mater. **3**, pp. 862-867, 2004.

15 Y. H. Wu, Lecture notes for Spinelectronics.

16 M. Jullière, "Tunneling between ferromagnetic films", Phys.Lett. **54** A, pp. 225-226, 1975.

17 R. A. de Groot, F. M. Mueller, P. G. van Engen, and K. H. J. Buschow, "New Class of Materials: Half-Metallic Ferromagnets", Phys. Rev. Lett. **50**, pp. 2024-2027, 1998.

18 J.-H. Park, E. Vescovo, H.-J. Kim, C. Kwon, R. Ramesh, and T. Venkatesan, "Magnetic properties at surface boundary of a half-metallic ferromagnet $La_{0.7}Sr_{0.3}MnO_3$", Phys. Rev. Lett. **81**, pp. 1953-1956, 1998.

19 J. M. D. Coey, J. J. Verslujis, and M. Veenkatesan, "Half-metallic oxide point contacts", J. Phys. D: Appl. Phys. **35**, pp. 2457-2466, 2002.

20 J. M. de Teresa, A. Barthélémy, A. Fert, J. P. Contuor, F. Montaigne, and P. Seneor, "Role of metal-oxide interface in determining the spin polarization of magnetic tunnel junctions", Science **286**, pp. 507-509, 1999.

21 R. J. Soulen, Jr., J. M. Byers, M. S. Osofsky, B. Nadgorny, T. Ambrose, S. F. Cheng, P. R. Broussard, C. T. Tanaka, J. Nowak, J. S. Moodera, A. Barry, and J. M. D. Coey, "Measuring the spin polarization of a metal with a superconducting point contact", Science **282**, pp. 85-88, 1998.

22 R. Meservey and P. M. Tedrow, "Spin polarized electron tunneling", Phys. Rep. **238**, pp. 173-243, 1994.

23 J. M. D. Coey and S. Sanvito, "Magnetic semiconductors and half-metals", J. Phys. D: Appl. Phys. **37**, pp. 988-993, 2004.

24 S. P. Lewis, P. B. Allen and T. Sasaki, "Band structure and transport properties of CrO_2", Phys. Rev. B **55**, pp. 10253, 1997.

25 J. S. Parker, S. M. Watts, P. G. Ivanov, and P. Xiong, "Spin polarization of CrO_2 at and across an artificial barrier", Phys. Rev. Lett. **88**, pp. 196601, 2001.

26 Y. S. Dedkov, M. Fonine, C. Konig, U. Rudiger, G. Guntherodt, S. Senz, and D. Hesse, "Room-temperature observation of high-spin polarization of epitaxial CrO_2(100) island films at the Fermi energy", Appl. Phys. Lett. **80**, pp. 4181-4183, 2002.

27 J. M. D. Coey, A. E. Berkowitz, L. I. Balcells, F. F. Putris, and A. Barry, "Magnetoresistance of chromium dioxide powder compacts", Phys. Rev. Lett. **80**, pp. 3815-3818, 1998.

28 K. I. Kobayashi, T. Kimura, H. Sawada, T. Terakura, Y. Tokura, "Room-temperature magnetoresistance in an oxide material with an ordered double-perovskite structure", Nature **395**, pp. 677-680, 1998.

29 M. Bibes, K. Bouzehouane, A. Barthélémy, M. Besse, S. Fusil, M. Bowen, P. Seneor, J. Carrey, V. Cros, A. Vaurès, J.-P. Contour, and A. Fert, "Tunnel magnetoresistance in nanojunctions based on Sr_2FeMoO_6", Appl. Phys. Lett. **83**, pp. 2629-2631, 2003.

30 B. Nadgorny, I. I. Mazin, M. Osofsky, R. J. Soulen, P. Broussard, P. M. Stroud, D. J. Singh, V. G. Harris, A. Arsenov and Ya Mukovskii, "Origin of high transport spin polarization in $La_{0.7}Sr_{0.3}MnO_3$: Direct evidence for minority spin states", Phys. Rev. B **63**, pp. 184433, 2001.

31 M. Viret, M. Drouet, J. Nassar, J. P. Contour, C. Fermon and A. Fert, "Low-field colossal magnetoresistance in manganite tunnel spin valves", Europhys Letters **39**, pp. 545-549, 1997.

32 M. Bowen, M. Bibes, A. Barthélémy, J.-P. Contour, A. Anane, Y. Lemaitre, and A. Fert, "Nearly total spin polarization in $La_{2/3}Sr_{1/3}MnO_3$ from tunneling experiments", Appl. Phys. Lett. **82**, pp. 233-235, 2003.

33 D. C. Worledge and T. H. Geballe, "Spin-polarized tunneling in $La_{0.67}Sr_{0.33}MnO_3$", Appl. Phys. Lett. **76**, pp. 900-902, 2000.

34 Y. Ji, C. L. Chien, Y. Tomioka, and Y. Tokura, "Measurement of spin polarization of single crystals of $La_{0.7}Sr_{0.3}MnO_3$ and $La_{0.6}Sr_{0.4}MnO_3$", Phys. Rev. B **66**, pp. 012410, 2002.

35 J.-H. Park, E. Vescovo, H.-J. Kim, C. Kwon, R. Ramesh, and T. Venkatesan, "Direct evidence for a half-metallic ferromagnet", Nature **392**, pp. 794-796, 1998.

36 M. Pencicaud, B. Silberchiot, C. B. Sommers, J. Kubler, "Calculated electronic band structure and magnetic moments of ferrite", J. Magn. Magn. Mater. **103**, pp. 212-220, 1992.

37 J. J. Verslujis, M. Bari znd J. M. D. Coey, "Magnetoresistance of half-metallic oxide nanocontacts", Phys. Rev. Lett. **87**, pp. 026601, 2001.

38 G. Hu and Y. Suzuki, "Negative spin polarization of Fe_3O_4 in magnetite/manganite-based junctions", Phys. Rev. Lett. **89**, pp. 276601, 2002.

39 Yu. S. Dedkov, U. Rüdiger, and G. Güntherodt, "Evidence for the half-metallic ferromagnetic state of Fe_3O_4 by spin-resolved photoelectron spectroscopy", Phys. Rev. B **65**, pp. 064417, 2002.

40 D. J. Singh, "Magnetoelectronic effects in pyrochlore $Tl_2Mn_2O_7$: Role of Tl-O covalency", Phys. Rev. B **55**, pp. 313-316, 1997.

41 P. Velasco, J. A. Alonso, M. T. Casais, M. J. Martinez-Lope, "Analysis of magnetotransport data of $Tl_2Mn_2O_7$ pyrochlore: evidence for half-metallicity", J. L. Martinez, J. Phys.: Condens. Matter. **16**, pp. 8725-8732, 2004.

42 I. I. Mazin, "Robust half metallicity in $Fe_xCo_{1-x}S_2$", Appl. Phys. Lett. **77**, pp. 3000-3002, 2000.

43 R. A. de Groot, F. M Mueller, P. G. Van Ebgen and K. H. Buschow, "New class of materials: half-metallic ferromagnets", Phys. Rev. Lett. **50**, pp. 2024-2027, 1983.

44 R. Weht, W. E. Pickett, "Dipole matrix elements and the nature of charge oscillation under coherent interband excitation in quantum wells", Phys. Rev. B **60**, pp. 13006-13309, 1999.

45 P. Brown, K. Neumann, P. Webster, and K. Ziebeck, "The magnetization distributions in some Heusler alloys proposed as half-metallic ferromagnets", J. Phys.: Condens. Matter **12**, pp. 1827-1835, 2000.

46 L. J. Singh, Z. H. Barber, Y. Miyoshi, Y. Bugoslavsky, W. R. Branford, and L. F. Cohen, Los Alamos national Laboratory Preprint archive, Condensed Matter, cond-mat/031116, 2003.

47 S. Fujii, S. Sugimura. S. Ishida, and S. Asano, "Hyperfine fields and electronic structures of the Heusler alloys Co_2MnX (X=Al, Ga, Si, Ge, Sn)", J. Phys.; Condend. Matter **2**, pp. 8583-8589, 1990.

48 M. Tanaka, "Ferromagnet/semiconductor hybrid structures grown by molecular-beam epitaxy", J. Crys. Growth. **201-202**, pp. 660-669, 1998.

49 G. Prinz, K. Hathaway, "Quantum information and computation", Phys. Today **48**, pp. 24-30, 1995.

50 H. Ohno, "Making nonmagnetic semiconductors ferromagnetic", Science **281**, pp. 951-956, 1998.

51 H. Munekata, H. Ohno, S. von Molnár, A. Segmüller, L. L. Chang, and L. Esaki, "Diluted magnetic III-V semiconductors", Phys. Rev. Lett. **63**, pp. 1849-1852, 1989.

52 H. Ohno, A. Shen, F. Matsukura, A. Oiwa, A. Endo, S. Katsumoto, and Y. Iye, "(Ga,Mn)As: A new diluted magnetic semiconductor based on GaAs", Appl. Phys. Lett. **69**, pp. 363-365, 1996.

53 H. Ohno, D. Chiba, F. Matsukura, T. Omiya, E. Abe, T. Dietl, Y. Ohno, and K. Ohtani, "Electric-field control of ferromagnetism", Nature **408**, pp. 944-946, 2000.

54 Y. Ohno, D. K. Young, B. Beschoten, F. Matsukura, H. Ohno, and D. D. Awschalom, "Electrical spin injection in a ferromagnetic semiconductor heterostructure", Nature **402**, pp. 790-792, 1999.

55 M. Yamanouchi, D. Chiba, F. Matsukura, and H. Ohno, "Current-induced domain-wall switching in a ferromagnetic semiconductor structure", Nature **428**, pp. 539-542, 2004.

56 S. Koshihara, A. Oiwa, M. Hirasawa, S. Katsumoto, Y. Iye, C. Urano, H. Takagi, and H. Munekata, "Ferromagnetic order Induced by photogenerated carriers in magnetic III-V semiconductor heterostructures of (In,Mn)As/GaSb", Phys. Rev. Lett. **78**, pp. 4617-4620, 1997.

57 T. Dietl, H. Ohno, F. Matsukura, J. Cibert, and D. Ferrand, "Zener model description of ferromagnetism in Zinc-Blende magnetic semiconductors", Science **287**, pp.1019-1022, 2000.

58 G. A. Medvedkin, T. Ishibashi, T. Nishi, K. Hayata, Y. Hasegawa, and K. Sato, "Room temperature ferromagnetism in novel diluted magnetic semiconductor $Cd_{1-x}Mn_xGeP_2$", Jpn. J. Appl. Phys. **39**, pp. L949-L951, 2000.

59 H. Akinaga, T. Manago, M. Shirai, "Material design of half-metallic Zinc-Blende CrAs and the Synthesis by molecular-beam epitaxy", Jpn. J. Appl. Phys. **39**, pp. L1118-L1120, 2000.

60 Y. Matsumoto, M. Murakami, T. Shono, T. Hasegawa, T. Fukumura, M. Kawasaki, P. Ahmet, T. Chikyow, S. Koshihara, H. Koinuma, "Room-Temperature ferromagnetism in transparent transition metal-doped titanium dioxide", Science **291**, pp. 854-856, 2001.

61 K. Ueda, H. Tabata, T. Kawai, "Magnetic and electric properties of transition-metal-doped ZnO films", Appl. Phys. Lett. **79**, pp. 988-900, 2001.

62 T. Wakano, N. Fujimura, Y. Morinaga, N. Abe, A. Ashida, T. Ito, "Magnetic and magneto-transport properties of ZnO:Ni films", Physica E **10**, pp. 260-264, 2001.

63 F. Tsui, L. He, L. Ma, A. Tkachuk, Y. S. Chu, K. Nakajima, and T. chikyow, "Novel Germanium-based magnetic semiconductors", Phys. Rev. Lett. **91**, pp. 177203, 2003.

64 Z.-B Gu, C.-S. Yuan, M.-H. Lu, J. Wang, D. Wu, S.-T. Zhang, S.-N. Zhu, Y.-Y. Zhu, and Y.-F. Chen, "Magnetic and transport properties of (Mn, Co)-codoped ZnO films prepared by radio-frequency magnetron cosputtering", J. Appl. Phys. **98**, pp. 053908, 2005.

65 D. P. Young, D. Hall, M. E. Torelli, Z. Fisk, J. L. Sarrao, J. D. Thompson, H.-R. Ott, S. B. Oseroff, R. G. Goodrich, R. Zysler., "High-temperature weak ferromagnetism in a low-density free-electron gas", Nature **397**, pp. 412-414, 1999.

66 J. H. Zhao, F. Matsukura, K. Takamura, E. Abe, D. Chiba, and H. Ohno, "Room-temperature ferromagnetism in zincblende CrSb grown by molecular-beam epitaxy", Appl. Phys. Lett. **79**, pp. 2776-2778, 2001.

67 M. Zajac, R. Doradziński, J. Gosk, J. Szczytko, M. Lefeld-Sosnowska, M. Kamiñska, and A. Twardowski, M. Palczewska, E. Grzanka, W. Gebicki, "Magnetic and optical properties of GaMnN magnetic semiconductor", Appl Phys. Lett. **78**, pp. 1276-1278, 2001.

68 Y. D. Park, A. T. Hanbicki, S. C. Erwin, C. S. Hellberg, J. M. Sullivan, J. E. Mattson, T. F. Ambrose, A. Wilson, G. Spanos, and B. T. Jonker, "A group-IV ferromagnetic semiconductor: Mn_xGe_{1-x}", Science **295**, pp. 651-654, 2002.

69 N. Theodoropoulou and A. F. Hebard, M. E. Overberg, C. R. Abernathy, S. J. Pearton, S. N. G. Chu, and R. G. Wilson, "Unconventional carrier-mediated ferromagnetism above room temperature in ion-implanted (Ga, Mn)P:C", Phys. Rev. Lett. **89**, pp. 107203, 2002.

70 H. Saito, V. Zayets, S. Yamagata, and K. Ando, "Room-temperature ferromagnetism in a II-VI diluted magnetic semiconductor $Zn_{1-x}Cr_xTe$", Phys. Rev. Lett. **90**, pp. 207202, 2003.

71 S. B. Ogale, R. J. Choudhary, J. P. Buban, S. E. Lofland, S. R. Shinde, S. N. Kale, V. N. Kulkarni, J. Higgins, C. Lanci, J. R. Simpson, N. D. Browning, S. Das Sarma, H. D. Drew, R. L. Greene, and T. Venkatesan, "High temperature ferromagnetism with a giant magnetic moment in transparent Co-doped $SnO_{2-\delta}$", Phys. Rev. Lett. **91**, pp. 077205, 2003.

72 S. N. Kale, S. B. Ogale, S. R. Shinde, M. Sahasrabuddhe, V. N. Kulkarni, R. L. Greene, and T. Venkatesan, "Magnetism in cobalt-doped Cu_2O thin films without and with Al, V, or Zn codopants", Appl. Phys. Lett. **82**, pp. 2100-2102, 2003.

73 M. Venkatesan, C. B. Fitzgerald and J. M. D. Coey, "Thin films: Unexpected magnetism in a dielectric oxide", Nature **430**, pp. 630, 2004.

74 J. M. D. Coey, M. Venkatesan, P. Stamenov, C. B. Fitzgerald, and L. S. Dorneles, "Magnetism in hafnium dioxide", Phys. Rev. B **72**, pp. 024450, 2005.

75 A. H. Macdonald, P. Schiffer, and N. Samarth, "Ferromagnetic semiconductors: moving beyond (Ga, Mn)As", Nat. Mater. **4**, pp. 195-202, 2005.

76 A. Kaminski and S. Das Sarma, "Polaron percolation in diluted magnetic semiconductors", Phys. Rev. Lett. **88**, pp. 247202, 2002.

CHAPTER 2

FABRICATION AND CHARACTERIZATION OF Fe_3O_4 NANOSTRUCTURES

2.1 Introduction

Magnetite (Fe_3O_4), historically known as lodestone, is the first known magnetic material with a Curie temperature of 858 K. It has a well-known ferrimagnetic spinel structure, in which the moment of Fe^{3+} localized on tetrahedral sites are aligned antiparallelly to the moments of the equal mixture of Fe^{2+} and Fe^{3+} on octahedral sites [see Fig. 2.1]. [1] Thus, the net moment is 4.0 μ_B per formula unit.

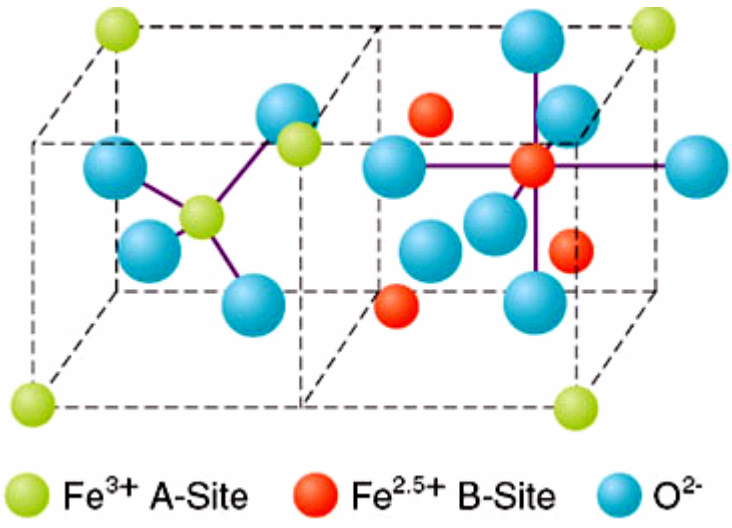

FIG. 2.1 1/4 Fe_3O_4 unit cell of inverse spinal structure. A and B sites are tetrahedral and octahedral position, respectively. [Ref. 1]

In 1939, Verwey discovered the metal-to-insulator transition at about 120 K in Fe_3O_4, where the resistivity increased sharply by two orders of magnitude. [2] This transition was named as Verwey transition. Verwey postulated that charge order-disorder on the octahedral sites was the origin of this transition. However, the mechanism about Verwey transition remained controversial despite the intensive studies more than half a century. [3-8]

Recently, Fe_3O_4 has received a renewed interest because band structure calculations indicate that it has a half-metallic or fully spin-polarized structure, [9,10] where the Fermi level lies in the $\downarrow$ t_{2g} band of octahedral irons [see Fig. 1.2(c)]. [11] Experimentally, spin-polarization (P) value as high as 80% has been obtained in the photoemission measurements [12] and large magnetoresistance was also found in point contacts at room temperature from which the value of P as large as ~72% can be inferred. The half-metallic property makes Fe_3O_4 a promising material as electrode for the application in various spintronic devices, such as spin valves and MTJs.

Various thin film growth techniques, including MBE, [13,14] sputtering, [15] ion beam deposition system, [16] evaporation, [17] and pulsed laser deposition (PLD), [18,19] have been employed to fabricate epitaxial and polycrystalline Fe_3O_4 thin films on a variety of substrates (Al_2O_3, MgO, Pt, Si, $SrTiO_3$, etc.). Most of the epitaxial [20-22] and polycrystalline films [23, 24] exhibit a clear Verwey transition near 120 K and a large negative MR under a high magnetic field at room temperature. There are several Fe:O compounds besides Fe_3O_4 such as FeO, α-Fe_2O_3 and γ-Fe_2O_3. The existence of other Fe:O phases in Fe_3O_4 thin films will significantly impair half-metallic property. Therefore, it is necessary to optimize the preparation conditions to avoid the formation of other Fe:O phases. Electrical transport and magnetic properties measurements can provide direct evidences to tell if other phases exist in Fe_3O_4 thin films, which will be

discussed later. Table 2.1 summaries the various preparation methods for Fe_3O_4 thin films.

Table 2.1 Various preparation methods for Fe_3O_4 thin films

Methods	Target	P (O_2)	T_s (K)	Substrate	Film Quality	Reference
MBE	Fe	10^{-6} mbar	-	MgO (100)	Epitaxy	13
	Fe	10^{-5} Pa	523	α-AL_2O_3 (0001) MgO (100)	Epitaxy	25
PLD	Fe_3O_4	10^{-6} Torr	573	MgO (100)	Epitaxy	26
	Fe_3O_4	$2.5x10^{-3}$ mbar	603	Si (001) with TiN/MgO buffer layer	Epitaxy	27
	α-Fe_2O_3	-	-	Si	Polycrystal	28
	α-Fe_2O_3	$1x10^{-5}$ Torr	843	α-Al_2O_3 (0001) $SrTiO_3$	Epitaxy	20
Sputtering	Fe_3O_4 and Fe_2O_3	-	-	Si (001) and glass	Polycrystal	29
	Fe_3O_4	-	573	MgO (100)	Epitaxy but with γ-Fe_2O_3 Phase	30
	Fe	-	273	Glass and Kapton	Polycrystal	15
Polarized neutron reflectivity	Fe	-	-	Pt (111)	Epitaxy	31
UHV Ion Beam deposition system		$3x10^{-4}$ Torr	623	MgO (110)	Epitaxy	16

Although Fe_3O_4 is theoretically regarded as an ideal material for use in the spintronic devices, the results of integrating Fe_3O_4 into spin valves and MTJs have not tallied with the expectation. A MR ratio of only 0.04% at room temperature was obtained in the CPP spin valve with the structure of Au (10 nm) /Ni80Fe20 (NiFe) (5 nm) /Au (5 nm)/ Fe_3O_4 (d nm)/Au (100 nm) on MgO (100) substrate. [32] A lower MR ratio of 0.16% at 90 K was observed in the spin valve of Fe_3O_4/Au/Fe_3O_4 and Fe_3O_4/Au/Fe on MgO (001)

Table 2.2 Device application of Fe_3O_4 thin films

Methods	Structure	Substrate	Results	Reference
Rf-sputtering	Au (10nm) / $Ni_{80}Fe_{20}$ (NiFe) (5nm) / Au (5nm)/ Fe_3O_4 (dnm)/Au (100nm)	MgO (100)	MR (%)=-0.04% at RT, ΔRA=1.5 mΩ μm^2	32
Dc-sputtering	Fe_3O_4/Au/Fe_3O_4 and Fe_3O_4/Au/Fe	MgO(100)	MR=-0.16% at 90 K	33
MBE	Fe_3O_4 / MgO/ Fe_3O_4	MgO (100)	MR (%)=0.5% at RT MR (%)=1.5% at 150 K	34
MBE	$Co_xFe_{3-x}O4$/Fe_3O_4/MgO/Fe_3O_4	$MgAl_2O_4$ (001)	MR<0.4% at RT	35
PLD	Fe_3O_4 / $CoCr_2O_4$ (CCO) / $La_{0.7}Sr_{0.3}MnO_3$	STO (110) and (100)	MR (%)=-25% at 60K, MR (%)=-1% at 275K,	36
UHV ion Beam Deposition System	V (10nm)/ Ru (60nm)/ Fe_3O_4 (25-100nm)/AlO/CoFe/NiFe/Ru	MgO (110)	MR (%)=14 % at room trempertature	16
Rf-sputtering	Fe_3O_4 (50nm)/ AlO_x (1.2nm) / $Co_{75}Fe_{25}$ (10nm)	MgO (110) buffered with TiN (300nm)	MR (%)=10% at RT	37
PLD	Fe_3O_4/Mg_2TiO_4/LSMO	STO (110)	MR(%)=26% at 70 K MR(%)<5% at RT	38

substrate. [33] In comparison with the spin valves, the MR ratios in MTJs with Fe_3O_4 electrodes were also disappointing. The MR ratios at room temperature in the epitaxial MTJs with the structure Fe_3O_4/MgO/Fe_3O_4 on MgO (100) substrate were lower than 1%. [34,35] Various other Fe_3O_4-based MTJs with the barrier materials of $CoCr_2O_4$, [36] AlO_x, [16,37] and Mg_2TiO_4 [38] have produced a highest MR ratio of only 14% at room temperature. Table 2.2 summaries the results related to the attempts of integrating Fe_3O_4 as an electrode for spin valves and MTJs. The low MR ratios have been attributed to the issues of stoichoimetry, crystal defects in Fe_3O_4, and the structural disorder in the interface between the multilayers. The presence of random spin direction at the interface would defeat the high spin-polarized property and the interface scattering in these

multilayer structures, which will lead to a lower MR ratio. However, MR ratios have been still low although a sharp interface was observed in high resolution transmission electron microscope (HRTEM). [21,39] In addition, Mössbauer spectroscopy has shown that there were no significant difference between the interfaces and the interior of the Fe_3O_4 layers in both the composition and magnetic structure. [40]

The most possible reason for the low MR ratio is the presence of antiphase boundaries (APBs) in Fe_3O_4 thin film. Margulies *et al.* first found APBs in Fe_3O_4 epilayer grown on MgO substrate. [41] After Margulies *et al.*, Zhou *et al.* and Moussy *et al.* also observed APBs in Fe_3O_4 thin films grown on Si and Al_2O_3 substrates, respectively. [24, 42] Now it is commonly believed that APBs are the intrinsic consequence of nucleation and growth defects independent of preparation methods and substrates. As shown in Fig. 2.2, APBs are due to the result of the coalescence of islands, which are either rotated over 90º with respect to each other, or shifted, or both. New antiferromagnetic 180º Fe-O-Fe superexchange paths which are not present in the bulk Fe_3O_4 samples are formed and indicated with solid lines in Fig. 2.2. Because the exchange interaction is antiferromagnetic across APBs, [13] the presence of APBs will block the path of the spin-polarized electrons, and make spin directions random. The presence of APBs is responsible for many abnormal magnetic and electrical phenomena observed in Fe_3O_4 thin films, such as the unsaturated magnetization in high fields [41] and the resistivity increase in the epitaxial Fe_3O_4 thin films [43].

So far, the work on APBs has been focused on thin-film samples, which makes it difficult to elucidate the electron transport mechanism due to the existence of too many randomly distributed APBs or tunnel junctions in a two-dimensional plane. In this chapter, we report a systematic study of structure, magnetic, and electrical transport properties of both epitaxial Fe_3O_4 thin films and nanowires grown on α-Al_2O_3 (0001)

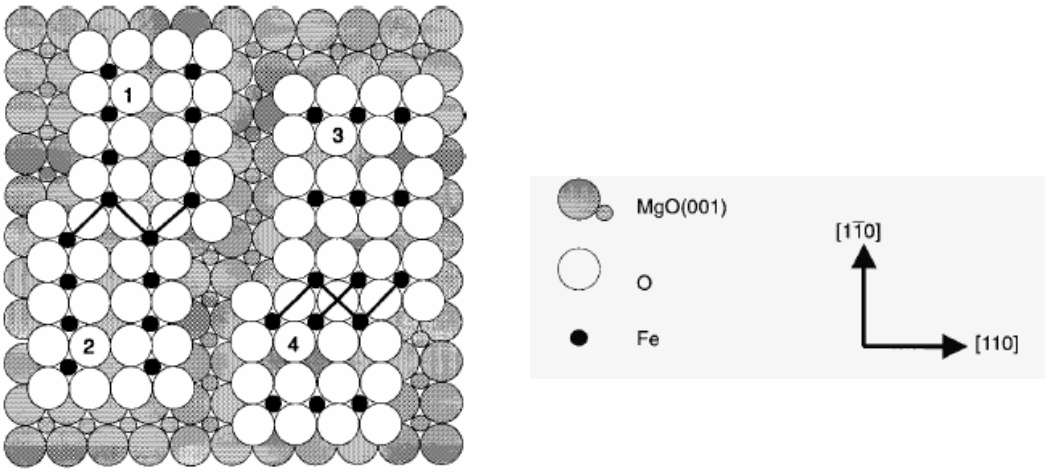

FIG. 2.2 Schematic representation of the formation of antiphase boundaries of a Fe_3O_4 film on MgO (100) substrate. [After F. C. Voogt, 1998, Ref. 40]

substrates. The latter allows one to confine the APBs or tunnel junctions in a one-dimensional nanowire, which reduces substantially the number of antiphase boundaries, or junctions. A schematic illustration to show the electrical transport difference across APBs between a thin film and a nanowire is shown in Fig. 2.3. This study will elucidate the effect of APBs on the electrical transport properties in Fe_3O_4 thin films, which is crucial to understand MR mechanism so as to further increase MR ratios in Fe_3O_4-based spintronic devices.

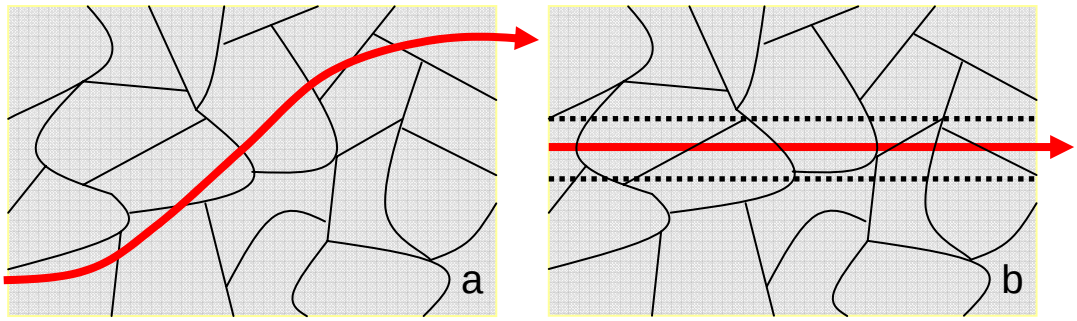

FIG. 2.3 Schematic illustration to show the electrical transport difference between (a) a thin film and (b) a nanowire, where the solid black and red lines denote the antiphase boundaries and current direction, respectively.

2.2 Experiments

2.2.1 Experimental setup

Fe_3O_4 thin films were fabricated by MBE (Model EW-5 of EIKO Corporation Ltd. of Japan). Its schematic diagram is shown in Fig. 2.4. It consists of two chambers: the loadlock chamber and the main chamber. Both rotary pump (RP) and turbo molecular pump (TMP) are used to evacuate the loadlock and the main chambers. The base pressures in the loadlock and the main chambers are $2x10^{-7}$ and $1x10^{-9}$ Torr, respectively.

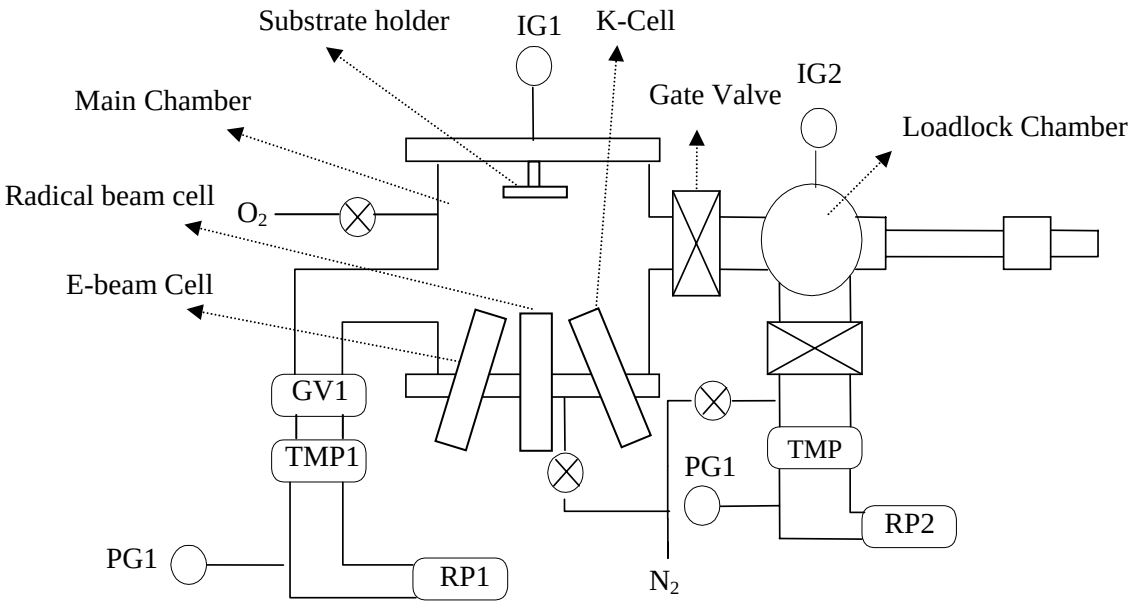

FIG. 2.4 Schematic diagram of EW-5 MBE system.

As shown in Fig. 2.4, the main chamber is equipped with three cells: an e-gun cell, a Knudsen-cell (K-cell), and a radical beam cell. In the e-gun cell, a tungsten filament is placed in the vicinity of a carbon crucible. When a high voltage is applied, the electrons from the filament will be accelerated toward the crucible and bombard the source materials, which causes local heating and evaporation of the source materials. If the mean free path of the evaporated source materials is larger than the distance between the

substrate and the crucible, the source materials will finally deposit on the substrate surface. In the K-cell, a conducting crucible, containing the source materials, is heated electrically with a high current to make the materials evaporate. The radical cell can generate O_2 plasma, which helps to oxidize the evaporated materials towards the heated substrate in the chamber. During the deposition, the substrate can be heated to as high as 1100 ºC so that the evaporated materials can be distributed evenly on the substrate. And the substrate holder can rotate continuously during the deposition to ensure a uniform growth of the thin film.

2.2.2 Experimental details

The Fe_3O_4 thin films (around 150 nm) were prepared on α-Al_2O_3 (0001) single crystal substrates. During the growth, the iron metal was evaporated by an electron beam with an oxygen partial pressure of 1.0×10^{-5} Torr. The deposition rate was about 0.04 nm/s with a substrate temperature of 573 K. Structural, magnetic, and electrical transport properties of the as-grown thin films were characterized by a Cu K_α radiation (λ=0.15418 nm) x-ray diffraction (XRD) and HRTEM, quantum design MPMS XL superconducting quantum interference device (SQUID) magnetometer, vibrating sample magnetometer (VSM), and dc four-probe techniques, respectively.

The Fe_3O_4 nanowires were fabricated using electroplated Ni nanowires (average diameter of 200 nm and a length of 30 μm) as the hard mask. The typical fabrication processes involved dispersing the Ni nanowires on the as-grown Fe_3O_4 thin film, ion milling of uncovered film, ultrasonic cleaning of the Ni nanowires and electrode formation using a double-layer resist process. The location of nanowires, positioning and deposition of electrodes (Ti (20 nm) / Au (100 nm)) were performed with laser writer (LW-2002) and e-beam evaporator (Edwards Auto 306), respectively. The finally

finished Fe_3O_4 nanowire exhibited a width of about 300 nm. Schematic illustration of the fabrication process of a nanowire was shown in Fig. 2.5. After the fabrication of the nanowire, it has further been etched by focused ion beam (FIB) to a smaller dimension to study MR effect. Nanoconstrictions with widths of 150 and 80 nm were obtained by consecutively etching the original nanowire. The FIB images of the nanowires with nanoconstriction were shown in Figs. 2.6(a) and 2.6(b).

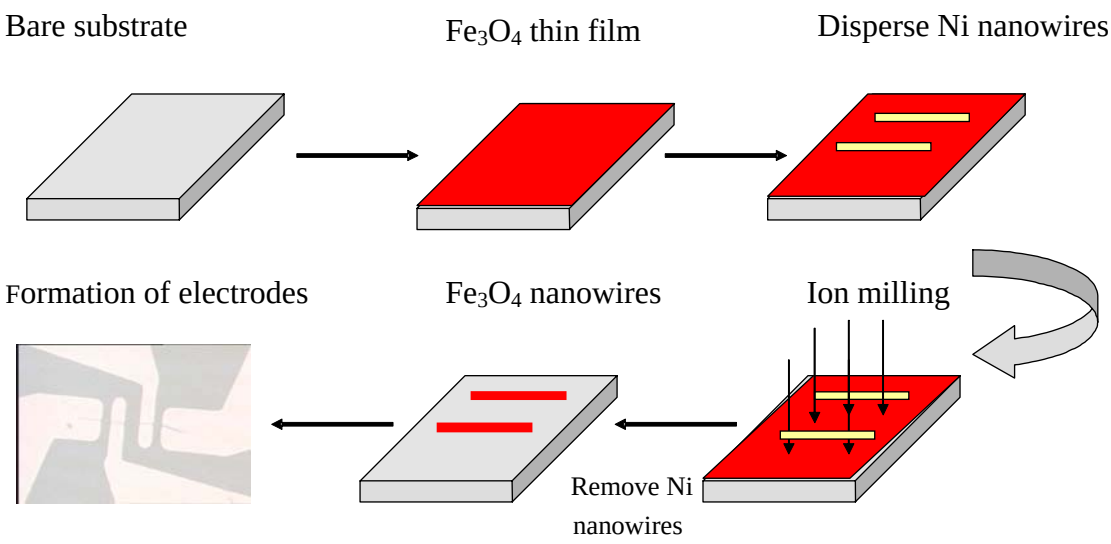

FIG. 2.5 Schematic illustration of the fabrication process of Fe_3O_4 nanowires.

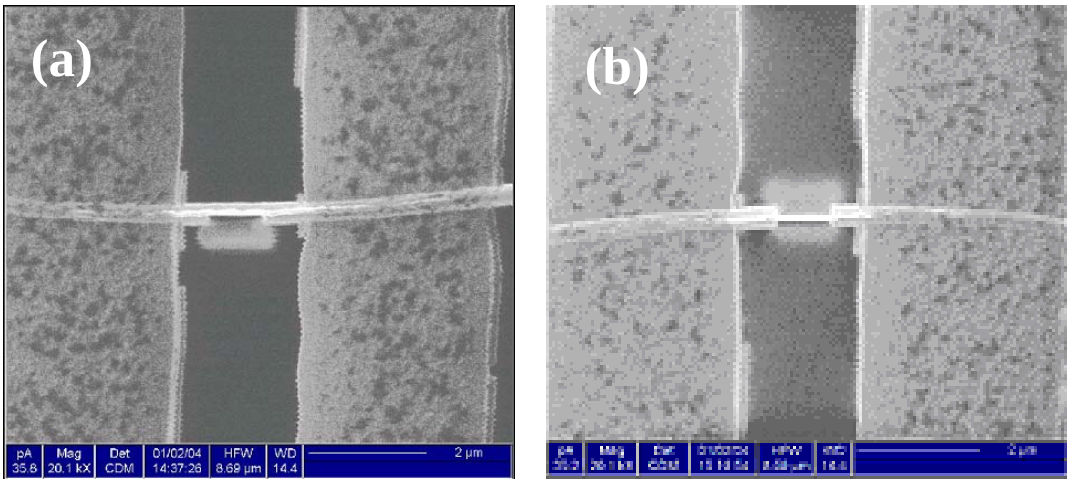

FIG. 2.6 FIB images of Fe_3O_4 nanoconstrictions with a width of (a) 150 and (b) 80 nm, and a length of 1 μm.

2.3 Results and discussion

2.3.1 Structural properties

Figure 2.7 shows the typical XRD spectrum of Fe_3O_4 thin films grown on α-Al_2O_3 (0001) substrate. Only the [111] peaks are observed in the figure without detecting any other peaks belonging to other Fe:O compounds such as FeO, α-Fe_2O_3 and γ-Fe_2O_3. The inset of Fig. 2.7 shows the rocking curve of (222) peak. The full width at half maximum of ~ 0.28^o is obtained, indicating that high quality Fe_3O_4 thin films have been fabricated.

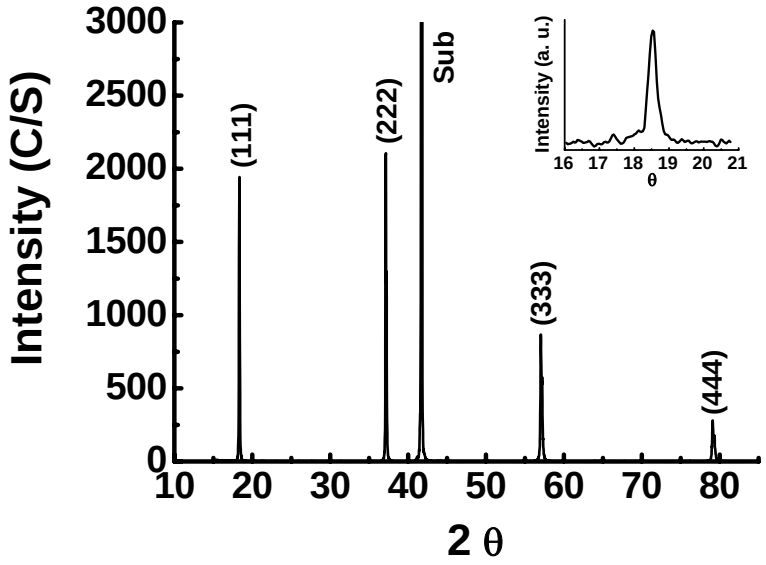

FIG. 2.7 XRD pattern of Fe_3O_4 thin films. Inset: the rocking curve of (222) peak.

Figure 2.8(a) shows the plane-view dark-field high resolution TEM image. The black lines in the figure are antiphase boundaries, which are irregular with an average size of ~ 100 nm. No other defects are found except APBs, which is consistent with the XRD results shown in Fig. 2.7. In comparison with the domain size of the thin film sample by Moussy *et al.*, [42] our sample shows a larger average domain size due to

thicker film. In Fig. 2.8(b), we can observe more clearly APBs by magnifying one of them along the arrow direction.

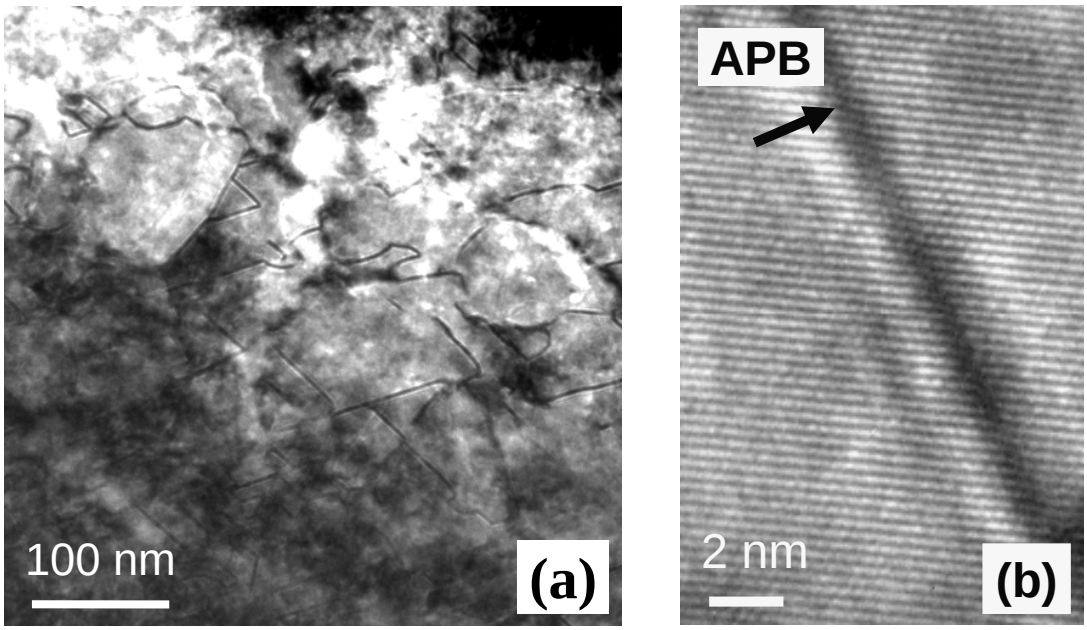

FIG. 2.8 (a) Plane-view dark-field high resolution TEM image of Fe_3O_4 thin films. The black lines are antiphase boundaries; (b) magnified APBs as indicated by the arrow.

2.3.2 Magnetic properties

The magnetization versus temperature curves of zero-field-cooled (ZFC) and field-cooled (FC) of the thin film with an applied magnetic field of 100 Oe are shown in Fig. 2.9. The ZFC curve is taken by first cooling the sample from 300 to 2 K at zero field and then measuring the magnetization at an applied field of 100 Oe. The FC curve is taken by the same procedure except that the cooling was done with an applied field of 100 Oe. Three temperature-dependent magnetization behaviours can be observed that reflects the various interaction mechanisms that are involved. These regions are (I) 2 K $< T <$ 120 K; (II) 120 K $< T <$ 130 K; (III) 140 K $< T <$ 400 K. In region (I), the moment is almost constant; in region (II), the sharp increase in the magnetic moment around 120 K can be clearly observed. This is another indication of good stoichiometry and high

crystalline phase of the fabricated thin film. In region (III), the moment decreases with increasing temperature.

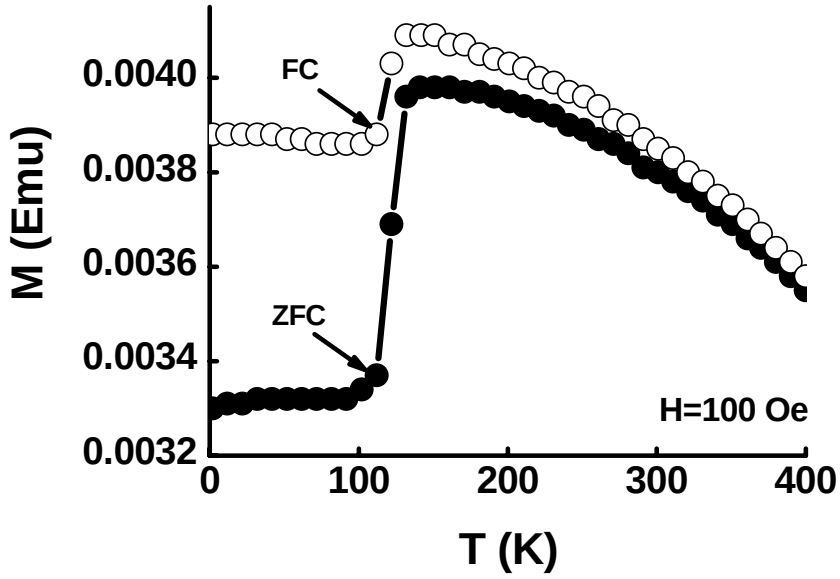

FIG. 2.9 ZFC and FC curves of Fe_3O_4 thin films with an applied magnetic filed of 100 Oe. The direction of the magnetic field is along the sample plane.

Figure 2.10 shows the *M-H* curves at different temperatures of Fe_3O_4 thin films. A clear ferromagnet-like hysteresis loop is seen with a coercivity of 300 Oe at room temperature. Figure 2.11 shows H_c and M_r at different temperatures. From the graph we can see that the coercivity decreases by only 60 Oe from 300 to 130 K. However, it undergoes a sudden change from 130 to 110 K, increasing from 220 Oe at 130 K to 730 Oe at 110 K. It shows a change of anisotropy due to Verwey transition around 120 K where a structural change from cubic to monoclinic occurs. In comparison with the change in H_c, M_r increases from 0.00171 emu at 300 K to 0.0026 emu at 130 K. Below Verwey transition, a plateau is observed, which is consistent with single crystalline data. [44]

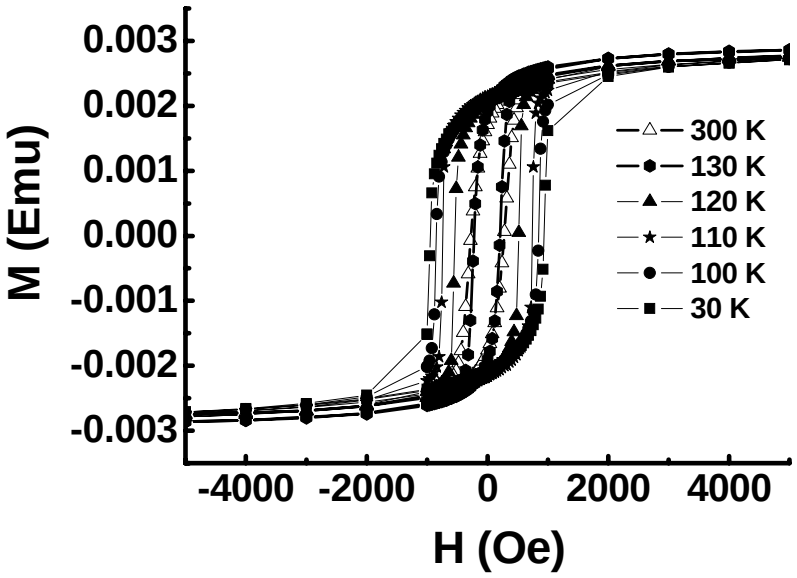

FIG. 2.10 *M-H* curves of Fe_3O_4 thin films at different temperatures.

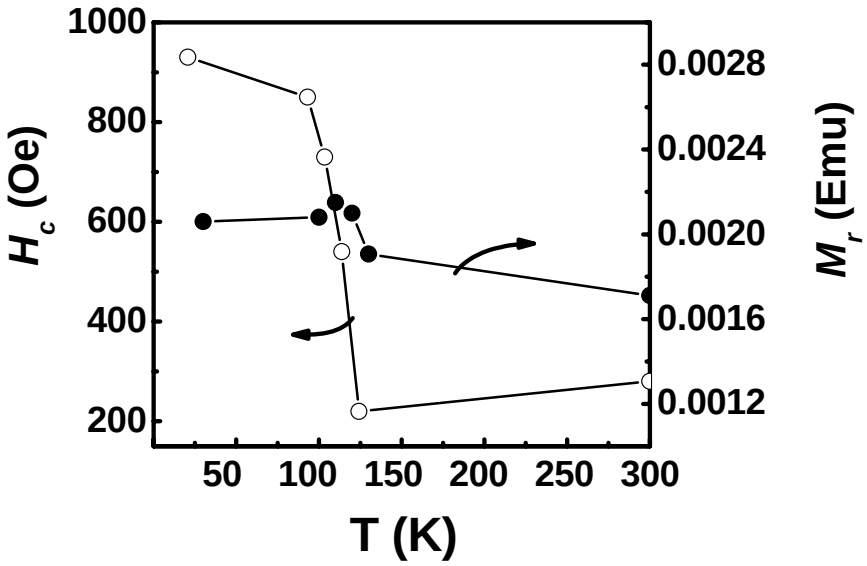

FIG. 2.11 Temperature-dependent coercivity (H_c) and remanence (M_r) of Fe_3O_4 thin films.

Figure 2.12 shows the *M-H* curves measured at 300 K when the magnetic field is parallel and perpendicular to the sample plane. It can be found that the magnetization in the perpendicular direction is more difficult to achieve saturation than that in the

parallel direction. The more slowly saturation in the perpendicular direction should be due to the strong in-plane anisotropy. Liu *et al.* [15] also observed the strong in-plane anisotropy in their polycrystalline thin films.

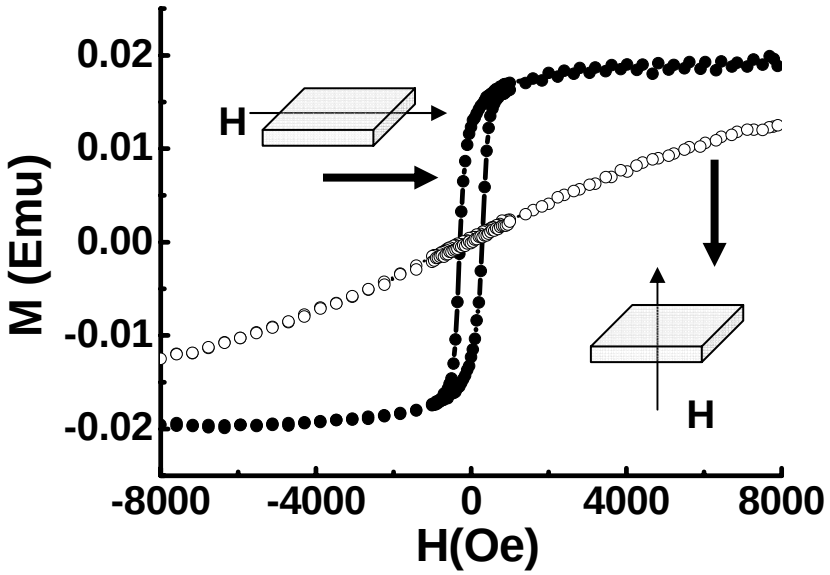

FIG. 2.12 Parallel and perpendicular *M-H* loops at 300 K of Fe_3O_4 thin films.

2.3.3 Electrical transport properties

We now turn to the electrical transport properties. Since the ultimate purpose of the work on Fe_3O_4 is to integrate it into current spin valves or MTJs using their features of high spin polarization and high Curie temperature, it is of great importance to carry out the electrical transport studies, especially the transport across the APBs. The resistivity of our film is ~ 0.008 Ω cm, which is a little higher than the bulk value of 0.005 Ω cm, and much less than 0.18 Ω cm of the polycrystalline samples reported [15]. Figure 2.13 shows the temperature dependence of the resistance R_T normalized to the room temperature resistance $R_{300\ K}$ for both a thin film and a nanowire. A clear Verwey transition is seen in both curves at 120 K. In comparison with the stoichoimetric single

crystals, our sample shows a slightly broader transition which might be caused by the departure of Fe:O stoichoimetry or large lattice mismatch between Fe_3O_4 and α-Al_2O_3 (0001) substrate. Although it is not so obvious, the nanowire indeed shows a slightly sharper transition compared to the thin film, which is expected due to the decrease in randomness inside a smaller volume of sample. Drabble *et al.* [45] and Gong *et al.* [22] found that the transport at low temperatures in Fe_3O_4 obeyed a variable hopping mechanism [$R = R_0 \exp(\alpha / T)^{1/4}$]. We replot the temperature dependence of resistivity as $\log R$ versus $T^{-1/4}$ of both the thin films and nanowires in the inset of Fig. 2.13. Both curves show nonlinear relation around the Verwey transition temperature, which is different from the grain boundary tunnelling mechanism observed in the polycrystalline samples by Liu *et al.* [15]

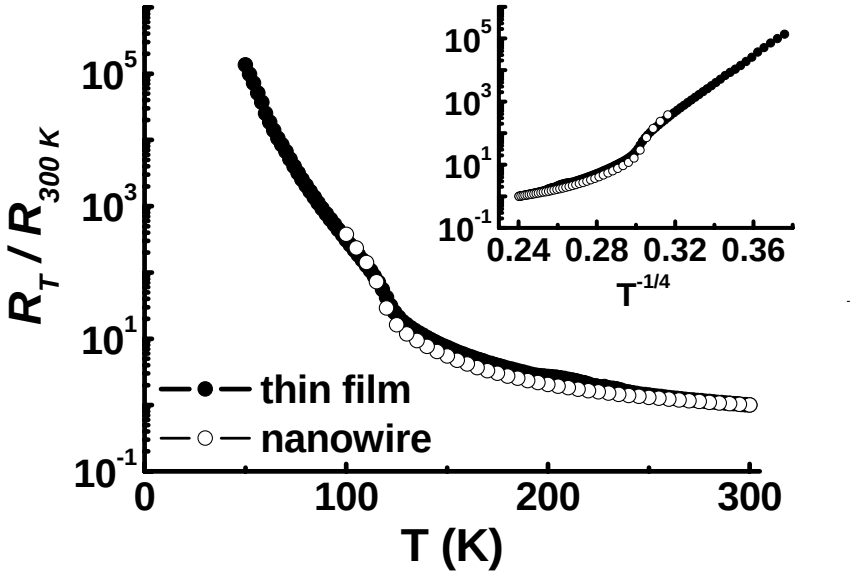

FIG. 2.13 Normalized *R-T* curves for both a thin film and a nanowire. The inset shows the dependence of resistance on $T^{-1/4}$ for both a thin film and a nanowire.

Figure 2.14 shows the typical MR curves at 300 K. The MR is defined as

$$MR = (R_H - R_0) / R_0 \ , \tag{2.1}$$

where R_H and R_0 are the resistance at an applied field and zero field. The in-plane MR is isotropic for thin films, but it is anisotropic for the nanowires. The MR ratio of thin films is about 1% at a magnetic field of 6000 Oe. The nanowire exhibits an almost same MR as that of the thin film in the longitudinal direction, but a somewhat reduced MR in the traverse direction. The former shows a shape which is universal to almost all the Fe_3O_4 films grown by different techniques. [13, 15, 18, 19] This can be understood as being caused by the AFM coupling across APBs as discussed in Refs. 13 and 18. Depending on the domain size, the spins at the centre of the grains may switch earlier or easier than those at the boundaries. This may explain the difference in the MR curves at low and high fields. This argument is also supported by the slow change of transverse MR of nanowires at the low field which can be understood as being caused by the shape anisotropy in the centre region of the domain, whereas in the high-field region the MR curve is almost the same as that in the longitudinal direction.

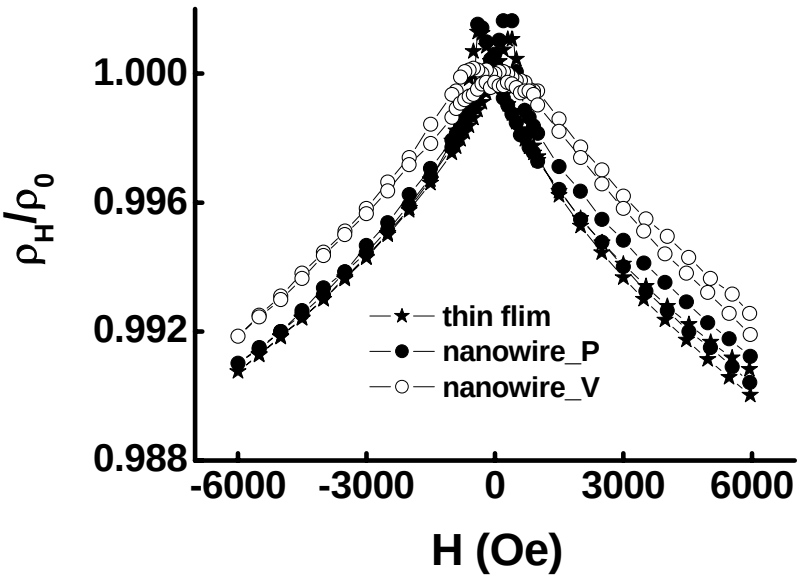

FIG. 2.14 Normalized MR curves for both thin films and nanowires at 300 K (Nanowire_P: field parallel to the wire axis; Nanowire_V: field perpendicular to the nanowire axis.

Figure 2.15 shows the MR curves of a nanowire before and after FIB etching. Although the basic shapes are almost same, the MR ratios in both longitudinal and transverse directions decrease with reduced dimension. Due to the smaller width, APBs may have a more pronounced effect on the electrical transport. The current has to pass across the APBs and by-pass current across APBS will be further reduced due to a smaller width. As for the transverse direction, the shape anisotropy will become more pronounced when the dimension decreases.

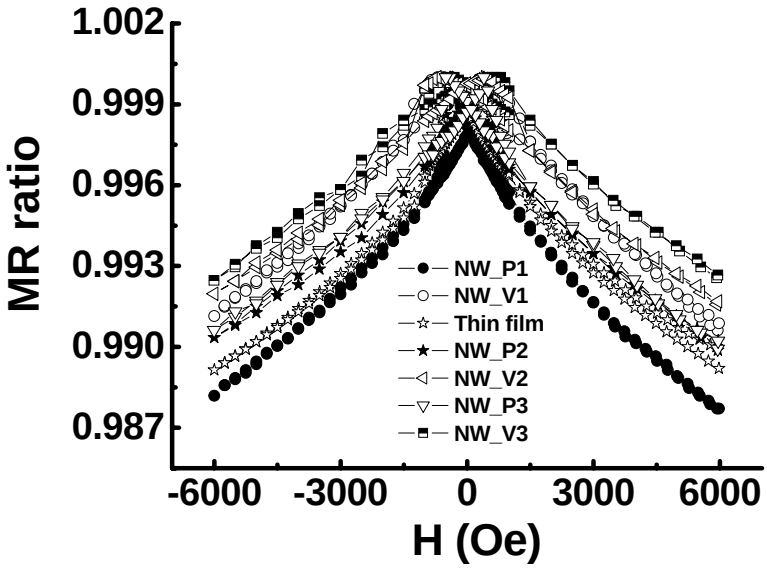

FIG. 2.15 MR ratios of the original nanowire and nanoconstriction. 1: original nanowire with a diameter of 300 nm; 2: nanowire after first FIB etching with a nanoconstriction of 150 nm; 3: nanowire after second FIB etching with a nanoconstriction of 80 nm.

Figure 2.16 shows the nanowire R_H / R_0 curves at a high magnetic field at different temperatures, where R_0 denotes the zero-field resistance and R_H denotes the resistance at an applied field. The MR ratio increases with decreasing temperature. A maximum MR ratio of 9.1% is obtained at 110 K when a magnetic field of 7 T is applied. It can be seen that the MR curve is unsaturated even at an applied field of 7 T, which is

consistent with most observations that the Fe_3O_4 magnetization is difficult to saturate due to the existence of atomically sharp antiphase boundaries. It is interesting to note that the large MR at high fields does not correspond to a large change of magnetization in the same field range. In other words, the MR at high field is caused mainly by the spin alignment at the boundaries instead of the centre region of the domains. As it will be discussed shortly in the dynamic conductance studies, the transport across the APBs is dominated by tunnelling.

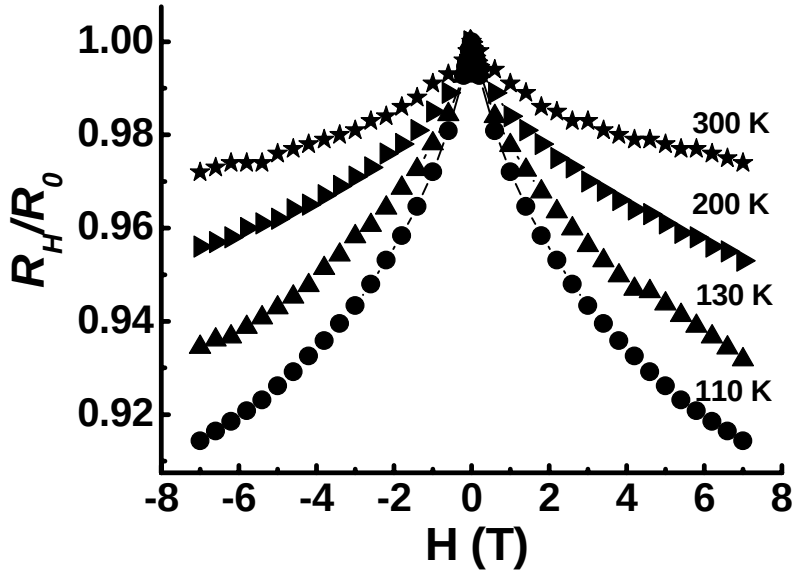

FIG. 2.16 Dependence of R_H / R_0 at various temperatures of a Fe_3O_4 nanowire.

Figure 2.17 shows the temperature-dependent MR ratios at different applied magnetic fields of 0.5, 1, 2, and 5 T, respectively. The MR ratios are obtained by repeating measurements of the temperature-dependent resistance curves at different magnetic fields. The peaks around Verwey transition for the different fields are consistent with the other groups' results. [20-22] Below the transition, the MR ratio increases slowly at low magnetic fields. However, the MR ratio increases more rapidly when a magnetic field of 5 T is applied.

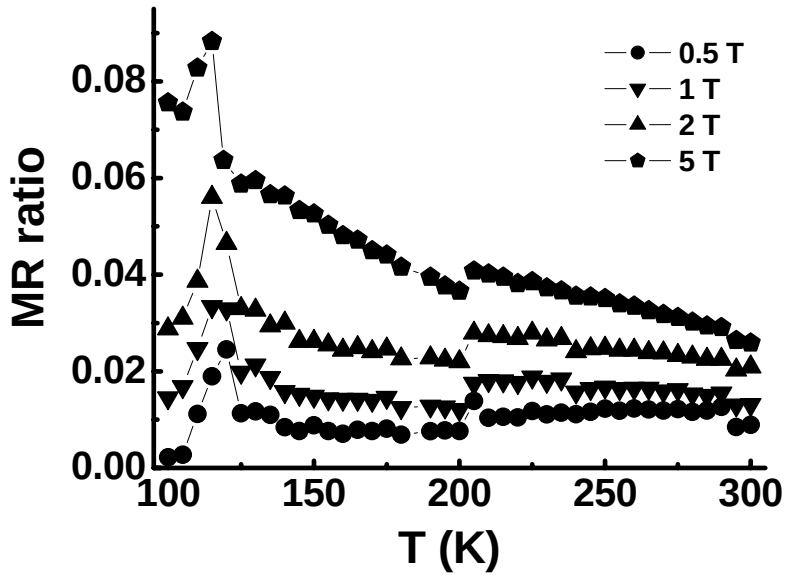

FIG. 2.17 Temperature-dependent MR ratios of a nanowire at different applied magnetic fields.

The typical differential conductance-voltage curve for a nanowire is shown in Fig. 2.18, which was measured at a temperature of 130 K. The curves at other temperatures ranging from 110 to 300 K exhibit almost the same parabolic shape except for the absolute values, which are dependent on temperature. As shown in Fig. 2.18, the conductance-voltage curve can be fitted almost perfectly to a parabola using Eq. 2.2:

$$G_V = \alpha V^2 + \beta V + G_0, \tag{2.2}$$

where α and β are constants, and G_0 is the zero-bias conductance. Although it is not shown here, a similar degree of agreement between experimental and fitted curves has also been obtained for the conductance curves at all other temperatures which we have investigated. β is negligibly small compared to α at the entire temperature range suggesting that the transport is dominated by tunnelling across APBs. Also shown in the figure is the conductance curve taken at an applied field of 5 T. If we assume a rectangular shape of potential barrier with a height of ϕ and thickness d, then according

to the Simmons model, [46] one has $G_0 \propto 1/d$ and $\alpha \propto d/\phi$. The increase of zero-bias conductance with an external field may be attributed to a decrease of barrier thickness.

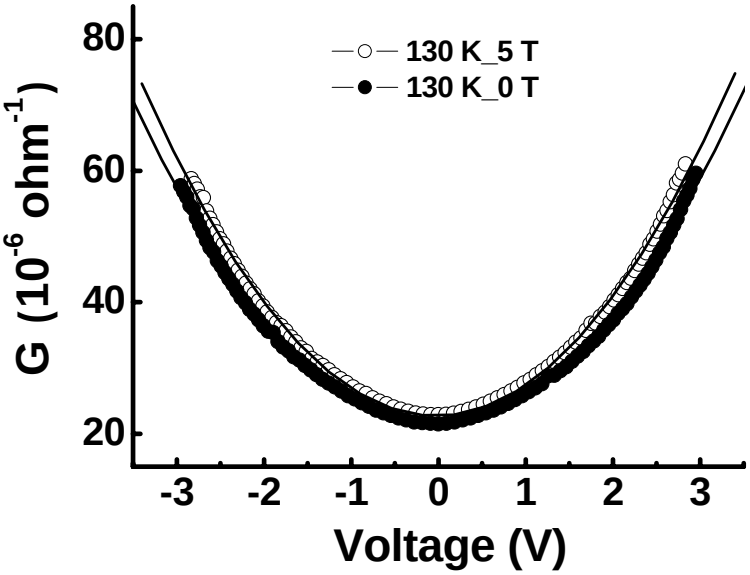

FIG. 2.18 Bias dependence of differential conductance for a nanowire at 130 K with applied magnetic fields of 0 and 5 T, respectively. Solid curve: fitted data according to the Simmons equation. Solid circles: experimental data at zero field; open circles: experimental data at 5 T.

Shown in the Fig. 2.19 is the bias voltage dependence of

$$G'_{(V)} = \frac{[G_{(H=0,V)'} / G_{(H=0,0)}]}{[G_{(H=5T,V)} / [G_{(H=5T,0}]} \quad . \tag{2.3}$$

Substituting $G_0 \propto 1/d$ and $\alpha \propto d/\phi$ into the equation, one can find $d^2(H)/\phi(T) < d^2(0)/\phi(0)$. As the potential barrier will either not change or decrease with the external field, it implies again that the barrier thickness decreases with the external field.

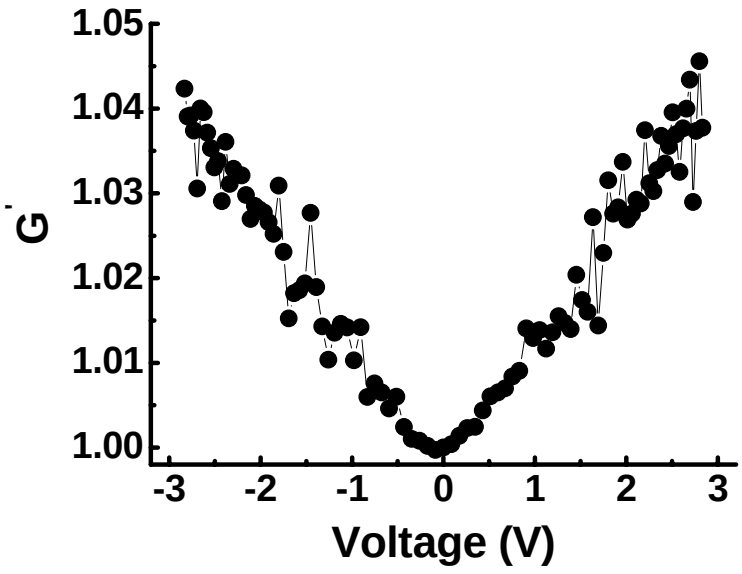

FIG. 2.19 Bias dependence of G´ at 130 K.

We now turn to the dynamic conductance-voltage curves of thin films which are shown in Fig. 2.20. The conductance is normalized as $G = G_{(V)} / G_{(V=1V)}$. Although the overall shape resembles well those of the nanowire, it exhibits a large asymmetry which can hardly be fitted to a parabola. This might be caused by the fact that the current path in the thin film is not well defined due to the random distribution of APBs boundaries. A certain portion of the current may bypass the junctions if the boundary-free regions exceed a certain percolation threshold. As to how the current will bypass or cross the antiphase boundaries, to a certain degree, depends on the polarity of the current which results in the asymmetry of the conductance curves. As the conductance of the thin film is still within the measurable range below the Verwey transition temperature, we have also measured the conductance curves below 120 K. The parabola gradually evolves into a straight line when the temperature decreased from 110 to 60 K. A close-up view of the low-voltage region at 60 K is shown in the inset of Fig. 2.20, which suggests that the transport mechanism has changed from tunnelling near or above the Verwey

transition temperature to transport in a disordered system at low temperature which eventually vanishes as the temperature decreases further.

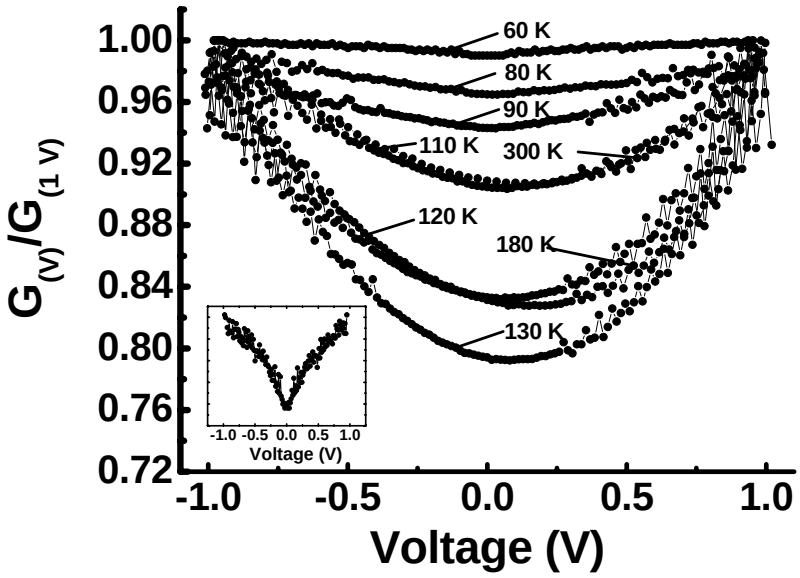

FIG. 2.20 Normalized dynamic conductance-voltage curves of Fe_3O_4 thin films at different temperatures. Inset: the normalized conductance-voltage curve at 60 K.

It is well known from the work on magnetic tunnel junctions that the MR ratio normally decreases with the bias voltage. Fig. 2.21 shows the bias dependence of MR ratio

$$\Delta R / R_0 = \frac{R_{5T} - R_0}{R_0}, \tag{2.4}$$

at 110, 120, and 130 K for the nanowire sample. It was obtained by first measuring the *I-V* curve at zero field and then repeating the measurement at an applied field of 5 T. The MR shows a maximum value at 120 K which is consistent with the results in Fig. 2.17. The MR ratio decreases with increasing bias, which is a typical behaviour of magnetic tunnelling junctions. The thin film also shows the same bias dependence of MR though it is not as obvious as the nanowire case [see the inset of Fig. 2.21]. As it is

shown in the inset, we also observed a zero-biased MR anomaly at 110 K for the nanowire sample that is not well understood at present.

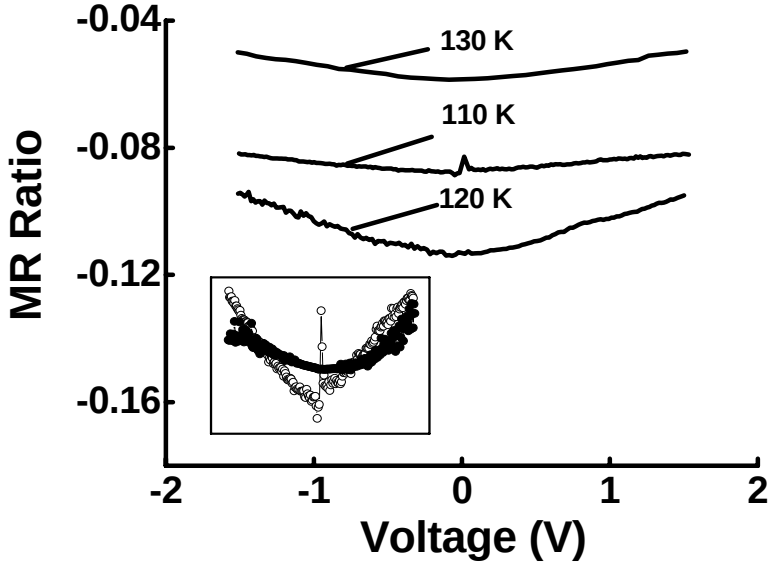

FIG. 2.21 Bias dependence of MR for a nanowire at 110, 120, and 130 K. Inset: comparison of bias dependence of MR for the thin film (solid circles) and nanowire (open circles) at 110 K.

Figure 2.22 shows the bias-dependent MR curve at 130 K fitted with V^2 (Voltage). The fitting result is better at the high-bias region than at the low-bias region. Céspedes *et al.* [47] also observed the V^2 dependence of MR in their Fe_3O_4 nanoconstrictions with the width of 20-50 nm patterned by FIB. They argued that hopping or tunnelling across the domain walls at the nanoconstriction regions were the dominant transport mechanism. However, they did not take the APBs into account to explain the phenomenon. As discussed above, tunnelling is the dominant transport mechanism across APBs whether or not a magnetic field is applied. Applying a magnetic field only decreases the barrier height and leads to a lower resistance. Therefore, the V^2 dependence of MR provides further evidence that the dominant transport mechanism across APBs is tunnelling.

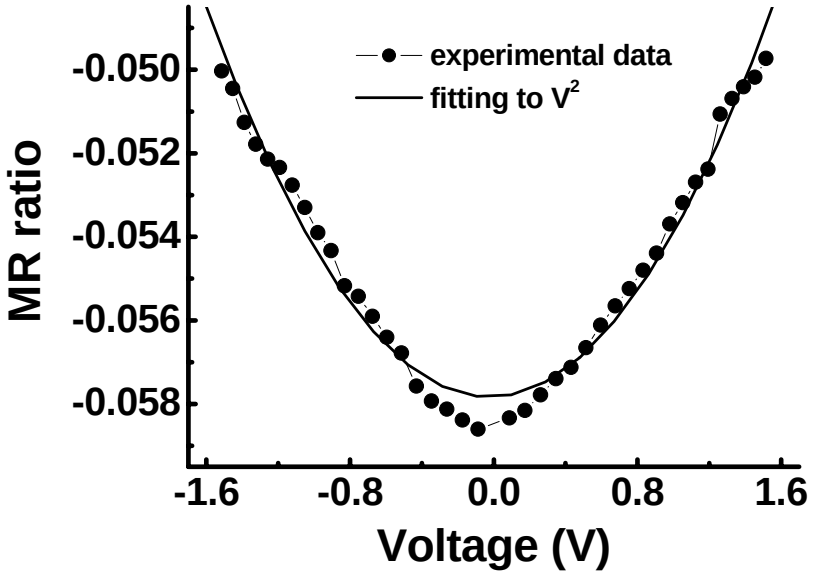

FIG. 2.22 MR ratio curve at 130 K fitted to a V^2 dependence.

2.3.4 Our model to explain the experimental results

Based on the discussion above, we propose a simple model to explain the universal MR curves observed so far in Fe_3O_4 thin films prepared by various techniques. In fact, several groups, such as Eerenstein *et al*. [13] and Ziese *et al.* [18], have already proposed their models to explain the MR effect. As it is illustrated in Fig. 2.23 above the Verwey temperature, Fe_3O_4 thin film may be considered as consisting of ferromagnetic domains separated by very strong antiferromagnetically coupled APBs. If the coupling is very strong and the boundary is atomically sharp, a spin-dependent potential barrier will appear even when there is no insulating phase at the boundary. When a small external field is applied to the sample, the spins far away from the boundary will try to align along the direction of the magnetic field due to the small anisotropy in the center region. This will cause a sharp drop of resistance across the boundary just as the case in a normal magnetic tunnel junction. The only difference is that the electrons will be scattered by electrons with different spin directions while they

are crossing the boundary. The application of a large field will reduce the width of the domain wall formed between the centre regions of APBs with neighbouring domain, which leads to a further decrease of the resistance. The resistance will saturate once the atomically sharp APBs are erased magnetically which requires a very large magnetic field.

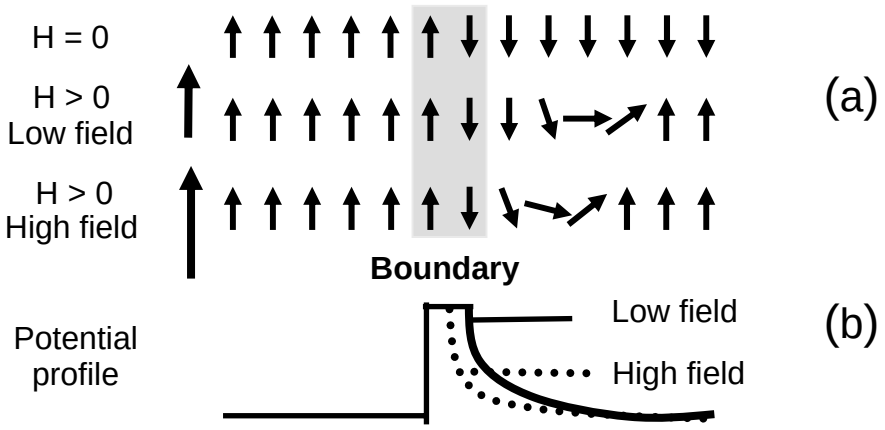

FIG. 2.23 A simple model to explain the experimental results: (a) spin distribution at different situations, (b) spatial profile of tunneling barrier.

2.4 Summary

In summary, our systematic study of the magnetic and electrical transport properties of Fe_3O_4 thin films, nanowires, and nanowires with nanoconstrictions suggested that APBs had a strong effect on electrical transport properties in Fe_3O_4 nanostructures. Antiferromagnetic coupling across APBs was responsible for the universal shape of the MR curves and the transport mechanism across APBs was dominated by tunnelling. The antiferromagnetically coupled regions might be responsible for the low MR ratios obtained from Fe_3O_4-based spin valves and MTJs.

References:

1 "Magnetic mineral", www.trincoll.edu/~cgeiss/GEOS_312/Rock_mag_2.ppt.

2 E. J. Verwey, "Electronic conduction of magnetite (Fe_3O_4) and its transition point at low temperatures", Nature **144**, pp. 327-328, 1939.

3 K. Siratori, Y. Shii, Y. Morii, S. Funahashi, S. Todo, and A. Yanase, "Neutron diffuse scattering study of the high temperature phase of Fe_3O_4-I, determination of atomic displacements at the X point in the Brillouin zone", J. Phys. Soc. Jpn. **67**, pp. 2818-2827, 1998.

4 P. Novak, H. Stepankova, J. Englich, J. Kohout, and V. A. M. Brabers, "NMR in magnetite below and around the Verwey transition", Phys. Rev. B **61**, pp. 1256-1260, 2000.

5 J. Garcia, G. Subias, M. G. Proietti, H. Renevier, Y. Joly, J. L. Hodeau, J. Blasco, M. C. Sanchez, and J. F. Berar, "Resonant "forbidden" reflections in magnetite", Phys. Rev. Lett. **85**, pp. 578-581, 2000.

6 J. Garcia, G. Subias, M. G. Proietti, J. Blasco, H. Renevier, J. L. Hodeau, and Y. Joly, "Absence of charge ordering below the Verwey transition temperature in magnetite", Phys. Rev. B **63**, pp. 054110, 2001.

7 G. Subias, J. Garcia, J. Blasco, M. Grazia Proietti, H. Renevier, and M. C. Sanchez, "Magnetite, a model system for mixed-valence oxides, does not show charge ordering", Phys. Rev. Lett. **93**, pp. 156408, 2004.

8 D. J. Huang, H.-J. Lin, J. Okamoto, K. S. Chao, H.-T. Jeng, G.Y. Guo, C.-H. Hsu, C.-M. Huang, D. C. Ling, W. B. Wu, C. S. Yang, and C. T. Chen, "Charge-orbital ordering and Verwey transition in magnetite measured by Resonant soft X-ray scattering", Phy. Rev. Lett. **96**, pp. 096401, 2006.

9 Z. Zhang and S. Satpathy, "Electron states, magnetism, and the Verwey transition in magnetite", Phys. Rev. B **44**, pp. 13319-13331, 1991.

10 A. Yanase and K. Siratori, "Band structure in the high temperature phase of Fe_3O_4", J. Phys. Soc. Jpn. **53**, pp.312-317, 1984.

11 J. M. D. Coey and S Sanvito, "Magnetic semiconductors and half-metals", J. Phys. D: Appl. Phys. **37**, pp. 988-993, 2004

12 Yu. S. Dedkov, U. Rüdiger, and G. Güntherodt, "Evidence for the half-metallic ferromagnetic state of Fe_3O_4 by spin-resolved photoelectron spectroscopy", Phys. Rev. B **65**, pp. 064417, 2002.

13 W. Eerenstein, T. T. M. Palstra, S. S. Saxena, and T. Hibma, "Spin-polarized transport across sharp antiferromagnetic boundaries", Phys. Rev. Lett. **88**, pp. 247204, 2002.

14 R. F. C. Farrow, P. M. Rice, M. F. Toney, R. F. Marks, J. A. Hedstrom, R. Stephenson, M. J. Carey, and A. J. Kellock, "Nanoscale phase separation in Fe_3O_4(111) films on sapphire(0001) and phase stability of Fe_3O_4(001) films on MgO(001) grown by oxygen-plasma-assisted molecular beam epitaxy", J. Appl. Phys. **93**, pp. 5626-5636, 2003.

15 H. Liu, E. Y. Jiang, H. L. Bai, R. K. Zheng, H. L. Wei, and X. X. Zhang, "Large room-temperature spin-dependent tunnelling magnetoresistance in polycrystalline Fe_3O_4 films", Appl. Phys. Lett. **83**, pp. 3531-3533, 2003.

16 Ken-ichi Aoshima and Shan X. Wang, "Fe_3O_4 and its magnetic tunneling junctions grown by ion beam deposition", J. Appl. Phys. **93**, 7954, 2003.

17 T. Furubayashi, "Magnetoresistance of magnetite films prepared by reactive evaporation", J. Appl. Phys. **93**, pp. 8026-8028, 2003.

18 M. Ziese and H. J. Blythe, "Magnetoresistance of magnetite", J. Phys: Condens. Matter **12**, pp. 13-28, 2000.

19 M. Ziese, R. Höhne, H. C. Semmelhack, H. Reckentin, N. H. Hong, and P. Esquinazi, "Mechanism of grain-boundary magnetoresistance in Fe_3O_4 films", Eur. Phys. J. B **28**, pp. 415-422, 2002.

20 S. B. Ogale, K. Ghosh, R. P. Sharma, R. L. Greene, R. Ramesh, and T. Venkatesan "Magnetotransport anisotropy effects in epitaxial magnetite (Fe_3O_4) thin films", Phys. Rev. B **57**, pp. 7823-7828, 1998.

21 X. W. Li, A. Gupta, Gang Xiao and G. Q. Gong, "Transport and magnetic properties of epitaxial and polycrystalline magnetite thin films", J. Appl. Lett. **83**, pp. 7049-7051, 1998.

22 G. Q. Gong, A. Gupta, Gang Xiao, W. Qian and V. P. Dravid, "Magnetoresistance and magnetic properties of epitaxial magnetite thin films", Phys. Rev. B **56**, pp. 5096-5099, 1997.

23 J. P. Hong, Jin Pyo Hong, Sung Bok Lee, Young Woo Jung, Jong Hyun Lee, Kap Soo Yoon, Ki Woong Kim, Chae Ok Kim, Chang Hyo Lee, and Myoung Hwa Jung, "Room temperature formation of half-metallic Fe_3O_4 thin films for the application of spintronic devices", Appl. Phys. Lett. **83**, pp. 1590-1592, 2003.

24 L. Zhou, K. –Y. Wang, C. J. O'Connor and J. Tang, "Granular growth of Fe_3O_4 thin films and its antiphase boundaries prepared by pulsed laser deposition", J. Appl. Phys. **89**, pp. 7398-7340, 2001.

25 T. Fujii, F. M. F. de Groot, G. A. Sawatzky, F. C. Voogt and T. Hibma and K. Okada, "In situ XPS analysis of various iron oxide films grown by NO_2-assisted molecular-beam epitaxy", Phys. Rev. B **59**, pp. 3195-3202, 1999.

26 T. Kiyomura, Y. Maruo, and M. Gomi, "Electrical properties of MgO insulating layers in spin-dependent tunneling junctions using Fe_3O_4", J. Appl. Phys. **88**, pp. 4768-4771, 2000.

27 D. Reisinger, M. Schonecke, T. Brenninger, M. Opel, A. Erb, L. Alff, and R. Gross, "Epitaxy of Fe_3O_4 on Si(001) by pulsed laser deposition using a TiN/MgO buffer layer", J. Appl. Phys. **94**, pp. 1857-1863, 2003.

28 J. Tang, "Magnetic properties of nanocrystalline Fe_3O_4 films", J. Appl. Phys. **89,** pp. 7690-7692, 2001.

29 Y. G. Peng, C. Park, and D. E. Laughlin, "Fe_3O_4 thin films sputter deposited from iron oxide targets", J. Appl. Phys. **93**, pp. 7957-7959, 2003.

30 S. Soeya, "Development of half-metallic ultrathin Fe_3O_4 films for spin-transport devices", Appl. Phys. Lett. **80**, pp. 823-825, 2002.

31 P. Morrall, F. Schedin, S. Langridge, G. Thornton, J. Bland and M. F. Thomas, "Magnetic moment in an ultrathin magnetite film", J. Appl. Phys. **93**, pp. 7960-7962, 2003.

32 H. Takahashi, S. Soeya, J. Hayakawa, K. Ito., A. Kida, C. Yamamoto, H. Asano, and M. Matsui, "Fabrication and magnetoresistive effect of current perpendicular to plane devices using half-metallic Fe_3O_4 thin films on metallic films", J. Appl. Phys. **93**, pp. 8029-8031,

33 S. van Dijken, X. Fain, S. M. Watts, K. Nakajima, and J. M. D. Coey, "Magnetoresistance of Fe_3O_4/Au/Fe_3O_4 and Fe_3O_4/Au/Fe spin valve structures", J. Magn. Magn. Mater. **280**, pp. 322-326, 2004.

34 X. W. Li, A. Gupta, Gang Xiao , W. Qian and V. P. Dravid, "Fabrication and properties of heteroepitaxial magnetite (Fe_3O_4) tunnel junctions", Appl. Phys. Lett. **73**, pp. 3282-3284, 1998.

35 P. J. van der Zaag, P. J. H. Bloemen, J. M. Gaines, R. M. Wolf, P. A. A. van der Heijden , R. J. M. van de Veerdonk, and W. J. M. de Jonge, "On the construction of an Fe_3O_4-based all-oxide spin valve", J. Mag. Magn. Mater. **211**, pp. 301-308, 2000.

36 G. H. Hu, R. Chopdekar, and Y. Suzuki, "Observation of inverse magnetoresistance in epitaxial magnetite/manganite junctions", J. Appl. Phys. **93**, pp. 7516-7518, 2003; G. Hu and Y. Suzuki, "Negative Spin Polarization of Fe_3O_4 in Magnetite/Manganite-Based Junctions", Phy. Rev. Lett. **89**, pp. 276601, 2002.

37 H. Matsuda, M. Takeuchi, H. Adachi, M. Hiramoto, N. Matsukawa, A. Odagawa, K. Setsune, and H. Sakakima, "Fabrication and magnetoresistance properties of spin-dependent tunnel junctions using an epitaxial Fe_3O_4 film", Jpn. J. Appl. Phys. **41,** L387-L390, 2002.

38 L. M. B. Alldredge, R. V. Chopdekar, B. B. Nelson-Cheeseman, and Y. Suzuki, "Complex oxide-based magnetic tunnel junctions with nonmagnetic insulating barrier layers", J. Appl. Phys. **99**, pp. 08K303, 2005.

39 T. Kasama, R. E. Dunin-Borkowski, and W. Eerenstein, "Off-axis electron holography observation of magnetic microstructure in a magnetite (001) thin film containing antiphase domains", Phys. Rev. B **73**, pp. 104432, 2006.

40 F. C. Voogt, T. T. M. Palstra, L. Niesen, O. C. Rogojanu, M. A. James, and T. Hibma, "Superparamagnetic behavior of structural domains in epitaxial ultrathin magnetite films", Phys. Rev. B **57**, R8107, 1998.

41 D. T. Margulies, F. T. Parker, M. L. Rudee, F. E. Spada, J. N. Chapman, P. R. Aitchison, and A. E. Berkowitz, "Origin of the anomalous magnetic behavior in single crystal Fe_3O_4 films", Phys. Rev. Lett. **79**, pp. 5162-5165, 1997.

42 J.-B. Moussy, S. Gota, A. Bataille, M.-J. Guittet, and M. Gautier-Soyer, F. Delille and B. Dieny, F. Ott and T. D. Doan, P. Warin and P. Bayle-Guillemaud, C. Gatel and E.

Snoeck, "Thickness dependence of anomalous magnetic behaviour in epitaxial Fe_3O_4(111) thin films: Effect of density of antiphase boundaries", Phys. Rev. B **70**, pp. 174448, 2004.

43 W. Eerenstein, T. T. M. Palstra, T. Hibma, and S. Celotto, "Origin of the increased resistivity in epitaxial Fe_3O_4 films", Phys. Rev. B **66**, pp. 201101, 2002.

44 R. Argon, "Magnetization and exchange in nonstoichiometric magnetite", Phys. Rev. B **46**, pp. 5328-5333, 1992.

45 J. R. Drabble, T. D. Whyte, and R. M. Hooper, "Electrical conductivity of magnetite at low temperatures", Solid State Commun. **9**, pp. 275-278, 1971.

46 J. G. Simmons, "Generalized formula for the electric tunnel effect between similar electrodes separated by a thin insulating film", J. Appl. Phys. **34**, pp. 1793-1803, 1963.

47 O. Céspedes, S. M. Watts, J. M. D. Coey, K. Dörr, and M. Ziese, "Magnetoresistance and electrical hysteresis in stable half-metallic $La_{0.7}Sr_{0.3}MnO_3$ and Fe_3O_4 nanoconstrictions", Appl. Phys. Lett. **87,** pp. 83102-83104, 2005.

CHAPTER 3

MAGNETIC AND ELECTRICAL TRANSPROT PROPERTIES OF AMORPHOUS $Ge_{1-x}Mn_x$ THIN FILMS

3.1 Introduction

As we discussed in Chapter 1, DMSs are promising materials for future spintronic applications. Depending on the host materials, DMSs that have been investigated so far can be divided into the following categories: III-V, II-VI, IV-VI, IV, and oxides, etc. Among all these DMSs, the Ge-based system has recently received special attention due to its possibility of being integrated with the mainstream Si-based electronic devices. After the report of ferromagnetism in $Ge_{1-x}Mn_x$ system (T_C = 25 ~ 116 K), [1] further studies on the $Ge_{1-x}Mn_x$ system have been performed by several groups [see Table 3.1 for the details]. [2-15] Most of the work has been focused on materials preparation and fundamental property studies, though Tsui *et al.* have demonstrated a Ge-based heterojunction diode of which the rectifying property can be controlled by either the bias voltage or an external magnetic field. [16] Through these studies, it is now commonly believed that secondary phases (such as Mn_5Ge_3 and $Mn_{11}Ge_8$) will form once the Mn concentration exceeds the solubility limit (~ 9%). [7] However, the mechanism of the ferromagnetic ordering in samples with a Mn concentration lower than the solution limit still remains controversial.

Table 3.1 Literature review about the research work on Ge:Mn

Fabrication Technique	Growth temperature and growth rate	Mn concentration	Sample features	Magnetic properties
MBE [1]	70 ºC, ~ 5 Å/min	0.006 to 0.035	Epitaxial p-type	T_C~25-116 K
MBE [2]	250 to 350 ºC, 5-6 Å/s	0.006	$Mn_{11}Ge_8$ embedded in $Ge_{1-x}Mn_x$	T_C ~295 K
Sinter [3]	1050 ºC	less than 0.06	Single crystal	T_C ~285 K
MBE [4]	Solid-phase epitaxy, 300-650 ºC annealing	-	Mn_5Ge_3 epitaxial on Ge (111)	T_C ~295 K
Sinter [5]	1050 ºC	Less tan 0.06	Single crystal	T_C ~285 K
MBE [6]	160 ºC, 0.02 nm/s	0.01 to 0.051	Epitaxial	T_C > 280 K
MBE [7]	50 to 85 ºC, 2-4 Å/min	Less than 0.09	Epitaxial	T^*_C =112 K, T_C = 12 K ($x = 0.05$)
Chemical method [8]	-	0.01 to 0.05	Nanowires	T_C = 300 K
Thermal evaporator [10]	100 ºC, 35 nm/min	0.036 to 0.31	Amorphous	80 K< T_C <160 K
MBE [11]	225 ºC, 1.0 Å/s	0.03	Mn_5Ge_3 clusters in epitaxially grown Ge: Mn matrix	T^*_C =290 K, T_C = 16 K (x = 0.03)
MBE [12]	110 to 225 ºC, 0.1 to 1 Å/s	0.04 and 0.2	Mn_5Ge_3 clusters in epitaxially grown Ge: Mn matrix	T_f =12 and 15 K, T_b =210 and 270 K

Kang *et al.* [5] observed the phase separation between the Mn-rich and Mn-depleted regions and concluded that the ferromagnetism observed in $Ge_{1-x}Mn_x$ may not be of an intrinsic nature, but arose from the magnetic properties of the Mn-rich phases in phase-separated $Ge_{1-x}Mn_x$. Pinto *et al.* [6] reported that the magnetic and electrical transport properties of $Ge_{1-x}Mn_x$ ($0.010 < x < 0.051$) grown on Ge substrates could be explained by a BMP percolation model. Based on this model, an infinitely percolative BMP formed at low temperatures, which divided into finite size regions gradually when the temperature increased. Depending on the size of the BMPs, they may behave either like a ferromagnet or a paramagnet. Li *et al.* [7] reported that ferromagnetism in $Ge_{1-x}Mn_x$ ($0 < x < 0.09$) was characterized by two different ordering temperature T_C (12 K for $x \sim 0.05$)

and T^*_C (112 K for $x \sim 0.05$), where T_C was the onset temperature of global ferromagnetic phase. The magnetism between T_C and T^*_C was thought of being originated from "clustered dopants" due to inhomogeneous distribution of Mn impurities. In all reported cases, no evidence of Ruderman-Kittel-Kasuya-Yoshida (RKKY)-type ferromagnetism was found at room temperature, though theoretical models based on the RKKY mechanism have predicated Curie temperatures ranging from 134 to 400 K, depending on the distance between the Mn ions. [17,18]

These reports pose a series of questions here: (1) what is the true origin of ferromagnetism in $Ge_{1-x}Mn_x$; (2) what determines the various characteristic temperatures; (3) what kind of properties will one obtain if the Mn concentrations can be increased further without the formation of dominative precipitates; and (4) what is the role of disordering and carrier localization in the $Ge_{1-x}Mn_x$ system? In order to shed some light on these issues, in particular, (3) and (4), in this chapter we report on a systematic study of heavily doped $Ge_{1-x}Mn_x$ thin films (with a Mn concentration at the range of 15.3% - 42%). Due to the extremely high Mn compositions, all the films grown at a substrate temperature of 160 ^oC are amorphous which provides a convenient way to study the effect of randomness and disordering on the magnetic and electrical transport properties of Ge-based DMS. [10] On the other hand, at a substrate temperature of 300 ^oC the as-grown samples are amorphous $Ge_{1-x}Mn_x$ embedded with Ge crystallites and high T_C secondary phases (Detailed discussion on these samples will be presented in chapter 4). These samples are mostly ferromagnetic near or above room temperature due to the formation of secondary phases such as Mn_5Ge_3 and $Mn_{11}Ge_8$. The samples grown at 200 ^oC belong to intermediate cases which consist of an amorphous $Ge_{1-x}Mn_x$ matrix embedded with Ge crystallites and Mn_5Ge_3 phase. The main difference between

the samples grown at 300 ^{o}C and those at 200 ^{o}C are that the magnetic properties of the latter are still dominated by the amorphous phase.

The temperature dependence of magnetic properties reveals that the amorphous samples consist of a low-temperature highly ordered spin-glass-like phase with an ordering temperature T_C ~ 20 K (x ~ 0.39) and a high-temperature "clustered dopant" phase [7] with an ordering temperature of T^*_C ~ 104 K (x ~ 0.39), both of which increase with the Mn concentration. The ordering temperature T^*_C of the high-temperature phase increases monotonically with the external applied field up to ~ 5000 Oe beyond which it saturates at ~ 200 K; at low applied field, T^*_C is very close to the so-called Curie temperature or T^*_C reported so far for relatively lightly-doped and epitaxially grown $Ge_{1-x}Mn_x$ thin films. [1,7] Due to the disorder and "magnetic discontinuity" of the high-temperature phase, the magnetization of the low-temperature phase couples antiferromagnetically with that of the high-temperature phase, leading to the appearance of a negative thermal remanent magnetization (TRM). Detailed magnetic and electrical measurements reveal that the low-temperature highly ordered spin-glass-like phase consists of both spin-glass-like phase and ferromagnetically ordered regions. All the amorphous samples exhibit a negative magnetoresistance and an anomalous Hall effect (AHE) at low temperatures. The magnetoresistance is almost constant below T_C; it then decreases with increasing temperature and reaches almost zero at T^*_C. The clear correlation between carrier localization and magnetic properties at low temperatures agrees well with the report in literature that the low-temperature phase originated from carrier-mediated coupling mechanism, [6,7] while the strong field dependence of T^*_C suggests that the high-temperature phase is due to magnetic clusters of different sizes.

3.2 Experiments

The samples were prepared using MBE at different growth temperatures on GaAs (001) substrates. Amorphous $Ge_{1-x}Mn_x$, and coexistence of amorphous $Ge_{1-x}Mn_x$, Ge crystallites and high T_C secondary phases ($Mn_{11}Ge_8$ and Mn_5Ge_3) [19] were obtained at substrate temperatures of 160 and 200 ^oC, respectively. The thicknesses of all samples were around 30 nm with a growth rate of 0.5 Å/s. Elemental Ge and Mn were used as the source materials and were evaporated by an electron gun and a Knudsen cell, respectively. The Mn composition was adjusted by controlling the K-cell temperatures. The structural properties of the samples were characterized by Raman scattering (Renishaw micro-Raman) and high resolution TEM. The surface morphology was obtained by a Digital Instruments atomic force microscopy (AFM) operated in tapping mode. The concentration of Mn was determined using both x-ray photoelectron spectroscopy (XPS) and Rutherford backscattering spectrometry (RBS). Details of the samples under study are tabulated in Table 3.2. The magnetic properties of the samples were characterized using SQUID. Electrical transport properties were obtained from the measurements on standard Hall bars with six Au electrical contacts in a Janis cryostat in the temperature range of 1.7 – 300 K and with a magnetic field up to 7 T. The distance between the two current contacts was 320 μm and that between the two voltage probes was 80 μm. The width of the Hall bar was 80 μm.

Figure 3.1 shows the typical process flow chart for Hall bar fabrication: (a) $Ge_{1-x}Mn_x$ thin film deposition by MBE, (b) resist coating on the $Ge_{1-x}Mn_x$ thin film by spin coater, (c) Hall bar patterning with a laser writer, (d) resist development to expose the Hall bar pattern, (e) deposition of a thin layer of Al_2O_3 to protect the Hall bar, (f) removal of the uncovered film by ion milling, (g) electrode patterning, and (h) deposition of 200 nm gold to form the electrodes, (i) SEM image of a completed Hall

bar, in which the red arrow shows the current flow direction. Electrodes (I) and (IV) serve as the current probes. The Hall voltage (V_{xy}) and longitudinal voltage (V_{xx}) are measured by electrodes (III) and (V) and electrodes (II) and (III), respectively.

Table 3.2 Details of the samples under study in this chapter

Sample name	T_{sub} (°C)	Resistivity at RT (Ω cm)	Mn composition (%)	Phase
A1	160	0.421	15.3	Amorphous
A2	160	0.03177	28.1	Amorphous
A3	160	0.005151	33.2	Amorphous
A4	160	0.001746	39.1	Amorphous
A5	160	-	42	Amorphous
A6	200	0.00113	42	Coexistence of amorphous, Ge crystallites, and Mn_5Ge_3 phase

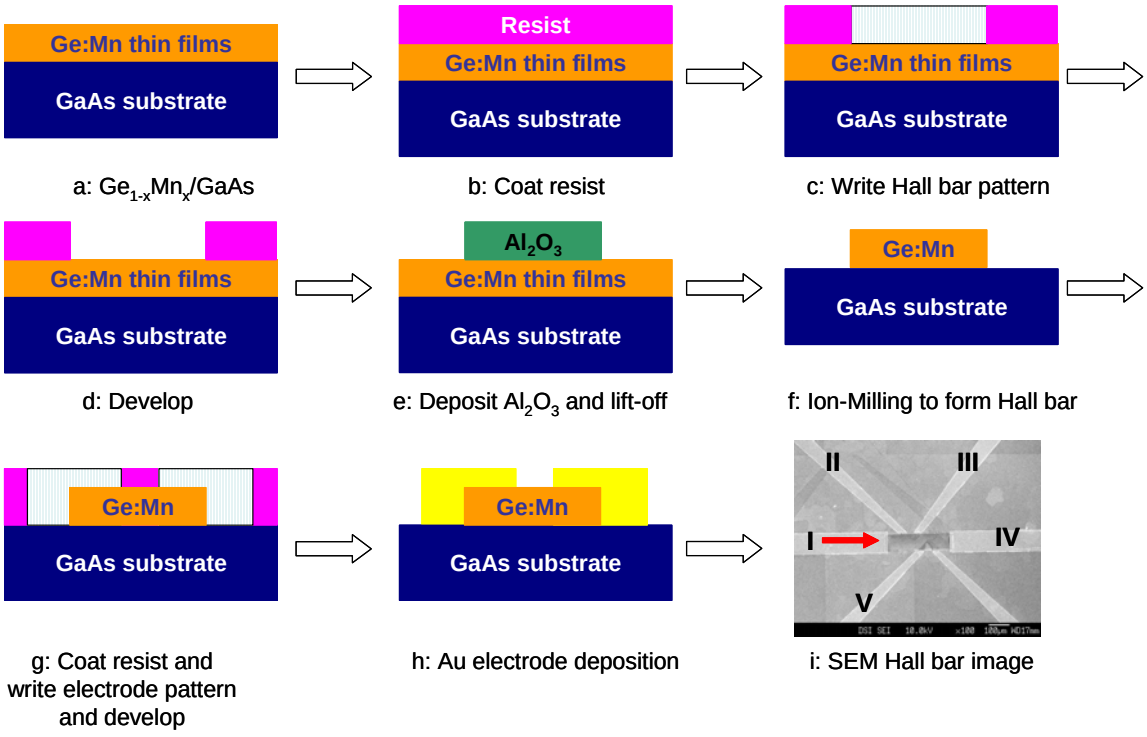

FIG. 3.1 Schematic illustration of the process flowchart for a Hall bar fabrication. The arrow in (i) indicates the current direction.

3.3 Results and discussion

3.3.1 Structural and surface morphology properties

As it is mentioned above, the samples grown at 160 and 200 ^{o}C are in amorphous, and coexistence of amorphous $Ge_{1-x}Mn_x$, Ge crystallites, and Mn_5Ge_3 phase, which have been confirmed by both TEM and Raman studies. Figure 3.2 shows the typical cross-sectional TEM image of the amorphous sample with a Mn concentration of 39 %. Although Yu *et al*. have reported that Mn crystallites formed in their amorphous $Ge_{1-x}Mn_x$ thin films with a Mn concentration higher than 31%, [10] we could not observe any crystallites in the amorphous samples.

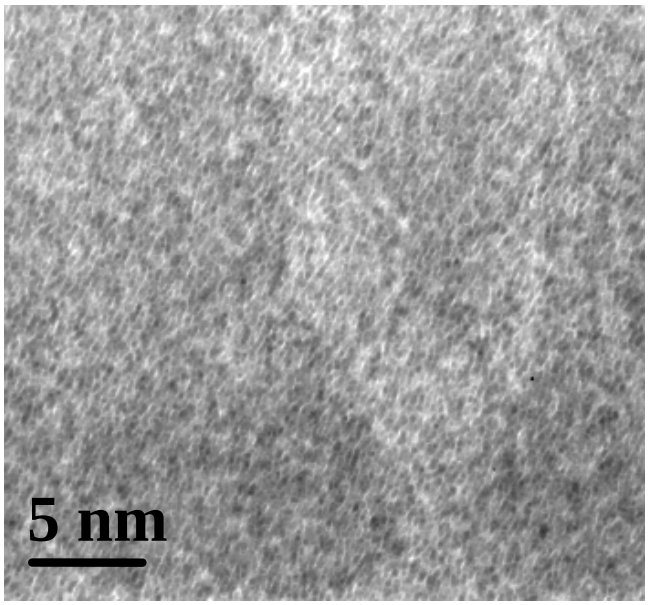

FIG. 3.2 HRTEM image for sample A4.

Figure 3.3 shows the Raman spectra of the amorphous samples with different Mn doping concentrations. The samples A1-A4 exhibit a broad peak at the position of 275 cm^{-1}, which is corresponding to the typical peak position of amorphous Ge. [20] The peaks at 267 and 292 cm^{-1} are due to the GaAs substrate. The intensity of Raman peak decreases with increasing Mn concentration. Also shown in the same figure is the

Raman spectrum of sample A6. The appearance of a sharp peak at about 298 cm^{-1} with a redshift of about 3 cm^{-1} from that of bulk Ge indicates that the host matrix consists of Ge crystallites. [21,22] As we will discuss later about the magnetic properties, Mn_5Ge_3 phase is embedded in the amorphous $Ge_{1-x}Mn_x$ matrix in sample A6.

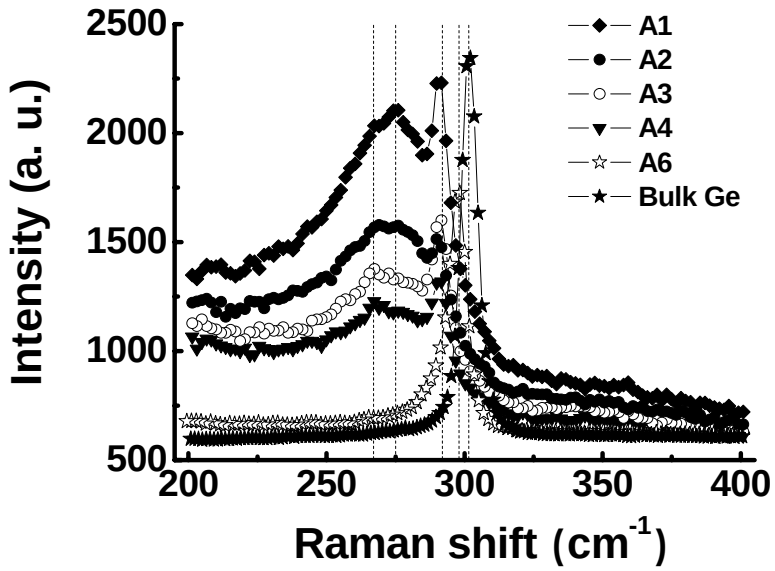

FIG. 3.3 Raman spectra of samples A1, A2, A3, A4, A6 and bulk Ge. The dotted lines indicate the peak positions of amorphous Ge and GaAs substrate at the position of 275, 267 and 292 cm^{-1}, Ge nanocrystal and bulk Ge at the position of around 298 and 301.5 cm^{-1}, respectively.

Figure 3.4 presents the typical AFM image of sample A4 with the scan area of 1 μm × 1 μm. A very flat surface is obtained in our amorphous $Ge_{1-x}Mn_x$ thin film with a surface roughness (R_a) value of 0.296 nm, indicating the uniform growth of our amorphous thin film. Although Park *et al.* [1] and Li *et al.* [7] had an indication of a predominately two-dimensional growth from the observation of reflection high energy electron diffraction (RHEED) pattern during the film deposition, they did not carry out a morphological investigation on their epitaxially grown samples at the end of the deposition. Pinto *et al.* [23] and Gunnella *et al.* [24] studied the surface morphology of

the epitaxial GeMn alloys on Ge (111) substrates. They observed a characteristic pin-hole on the surface although clear streaky RHEED patterns were observed. Our amorphous samples have a higher growth rate (0.5 Å/s) in comparison with that of the epitaxially grown samples (typically less than 0.5 Å/min), which may result in the low surface roughness.

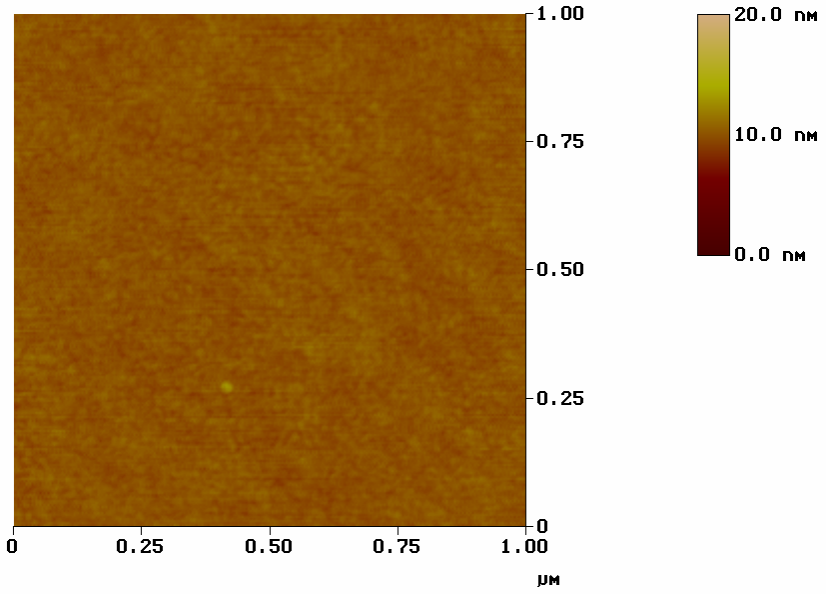

FIG. 3.4 AFM image for sample A4.

3.3.2 Magnetic properties

3.3.2.1 *M-H* curves

Figure 3.5 shows the normalized field-dependent magnetization curves at 5 K for samples under study in this chapter. Typical hysteresis behaviour is clearly observed in all the samples, which is a clear sign of ferromagnetic ordering. The coercivity increases with the doping concentration from samples A1 to A4, which is around 360 Oe for sample A1 and 1550 Oe for sample A4. As can be seen from the figure, along with coercivity, the squareness also increases with increasing Mn concentration. However,

the coercivity for sample A6 becomes smaller than that of sample A4 although the squareness still increases with increasing Mn concentration.

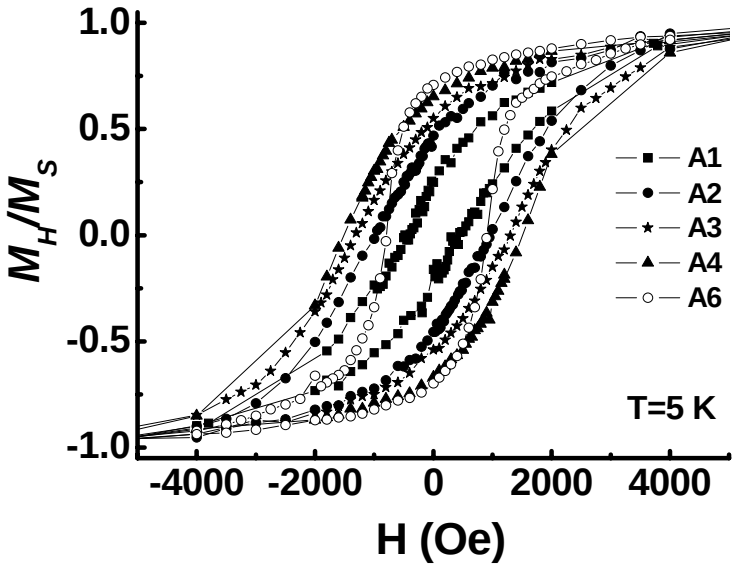

FIG. 3.5 Normalized *M-H* curves at 5 K for the samples under study.

We now look at the detailed field-dependent magnetization properties for sample A5. This sample exhibits well-defined hysteresis curves below 120 K, which is also the ordering temperature determined through fitting the high-temperature tail of the dc susceptibility to the Curie-Weiss law [$M/H = C/(T-\theta)$]. This temperature is very close to the global or local ferromagnetic transition temperature reported in either uniform or disordered Ge:Mn samples. [1, 7] However, what is peculiar in our sample is that inverted hysteresis curves were observed at temperatures above 30 K below which a normal hysteresis curve is observed. The coercivity decreases rapidly with increasing temperatures from 5 K, reaches zero at 30 K, then increases slightly in the negative direction and finally returns to zero again at about 120 K, as shown in Fig. 3.6. To illustrate this phenomenon, the insets show the hysteresis curves at 10 and 70 K,

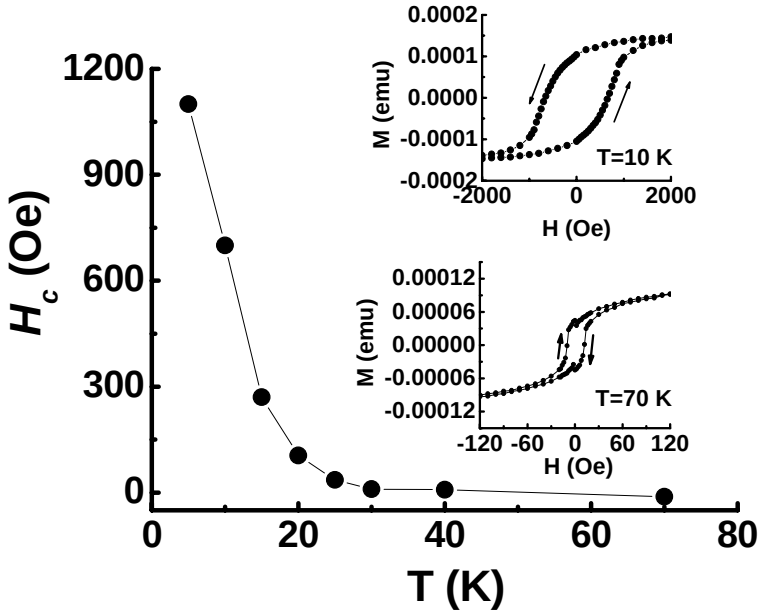

FIG. 3.6 Temperature dependence of coercivity for sample A5. Insets: *M-H* curves at 10 (above) and 70 K (below).

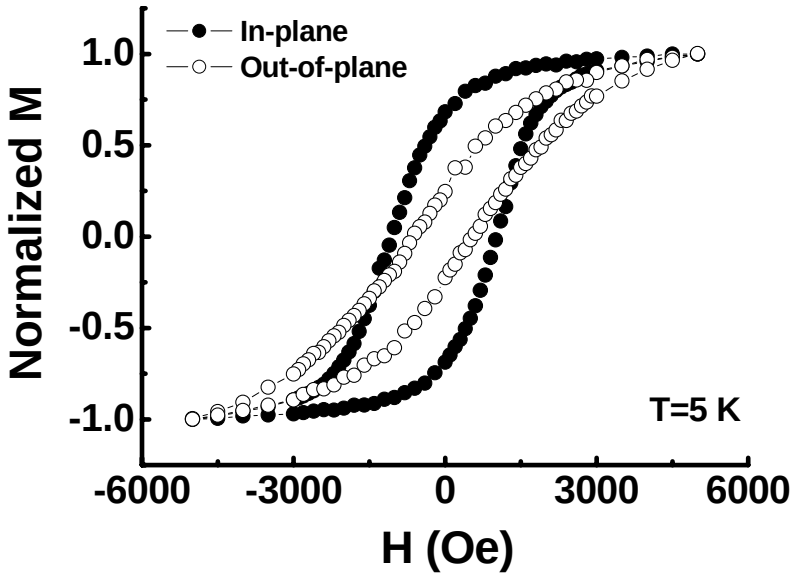

FIG. 3.7 Normalized in-plane and out-of-plane *M-H* loops measured at 5 K for sample A5.

respectively. In contrast to a normal hysteresis curve at 10 K, the curve at 70 K is inverted, as indicated by the directions of the arrows. This might be understood as being

originated from two magnetic phases coupled in antiparallel, which will be discussed later. Figure 3.7 shows the normalized in-plane and out-of-plane hysteresis loops measured at 5 K for sample A5. In comparison with the in-plane direction, a smaller coercivity and squareness are observed in the out-of-plane direction, indicating that amorphous $Ge_{1-x}Mn_x$ is an easy plane magnet.

3.3.2.2 ZFC, FC and TRM

Figures 3.8(a)-3.8(f) show the magnetic properties for samples A1-A6. Shown in each figure are three curves: ZFC (open circle), FC (filled circle), and TRM (star) curves. ZFC curves were obtained by first cooling the sample in zero field from room temperature to 5 K and then measure the magnetic moment while warming up the sample with the presence of a magnetic field of 20 Oe (200 Oe for sample A1 due to the weak signal). FC curve was obtained in a similar procedure except that the sample was cooled with the presence of a magnetic field of 20 Oe (200 Oe). On the other hand, the TRM curve was obtained by cooling the sample with a magnetic field of 20 Oe (200 Oe) and then the magnetic moment was measured while warming up the sample without a field. Some typical features of the magnetic properties of the amorphous samples are summarized as follows: (a) a hump appears in ZFC curves of the high Mn composition samples (A3-A6) which shifts to lower temperatures with decreasing Mn composition. The hump eventually evolves into a cusp at the lower doping concentration (samples A1 and A2). The temperatures at which the hump (cusp) shows a maximum are 11, 21, 38, 60, 66, and 70 K for samples A1-A6, respectively; (b) irreversibility of ZFC and FC is observed in all the samples; (c) a negative TRM was found in samples A2-A6 above a certain temperature. The temperatures at which the magnetization changes sign are 18, 27, 33, 37, and 103 K for samples A2-A6,

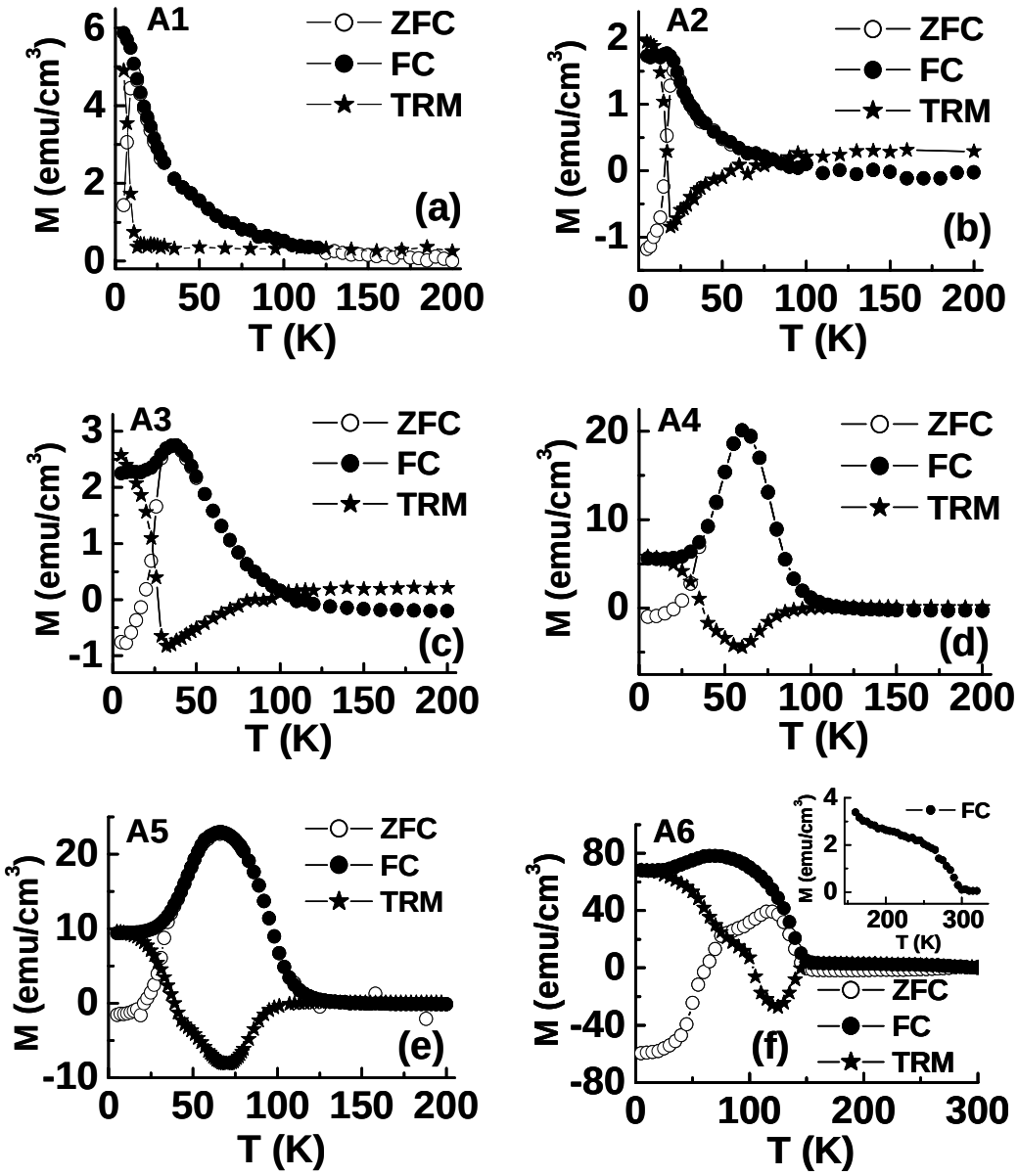

FIG. 3.8 Temperature-dependent magnetization curves for the samples under study with an applied magnetic field of 20 Oe (200 Oe for A1). (a) Sample A1, (b) sample A2, (c) sample A3, (d) sample A4, (e) sample A5, and (f) sample A6. The inset in (f) shows the FC curve at the temperature range from 150 to 300 K.

respectively; (d) a flat region appears in the FC curves at the temperature range from 5 K to 13, 17, 20, 21, and 25 K for sample A2-A6, respectively. We define T_C as the highest temperature point in the flat region for sample A2-A6. For sample A1, T_C is defined at the temperature of the cusp at the ZFC curve (11 K). Comparing to the other

samples, FC and ZFC curves of sample A6 is slightly different and can be divided into two regions: (I) 5 K < T < 150 K and (II) 155 K < T < 320 K. In region (I), the magnetic properties are dominated by the features due to the amorphous phase as discussed above. Shown in the inset of Fig. 3.7(f) is the FC curve in region (II). The sample exhibits a Curie temperature of about 295 K which is probably due to the existence of Mn_5Ge_3 phase, whose T_C is 295 K.

The negative TRM is an abnormal phenomenon and has not been observed in other Ge:Mn systems. Detailed measurements for sample A5 have been performed to study this abnormal phenomenon. The TRM curves are measured without a field after the sample is either zero-field cooled or field cooled at different applied fields ranging from 20 to 5000 Oe. For the case of $H = 20$ Oe, the magnetic field is first applied at 300 K but turned off at different temperatures after which the sample is continuously cooled to 5 K without a magnetic field. For the sake of clarity, in Fig. 3.9, only the curve which is obtained by stopping the applied field at 31 K is shown. The most striking feature of the ZFC curve is that the magnetic moment becomes negative below 27 K [see curve (a)]. To shed a further light on this, we measure the TRM curves with zero-field cooling. As can be seen from curve (c) in Fig. 3.9, the zero-field cooled TRM is negative in the entire temperature range from 5 to 150 K. A question naturally arises here: why is the zero-field cooled TRM negative? We find that whether the zero-field cooled TRM is negative or positive is determined by the polarity of the field that is used to fit the measurement curves of SQUID at room temperature. A positive fitting field gives a negative zero-field cooled TRM and vice versa [see Fig. 3.10]. The reason why the application of a magnetic field far above the ordering temperature still affects the magnetic properties of the sample at low temperature is not well understood at present.

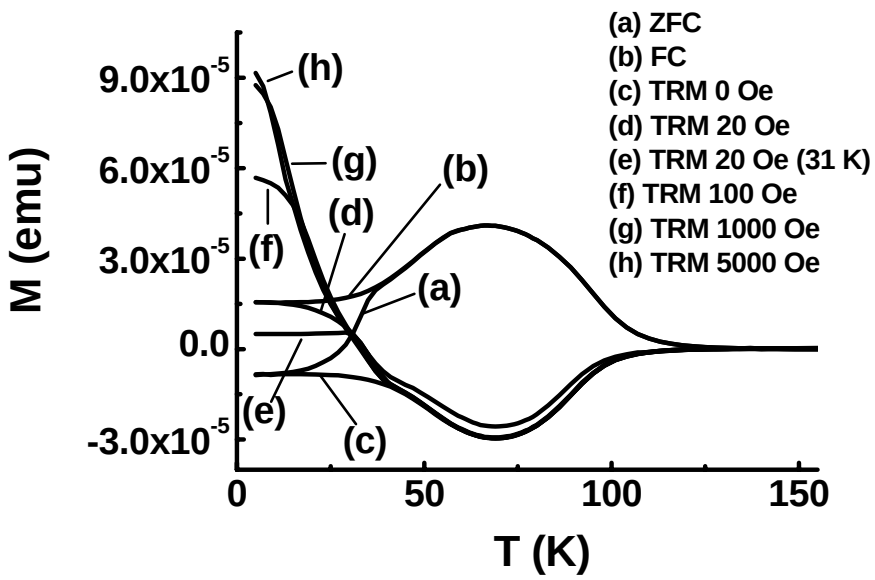

FIG. 3.9 ZFC, FC and TRM curves for sample A5. (a) ZFC curve (cooled at zero field, measured at 20 Oe); (b) FC curve (cooled and measured at 20 Oe); (c) TRM (cooled and measured at zero field); (d) TRM (cooled at 20 Oe from 300 to 5 K, measured at zero field); (e) TRM (cooled at 20 Oe from 300 to 31 K and at zero field from 31 to 5 K, measured at zero field); (f) TRM (cooled at 100 Oe from 300 to 5 K, measured at zero field); (g) TRM (cooled at 1000 Oe from 300 to 5 K, measured at zero field); (h) TRM (cooled at 5000 Oe from 300 to 5 K, measured at zero field).

Next we looked at how the cooling history affects the TRM curve. To this end, we measure a series of TRM curves by cooling the sample from 300 K with an applied field of 20 Oe. However, the field is removed at different temperatures of 70, 42, 31, 20, and 15 K, while the cooling process is continued until the temperature reached 5 K. The TRM curves obtained when the magnetic field is stopped above 41 K follow exactly curve (c), i.e., the ZFC-TRM curve. However, for the cases where the magnetic field is stopped below 41 K, the TRM is almost constant below the temperature point where the magnetic field is removed. As one of the examples, the TRM that is obtained when the field is removed at 31 K during cooling is shown in curve (e) in Fig. 3.9. As can be seen from the figure, above 31 K the curve traces back exactly the same TRM curve when the field is applied in the entire temperature range [see curve (d)]. Finally, we study the

effect of the strength of the applied field on the TRM curves. As can be seen from curves (f), (g) and (h), the effect of field strength is mainly confined to the low temperature region; it has essentially no effect on the curves above 31 K, in particular when the field is below 1000 Oe. As is with the case of hysteresis curves, the TRM curves can also be understood as being caused by the existence of two phases which are coupled in antiparallel. The two phases have different onset temperatures, magnetic moments and coercivity fields. So now the question is: what are the two possible phases? To answer this question, we have carried out the following studies about the high-temperature and the low-temperature phases, respectively.

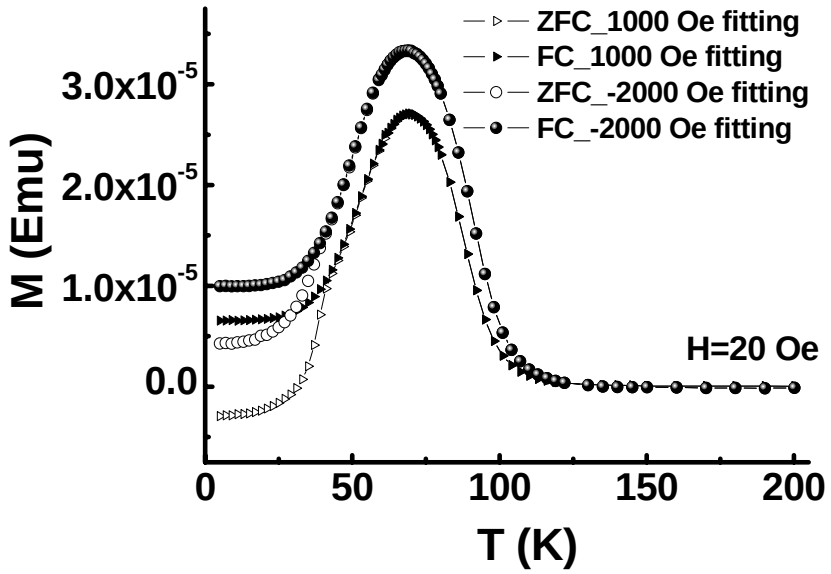

FIG. 3.10 ZFC and FC curves for sample A5 with different fitting fields of 1000 and -2000 Oe before measurements.

3.3.2.3 High temperature phase

A. ZFC and FC curves at different magnetic fields

In Fig. 3.11(a), we plot the ZFC and FC curves at different magnetic fields for sample A4 of which the major features can be summarized as follows. Firstly, the

merging point of ZFC and FC curve shifts to lower temperatures with increasing applied magnetic field, and the two curves completely overlap with each other at an applied field of > 1 T. These behaviours are not expected for ferromagnets and are thus indicating the presence of magnetic nanoclusters in the film or spin-glass nature of the system. [25 - 27] Secondly, the hump gradually becomes smaller and eventually disappears at a field of > 1 T. A sharp increase of the magnetization below 15 K is also observed at an applied field of 2 T. Bihler *et al.* also observed the same increase in the $Mn_{0.03}Ge_{0.97}$ epilayer with Mn_5Ge_3 secondary phase, and attributed it to a DMS formed by Mn atoms incorporated substitutionally into the Ge matrix. [11] As we will discuss later in the dynamic conductance analysis, below 15 K there is a strong localization of carriers in this region. Due to the antiferromagnetic coupling between the high-temperature and low-temperature phases, the later becomes observable only when a strong magnetic field is applied. This is further confirmed by the fact that the net increase of moment at 2 T at low temperature is almost equal in magnitude to the drop of moment in the same temperature region at the low applied field. Finally, the high-temperature tail increases in magnitude and its position shifts to higher temperature with increasing field. We obtained the ordering temperature T^*_C values by fitting the curves with Curie-Weiss law. As shown in Fig. 3.11(b), the ordering temperature of the high-temperature phase in sample A4 increases monotonically from 104 K at low field to about 190 K at 0.5 T beyond which it saturates at ~ 200 K. The ordering temperature at the low field agrees well with the values reported for crystalline samples with much lower Mn compositions in Refs. 1 and 7.

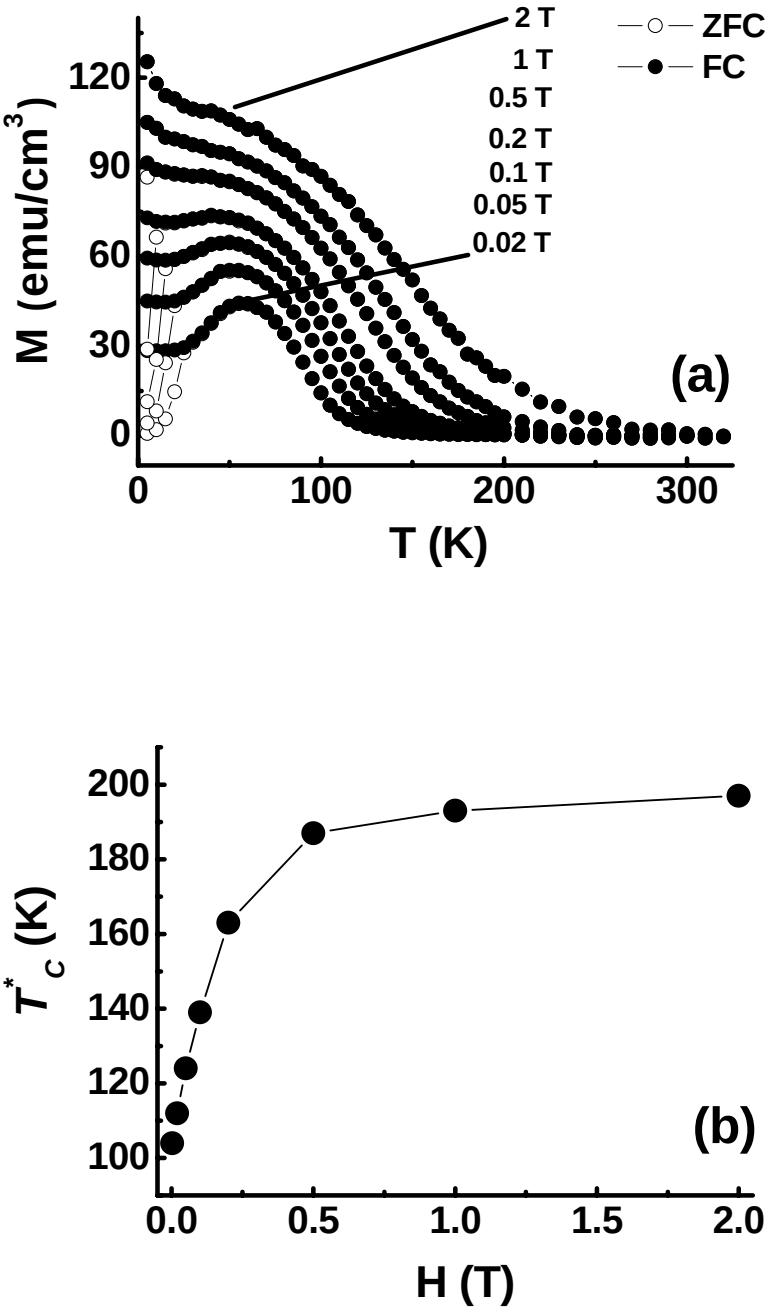

FIG. 3.11 (a) ZFC and FC curves at different magnetic fields for sample A4; (b) the ordering temperature (T^*_C) as a function of the applied magnetic field in sample A4.

B. Saturation *M-T* curves

Figure 3.12 shows the normalized saturation *M-T* curves for the amorphous samples A1, A2, A3, A4, and A6 at a magnetic field of 2 T. The magnetizations of all samples saturate at such a high applied magnetic field, i.e. ZFC and FC curves overlap with each

other. For the lowest Mn concentration of sample A1, a concave *M-T* curve is observed, which is typical for the localized system. [28] For samples A2, A3, and A4, the curves almost coincide above the temperature of 180 K, below which the curves become more convex with the increased Mn concentration. For sample A6, the magnetization curve is different from those of other amorphous samples and a pronounced convex curve is observed. The ferromagnetic behaviour is even observed above 330 K. In addition, an obvious increase in the magnetization below 15 K can be observed in all samples. And the increase becomes less pronounced with increasing Mn concentration. The mechanism should be the same as those discussed above for sample A4. Further discussion will be presented in the section of dynamic conductance studies. The above saturation magnetization behaviour can be understood as follows. For sample A1, no negative TRM is observed in this sample, indicating that a single low-temperature phase exists in the film. With increasing Mn concentration, Mn-rich nanoparticles begin to form in sample A2 although we cannot observe them from both high resolution TEM and low-field magnetic measurements. The Mn-rich nanoparticles will exhibit a more pronounced response to the external field with increasing Mn concentration (The details will be discussed in the following simulation section). When the secondary phase forms, as in sample A6, it will have a contribution to both the high-temperature and low-temperature magnetic properties.

C. Simulation results

In this section, we will discuss the simulation results about the magnetic field effect on the nanoparticles. The above-mentioned behaviours, in principle, can be understood as being caused by a wide-range distribution of the cluster sizes. In order to understand quantitatively this behaviour, we have simulated the temperature

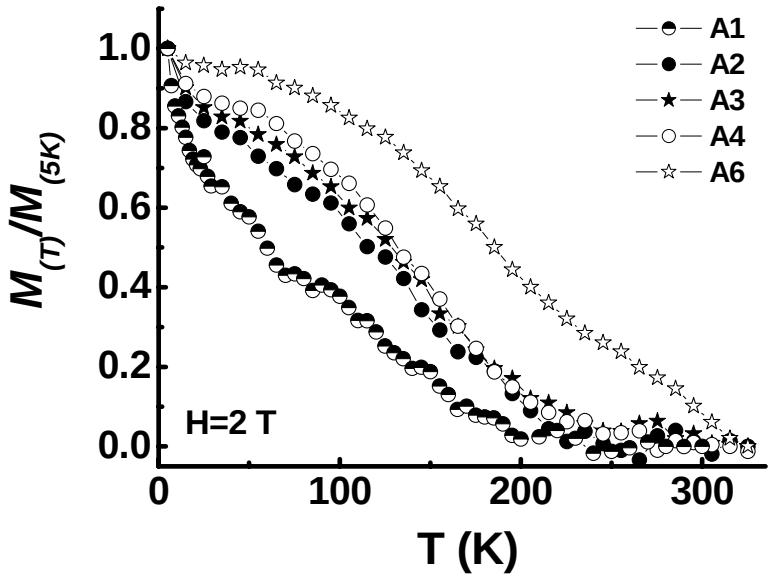

FIG. 3.12 Normalized *M-T* curves for amorphous samples A1, A2, A3, A4, and A6 at a magnetic field of 2 T.

dependence of magnetic moment at different applied magnetic fields. Here, we assume that the sizes of the nanoclusters follow a normal distribution and there is no interaction among the clusters. Under these assumptions, we only need to consider the competition between the Zeeman and thermal energies. At a given temperature and magnetic field, the average moment for clusters with a normal distribution is given by:

$$M(T,H) = \int_0^\infty \frac{4}{3}\pi r^3 M_s f(r) \frac{e^y - e^{-y}}{e^y + e^{-y}} dr \,. \tag{3.1}$$

Here,

$$f(r) = \frac{1}{\sqrt{2\pi}\sigma} e^{-\frac{(r-\mu)^2}{2\sigma^2}}, \tag{3.2}$$

$$y = \frac{\frac{4}{3}\pi r^3 M_s H}{K_B T}, \tag{3.3}$$

where H is the applied magnetic field, r is the radius of the cluster, K_B is the Boltzmann constant, T is the temperature in Kelvin, μ is the mean and σ is the standard deviation of the normal distribution, and M_s is the saturation magnetization

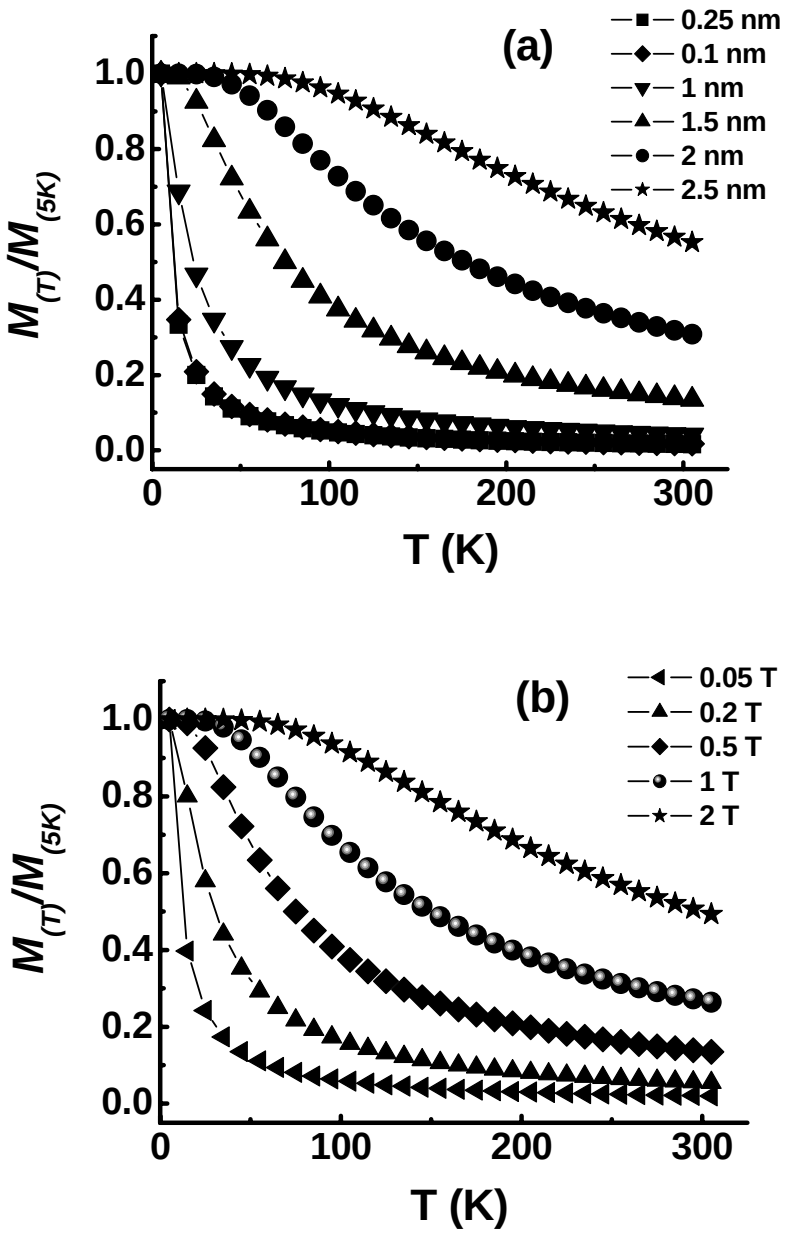

FIG. 3.13 (a) Simulation results of normalized *M-T* curves with different μ values ($\sigma = 0.1$ nm and $H = 0.5$ T); (b) simulation results of normalized *M-T* curves at different applied magnetic fields ($\mu = 3$ nm and $\sigma = 0.1$ nm).

which can be estimated from the average saturation magnetization of samples grown at 300 ^{o}C with Mn concentration 24.8% and 25.1% [see the details in chapter 4]. Figure 3.13(a) shows the simulated temperature dependence of magnetization for different μ values (average cluster size) with $\sigma = 0.1$ nm and $H = 0.5$ T. As it is expected, the

larger the average clusters size, the higher the ordering temperature. The effect of magnetic field is shown in Fig. 3.13(b), in which we have assumed that μ = 1.5 nm and σ = 0.1 nm. The simulation results agree well qualitatively with the experimental results shown in Fig. 3.11(a), even though we have not taken into account the interactions among the clusters. This further confirms that ferromagnetism of the high-temperature phase indeed originates from secondary phases.

3.3.2.4 Relaxation

We now turn to the discussion of the low-temperature phase. Considering the structure of the sample, it is plausible to interpret the low-temperature phase as a spin glass. However, the high squareness (typically 0.72 at 5 K) of *M*-*H* curves at low temperature makes the sample distinguishable from the pure spin-glass behaviour, though we cannot exclude the possibility that in certain regions such as those without magnetic clusters, the spin glass will form. In order to confirm this, we have performed the ac susceptibility and TRM relaxation measurement for sample A4. The TRM measurements have been performed by using the following procedures: the sample is field cooled with a magnetic field of 1000 Oe from 300 K to the desired temperature; after temperature stabilization and a waiting time of 300 s, the external field was switched off and the magnetization was recorded as a function of the elapsed time. The magnetization of the first point is denoted as $M(t_1)$ to which $M(t)$ (the magnetization at time t) is normalized to show the decay of the magnetization. The results for different temperatures are presented in Fig. 3.14. At the lowest temperature of 5 K, the magnetization is almost constant and no decay is observed. With the increase of temperature, an obvious time-dependent decay can be observed and the decay rate reaches the maximum at 25 K. In the temperature range from 25 to 30 K, TRM is too

small to allow a precise measurement of the temperature dependence. However, when the temperature reaches 35 K and above, the TRM becomes negative and there was no decay of magnetization observed.

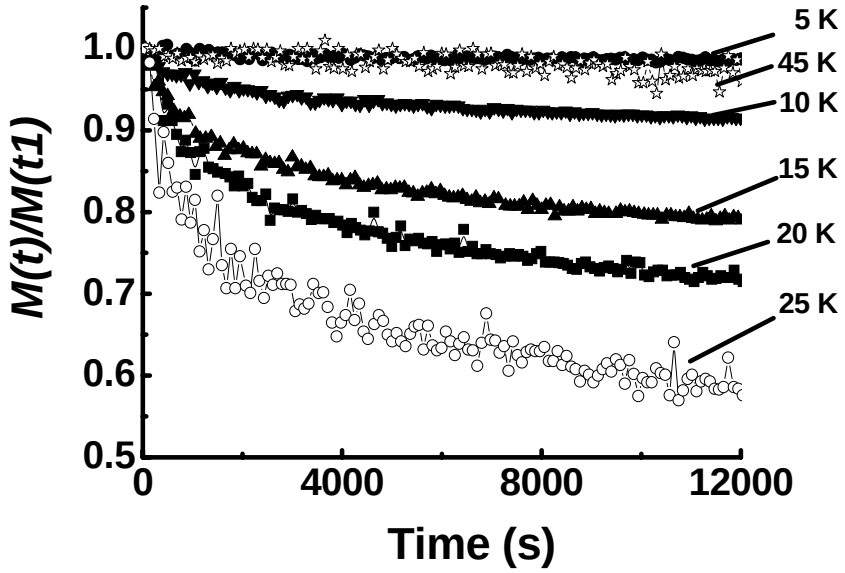

FIG. 3.14 TRM relaxation curves for sample A4 at different temperatures.

3.3.2.5 Ac susceptibility

A. Sample A4

Although the irreversibility in ZFC and FC curves and time-dependent relaxation are often interpreted as fingerprints of the spin-glass system, [29-33] the frozen state can further be elucidated by the measurement of the ac susceptibility. The ac susceptibility of both real part (χ′) and imaginary part (χ″) for sample A4 is shown in Figs. 3.15(a) and 3.15(b) with the ac excitation amplitude of 5 Oe and a dc field of 8 Oe at different frequencies ranging from 1 to 500 Hz. In the real part (χ′) of the ac susceptibility (Fig. 3.15(a)), the curve shape is very similar to that of ZFC curve shown in Fig. 3.8(d). A hump is also observed around 60 K coinciding with the temperature in the ZFC measurement. A frequency-dependent shift is observed at the temperature

range between 25 and 55 K, and at other temperatures, the curves overlap with each other at different measuring frequencies. In the imaginary part (χ'') of the ac susceptibility [see Fig. 3.15(b)], a peak at 45 K was observed at 500 Hz and shifts to the lower temperature with decreasing frequency. We obtained the value of $\Delta T_f^{'} /[T_f^{'} \Delta \log f] \approx 0.046$, where $T_f^{'}$ is the peak position at frequency f. This value is very close to other reported spin-glass systems [34] and smaller than the value of ≈ 0.28 obtained for a superparamagnet system [35]. The behaviour of frequency-dependent shift in the real and imaginary part measurements is observed in many spin-glass systems and is regarded as the fingerprint for the spin-glass behaviour. [29-33] However, the frequency-dependent behaviour in our amorphous $Ge_{1-x}Mn_x$ thin films is different from both the traditional spin-glass and cluster-glass materials. The former exhibits a frequency-dependent cusp in the real part. [33, 36] The latter present a two-peak structure. [31,37] The peak at high temperature indicates a paramagnetic (PM) to ferromagnetic transition. The peak at low temperature is attributed to the frustration of the long-range antiferromagnetic state. [31] Although a frequency-dependent peak is observed in the imaginary part, no peak is observed in the real part of the ac susceptibility for our amorphous Ge_xMn_{1-x} system. Jaeger *et al.* [12] also observed both the frequency-dependent ac susceptibility behaviour and relaxation effects of the magnetization in both samples of $Ge_{0.96}Mn_{0.04}$ and $Ge_{0.8}Mn_{0.2.}$ They suggested that the formation of ferromagnetic clusters (BMPs) occurs at high temperature and these local ferromagnetic regions grow in size, finally leading to a disordered freezing glassy state at low temperature. In this case, according to our results, the spin-glass-like phase may have formed at the peak temperature position of imaginary part (χ''). However, the spins should be more ordered than those in normal spin glasses; otherwise, it is difficult to

explain the large squareness of *M-H* curves and negative TRM to be discussed in the following section.

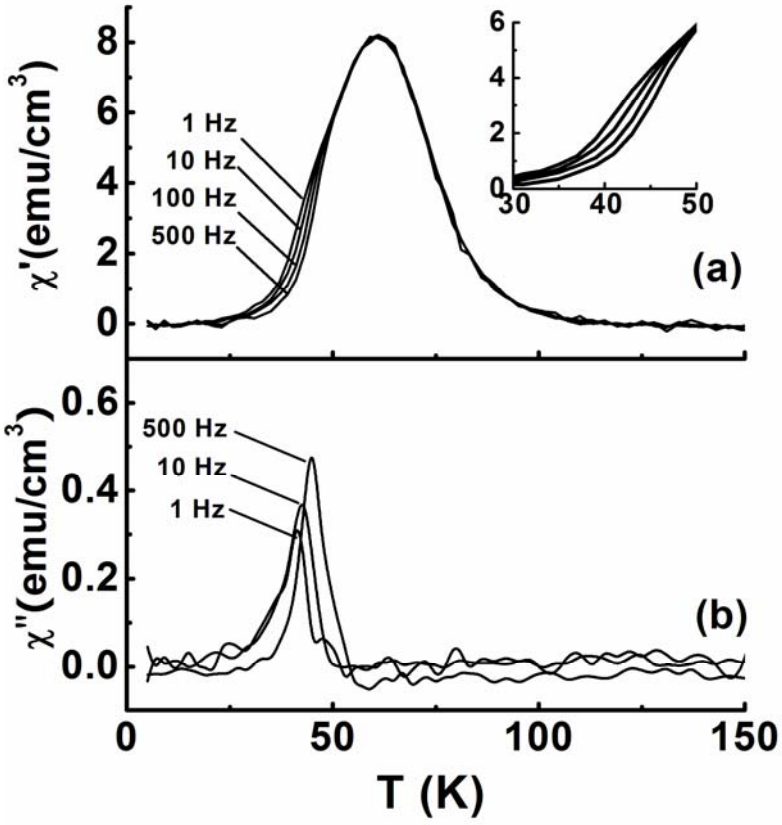

FIG. 3.15 Temperature dependence of (a) real part (χ′) and (b) imaginary part (χ″) of the ac susceptibility for sample A4 at different frequencies ranging from 1 to 500 Hz. The inset in (a) shows the central part of the frequency-dependent shift in χ′.

In Figs. 3.16(a) and 3.16(b), the temperature dependence of real part (χ′) and imaginary part (χ″) of the ac susceptibility for sample A4 at different dc fields at a frequency of 10 Hz are shown. At the low dc magnetic fields, the real part (χ′) of the ac susceptibility at the temperature range from 40 to 80 K is enhanced obviously and reaches a maximum at 8 Oe. When the field is further increased, the suppression of the real part and the broadening of the susceptibility hump are observed. When the field is increased to 100 Oe, the curves become almost flat. The same trend is also observed in

the imaginary part (χ″). The intensity of peak reaches a maximum at the dc field of 8 Oe and become very small at the dc field of 100 Oe. The decline of the real part (χ′) and imaginary part (χ″) under a magnetic field is observed in many spin-glass systems. [38-41] Sahana *et al.* argued that a field saturated the FM contribution to the initial susceptibility and suppressed the energy barriers and therefore reduced the freezing temperature. [41] However, the authors in Refs. 38 to 38 failed to observe the enhancement of ac susceptibility when a small dc field was applied. Thus, our amorphous $Ge_{1-x}Mn_x$ system is really different from the traditional spin-glass and reentrant spin-glass systems.

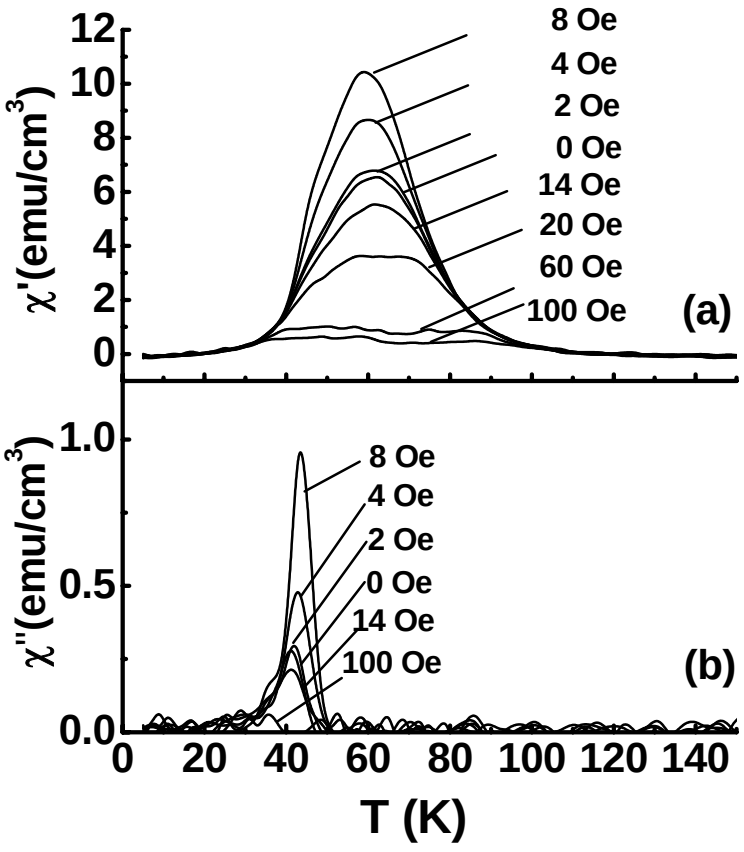

FIG. 3.16 Temperature dependence of (a) real part (χ′) and (b) imaginary part (χ″) of the ac susceptibility for sample A4 at different dc fields and a frequency of 10 Hz.

B. Sample A6

The temperature dependence of the real part (χ′) of the ac susceptibility with a dc field of 4 Oe at different frequencies for sample A6 is shown in Fig. 3.17. The ac susceptibility behaviour is obviously different from the sample A4. For all frequencies, the real part (χ′) increases until 60 K and subsequently shows a plateau-like behaviour up to 120 K. Then, a peak around 135 K is observed and the position of the peak is almost independent of the applied ac frequency. The peak position is very close to the ordering temperature (~ 140 K) obtained from the fitting with the Curie-Weiss law. Above this peak temperature, the susceptibility decreases rapidly to zero around 150 K, the same temperature at which Mn_5Ge_3 phase appears in the ZFC and FC curves. The frequency-dependent behaviour is observed between 60 and 140 K. The curves overlap at other measured temperatures. The imaginary part (χ″) at a frequency of 10 Hz is also shown in Fig. 3.17. The imaginary part exhibits a similar shape with the real part except that it peaks at 133 K, 4 K lower than that in the real part.

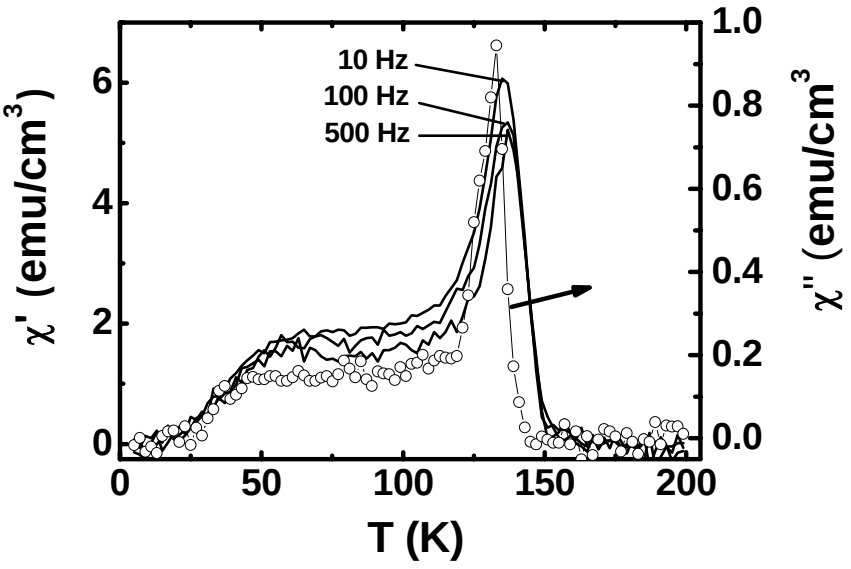

FIG. 3.17 Temperature dependence of the real part (χ′) of the ac susceptibility with a dc field of 4 Oe at different frequencies (the solid lines) for sample A6. The imaginary part (χ″) at a frequency of 10 Hz is also shown in the figure (open circle).

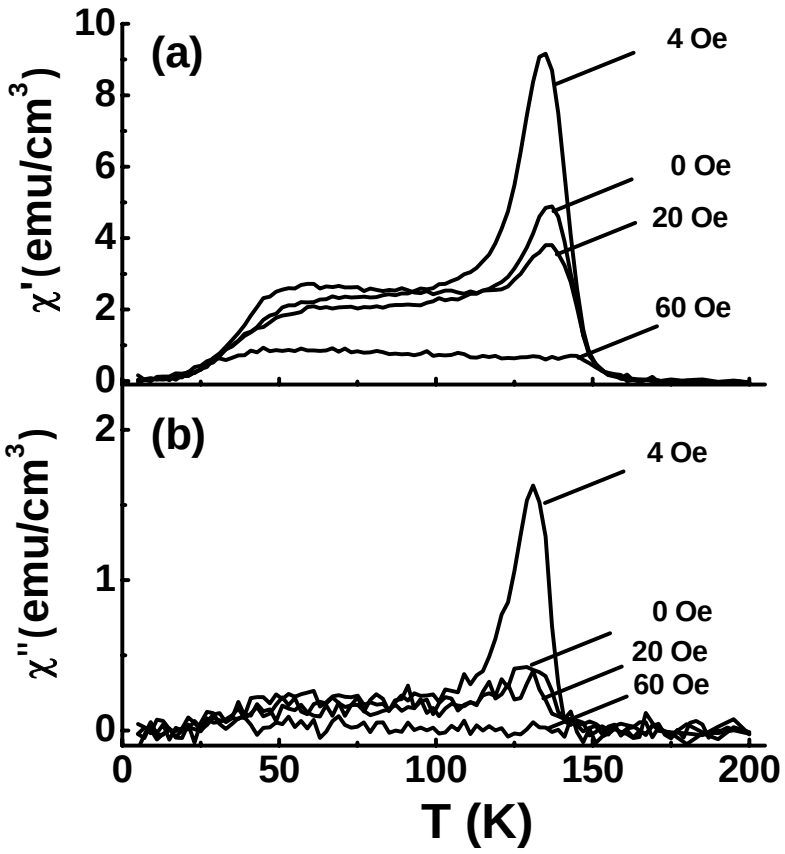

FIG. 3.18 Temperature dependence of both (a) real part (χ′) and (b) imaginary part (χ″) of the ac susceptibility at different dc fields and a frequency of 10 Hz for sample A6.

In Figs. 3.18(a) and 3.18(b), the temperature dependence of both the real part (χ′) and imaginary part (χ″) of the ac susceptibility at different dc fields with an ac frequency of 10 Hz for sample A6. When a small dc field of 4 Oe is applied, an upward shift can be clearly observed at the temperature range from 31 to 145 K and the intensity of peak increases dramatically. When the magnetic field is further increased to 20 Oe, the height of the peak begins to decrease. However, the height of the plateau-like region at the temperature range of 31 to 111 K still increases. The different response of the real part (χ′) to a dc field at low and high temperature range indicates that at least two phases coexist in the thin film. However, the interaction mechanism between the Mn_5Ge_3 clusters and amorphous $Ge_{1-x}Mn_x$ matrix is not understood now. When a

magnetic field of 60 Oe is applied, the real part (χ′) is suppressed and becomes flat. In Fig. 3.18(b), the imaginary part (χ″) at different frequencies is also shown. The height of the peak exhibits the same trend as that of the real part (χ′).

3.3.2.6 Our model for the explanation of the observed abnormal magnetic phenomena

So far, several groups have reported the negative TRM in different magnetically inhomogeneous systems, including amorphous Gd-Co films, [42] (Ni, Fe)-SiO_2 granular films, [43] $Dy_{50}Fe_{50}$/ (Ti or Ga) multilayers, [44] bulk materials (samarium (III) gadolinium (III) hexacyano-chromate (III) system), [45] and Cr_2O_3 coated with CrO_2 particles [46]. A number of models [43, 44, 46-48] have been proposed to explain the negative TRM and the accompanying inverted hysteresis phenomena. Based on these models, the negative TRM in our samples can be understood as following with the assistance of the schematic shown in Fig. 3.19. In the following discussion, the magnetization contribution of two different magnetic phases will be considered, including the high-temperature magnetic cluster phase and low-temperature highly ordered spin-glass-like phase. During the field cooling process, the magnetic clusters (gray circles) become gradually aligned with the external field when the temperature decreases [see section (I) of Fig. 3.19]. After the temperature reaches a certain critical value, the carrier-mediated spin ordering will occur in some localized regions due to electrical potential fluctuation in the sample. Without the influence of clusters, the spins will align along the external field direction and these regions will grow and eventually merge to form a global ferromagnetic phase. However, with the presence of magnetic clusters, the spins in the proximity of clusters will couple antiferromagnetically with the spins of the clusters [see section (II) of Fig. 3.19]. These spins will then serve as

"anchor" points for other spins so that all the spins near the non-cluster regions will eventually be aligned antiparallelly to the magnetization direction of the clusters. In reality, the spin-freezing process may take place simultaneously with the carrier-mediated and cluster-assisted FM ordering process; therefore, the spin-glass phase may form in regions which are far away from FM clusters and with low carrier density. The competition between FM ordering and spin-glass formation will eventually lead to a material with the coexistence of spin-glass phase and FM regions. The latter in the proximity of FM clusters is coupled antiferromagnetically to the FM clusters [see section III in Fig. 3.19]. In order to differentiate it from the normal spin-glass phase, we call it a highly ordered spin-glass-like phase.

Consider now that, the magnetic field is switched off at 5 K and the sample is warmed up to take the TRM. As the antiferromagnetically coupled system is formed when an external field is applied, its magnetization will be flipped or flopped [49] by thermal agitation when the field is removed [see section (IV) of Fig. 3.19]. This results in the initial decay and eventually reversal of direction of the net magnetization. Once the magnetization flipping / flopping process is completed, the magnitude of the net magnetization will decrease as the temperature continues increasing and it will eventually disappear at the temperature where the magnetic moment appears during the cooling process [see section (V) of Fig. 3.19]. Although it is not shown here, we have confirmed that a positive TRM will appear when a negative field is applied during the field cooling process. It is readily to understand that the antiferromagnetic coupling between the two phases also accounts for the *M*-*T* curves shown in Figs. 3.8(b)-3.8(f) and 3.11(a).

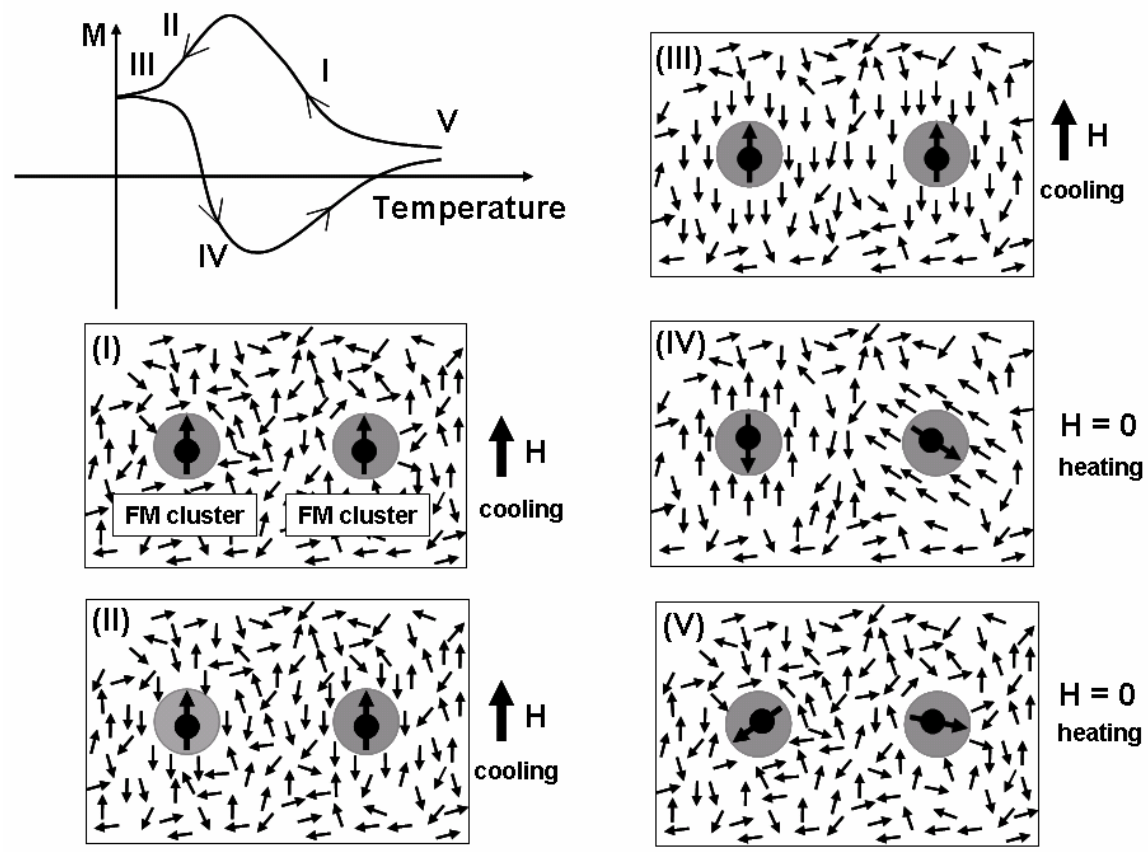

FIG. 3.19 Schematic illustration for interpreting the origin of negative TRM. The spins of the magnetic clusters are shown with gray circles. The small arrows indicate the spins in the amorphous $Ge_{1-x}Mn_x$ matrix.

3.3.2.7 Effect of H_2 plasma annealing

A. ZFC-FC curves

The effect of hydrogen on nonmagnetic materials has been studied extensively. It has been found that hydrogen forms complexes with defects and dopants and passivates their electronic properties. Goennenwein *et al.* have incorporated hydrogen into $Ga_{1-x}Mn_xAs$ thin films. The incorporation of hydrogen electrically passivated the Mn acceptors and removed the holes crucial to the itinerant ferromagnetism. [50] They observed ferromagnetism to paramagnetism transition in $Ga_{0.963}Mn_{0.037}As$ after the hydrogenation. [50] Thus, such a hydrogenation provides us a new way to control the ferromagnetic properties in DMSs. In our studies, sample A5 was hydrogenated using

remote dc H_2 plasma of 500 W for 4 hours. During the plasma annealing process, the sample was heated to 160 ^oC, well below the growth temperature of 200 ^oC, in a CVD system (Type: CN-CVD-100, ULVAC Japan Ltd). After annealing, the sample was taken out to measure the magnetic properties. All the magnetic measurements were performed on the same piece of sample.

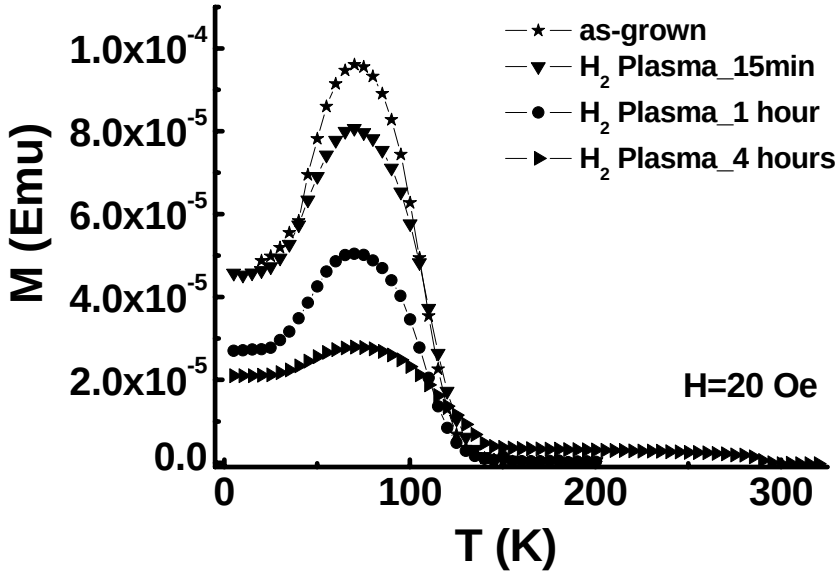

FIG. 3.20 FC curves with a magnetic field of 20 Oe for different H_2 plasma annealing time for sample A5.

In Fig. 3.20, we plot the FC curves with a magnetic field of 20 Oe for different annealing durations. In comparison with the as-grown sample, an obvious reduction of the moment is observed and become more obvious with the increase of the annealing time, though the shapes of the curves below 200 K are almost same. The magnetization drops to around 25% of the as-grown sample after 4 hours H_2 plasma annealing. Goennenwein *et al.* argued that the Mn acceptors could be deuterated quantitatively, leading to a reduction of the hole density in $Ga_{1-x}Mn_xAs$ system. [50] Similar phenomenon may also happen in our amorphous $Ge_{1-x}Mn_x$ thin film system.

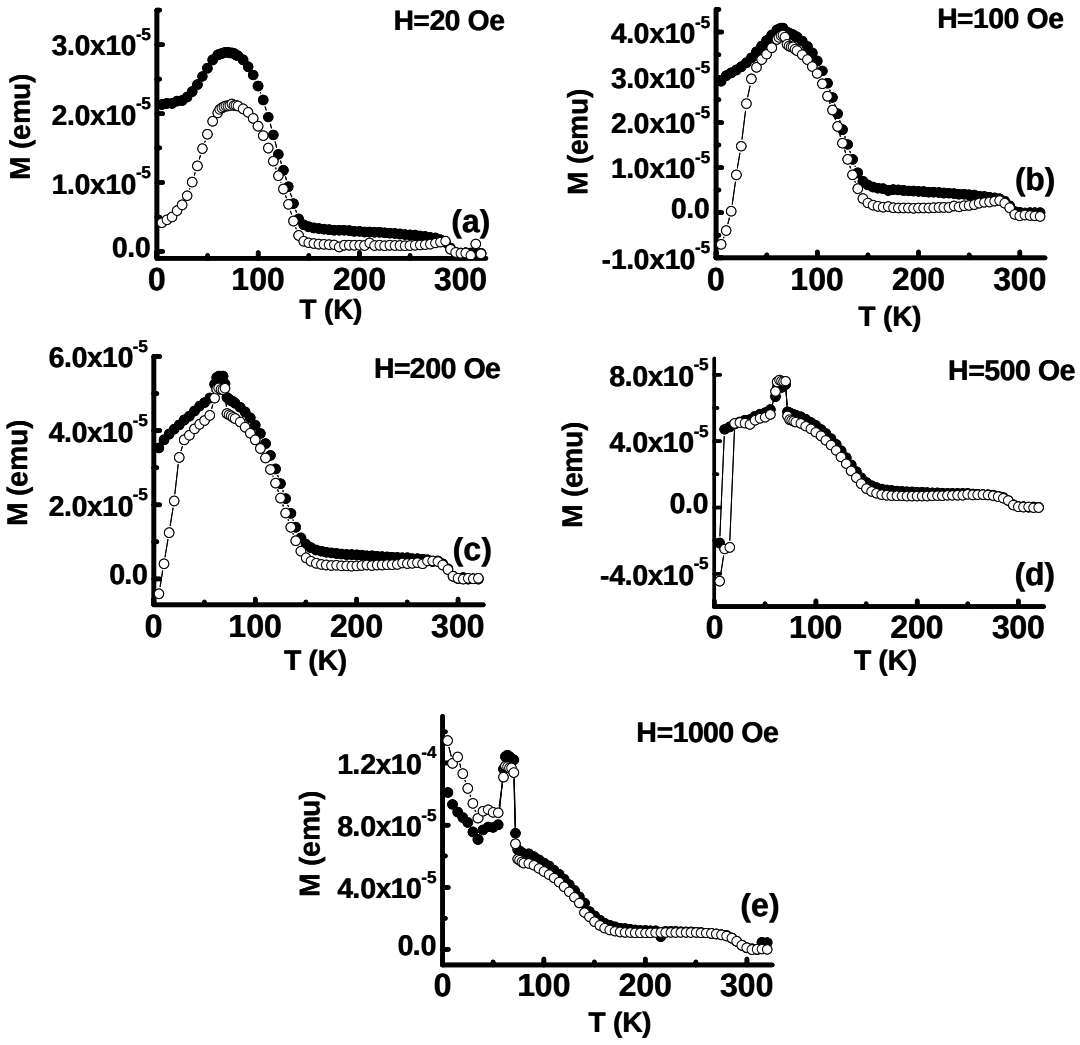

FIG. 3.21 ZFC (open circles) and FC (solid circles) curves at different magnetic fields for sample A5 after 4 hours H_2 plasma annealing at 160 ^oC.

However, Mn_5Ge_3 phase was observed after 4 hours hydrogenation process, which can be clearly seen in Fig. 3.21(a). ZFC and FC curves at an applied magnetic field of 20 Oe in Fig. 3.21(a) are obviously different from those in the as-grown sample shown in Fig. 3.8(e) and exhibit a Curie-temperature of 295 K, which is a typical feature of the Mn_5Ge_3 phase. The ZFC and FC curves remains separated until 285 K, a little lower than the Curie temperature of the Mn_5Ge_3 phase. Crystalline Ge peak at the position around 298 cm^{-1} is also observed for the sample after 4 hours H_2 annealing in the Raman measurement. Sriraman *et al.* observed the hydrogen-induced crystallization in

the amorphous Si thin film. [51] They argued that during H exposure of *a*-Si:H the reactions that occur include surface H adsorption, surface H abstraction, etching of surface silicon hydrides, dangling-bond-mediated dissociation of surface hydrides, surface H sputtering/desorption, diffusion of H into the a-Si:H film, and insertion of H into strained Si–Si bonds, which will stimulate the crystallization of the amorphous Si. [51] It seems that hydrogen plasmas have similar effect on our amorphous $Ge_{1-x}Mn_x$ system and can also stimulate the crystallization of both amorphous Ge and Mn_5Ge_3 phase. Also shown in Figs. 3.21(b) to 3.21(e) are the ZFC-FC curves at different magnetic fields of 100, 200, 500, and 1000 Oe, respectively. The major features can be summarized as the following: (1) a jump in both ZFC and FC curves around 70 K can be found when applying a magnetic field of 100 Oe, and the jump become more pronounced with increasing magnetic field; (2) a dramatic drop in both ZFC and FC curves at low temperatures can be observed when a magnetic field of 500 Oe is applied; (3) The drop disappears and upturn curves are observed when a magnetic field of 1000 Oe is applied.

B. *M-H* curves

Figure 3.22 shows *M-H* curves for sample A5 at 20, 30 and 70 K after 4 hour H_2 plasma annealing. Clear hysteresis loops can be observed until 70 K, and the coercivity decreases with increasing temperature and become almost zero at 70 K. These are similar to those in the amorphous $Ge_{1-x}Mn_x$ samples discussed in the section 3.3.2.1. However, several differences, in comparison with the amorphous $Ge_{1-x}Mn_x$ samples, can be observed in the annealing sample and summarized as follows: (1) no inverted *M-H* curve at 70 K is observed; (2) the shapes of *M-H* curves are irregular. Irregular *M-H* curves are generally observed in the inhomogeneous magnetic system, which indicates

that at least two magnetic phases coexist in the same system. As discussed in the section of ZFC and FC curves, amorphous $Ge_{1-x}Mn_x$ and Mn_5Ge_3 phases coexist in the annealing sample. Thus, both of them have contributions to *M-H* curves. At the low temperatures and low magnetic fields, the contribution from the amorphous phase is dominant. At the high temperatures and high magnetic fields, the dominant contribution is from the Mn_5Ge_3 phase; (3) higher coercivities are obtained in the annealing sample, which is due to the additional contribution from the Mn_5Ge_3 phase.

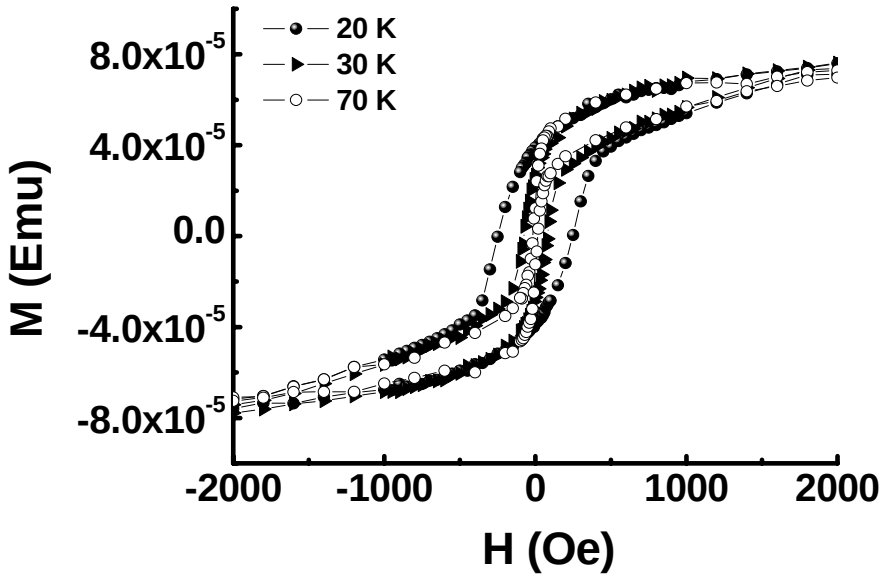

FIG. 3.22 *M-H* curves at 20, 30 and 70 K for sample A5 after 4 hours H_2 plasma annealing.

3.3.3 Electrical transport properties

3.3.3.1 Temperature-dependent resistivity

Figures 3.23(a)-3.23(d) show the temperature-dependent resistivity curves for samples A2, A3, A4, and A6. The resistivity of all the samples increases with decreasing temperature. Although the magnetization shows a hump (cusp) or drop at intermediate temperatures, the resistivity does not show a corresponding change in the same temperature region. This again suggests that the high-temperature phase is due to

the extrinsic origin. Among four amorphous samples (A2, A3, A4, and A6), sample A2 exhibits the highest resistivity and a sharp increase of the resistivity at low temperature. In comparison, samples A3, A4, and A6 have a much lower resistivity and show a relatively slow increase when the temperature decreases. This difference is to be compared with the shape of the ZFC curves in which sample A2 exhibits a cusp at low temperatures while the other three samples show a hump at relatively higher temperatures. As the cusp shape is normally observed for spin glasses, it suggests that the ferromagnetic interaction in sample A2, if any, is much weaker than those in the other three samples. It is well known that the transport properties of an inhomogeneous metal or semiconductor are generally dominated by variable range hopping at low temperature. In the cases of highly disordered DMSs, in addition to the normal hopping mechanism, one should also consider the scattering due to magnetic impurities. Thus, the temperature dependence of resistivity is a quite complex issue in these samples.

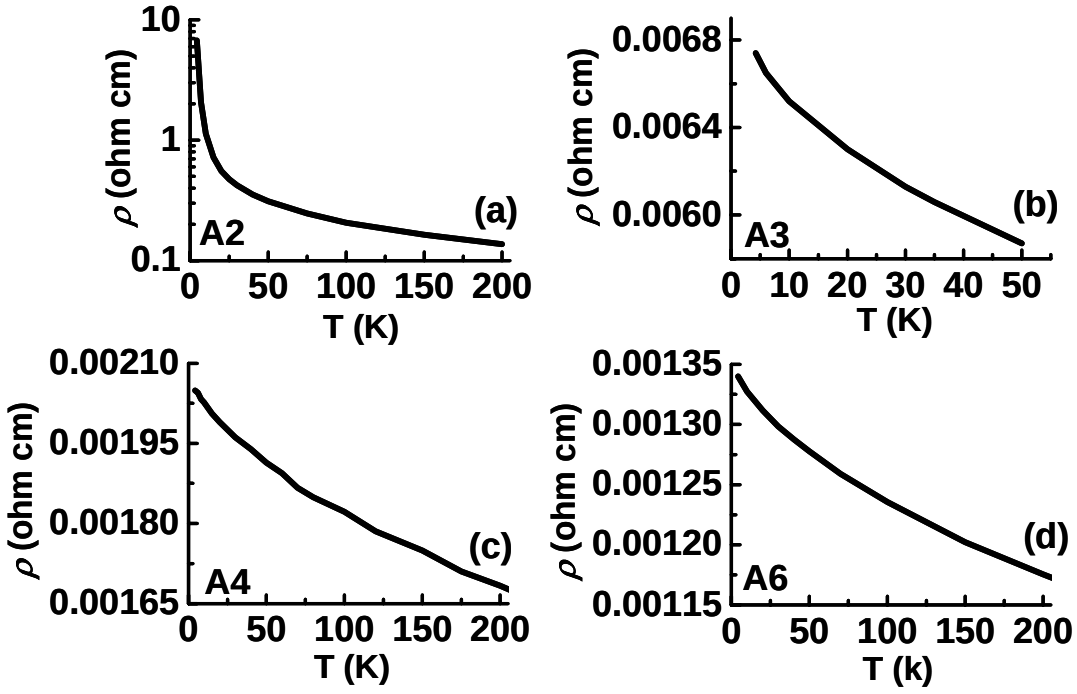

FIG. 3.23 *R-T* curves of the samples under study. (a) Sample A2, (b) sample A3, (c) sample A4, (d) sample A6.

3.3.3.2 Temperature-dependent conductance

In addition to the temperature dependence of resistivity, we are particularly interested in the dynamic conductance as a function of bias voltage because it is sensitive to carrier localization and inhomogeneity of the samples. Figures 3.24(a) - 3.24(d) show the dynamic conductance curves for four samples under study. Due to the strong dependence on bias voltage, the conductance for samples A2 is normalized to its value at zero bias, while for other samples we show the absolute values. Almost all the curves show a V-shape at low temperatures, and became flattened as the temperature increases. The V-shape conductance-voltage curves were observed in many inhomogeneous systems [52-55] and were interpreted as being caused by the carrier localization due to the potential disorder. With the decrease of the Mn composition, the nonlinearity becomes more prominent, i.e. the G_V / G_0 value increases at the same temperature as the Mn composition decreases (G_V: the conductance at voltage V, G_0: zero-bias conductance). In order to characterize quantitatively the degree of localization, we plot in Figs. 3.25(a)-3.25(d) the normalized temperature dependence of

$$G' = (G_{2.5V,T} / G_{0,T}) / (G_{2.5V,4.2K}) / G_{0,4.2K}), \tag{3.4}$$

where $G_{2.5V,T}$ ($G_{0,T}$) and $G_{2.5V,4.2K}$ ($G_{0,4.2K}$) are the conductance at temperature T and 4.2 K when the bias is 2.5 V (0 V). We define a critical temperature (T'_C) as the cross-point of the slope at low- and high-temperature regions in the temperature-dependent curves. It can be observed that T'_C increases with increasing Mn composition. T'_C is 10, 14, 18, and 31 K for samples A2, A3, A4, and A6, respectively. These temperatures are very close to T_C, the highest temperatures where the flat regions in the FC curves appear in Fig. 3.8. It indicates that the magnetic properties in the amorphous samples at low temperature are closely related to the carrier localization.

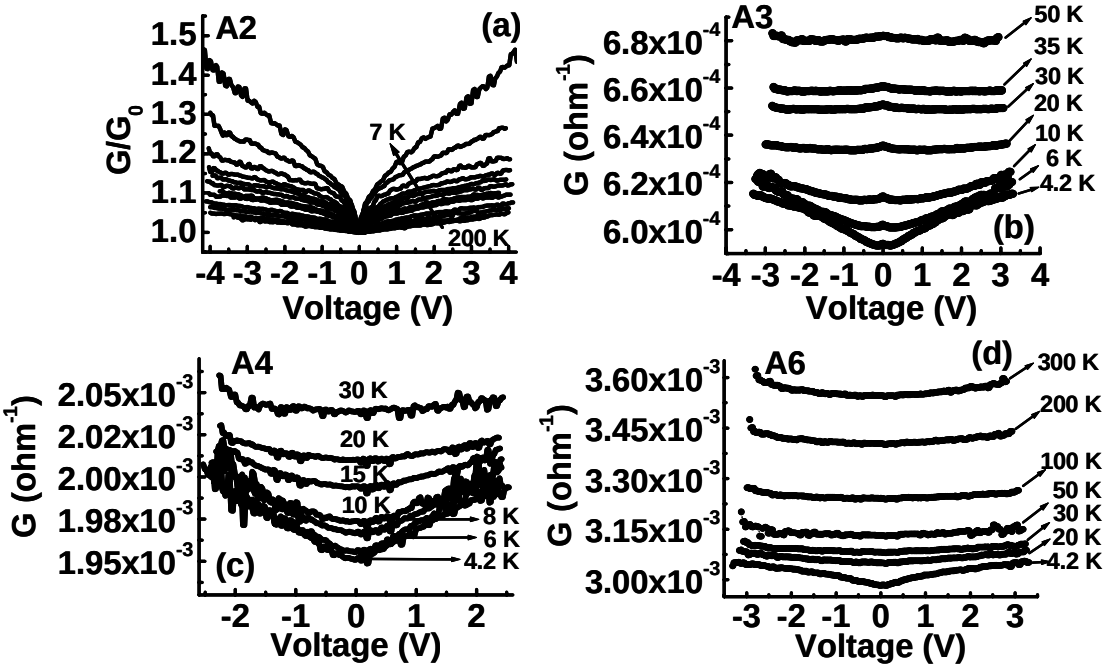

FIG. 3.24 Dynamic conductance-voltage curves at different temperatures for the samples under study. (a) Sample A2, (b) sample A3, (c) sample A4, (d) sample A6.

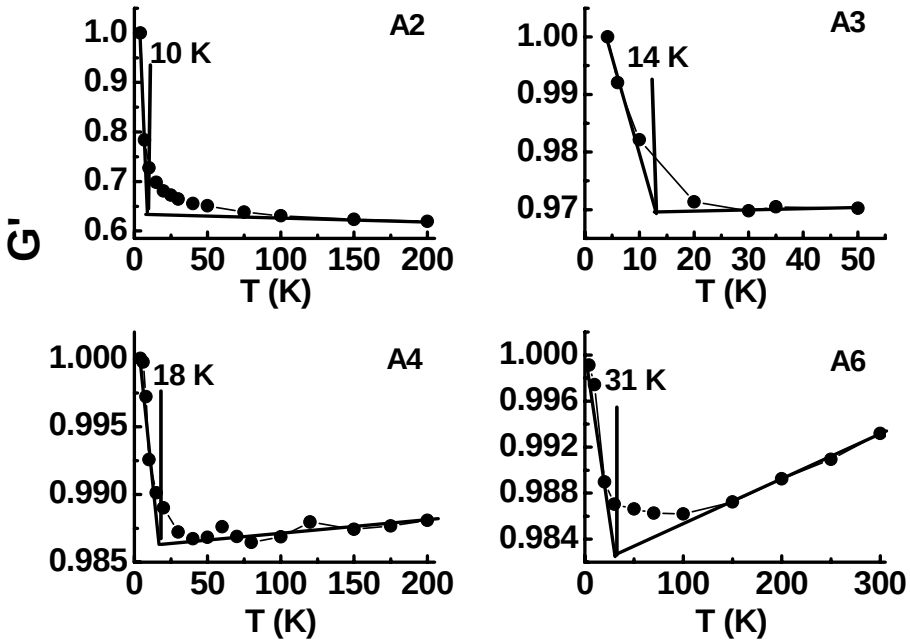

FIG. 3.25 Temperature-dependent *G*' curves for different samples. The critical point (T_C') is defined as the cross point of the slopes at high- and low-temperature regions. (a) Sample A2, (b) sample A3, (c) sample A4, (d) sample A6.

3.3.3.3 Magnetoresistance effect

Figure 3.26(a) shows the MR curves of sample A4 at different temperatures with a maximum field of 6 T, where the magnetic field is applied perpendicular to the sample surface. The MR is defined as

$$MR = \frac{R_H - R_0}{R_H}, \tag{3.5}$$

where R_0 denotes the zero-field resistance and R_H denotes the resistance at an applied field. A negative MR is observed for all the amorphous samples. The MR ratio for sample A4 is 0.51% at 4.2 K and decreases with increasing temperature to almost zero at 200 K. A maximum MR ratio or resistivity value has been observed around T_C in the manganese perovskites or (Ga, Mn)As [56,57]. However, we do not observe any similar critical points in the temperature-dependent resistivity or MR measurements in amorphous $Ge_{1-x}Mn_x$ alloy thin films. In the samples under study, the MR should come from both the low- and high-temperature phases. When a magnetic field is applied, the spins of low-temperature phase as well as the magnetization of the clusters will align along the direction of the magnetic field, leading to a smaller resistance or negative MR. Figure 3.26(b) shows the temperature dependence of MR ratio of sample A4. The MR ratio is almost constant below the ferromagnetic ordering temperature (T_C), but decreases rapidly at high temperatures. Again here we can see that there is a difference between the low- and high-temperature regions. Figure 3.26(c) compares the MR ratio for all the amorphous samples studied at 4.2 K. Although it is not so obvious, the MR ratio increases slightly with decreasing Mn composition. This can be understood as being caused by the increased contribution from the low-temperature and reduced contribution from the high-temperature phase.

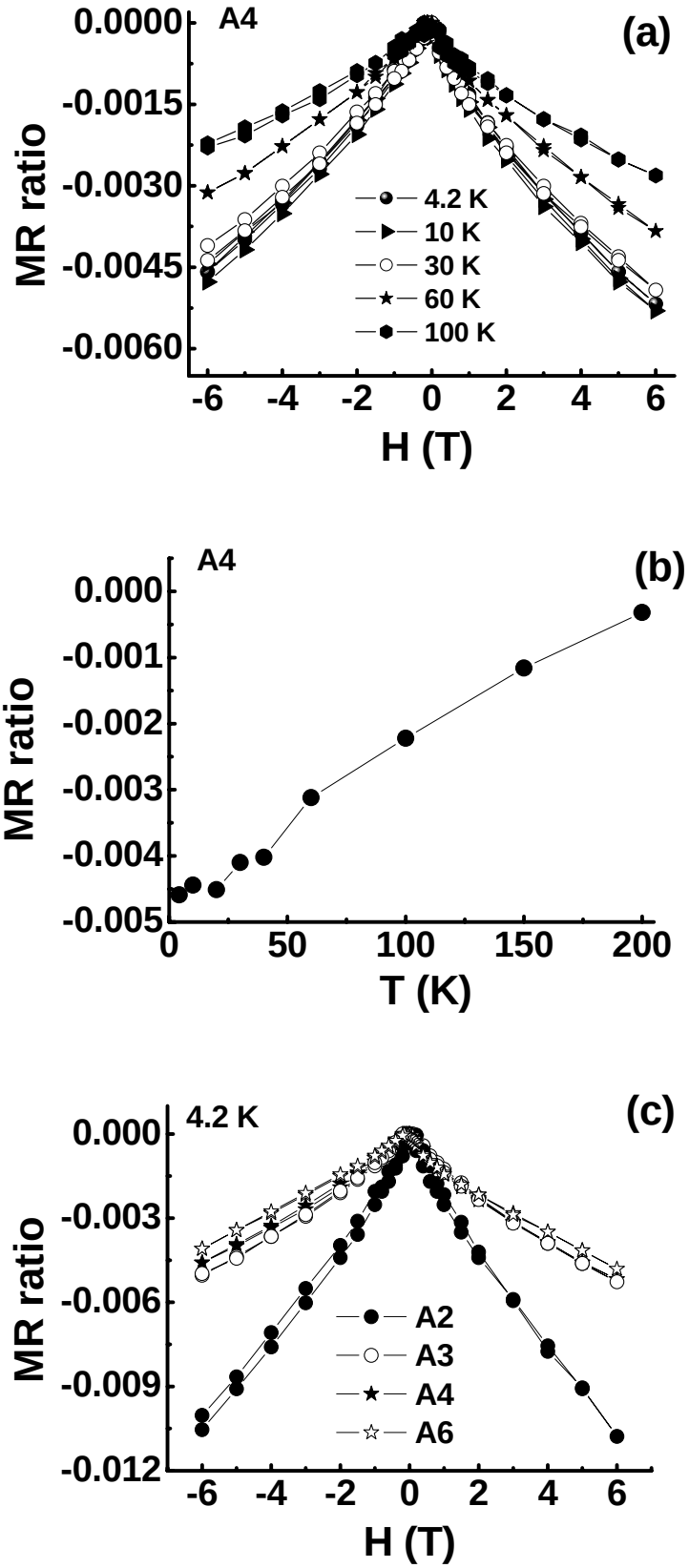

FIG. 3.26 (a) MR curves of sample A4 at different temperatures; (b) MR ratio as a function of temperature for sample A4; (c) MR curves for samples A2, A3, A4, and A6 at 4.2 K.

3.3.2.4 Hall effect

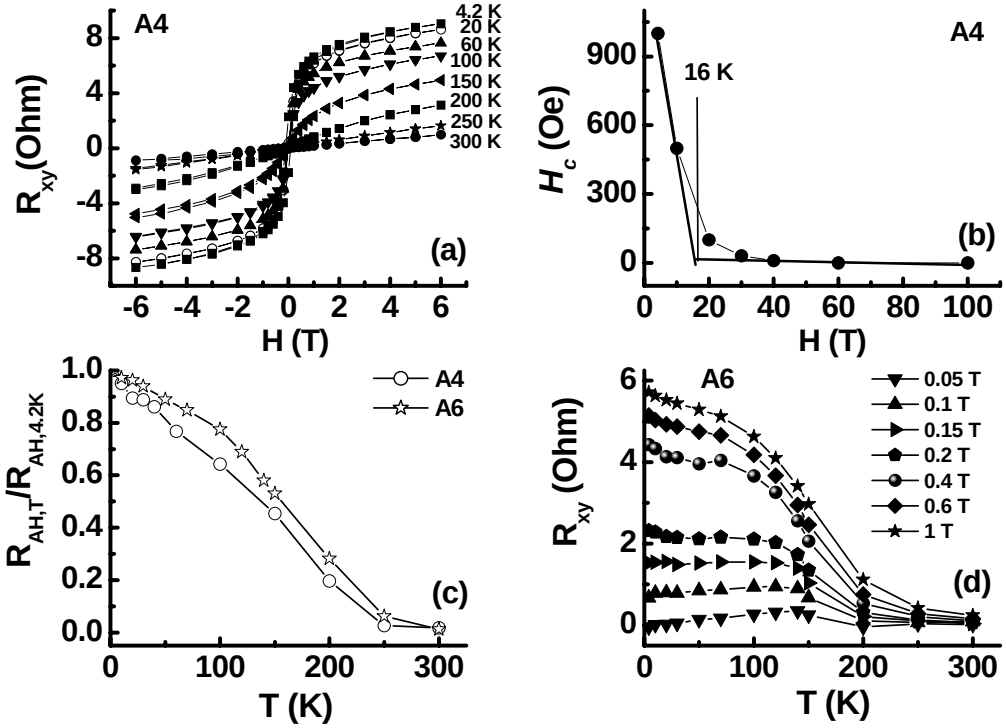

FIG. 3.27 (a) Hall effect for sample A4 at different temperatures; (b) coercivity as a function of temperature for sample A4; (c) normalized temperature dependence of anomalous Hall resistance for samples A4 and A6; (d) Hall resistance as a function of temperature at different magnetic fields for sample A6.

Next we turn to the Hall effect. The Hall resistance in a ferromagnet is generally expressed as

$$R_{xy} = R_0 B + R_S \mu_0 M \,, \tag{3.6}$$

where B is the magnetic induction, μ_0 is the magnetic permeability, M is magnetization, R_0 and R_S are the normal and anomalous Hall coefficients, respectively. The first term represents the ordinary Hall effect (OHE) linear in B, and the second term represents the AHE. The AHE is thought to be originated from either intrinsic or extrinsic spin-orbit couplings. Figure 3.27(a) shows the Hall resistance for sample A4 at

various temperatures with a maximum magnetic field of 6 T. The nonlinear Hall response is observed up to 200 K. In the samples under discussion, there should be two different sources for AHE. The response at low temperature should consist of the contributions from both the highly ordered spin-glass-like phase and the clusters phase. However, at high temperature, the contribution from the clusters should dominate. In Fig. 3.27(b), we plot the coercivity obtained form the AHE curves as a function of temperature for sample A4. It can be found that the coercivity decreases rapidly with increasing temperature (varying from 1000 Oe at 4.2 K to 10 Oe at 40 K). If we draw two slopes to the low- and high-temperature portions of the curves, again we found that the two straight lines cross each other at a temperature of 16 K, which is very close to the temperature of T_C and T'_C obtained from the magnetic measurements and dynamic conductance study, respectively. This suggests that the AHE at low temperature originates from a coupled phase of the clusters and the host matrix, while that at high temperature originates from the uncoupled clusters. The additional contribution from the coupled phase at low temperature can also be seen from additional increment of AHE below 15 K, as shown in Fig. 3.27(c) for samples A4 and A6, respectively where $R_{AH,T}$ (anomalous Hall resistance at temperature T) is obtained from the extrapolation of the linear portion of R_{xy} (Hall resistance) at high fields to B = 0 and normalized to its value at 4.2 K. Figure 3.27(d) shows the temperature dependence of AHE at different magnetic fields for sample A6. At low magnetic fields of 0.05 and 0.1 T, it can be observed that R_{xy} decreases with decreasing temperature. The decrease of R_{xy} becomes less prominent with the increase of the magnetic field and an increase of R_{xy} replaces the decrease when the magnetic field is higher than 0.6 T. This is in good agreement with the model we proposed earlier, i.e., the low-temperature phase couples

antiferromagnetically with the high-temperature nanocluster phase below T^*_C at low field.

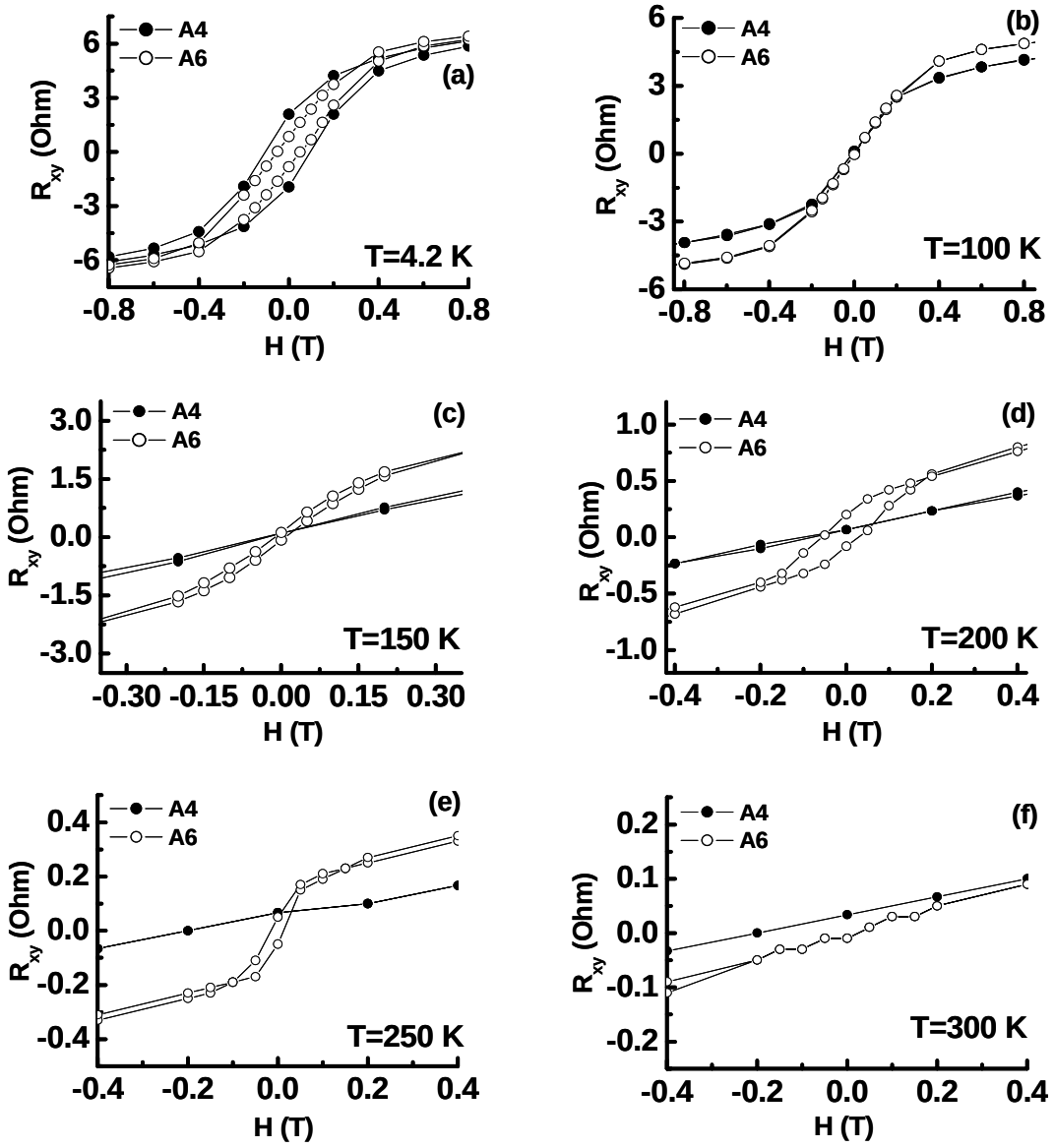

FIG. 3.28 Comparison of anomalous Hall resistance at different temperatures for samples A4 and A6.

In Fig. 3.28, the anomalous Hall resistance for samples A4 and A6 at different temperatures are presented. Clear hysteresis behaviour can be observed at 4.2 K in both samples [see Fig. 3.28(a)]. With the increase of temperature, the coercivities of both samples become smaller and disappear above 100 K [see Fig. 3.28(b)]. Figure 3.28(c)

shows the AHE curves at 150 K. Clear hysteresis behaviour is observed again in sample A6 and the coercivity becomes larger at 200 K, then decreases again at 250 K and finally disappears at 300 K. The temperature of the appearance of coercivity at around 150 K in sample A6 corresponds to that of the appearance of Mn_5Ge_3 phase [see Fig. 3.8(f)]. It is obvious that the hysteresis behaviour above 150 K in sample A6 originates from Mn_5Ge_3 secondary phase. In general, the secondary phase should also have a contribution to Hall effect at low temperature although it is not the dominant one. However, we do not observe this phenomenon at low temperature. For samples grown at 300 ^oC (The details will be discussed in Chapter 4), where the magnetic properties are dominant by the secondary phases, we cannot observe any AHE effect. The true role of Mn_5Ge_3 secondary phases in AHE effect in amorphous Ge:Mn system is recommended for the future studies.

Figure 3.29 displays the carrier density variation at different temperatures for samples A4 and A6. The carrier density is obtained from equation 3.7:

$$n = \frac{IB}{edV}, \tag{3.7}$$

where n is the carrier density, I is the applied current, $e = 1.60 \times 10^{-19}$ C, d is the sample thickness, V is the Hall voltage, B is the applied magnetic field. Due to the heavily doped Mn, both samples exhibit high carrier density at room temperature. The carrier densities at room temperature are 1.33×10^{21} and 1.11×10^{21} cm^{-3} for sample A4 and A6, respectively. Three different regions can be observed in the curves. (I) 200 K $< T <$ 300 K. In region (I), the carrier density deceases very fast with decreasing temperature; (II) 40 K $< T <$ 200 K. In region (II), the carrier density first increases with decreasing temperature and reaches the maximum around 100 K. Then, the carrier density slightly decreases with decreasing temperature; (III) $T <$ 40 K. In this region,

the carrier density is almost constant and the carrier localization occurs at this temperature range, which agrees well the results of the dynamic conductance studies. This provides further evidence that the magnetization at low temperatures is a carrier-induced phenomenon. The overall curve shape of temperature-dependent carrier density below 200 K is very similar to that of the FC curve at an applied magnetic field of 20 Oe. This again indicates the close correlation between the magnetic and electrical transport properties, even though we have not taken into account the magnetic scattering effect in this system.

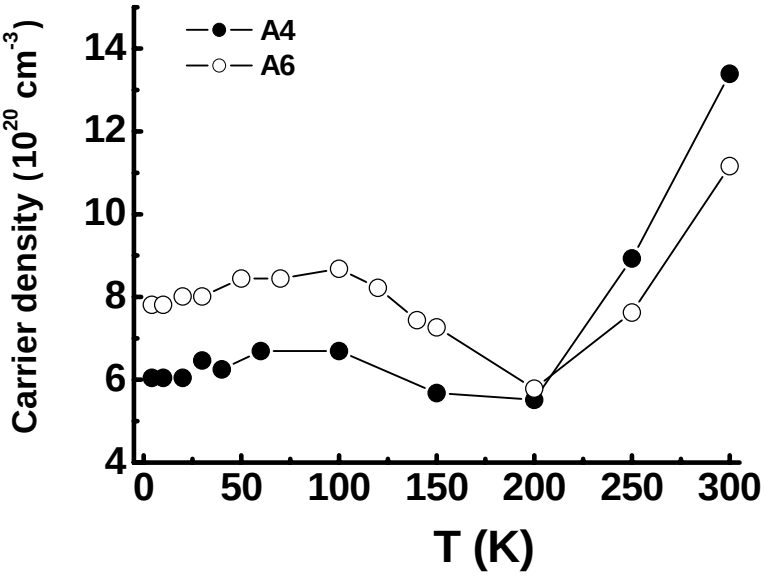

FIG. 3.29 Carrier density at different temperatures for samples A4 and A6.

3.4 Summary

We have systematically studied structural, magnetic and electrical transport properties of amorphous $Ge_{1-x}Mn_x$ (x = 15.3% - 42%) alloy thin films. Focusing on the correlation between magnetic and electrical transport properties, we have shown that the amorphous samples consist of a low-temperature highly ordered spin-glass-like phase

and a high-temperature "clustered dopant" phase. The magnetizations of the two phases were found to be coupled antiferromagnetically with each other at low temperature. The good agreement between the values of T_C and T^*_C for amorphous samples and those of the two characteristic temperatures reported in literature for epitaxially grown samples suggested that the ferromagnetic phase of the latter observed in the temperature range of 110 - 120 K is of extrinsic origin. The high-temperature phase was of characteristic nature of the Ge:Mn system, independent of crystalline structure and Mn composition unless secondary phases were formed uniformly in the sample. Carrier localization only occurred at low temperature, which has been confirmed by the dynamic conductance and Hall effect studies. The dynamic conductance measurements could also be applied to study other types of inhomogeneous DMSs system.

References:

1 Y. D. Park, A. T. Hanbicki, S. C. Erwin, C. S. Hellberg, J. M. Sullivan, J. E. Mattson, T. F. Ambrose, A. Wilson, G. Spanos, and B. T. Jonker, "A group-IV ferromagnetic semiconductors: Mn_xGe_{1-x}", Science **295**, pp. 651-654, 2002.

2 Y. D. Park, A. Wilson, A. T. Hanbicki, J. E. Mattson, T. Ambrose, G. Spanos, and B. T. Jonker, "Magnetoresistance of Mn: Ge ferromagnetic nanoclusters in a diluted semiconductors matrix", Appl. Phys. Lett. **69**, pp. 363-365, 1996.

3 Sunglae Cho, Sungyoul Choi, Soon Cheol Hong, Yunki Kim, John B. Ketterson, Bong-Jun Kim, Y. C. Kim and Jung-Hyun Jung, "Ferromagnetism in Mn-doped Ge", Phys. Rev. B **66**, pp. 033303, 2002.

4 C. Zeng, S. C. Erwin, L. C. Feldman, A. P. Li, R. Jin, Y. Song, J. R. Thompson, and H. H. Weitering, "Epitaxial ferromagnetic Mn_5Ge_3 on Ge(111)", Appl. Phys. Lett. **83**, pp. 5002-5004, 2003.

5 J.-S. Kang, G. Kim, S. C. Wi, S. S. Lee, S. Choi, Sunglae Cho, S. W. Han, K. H. Kim, H. J. Song, H. J. Shin, A. Sekiyama, S. Kasai, S. Suga, and B. I. Min, "Spatial chemical inhomogeneity and local electronic structure of Mn-doped Ge ferromagnetic semiconductors", Phys. Rev. Lett. **94**, pp. 147202, 2005.

6 N. Pinto, L. Morresi, M. Ficcadenti, R. Murri, F. D'Orazio, F. Lucari, L. Boarino, and G. Amato, "Magnetic and electronic transport percolation in epitaxial $Ge_{1-x}Mn_x$ films", Phys. Rev. B **72**, pp. 165203, 2005.

7 A. P. Li, J. Shen, J. R. Thompson, and H. H Weitering, "Ferromagnetic percolation in Mn_xGe_{1-x} dilute magnetic semiconductor", Appl. Phys. Lett. **86**, pp. 152507-152509, 2005; A. P. Li, J. F. Wendelken, J. Shen, L. C. Feldman, J. R. Thompson, and H. H. Weitering, "Magnetism in Mn_xGe_{1-x} semiconductors mediated by impurity band carrier", Phys. Rev. B **72**, pp. 195205, 2005.

8 O. Kazakova, J. S. Kulkarni, J. D. Holmes, and S. O. Demokritov, "Room-temperature ferromagnetism in $Ge_{1-x}Mn_x$ nanowires", Phys. Rev. B **72**, pp. 094415, 2005; J. S. Kulkarni, O. Kazakova, D. Erts, M. A. Morris, M. T. Shaw, and J. D. Holmes, "Structural and magnetic characterization of $Ge_{0.99}Mn_{0.01}$ nanowire arrays", Chem. Mater. **17**, pp. 3615-3619, 2005.

9 S. Picozzi, L. Ottaviano, M. Passacantando, G. Profeta, A. Continenza, F. Priolo, M. Kim, and A. J. Freeman, "X-ray absorption spectroscopy in Mn_xGe_{1-x} diluted magnetic semiconductor: Experiment and theory", Appl. Phys. Lett. **86**, pp. 062501-062503, 2005.

10 S. Yu, T. L. Anh, Y. E. Ihm, D. Kim, H. Kim, S. Oh, C. S. Kim, and H. Ryu, "Feromagnetism in amorphous $Ge_{1-x}Mn_x$ grown by low temperature vapor deposition", Solid State Commun. **134**, pp. 641-645, 2005.

11 C. Bihler, C. Jaeger, T. Vallaitis, M. Gjukic, M. S. Brandt, E. Pippel, J. Woltersdorf, and U. Gösele, "Structural and magnetic properties of Mn_5Ge_3 clusters in a diluted magnetic germanium matrix", Appl. Phys. Lett. **88**, pp. 112506-112508, 2006.

12 C. Jarger, C. Bihler, T. Vallaitis, S. T. B. Goennenwein, M. Opel, R. Gross, and M. S. Brandt, "Spin glass-like behavior of Ge: Mn", Phys. Rev. B **74**, pp. 045330, 2006.

13 Y. X. Chen, Shi-shen Yan, Y. Fang, Y. F. Tian, S. Q. Xiao, G. L. Liu, Y. H. Liu, and L. M. Mei, "Magnetic and transport properties of homogeneous Mn_xGe_{1-x} ferromagnetic semiconductor with high Mn concentration", Appl. Phys. Lett. **90**, pp. 052508, 2006.

14 D. Bougeard, S. Ahlers, A. Trampert, N. Sircar, and G. Abstreiter, "Clustering in a Precipitate-Free GeMn Magnetic Semiconductor", Phys. Rev. Lett. **97**, pp. 237202, 2006.

15 M. Jamet, A. Barski, T. Devillers, V. Poydenot, R. Dujardin, P. Bayle-guillemaud, J. Rothman, E. Bellet-Amalric, A. Marty, J. Cibert, R. Mattana, and S. Takarenko, Nature Mater. **5**, pp. 653-659, 2006.

16 F. Tsui, L. Ma, and L. He, "Magnetization-dependent rectification effect in a Ge-based magnetic heterojunction", Appl. Phys. Lett. **83**, pp. 954-956, 2003.

17 Y.-J. Zhao, T. Shishidou, and A. J. Freeman, "Ruderman-Kittel-Kasuya-Yosida-like ferromagnetism in Mn_xGe_{1-x}", Phys. Rev. Lett. **90**, pp. 47204, 2003.

18 A. Stroppa, S. Picozzi, A. Continenza, and A. J. Freeman, "Electronic structure and ferromagnetism of Mn-doped group-IV semiconductors", Phys. Rev. B **68**, pp.155203, 2003.

19 N. Yameda, K. Maeda, Y. Usami, and T. Ohoyama, "Magnetic Properties of Intermetallic Compound $Mn_{11}Ge_8$", J. Phys. Soc. Japan, **55**, pp.3721-3724, 1986; T. Ohoyama, "X-ray and Magnetic Studies of the Manganese-Germanium System", *ibid.* **16**, pp.1995-2002, 1961.

20 G. Patriarche, E. Le Bourhis. M. M. O. Khayyat and M. M. Chaudhri, "Indentation-induced crystallization and phase transformation of amorphous germanium", J. Appl. Phys. **96,** pp. 1464-1468, 2004.

21 L. Liu, Z. X. Shen, K. L. Teo, A.V. Kolobov, and Y. Maeda, "Raman scattering of germanium nanocrystals embedded in glass matrix under hydrostatic pressure", J. Appl. Phys. **93**, pp. 9392-9394, 2003.

22 K. L. Teo, S. H. Kwok, P.Y. Yu, S. Guha, "Quantum confinement of quasi-two-dimensional E1 excitons in Ge nanocrystals studied by resonant Raman scattering", Phys. Rev. B **62**, pp.1584-1587, 2000.

23 N. Pinto, L. Morresi, R. Gunnella, R. Murri, F. D' Orazio, F. Lucari, S. Santucci, P. Picozzi, M. Passacantando, and A. Verna, "Growth and magnetic properties of MnGe films for spintronic application", J. Mater. Sci.-Mater. Electr. **14**, pp. 337-340, 2003.

24 R. Gunnella, L . Morresi, N. Pinto, R. Murri, L. Ottaviano, M. Passacantando, F. D'Orazio, and F. Lucari, "Magnetization of epitaxial MnGe alloys on Ge (111) substrates", Surf. Sci **577**, pp. 22-30, 2005.

25 S. R. Shinde, S. B. Ogale, J. S. Higgins, H. Zheng, A. J. Millis, V. N. Kulkarni, R. Ramesh, R. L. Greene, and T. Venkatesan, "Co-occurrence of Superparamagnetism and Anomalous Hall Effect in Highly Reduced Cobalt-Doped Rutile $TiO_{2-\delta}$ Films", Phys. Rev. Lett. **92**, pp. 166601, 2004.

26 T. Fukumura, Zhengwu Jin, M. Kawasaki, T. Shono, T. Hasegawa, S. Koshihara, and H. Koinuma, "Magnetic properties of Mn-doped ZnO", Appl. Phys. Lett. **78**, pp. 958-960, 2001.

27 J. K. Furdyna, "Diluted magnetic semiconductors", J. Appl. Phys. **64**, pp. R29-R64, 1988.

28 A. Kaminski and S. Das Sarma, "Polaron Percolation in Diluted Magnetic Semiconductors", Phys. Rev. Lett. **88**, pp. 247202, 2002.

29 M. Sahana, A. Venimadhav, M. S. Hegde, K. Nenkov, U. K. Röβler, K. Dörr, K.-H. Müller, "Magnetic properties and specific heat of $LaMn_{1-x}Ti_xO_{3+\delta}$", J. Magn. Magn. Mater. **260**, pp. 361-370, 2003.

30 A. Ray and R. Ranganathan, "Giant magnetoresistance in the disordered magnetic alloy $(FeNi)_{25}Au_{75}$", Phys. Rev. B **56**, pp. 6073-6078, 1997.

31 J. Dho, W. S. Kim, and N. H. Hur, "Reentrant spin glass behavior in Cr-doped perovskite manganites", Phys. Rev. Lett. **89**, pp. 027202, 2002.

32 R. Mathieu, P. Nordblad, D. N. H. Nam, N. X. Phuc, and N. V. Khiem, "Short-range ferromagnetism and spin-glass state in $Y_{0.7}Ga_{0.3}MnO_3$", Phys. Rev. B **63**, pp. 174405 ,2001.

33 Fang Wang, Jian Zhang, Yuan-fu Chen, Guang-Jun Wang, Ji-rong Sun, Shao-ying Zhang, and Bao-gen Shen, "Spin-glass behavior in $La(Fe_{1-x}Mn_x)_{11.4}Si_{1.6}$ compounds", Phys. Rev. B **69**, pp. 094424, 2004.

34 A. Mauger, J. Ferre, M. Ayadi, and P. Nordblad, "Dynamics of the spin-glass freezing in $Cd_{0.6}Mn_{0.4}Te$", Phys. Rev. B **37**, pp. 9022-9028, 1988; S. Dhar, O. Brandt, A. Trampert, K. J. Friedland, Y. J. Sun, and K. H. Ploog, "First-principles prediction of half-metallic ferromagnetic semiconductors: V- and Cr-doped BeTe", *ibid.* **67**, pp. 165205, 2003.

35 J. A. Mydosh, *Spin Glasses- An experiment introduction*, Taylor & Francis, London, 1993.

36 F. Helman, D. R. Queen, R. M. Potok, and B. L. Zink, "Spin-glass freezing and RKKY interactions near the metal-insulator transition in amorphous Gd-Si alloys", Phys. Rev. Lett. **84**, pp. 5411-5414, 2000.

37 R. S. Freitas, L. Ghivelder, F. Damay, F. Dias, and L. F. Cohen, "Evidence for ordered moments on the Rh sites in $CeRhIn_5$", Phys. Rev. B. **64**, pp. 144404, 2001.

38 A. Ito, H. Aruga, E. Torikai, M. Kikuchi, Y. Syono, and H. Takei, "Time-Dependent Phenomena in a short-range Ising spin-Glass, $Fe_{0.5}Mn_{0.5}TiO_3$", Phys. Rev. Lett. **57**, pp. 483-486, 1986.

39 L. Lundgren, P. Svedlindh, and O. Beckman, "Experimental indications for a critical relaxation time in spin-glasses", Phys. Rev. B **26**, pp. 3990-3993, 1982.

40 J. A. H. Coaquira and H. R. Rechenberg, "Spin-glass behavior of $Zr(Fe_xCr_{1-x})_2$ compounds", J. Magn. Magn. Mater. **226-230**, pp. 1306-1308, 2001.

41 M. Sahana, A. Venimadhav, M. S. Hegde, K. Nenkov, U. K. Röβler, K. Dörr, and K.-H. Müller, "Magnetic properties and specific heat of $LaMn_{1-x}Ti_xO_{3+\delta}$ ($0< x <0.2$)", J. Magn. Magn. Mater. **260**, pp. 361-370, 2003.

42 S. Esho, "Anomalous magneto-optical hysteresis loops of sputtered Gd-Co films", Jpn. J. Appl. Phys. Suppl. **15**, pp. 93-98, 1976.

43 X. Yan and Y. Xu, "Negative remanence in magnetic nanostructures", J. Appl. Phys. **79**, pp. 6013-6015, 1996.

44 C. Gao and M. J. O'shea, "Inverted hysteresis loops in CoO-based multilayers", J. Magn. Magn. Mater. **127**, pp. 181-189, 1993.

45 S. I. Ohkoshi, T. Hozumi, and K. Hashimoto, "Design and preparation of a bulk magnet exhibiting an inverted hysteresis loop", Phys. Rev. B **64**, pp. 132404, 2001.

46 R. K. Zheng, Hui Liu, Y. Wang, and X. X. Zhang, "Inverted hysteresis in exchange biased Cr_2O_3 coated CrO_2 particles", J. Appl. Phys. **96**, pp. 5370-5372, 2004.

47 J. Geshev, A. D. C. Viegas, and J. E. Schmidt, "Negative remanent magnetization of fine particles with competing cubic and uniaxial anisotropies", J. Appl. Phys. **84**, pp.1488-1492, 1998.

48 S. M. Valvidares, L. M. Alvarez-Prado, J. I. Martin, and J. M. Alameda, "Inverted hysteresis loops in magnetically coupled bilayers with uniaxial competing anisotropies: Theory and experiments", Phys. Rev. B **64**, pp.134423, 2001.

49 U. K. Röβler and A. N. Bogdanov, "Magnetic states and reorientation transitions in antiferromagnetic superlattices", Phy. Rev. B **69**, pp. 094405, 2004; A. Ney and J. S. Harris, Jr., "Reconfigurable magnetologic computing using the spin flop switching of a magnetic random access memory cell", Appl. Phys. Lett. **86**, pp. 013502, 2005.

50 S. T. B. Goennenwein, T. A. Wassner, H. Huebl, M. S. Brandt, J. B. Philipp, M. Opel, R.Gross, A. Koeder, W. Schoch, and A. Waag, "Hydrogen control of ferromagnetism in a dilute magnetic semiconductor", Phys. Rev. Lett. **92**, pp. 227202, 2004.

51 S. Sriraman, M. S. Valipa, E. S. Aydil, and D. Maroudas, "Hydrogen-induced crystallization of amorphous silicon thin films. I. Simulation and analysis of film postgrowth treatment with H_2 plasmas", J. Appl. Phys. **100**, pp. 053514, 2006.

52 A. K. Raychaudhuri, "Metal-insulator transition in perovskite oxides: A low-temperature perspective", Adv. Phys. **44**, pp. 21-46, 1995; A. K. Raychaudhuri, K. P. Rajeev, H. Srikanth, and N. Gayathri, "Metal-insulator transition in perovskite oxides: Tunneling experiments", Phys. Rev. B **51**, pp. 7421-7428, 1995.

53 L. I. Glazman and K. A. Matveev, "Inelastic tunneling across thin amorphous films", Zh. Eksp. Teor. Fiz. **94**, 332, 1988. [Sov. Phys. JETP 67, 1276 (1988)].

54 M. Ziese, "Grain-boundary magnetoresistance in manganites: Spin-polarized inelastic tunneling through a spin-glass-like barrier", Phys. Rev. B **60**, pp. R738, 1999.

55 M. Ziese. G. Heydon, R. Höhne, P. Esquinazi, and J. Dienelt, "Step-edge magnetoresistance in $La_{0.7}Ca_{0.3}MnO_3$ films", Appl. Phys. Lett. **74**, pp.1481-1483, 1999.

56 J. Volger, "Further experimental investigations on some ferromagnetic oxide compounds of manganese with perovskite structure", Physica **20**, pp. 49-66, 1954.

57 A. Van Esch, L. Van Bockstal, J. De Boeck, G. Verbanck, A. S. Van Steenbergen, P. J. Wellmann, B. Grietens, R. Bogaerts, F. Herlach, and G. Borghs, "Interplay between the magnetic and transport properties in the III-V diluted magnetic semiconductor $Ga_{1-x}Mn_xAs$", Phys. Rev. B **56**, pp. 13103-13112, 1997.

CHAPTER 4

MAGNETISM AND ELECTRICAL TRANSPORT PROPERTIES OF AMORPHOUS $Ge_{1-x}Mn_x$ THIN FILMS EMBEDDED WITH Ge CRYSTALLITES AND HIGH T_C SECONDARY PHASES AND GRANULAR $Ge_{0.74}Mn_{0.26}$ THIN FILM

4.1 Introduction

After discussing the amorphous $Ge_{1-x}Mn_x$ thin films, we will discuss another $Ge_{1-x}Mn_x$ structure (amorphous $Ge_{1-x}Mn_x$ thin films embedded with Ge crystallites and secondary phases) in this chapter. Although much effort has been made to epitaxially grow $Ge_{1-x}Mn_x$ thin films with low Mn doping concentrations, so far only two groups have successfully reported the epitaxial growth of $Ge_{1-x}Mn_x$ thin films. [1,2] Growth rate and growth temperature are the two crucial factors which determine the growth mode of $Ge_{1-x}Mn_x$ thin films. Ge:Mn secondary phases will form once the Mn concentration exceeds the solution limit (> 9%) and the substrate temperature is higher than 70 ^{o}C. [2] Among different Ge:Mn secondary phases, Mn_5Ge_3, $Mn_{11}Ge_8$ and $M_{3.4}Ge$ have Curie temperatures of near or above room temperature. Although the secondary phases are undesirable for forming uniform Ge-based DMSs, thin films with

high T_C secondary phases are of great interest from the point of view that they serve as ideal systems to study the spin-dependent transport across the interface between high T_C secondary phases and the host matrix. Furthermore, we can continue to find the possible solutions for the two key unsettled problems in $Ge_{1-x}Mn_x$, i. e. (1) what are the origins of ferromagnetism and characteristic temperatures; (2) what is the correlation between magnetic and electrical transport properties. In this chapter, we firstly discussed the fabrication and characterization of amorphous $Ge_{1-x}Mn_x$ thin films embedded with Ge crystallites and different types of high T_C secondary phases. Detailed structural, surface morphology, magnetic, and electrical transport properties have been studied. Then, the nanowires with diameters of 5, 1, and 0.1 μm were fabricated with sample Mn12% (Sc29), and the spin-dependent transport properties were investigated with the dynamic conductance technique. Finally, a $Ge_{0.74}Mn_{0.26}$ granular thin film was fabricated and its structural, magnetic, and electrical transport properties were investigated.

4.2 Experimental details

Amorphous $Ge_{1-x}Mn_x$ thin films embedded with Ge crystallites and different types of high T_C secondary phases were grown by MBE at a substrate temperature of 300 ^oC. Samples with Mn concentrations ranging from 1.5% to 56.1% were obtained by varying the K-cell temperatures. The thickness of the as-grown films was around 34 nm with a growth rate of 0.009 nm s^{-1}. The surface morphology and Mn composition of the as-grown films were characterized by AFM and XPS, respectively. Raman scattering and HRTEM were used to characterize the structural properties. The measurements of magnetic properties were performed with SQUID. In order to study electrical transport properties, the samples were fabricated into standard Hall bars using the same process described in chapter 3. The electrical measurements were performed in a Janis cryostat

at the temperature range from 1.7 to 300 K and with a magnetic field up to 7 T. Table 4.1 listed the parameters of the samples that have been studied in this chapter. The spin-dependent transport across high T_C secondary phases and host matrix interface was studied using sample Mn12% (Sc29). In order to confine the current into a narrow path, the sample was firstly fabricated into a strip with a width of 5 μm using a laser writer. The typical nanowire fabrication procedure was similar to that of the Hall bar fabrication discussed in Fig. 3.1. The fabricated strips were further narrowed down to 1 and 0.1 μm by both ion-milling and FIB techniques. The dynamic conductance ($G=dI/dV$) curves at different strip widths were measured to study the spin-dependent transport properties.

Table 4.1 The parameters of the samples studied in this chapter

	K-Cell Temperature (^oC)	Resistivity (Ω.cm)	Mn concentration (%)	Secondary phases in the thin film
SC24	750	0.000394	56.1	$Mn_{11}Ge_8$ and $Mn_{3.4}Ge$
SC25	730	0.000883	46.7	$Mn_{11}Ge_8$ and Mn_5Ge_3
SC26	710	0.002242	28.1	$Mn_{11}Ge_8$ and Mn_5Ge_3
SC27	690	0.005028	24.8	$Mn_{11}Ge_8$ and Mn_5Ge_3
SC28	670	0.006401	18.5	Mn_5Ge_3
SC29	650	0.024462	12.0	$Mn_{3.4}Ge$
SC30	630	0.129105	10.9	$Mn_{3.4}Ge$
SC31	610	0.118315	5.85	$Mn_{3.4}Ge$
SC32	590	0.131144	1.5	$Mn_{3.4}Ge$

4.3 Results and discussion

4.3.1 Structural and surface morphology properties

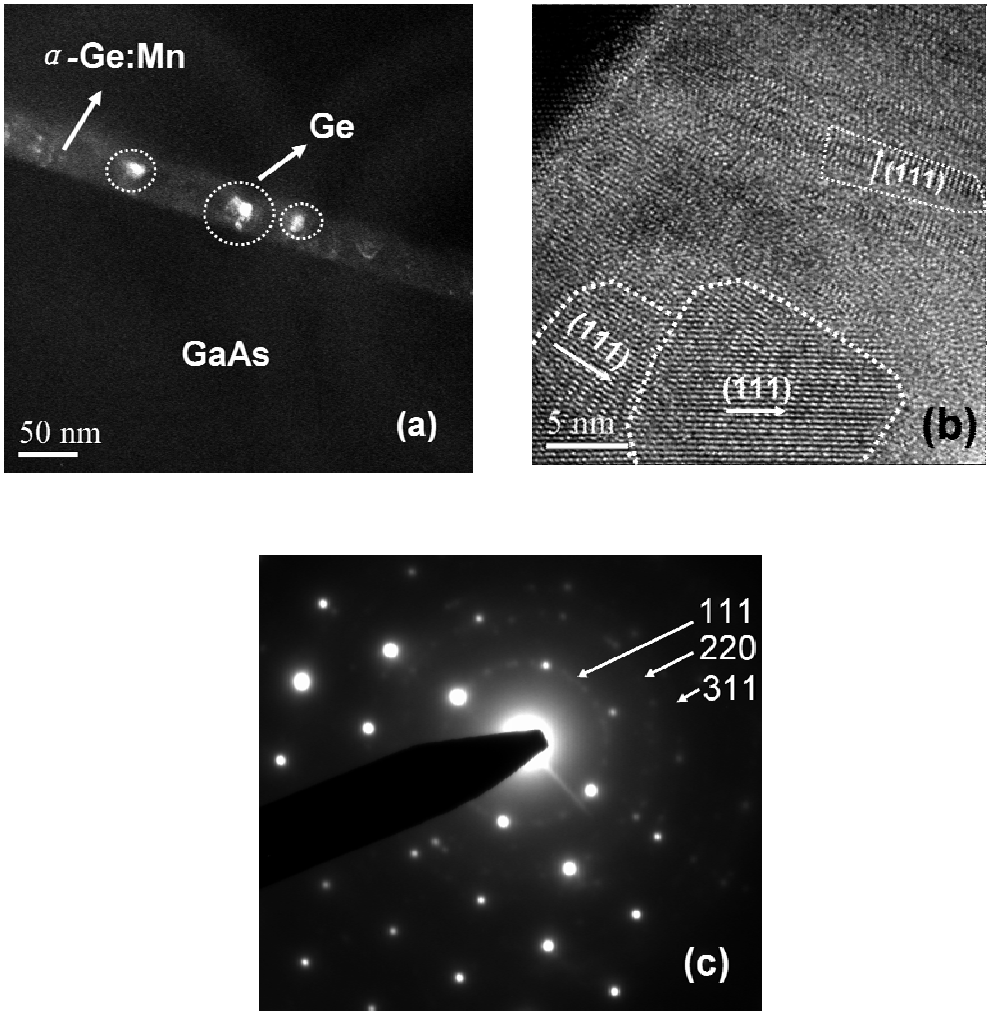

FIG. 4.1 Cross-sectional TEM images of sample Mn24.8%. (a) Dark-field TEM micrograph of this film. The bright spots enclosed by white dotted lines are Ge crystallites. The dark areas are the amorphous $Ge_{1-x}Mn_x$ matrix; (b) HRTEM image of one bight area in (a). The regions enclosed by white dotted lines show Ge crystallites with (111) orientation; (c) electron diffraction pattern taken from one of the bright spots in the dark-field image. The rings are indexed as 111, 220, and 311 orientations of Ge crystallites. The strong and bright spots are from GaAs (100) substrate.

Figure 4.1 shows the typical cross-sectional TEM image of sample Mn24.8%. The dark-field TEM image of the thin film is shown in Fig. 4.1(a). Some bright regions can be clearly observed in this figure. Figure 4.1(b) shows HRTEM image of one of the

bright spots in Fig. 4.1(a), which clearly shows the presence of Ge crystalline phase with (111) orientation. In contrast with the bright areas, the dark regions in Fig. 4.1(a) are totally in the amorphous state and any crystallites cannot be found. Figure 4.1(c) is a selected-area diffraction pattern taken from one of the bright spots in the dark-field image. Spots corresponding to 111, 220, and 311 diffractions of cubic Ge structure can be clearly seen. The strong and bright spots are from GaAs (100) substrate. We cannot observe any secondary phases in TEM images although it can be inferred from the magnetic measurements. There may be two possible reasons for this: (1) the secondary phases are too small to be seen, and (2) the secondary phases may be too dilute in density which cannot be picked up easily by TEM.

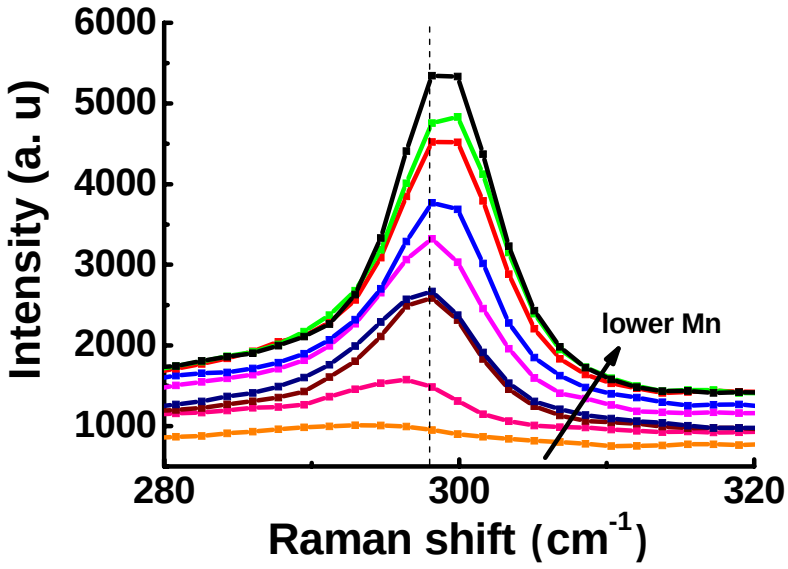

FIG. 4.2 Raman spectrum of the samples studied in this chapter. The arrow points to the lower Mn concentrations. The dotted lines indicate the peak position of Ge nanocrystal at the position of around 298 cm^{-1}.

Figure 4.2 shows Raman spectrum of the samples under study in this chapter. The arrow points to the lower Mn concentration. A peak at the position of around 298 cm^{-1}

with an asymmetry at the lower frequency can be clearly observed in the low doping concentration samples. The asymmetric shape of the peak is a typical characteristic of small Ge crystallites, [3,4] which agrees well with TEM results. The intensity of the peaks decreases with the increase of the Mn concentration and the peak becomes almost invisible in sample Mn56.1% (Sc24) with the highest Mn concentration. The peak position of Ge crystallites shifts to the lower frequency with increasing Mn concentrations.

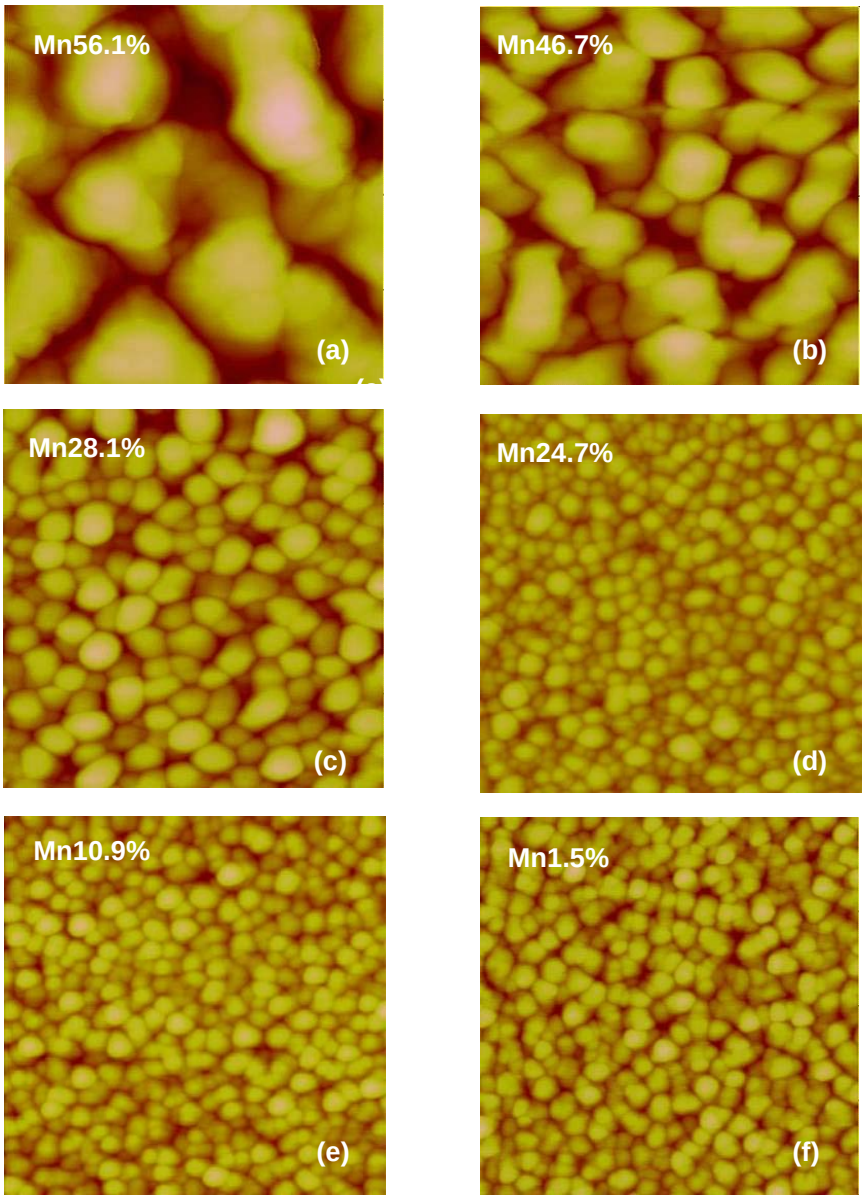

FIG. 4.3 (a)-(f) AFM images of the samples with different Mn concentrations.

Figures 4.3(a)-4.3(f) show AFM images of the selected samples with different Mn concentrations. The scanned areas are 1 μm x 1 μm for all the samples. A wide distribution of particle sizes can be observed in different Mn concentrations. Typical 3-D island growth can be observed in all samples. The particles size is uniform even in the highest Mn concentration and decreases with the decrease of the Mn concentrations. In comparison with the amorphous samples studied in chapter 3 (grown below 200 ^{o}C), the samples grown at 300 ^{o}C have a higher surface roughness.

Figure 4.4 shows the relation between the surface roughness (R_a) and the Mn concentrations. In the highest Mn concentration samples (Mn56.1% and Mn46.7%), R_a values are 11.064 and 6.793 nm, respectively. With the decrease of Mn concentration, R_a value dramatically drops to 2.221 nm for sample Mn28.1%. A minimum of 1.238 nm is obtained in sample Mn18.5%. Then, R_a slightly increases with the decrease of Mn concentration.

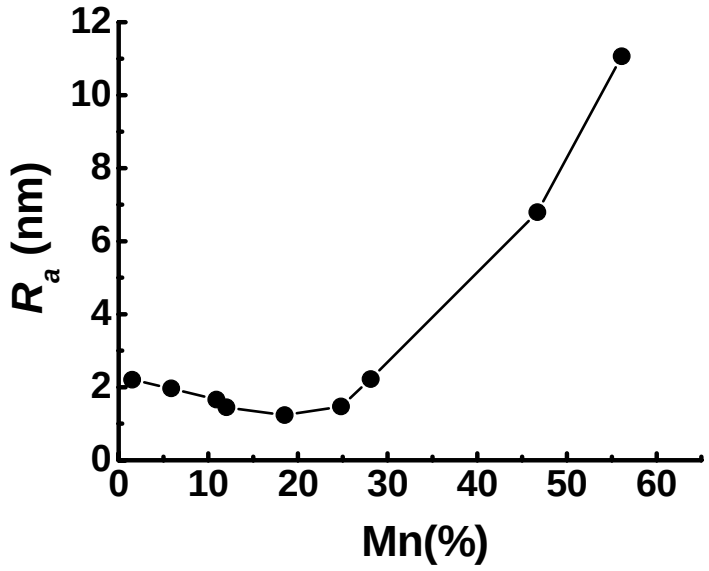

FIG. 4.4 The relation between the surface roughness (R_a) and Mn concentrations.

4.3.2 Magnetic properties

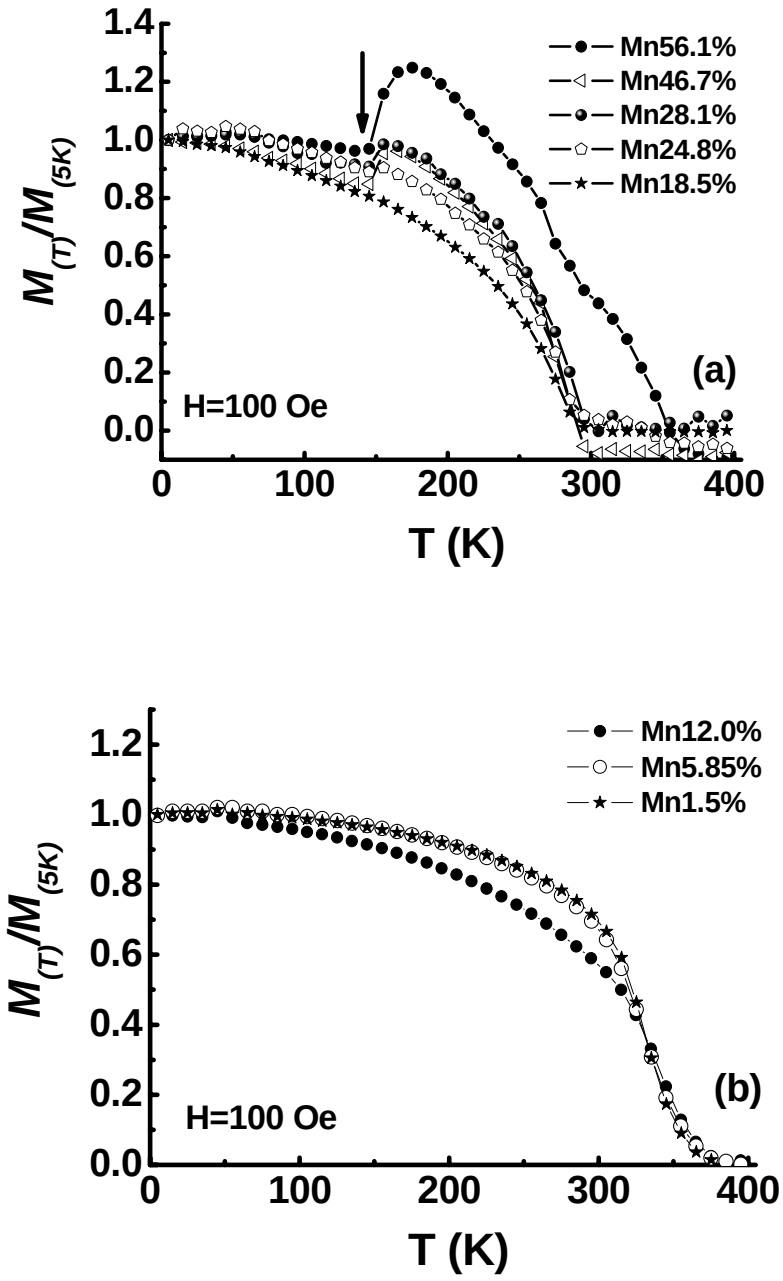

FIG. 4.5 (a) and (b) normalized *M-T* curves of the samples with different Mn concentrations. The ferromagnetic to antiferromagnetic transition point for $Mn_{11}Ge_8$ phase is indicated by the arrow in (a).

Figures 4.5(a) and 4.5(b) show the normalized temperature-dependent FC curves for different samples at an applied magnetic field of 100 Oe. Different temperature-

dependent magnetic behaviours can be observed in the figures. Researchers have made detailed studies about the magnetic behaviour of different Ge:Mn secondary phases. [5-11] Thus, we can infer which kind of the secondary phase is embedded in the samples from FC measurements. In Fig. 4.5(a), the magnetization of the sample with Mn56.1% first decreases gradually with increasing temperature and a steep increase at 145 K is observed. After that, the magnetization decreases with the increase of the temperature and becomes zero around 365 K. It is well known that $Mn_{11}Ge_8$ exhibits a ferromagnetic to antiferromagnetic transition around 145 K. Thus, we can tell that $Mn_{11}Ge_8$ phase exists in this sample. However, $Mn_{11}Ge_8$ has a T_C of only 274 K, which is lower than the experimental value. Therefore, $Mn_{3.4}Ge$ phase with a T_C of 365 K [11] should also coexist in the films. When the Mn concentration further decreases, the transition around 145 K becomes less pronounced and cannot be observed at sample Mn18.5%. Samples Mn46.7%, Mn28.1%, Mn24.8%, and Mn18.5% have the same T_C of 295 K. It is well known that Mn_5Ge_3 has a T_C around 296 K. [11] Thus, the ferromagnetism in these samples origins from the Mn_5Ge_3 secondary phase. In Fig. 4.5(b), FC curves of samples Mn12.0%, Mn5.85%, and Mn1.5% are shown. A T_C around 365 K is obtained in all three samples, independent of the Mn concentration. Thus, the ferromagnetism in these samples results from the $Mn_{3.4}Ge$ phase. The FC curves become more convex with the decrease of the Mn concentration and almost overlap for samples Mn5.85% and Mn1.5%.

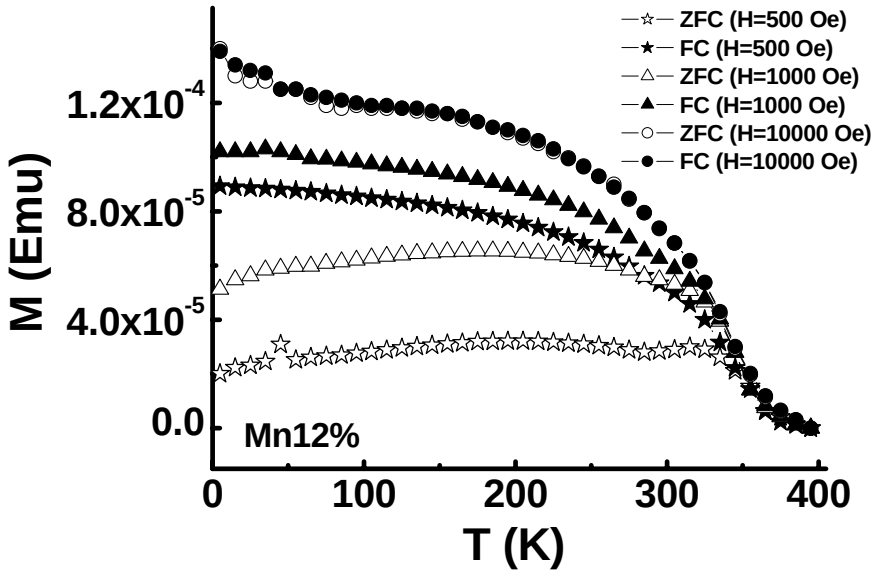

FIG. 4.6 ZFC and FC curves for sample Mn12% at different applied magnetic fields.

Figure 4.6 shows ZFC and FC curves for sample Mn12% at applied magnetic fields of 500, 1000, and 10000 Oe. With the increase of applied magnetic field, the separation points between ZFC and FC curves shift to lower temperatures and overlap when a 10000 Oe magnetic field is applied. We obtain the same Curie temperature of 365 K by fitting FC curves at different magnetic fields with the Curie-Weiss law, which is a typical ferromagnetic behaviour different from the amorphous $Ge_{1-x}Mn_x$ system discussed in chapter 3.

Figure 4.7 exhibits ZFC, FC, ZFC-FC, and TRM curves for sample Mn12% with an applied magnetic field of 100 Oe. No negative TRM is observed in this sample and TRM is very close to the value of M_{FC}-M_{ZFC}, which is different from amorphous $Ge_{1-x}Mn_x$ thin films discussed in chapter 3. Although the amorphous phase is also observed in TEM images, the magnetic properties are still dominant by the $Mn_{3.4}Ge$ secondary phase.

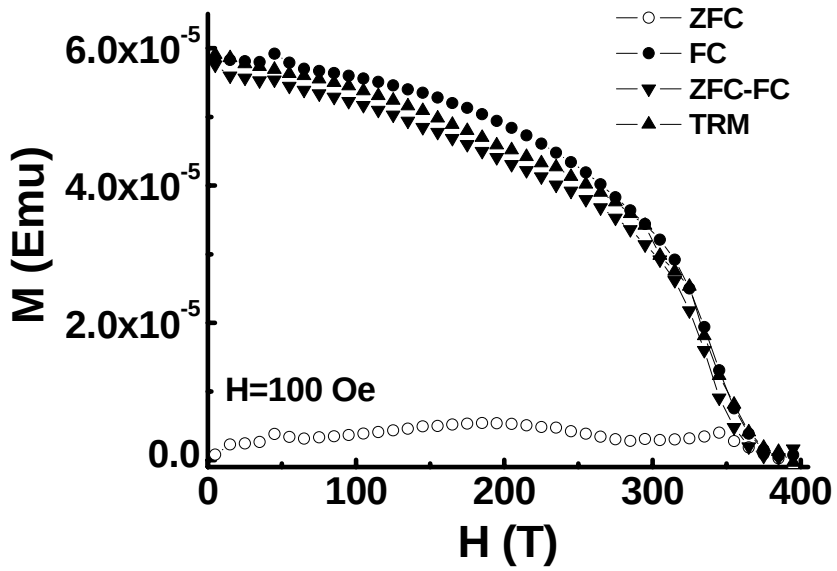

FIG. 4.7 ZFC, FC, ZFC-FC, and TRM curves for sample Mn12% at an applied magnetic field of 100 Oe.

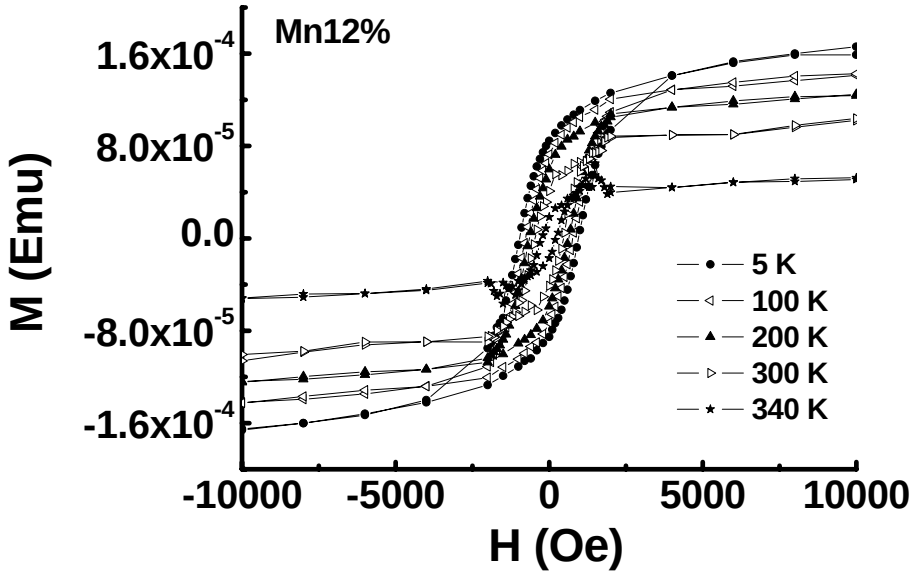

FIG. 4.8 *M-H* curves for sample Mn12% at different temperatures.

In Fig. 4.8, field-dependent magnetization curves at different temperatures for sample Mn12% are shown. Clear hysteresis behaviours can be observed until 340 K, indicating the ferromagnetic behaviour. The remanence at 5 and 340 K are

approximately 53% and 35%. The coercivity at 5 and 340 K are 950 and 200 Oe. There is no obvious difference in the magnetization between in-plane and out-of-plane orientations.

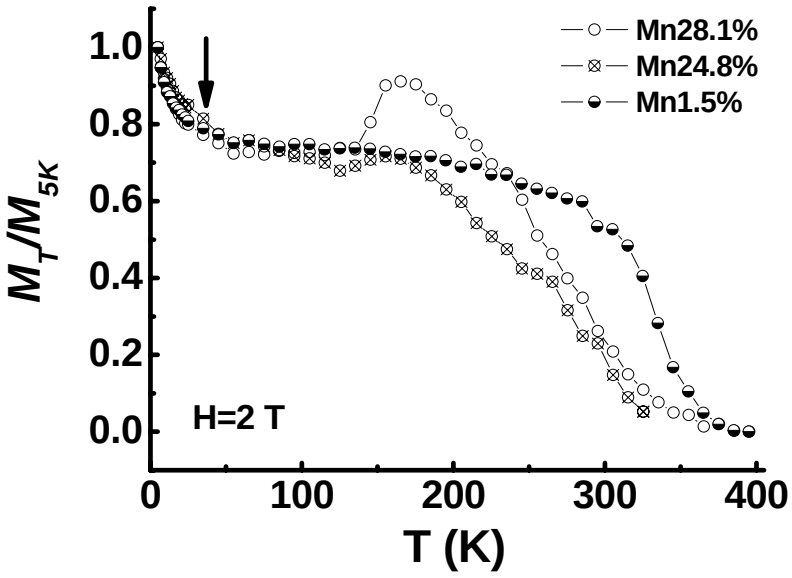

FIG. 4.9 *M-T* curves for samples Mn28.1%, Mn24.8%, and Mn1.5% at an applied magnetic field of 2 T.

Figure 4.9 exhibits the normalized temperature-dependent magnetization for samples Mn28.1%, Mn24.8%, and Mn1.5% at an applied magnetic field of 2 T. The magnetizations of all three samples saturate at such a high applied magnetic field and ZFC and FC curves overlap with each other. It is interesting that a sharp increase below 25 K (shown with an arrow in the figure) is observed in all three samples although the magnetizations in the high-temperature region are completely different. Bihler *et al.* [12] observed a steep magnetization increase below 16 K in their sample of $Ge_{0.97}Mn_{0.03}$, in which Mn_5Ge_3 clusters are embedded in epitaxially grown Ge crystalline matrix. They attribute it to a DMS formed by Mn atoms incorporated substitutionally in the Ge matrix. Li *et al.* [13] thought that to be a characteristic for Ge-based DMSs based on the

BMP model. We also observed the same steep increase in the amorphous samples as the discussion in chapter 3. It seems that this is a characteristic of $Ge_{1-x}Mn_x$ thin film systems independent of Mn concentrations and structure properties. The steep increases in the magnetization can also be explained with the carrier localization, [14] which will be discussed in the following section of electrical transport properties.

4.3.3 Electrical transport properties

4.3.3.1 Temperature-dependent resistivity

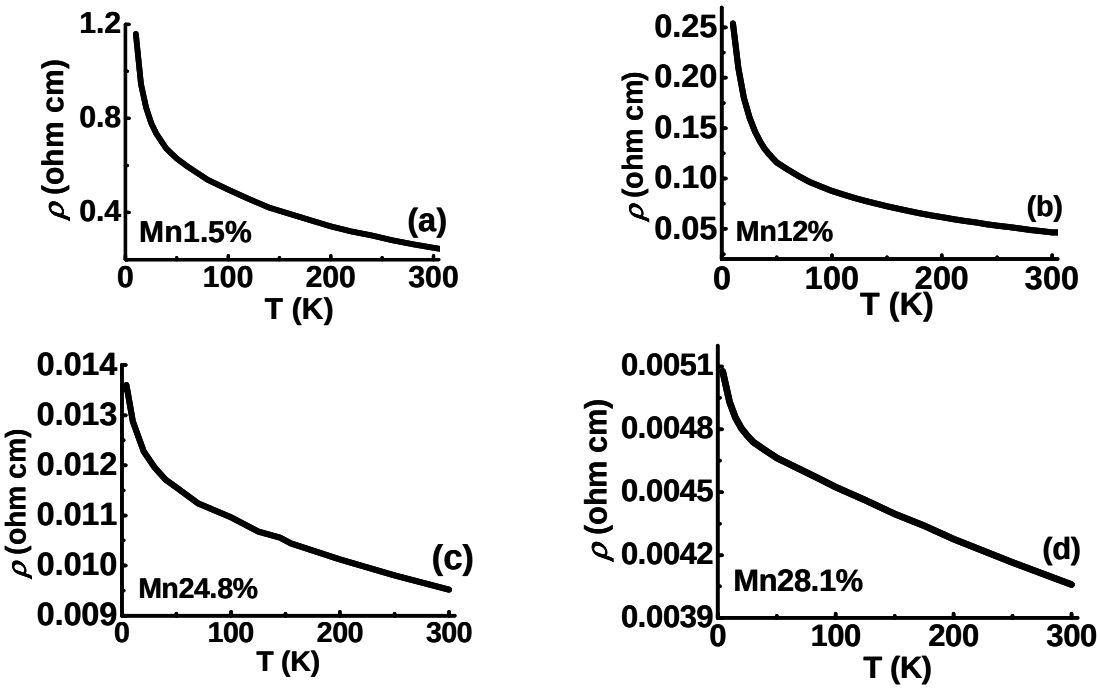

FIG. 4.10 *R-T* curves for the selected samples with different Mn concentrations. (a) Sample Mn1.5%, (b) sample Mn12%, (c) sample Mn24.8%, and (d) sample Mn28.1%.

Figures 4.10(a)-4.10(d) show the temperature-dependent resistivity curves for four samples with different Mn concentrations. Semiconducting-like behaviour is observed in all the samples. The semiconducting-like behaviour becomes less prominent with the

increase of the Mn concentrations, and a lower ratio of $\rho_{300\ K} / \rho_{5\ K}$ is obtained in the samples with the higher Mn concentration.

4.3.3.2 Temperature-dependent conductance

Figure 4.11 shows the dynamic conductance-voltage curves for three samples with different Mn concentrations. V-shape curves can be observed in all three samples, which is similar to the amorphous samples discussed in chapter 3. Due to the strong dependence on the bias voltage, the conductance for sample Mn1.5% is normalized to its value at zero bias, while for other samples we show the absolute values. We also plot the figures of $G' = (G_{2.5V,T} / G_{0,T}) / (G_{2.5V,4.2K} / G_{0,4.2K})$ and get the critical temperatures (T_C') using the same method in chapter 3. The critical temperatures (T_C') of 9, 12, and 15 K [see Fig. 4.12] are obtained for samples Mn1.5%, Mn24.8%, and Mn28.1%, respectively. The temperature range of the critical temperatures obtained from dynamic conductance studies is very close to the T_C or T_f reported by other groups. [2,15] It seems that the critical temperatures are independent of the Mn concentrations and the secondary phases, suggesting that may be the intrinsic property of $Ge_{1-x}Mn_x$ thin film system. The results obtained from the electrical measurements agree well with those from the magnetic measurements in Fig. 4.9 although the temperature of the sharp increase in the magnetization is a little higher than the critical temperatures obtained from the dynamic conductance studies.

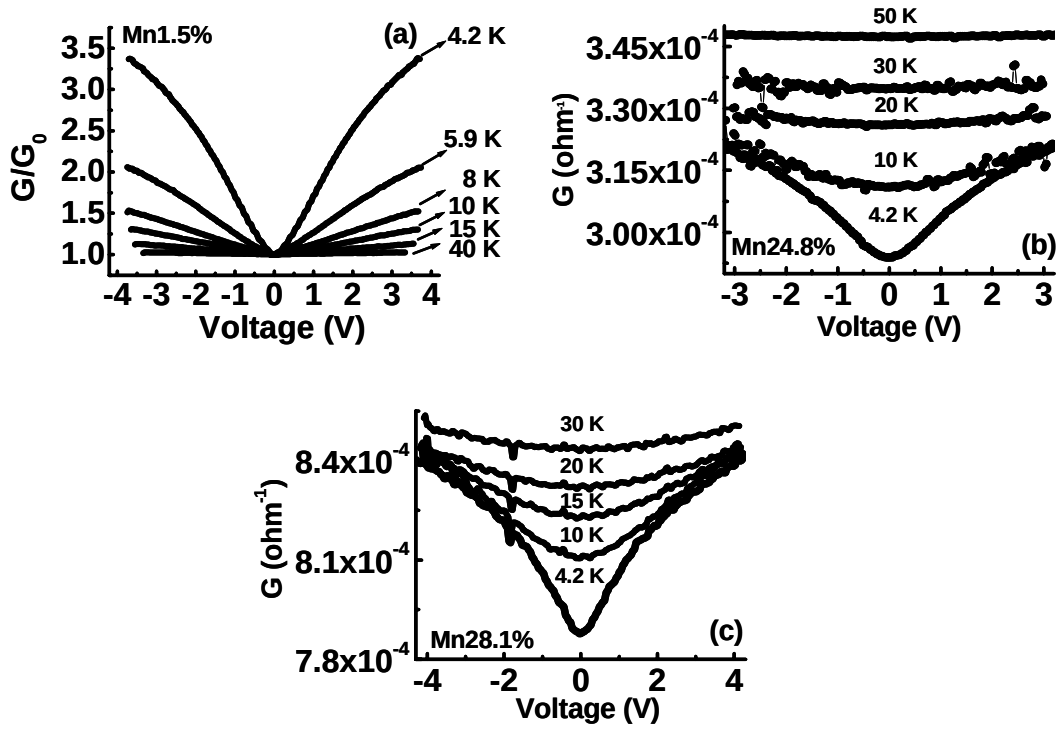

FIG. 4.11 Dynamic conductance-voltage curves at different temperatures for the samples under study. (a) Sample Mn1.5%, (b) sample Mn24.8%, (c) sample Mn28.1%.

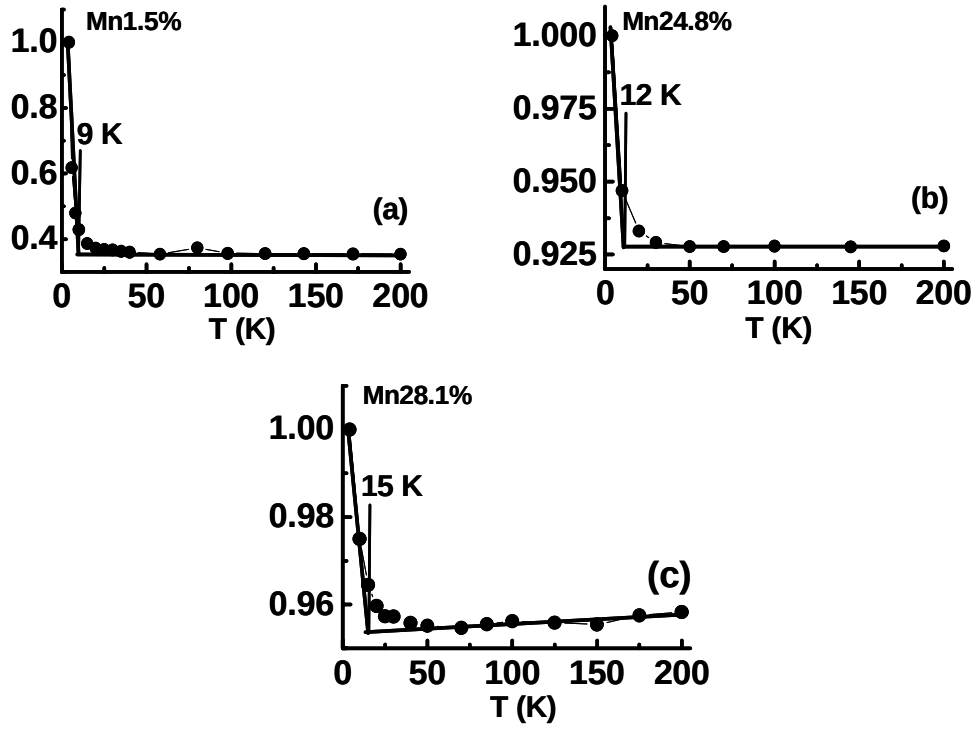

FIG. 4.12 Temperature-dependent G' curves for different samples. (a) Sample Mn1.5%, (b) sample Mn24.1%, and (c) sample Mn28.1%.

4.3.3.3 Magnetoresistance effect

In contrast to the negative MR obtained in the amorphous $Ge_{1-x}Mn_x$ thin films in chapter 3, a positive MR was obtained in all three samples under study in this chapter although the Mn concentration and embedded high T_C secondary phases are different. The MR curves at different temperatures for sample Mn24.8% are shown in Fig. 4.13. The MR ratio is about 1.2% at 4.2 K, decreasing with the increase of the temperature and becoming almost zero at 155 K. Several groups have also observed the positive MR behaviour and proposed different explanations to account for this effect: (i) Zeeman splitting in $Ti_{1-x}Co_xO_{2-\delta}$, [16], (ii) *s-d* exchange interaction in $Zn_{1-x}Co_xO$, [17] (iii) spin-related scattering in BMP in $(Mn_{0.03}, Co_{0.07})Zn_{0.90}O$, [18] (iv) geometric magnetoresistance of Ge:Mn nanoclusters in a diluted magnetic semiconductor matrix, [19] and (v) quantum interference effects in $Fe_{0.85}Co_{0.15}Si$ [20].The positive MR effect in the samples under studies may be understood with the BMP model similar to that reported in Ref. 18. In this model, BMPs play a role as spin-disorder scattering centres and the spin-dependent scattering will be enhanced when a magnetic field is applied, which gives a higher resistance. In Fig. 4.14, we plot the temperature-dependent MR ratios for three samples. The MR ratios decrease with the increase of both the Mn concentrations and temperatures.

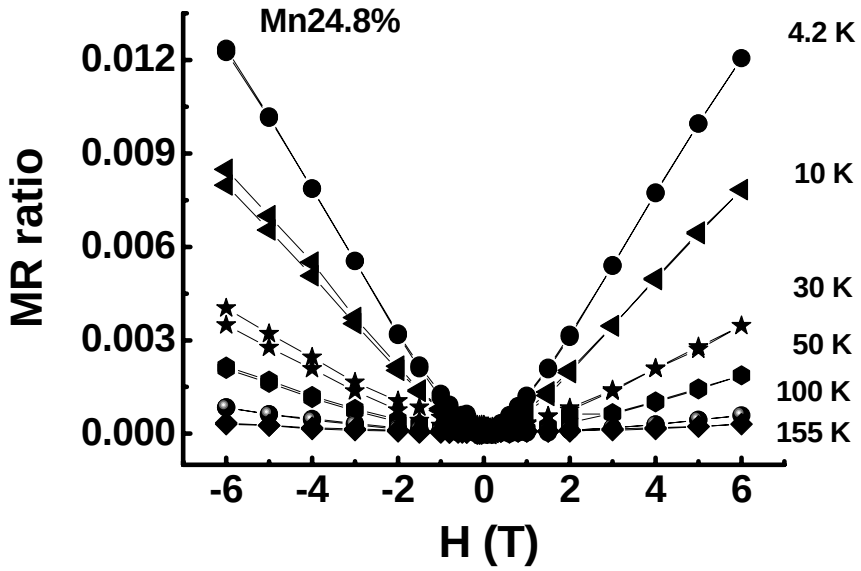

FIG. 4.13 MR curves for sample Mn24.8% at different temperatures.

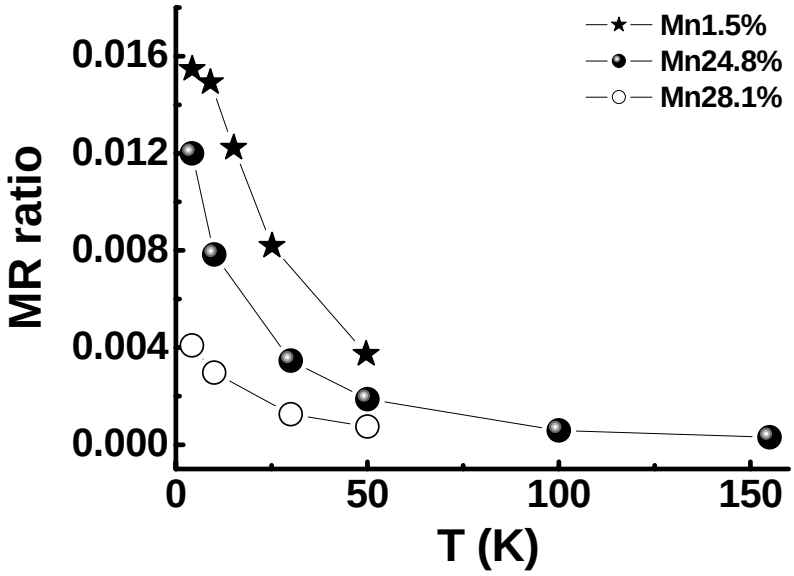

FIG. 4.14 MR ratios for samples Mn1.5%, Mn24.8%, and Mn28.1% at different temperatures.

4.3.4 Electrical transport properties for Ge:Mn nanowires

4.3.4.1 Temperature-dependent resistivity

Figure 4.15 shows the log-scale normalized temperature-dependent resistivity for the thin film, nanowires with the widths of 5, 1, and 0.1 μm based on sample Mn12% (Sc29). The conduction behaviors are a little different although the typical semiconducting-like behaviors can be observed in all the samples. *R-T* curves for the thin film and 5 μm nanowire are very similar. With the decrease of the dimension, the *R-T* curve for 1 μm nanowire is a little different from that of 5 μm nanowire. A steeper resistance increase at low temperatures can be observed, which indicates that the carrier localization becomes more pronounced at low temperatures when the dimension decreases. This can also be observed in the dynamic conductance studies and will be discussed later. For 0.1 μm nanowire, the conduction behavior is completely different from others. A flat region below 150 K can be observed. Then, the resistance decreases with the increase of the temperature. During the fabrication process of 0.1 μm nanowire, FIB is used to etch 1 μm $Ge_{0.88}Mn_{0.12}$ nanowire to a smaller dimension. Ga^{2+} ions may be implanted into the nanowire during the etching process, leading to the change of the carrier density in the $Ge_{0.88}Mn_{0.12}$ nanowire. As magnetic and electrical transport properties of DMSs materials are a function of the carrier density, a completely different *R-T* curve may be obtained when the carrier density changes. Although the mechanism how Ga^{2+} ions mediate the carrier density and electrical transport properties in this Ge:Mn system is not understood now, it may provide a new way to control the magnetic and electrical transport properties in DMSs except adding the magnetic impurities into the semiconductor matrixes. Further studies about it are recommended for future work.

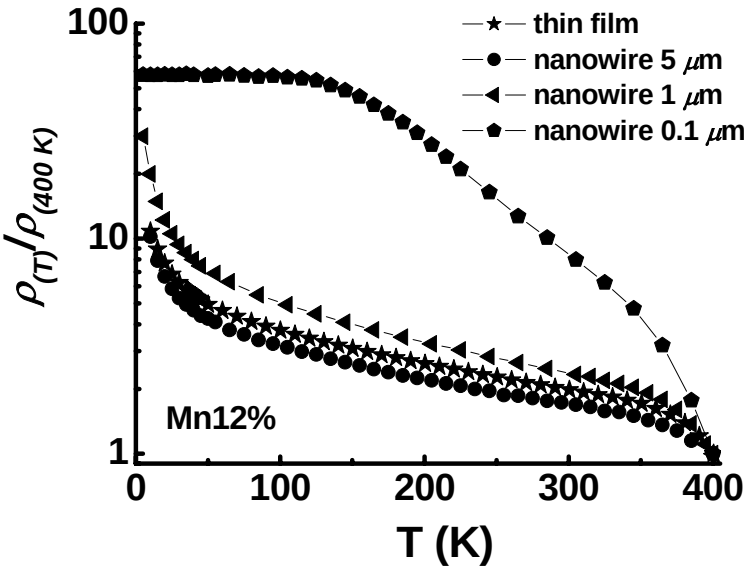

FIG. 4.15 Normalized log-scale *R*-*T* curves for the thin film, nanowires with diameters of 5, 1 and 0.1 μm of sample Mn12%.

4.3.4.2 Temperature-dependent conductance

A. 5 μm nanowire

Figures 4.16(a)-4.16(c) show the temperature-dependent dynamic conductance-voltage curves at different temperature ranges for 5 μm nanowire. The dynamic conductance-voltage curves can be divided into three temperature regions: (I) 5 K < T < 80 K [see Fig. 4.16(a)]; (II) 80 K < T < 300 K [see Fig. 4.16(b)]; (III) 300 K < T < 400 K [see Fig. 4.16(c)]. In regions (I), V-shape curves can be observed and becomes less pronounced with the increase of the temperature. As discussed before, V-shape curves are an indication of the carrier localization. In region (II), the curves become flatter and conductance increases with the increase of the temperature. In region (III), the conductance-voltage curves from 300 to 360 K are a little different from those in regions (I) and (II). The conductance is almost constant at the center part of the curves. However, the dynamic conductance suddenly increases at the high bias, then

decreases to some value higher than that at the center part. The phenomenon is most obvious at 360 K. Above 360 K, the curves become flat again. As discussed before, the Curie temperature of this sample is around 365 K. Thus, the change in the dynamic conductance-voltage curves may have some relations with the change in the magnetic properties.

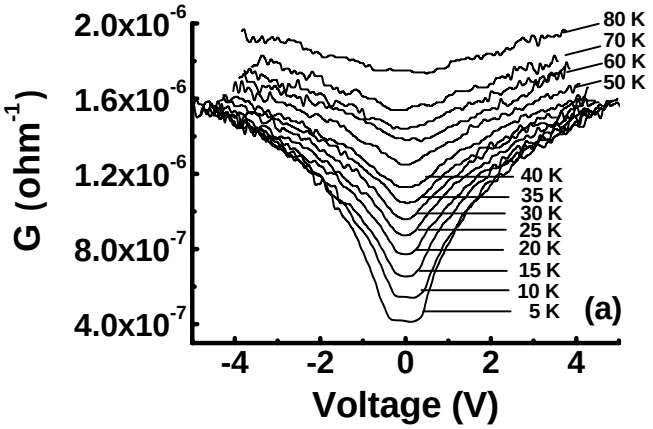

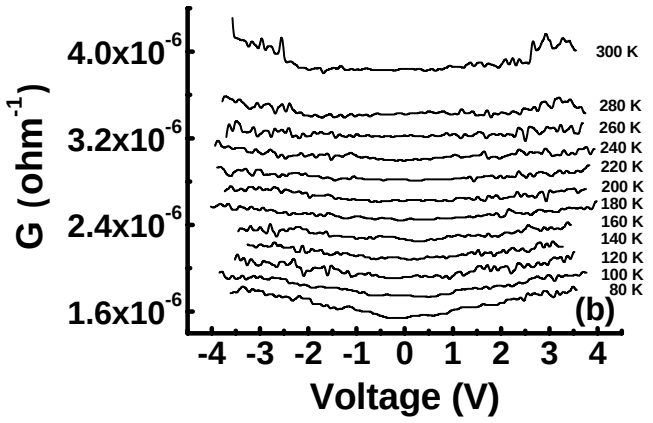

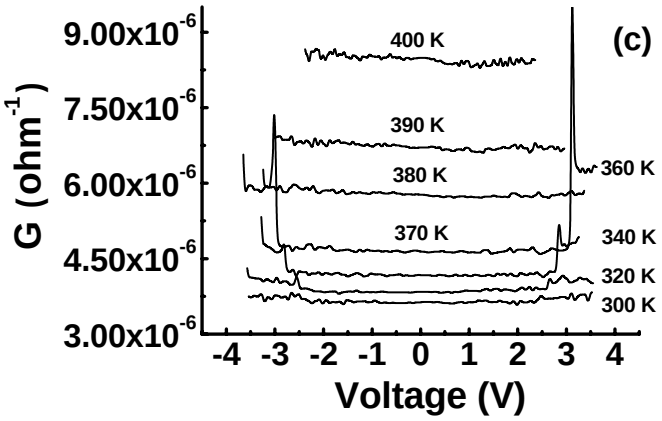

FIG. 4.16 Dynamic conductance-voltage curves for 5 μm nanowire at different temperature ranges: (a) 5 to 80 K, (b) 80 to 300 K, (c) 300 to 400 K.

B. 1 μm nanowire

Figures 4.17(a)-4.17(c) shows the dynamic conductance-voltage curves for 1 μm nanowire at different temperature ranges. The dynamic conductance-voltage curves can also be separated into three regions: (I) 5 K < T < 145 K [see Fig. 4.17(a)]; (II) 145 K < T < 305 K [see Fig. 4.17(b)]; (III) 315 K < T < 395 K [see Fig. 4.17(c)]. In region (I), V-shape curves are also observed and become flatter with the increase of the temperature. In comparison with the curves for 5 μm nanowire, the dips of V-shape curves become more obvious at low temperatures and the temperature that the curves become flat is higher, which indicates that the carrier localization becomes more pronounced when the dimension decreases. In region (II), the curves become flatter and conductance increases with the increase of the temperature, which is similar to the 5 μm nanowire. In region (III), the dynamic conductance also suddenly increases at the high bias, then decreases to some value higher than that at the center part. The increase of the conductance becomes more obvious with the increase of the temperature and become the most pronounced at 395 K.

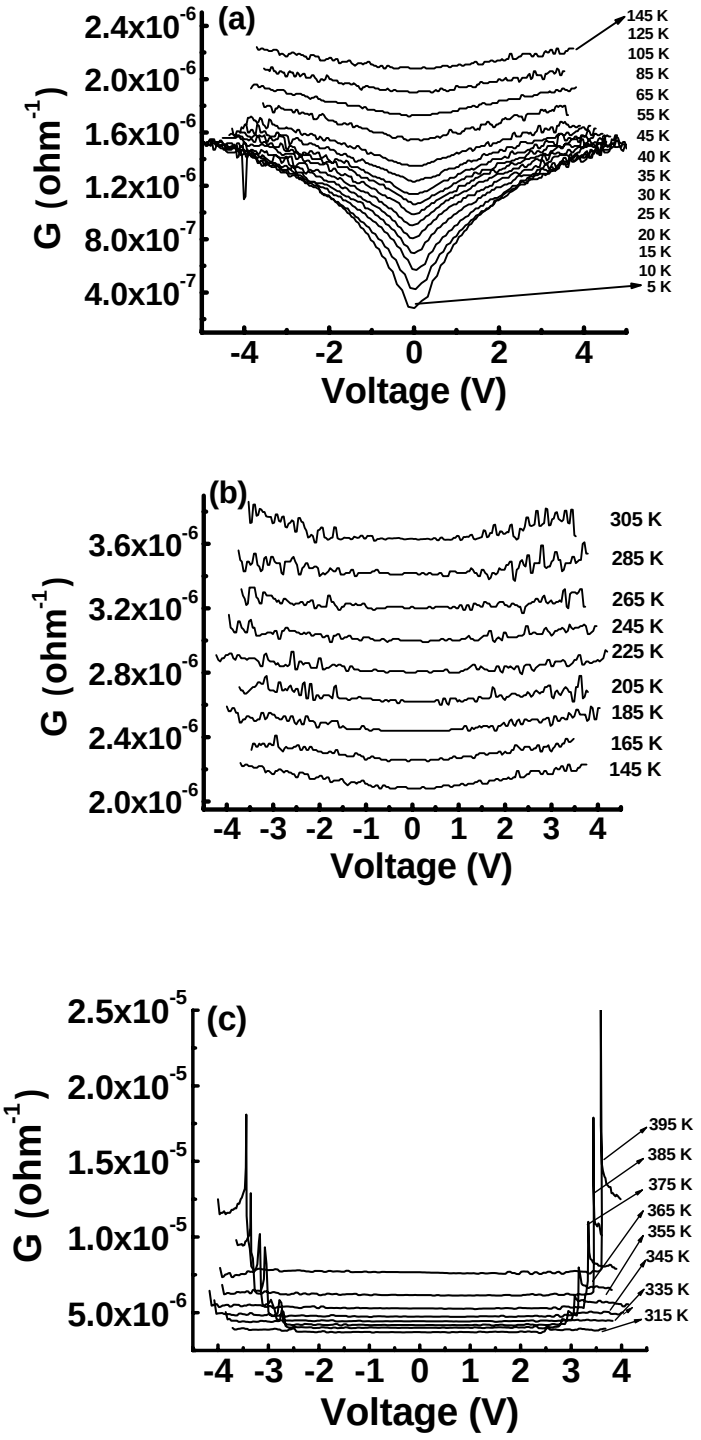

FIG. 4.17 Dynamic conductance-voltage curves for 1 μm nanowire at different temperature ranges: (a) 5 to 145 K, (b) 145 to 305 K, (c) 315 to 395 K.

C. 0.1 μm nanowire

Figures 4.18(a)-4.18(c) shows the dynamic conductance-voltage curves for 0.1 μm nanowire at different temperature ranges. The dynamic conductance-voltage curves can also be divided into three regions: (I) 5 K $< T <$ 105 K [see Fig. 4.18(a)]; (II) 105 K $< T <$ 285 K [see Fig. 4.18(b)]; (III) 305 K $< T <$ 400 K [see Fig. 4.18(c)]. When the dimension becomes smaller, more pronounced carrier localization is expected at low temperatures. However, V-shape curves observed in 5 and 1 μm nanowires at low temperatures cannot be found for 0.1 μm nanowires at low temperatures. Instead, the dynamic conductance is almost constant with a little oscillation until 95 K. The oscillation in the curves is due to the high resistance noise. Because Ga^{2+} ions are implanted into $Ge_{0.88}Mn_{0.12}$ thin films and leads to a higher carrier density, the carrier localization does not happen again at low temperatures. However, V-shape curves are observed in region (II) and become more pronounced with the increase of the temperature. Generally, the carrier localization will become less pronounced with the increase of the temperature. This abnormal phenomenon cannot be understood now. The dynamic conductance-voltage behavior in region (III) is similar to that of 1 μm nanowire.

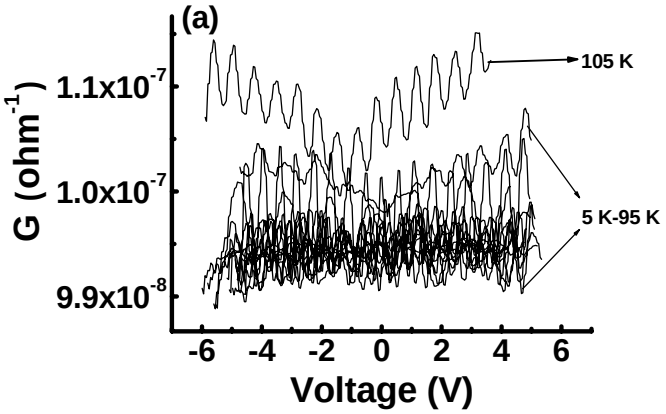

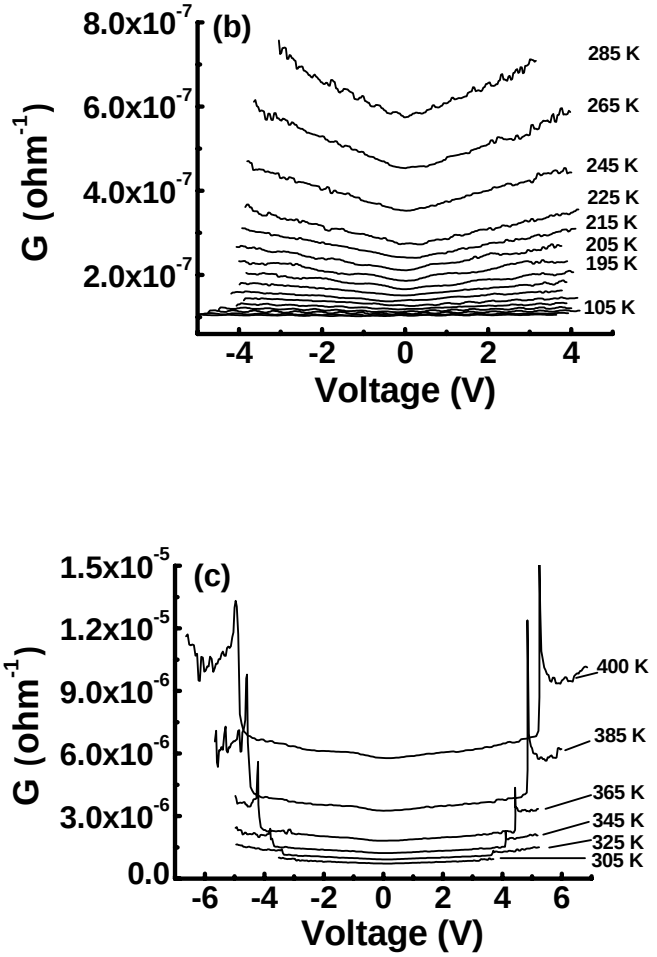

FIG. 4.18 Dynamic conductance-voltage curves for 0.1 μm nanowire at different temperature ranges: (a) 5 to 105 K, (b) 105 to 285 K, (c) 305 to 400 K.

4.3.5 $Ge_{0.74}Mn_{0.26}$ granular thin film

4.3.5.1 Introduction

In this section, a granular $Ge_{0.74}Mn_{0.26}$ thin film was fabricated. The sample was grown at 300 ^oC. In comparison with the samples discussed before, a higher growth rate (0.07 nm/s) favoured the formation of the granular structure. A schematic illustration of the granular materials is shown in Fig. 4.19, where some granular materials are uniformly distributed in the matrix material. The granular thin-film structure is a very well controlled nanostructure and has promising applications for spintronic devices.

Intensive studies in this field have been done and numerous papers have been published every year. Among them, nanogranular composite materials formed by combining the magnetic and nonmagnetic elements exhibit some exciting physical properties and are of particular interest in data-storage technology (e.g., hard disk drives) as well as for fundamental studies concerning new phenomena induced by the nanostructure. [21-25]

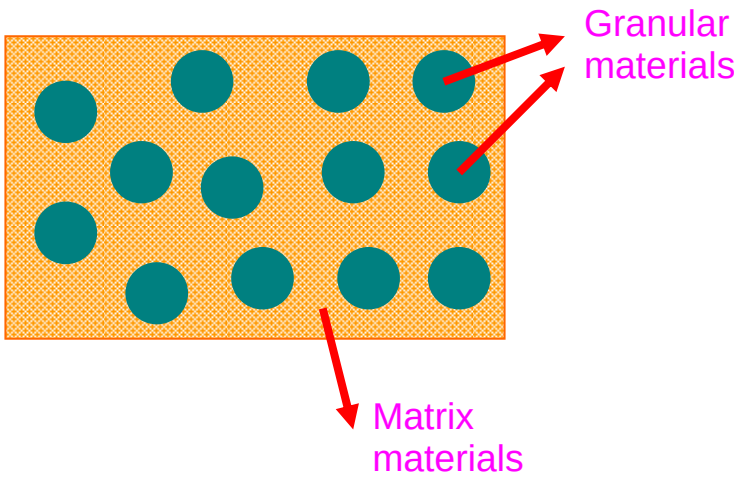

FIG. 4.19 Schematic illustration of the granular structure.

4.3.5.2 Structural properties

Figure 4.20 shows the bright-field cross-sectional TEM image of the $Ge_{0.74}Mn_{0.26}$ thin film. Different crystalline orientations can be seen clearly in the TEM images, indicating the polycrystalline nature of the thin film. As indicated by the arrow, granules with a diameter of ~ 5 nm embedded in the crystalline matrix can be seen clearly. Although the structure of the clusters can not be determined by the TEM image, as we will discuss shortly, the magnetic property measurements suggest that they are Mn_5Ge_3.

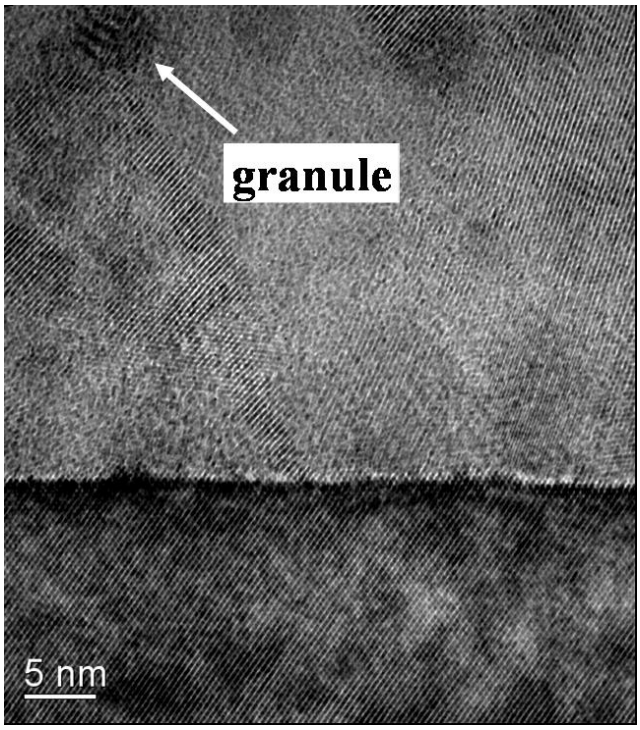

FIG. 4.20 Bright-field cross-sectional TEM image of the $Ge_{0.76}Mn_{0.24}$ thin film. The arrow points to a granule with a diameter of ~ 5 nm.

4.3.5.3 Magnetic properties

Figure 4.21 shows the temperature-dependent magnetization of both ZFC and FC curves in the temperature range from 5 to 320 K at an applied magnetic field of 100 Oe. The sample exhibits a ferromagnetic ordering temperature of approximately 300 K. The separation between ZFC and FC curves is observed at ~ 285 K. According to the discussion before, the granules in this system should be Mn_5Ge_3, whose T_C is 296 K.

The hysteresis loops of the $Ge_{0.74}Mn_{0.26}$ granular sample are measured at different temperatures with a maximum magnetic field of 10000 Oe [see Fig. 4.22]. Clear hysteresis loops have been observed up to 280 K. The slow saturation at low temperatures and small squareness (Mr=0.21 Ms at 20 K) of the curves provide further evidence that the ferromagnetism originates from the magnetic granules.

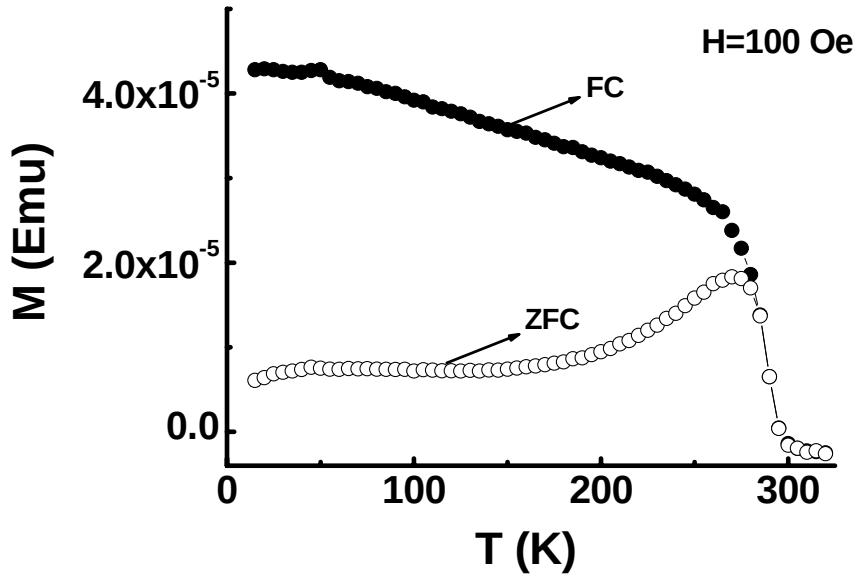

FIG. 4.21 ZFC and FC curves measured at an applied magnetic field of 100 Oe at the temperature range from 5 to 320 K for the granular $Ge_{0.74}Mn_{0.26}$ thin film.

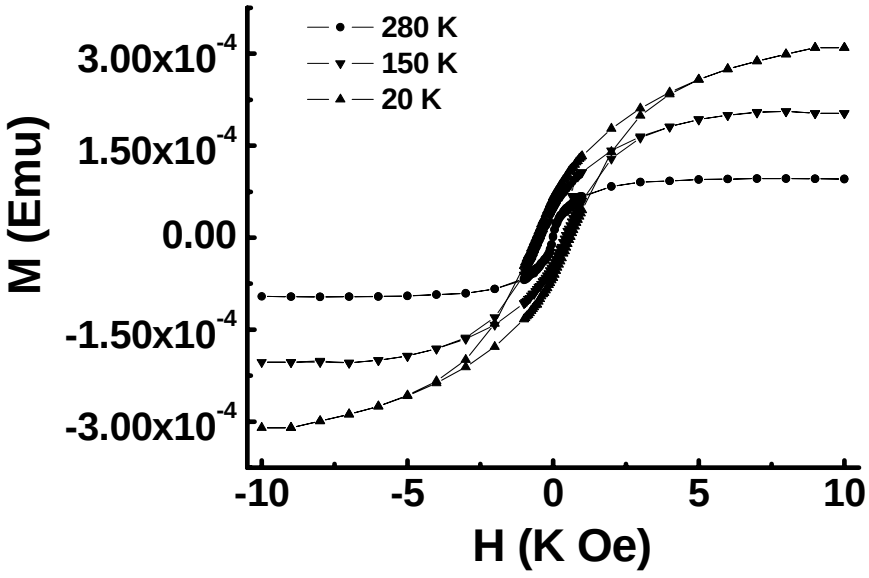

FIG. 4.22 *M-H* curves measured at 20, 150 and 280 K for the granular $Ge_{0.74}Mn_{0.26}$ thin film.

In Fig. 4.23, the normalized *M-H* curves for the granular sample ($Ge_{0.76}Mn_{0.24}$), amorphous sample A5 ($Ge_{0.58}Mn_{0.42}$), and amorphous sample A5 after 4 hours

annealing are plotted together for comparison. After annealing, the coercivity increases. However, the *M-H* shape is irregular, indicating the inhomogeneous properties. Both amorphous and Mn_5Ge_3 phases contribute to the magnetization behaviour. For the granular sample $Ge_{0.74}Mn_{0.26}$, the coercivity becomes higher and the magnetization is more difficult to saturate.

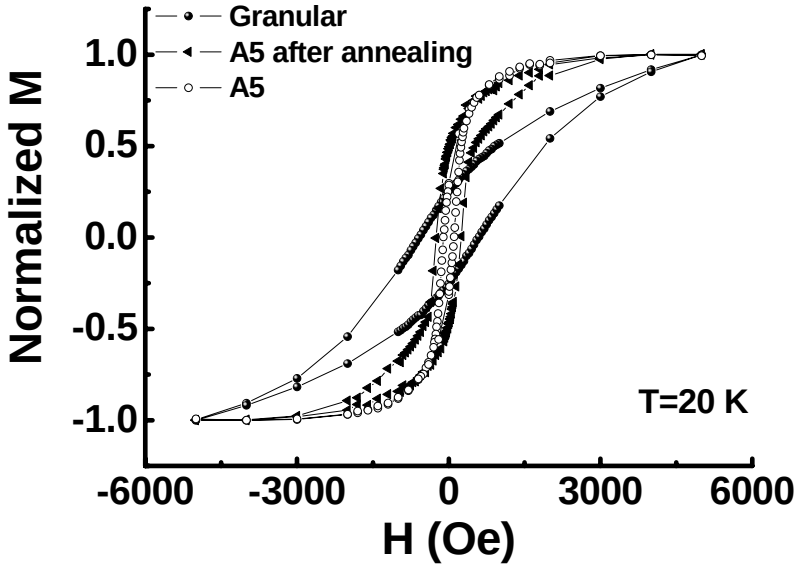

FIG. 4.23 Normalized *M-H* curves at 20 K for the $Ge_{0.74}Mn_{0.26}$ granular sample (solid circles), amorphous $Ge_{0.58}Mn_{0.42}$ sample A5 (open circles), and amorphous $Ge_{0.58}Mn_{0.42}$ sample A5 after 4 hours H_2 plasma annealing (solid triangles).

4.3.5.4 Electrical transport properties

Figure 4.24 shows the *R-T* curve of the granular $Ge_{0.74}Mn_{0.26}$ thin film. As can been seen from the figure, the resistance increases with decreasing temperature, which is a typical semiconducting behaviour. The rate of resistance change can be divided into two regions: (I) 5 K < *T* < 100 K and (II) 100 K < *T* < 300 K. In comparison with region (I), the resistance increases more rapidly with the decrease of temperature in region (II). As was reported in Ref. 26, Mn_5Ge_3 epitaxial thin film shows a metallic behaviour and

the resistivity ratio $\rho_{300\ \mathrm{K}} / \rho_{4\ \mathrm{K}}$ is ~ 12. Thus, the competition between the metallic granules and the semiconductor matrix may result in a slow change of resistance below 100 K. The inset of Fig. 4.24 shows the plot of $\log R$ versus T^{-1}. Clearly, the temperature-dependent resistance can be well fitted with an Arrhenius function $\rho = \rho_0 \exp(E_a / kT)$, where E_a is the activation energy, suggesting that the transport is dominated by a thermal activation mechanism.

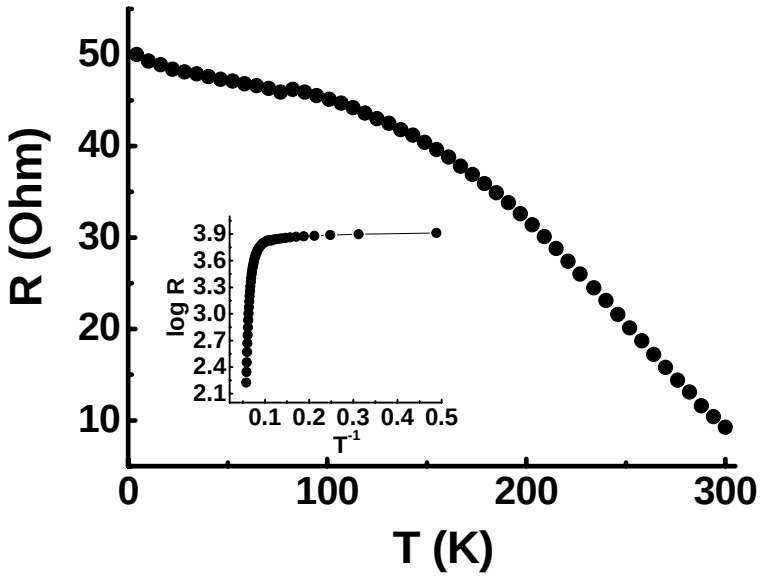

FIG. 4.24 *R-T* curve of the granular $Ge_{0.74}Mn_{0.26}$ thin film at the temperature range from 5 to 300 K for the granular $Ge_{0.74}Mn_{0.26}$ thin film. Inset: the plot of $\log R$ versus T^{-1}.

The thermally activated process can be seen even more clearly in the dynamic conductance-voltage curves at different temperatures [see Fig. 4.25]. The nonlinear *I-V* curves and corresponding asymmetry between the forward and reverse bias curves are observed at all measured temperatures. At the high temperature range, the conductance increases sharply with the increase of the bias. The curves become broader when the temperature decreases. A flat region appears at low bias when the temperature is below

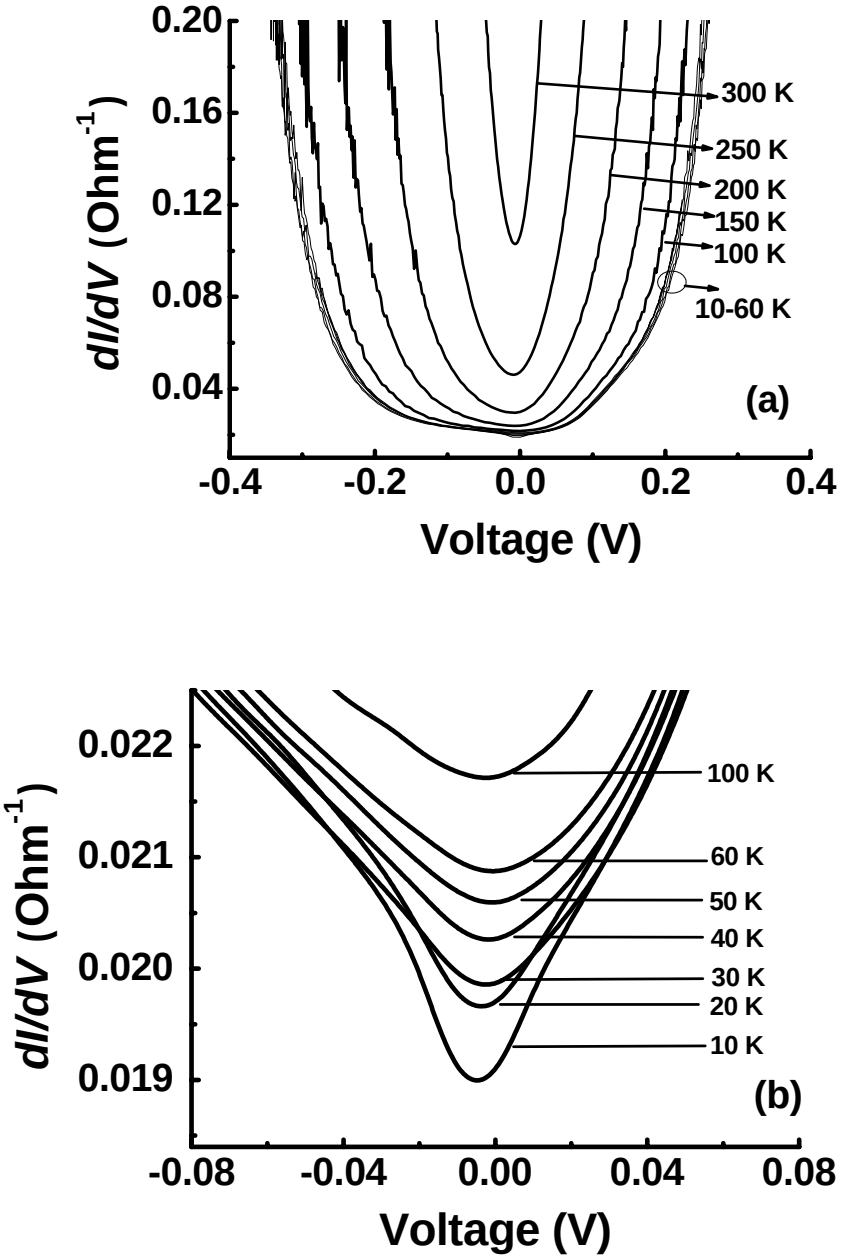

FIG. 4.25 (a) Dynamic conductance-voltage curves at different temperatures; (b) enlarged portion near the zero-bias region below 100 K.

100 K, suggesting the existence of a Schottky barrier at the nanoparticles / host matrix interface. The enlarged portion near the zero-bias region at low temperatures is shown in Fig. 4.25(b). A sharp dip near zero bias appears below 30 K. The dip becomes less pronounced when the temperature increases and disappears above 30 K. Different

causes of the conductance dip have been discussed before, [27,28] which include the localization in amorphous materials or ultrathin film, tunnelling through an intermediate state, and magnetic scattering in the electrodes or in the barrier. In our case, the charge localization resulting from the disordered granular system may be the cause of the anomaly observed.

4.4 Summary

Amorphous $Ge_{1-x}Mn_x$ ($1.5\% < x < 56.1\%$) thin films embedded with Ge crystallites, and different high T_C secondary phases were fabricated. The magnetic properties were dominated by the high T_C secondary phases. Semiconducting-like conducting behaviors were observed in all samples. Dynamic conductance studies revealed that the carrier localization happened at low temperatures. A sharp increase of the magnetization was observed below 25 K. The critical temperatures (T'_C) obtained from dynamic conductance study were independent of the Mn compositions and the secondary phases and were very close to T_C or T_f reported in literature for the epitaxially grown $Ge_{1-x}Mn_x$ thin films. The spin-dependent transport properties were studied in the nanowires with diameters of 5, 1, and 0.1 μm. Structure, magnetic, and electrical transport properties of a $Ge_{0.74}Mn_{0.26}$ granular thin film were discussed in details. Existence of a Schottky barrier at the nanoparticles / host matrix interface and the carrier localization at low temperatures were observed.

References:

1 Y. D. Park, A. T. Hanbicki, S. C. Erwin, C. S. Hellberg, J. M. Sullivan, J. E. Mattson, T. F. Ambrose, A. Wilson, G. Spanos, and B. T. Jonker, "A group-IV ferromagnetic semiconductor: Mn_xGe_{1-x}", Science **295**, pp. 651-654, 2002.

2 A. P. Li, J. Shen, J. R. Thompson, and H. H. Weitering, "Ferromagnetic percolation in Mn_xGe_{1-x} dilute magnetic semiconductor", Appl. Phys. Lett. **86**, pp. 1552507, 2005.

3 L. Liu, Z. X. Shen, K. L. Teo, A.V. Kolobov, and Y. Maeda, "Raman scattering of germanium nanocrystals embedded in glass matrix under hydrostatic pressure", J. Appl. Phys. **93**, pp. 9392-9394, 2003;

4 K. L. Teo, S. H. Kwok, P. Y. Yu, S. Guha, "Quantum confinement of quasi-two-dimensional E1 excitons in Ge nanocrystals studied by resonant Raman scattering", Phys. Rev. B **62**, pp.1584-1587, 2000.

5 K. Yasuköchi and K. Kanematsu, "Ferromagnetism of Mn_5Ge_2", J. Phys. Soc. Jpn. **15**, pp. 932, 1960.

6 T. Ohoyama, "A new phase of an intermetallic compound $Mn_{3.4}Ge$ and its magnetism", J. Phys. Soc. Jpn. **16**, pp. 352-353, 1961.

7 T. Ohoyama, "X-ray and magnetic studies of the Manganese-Germanium system", J. Phys. Soc. Jpn. **16**, pp. 1995-2002, 1961.

8 N. Yamada, T. Ohashi, and T. Ohoyama, "Magnetic phase transition of ξ-$Mn_{2.6}Ge$", J. Phys. Soc. Jpn. **51**, pp. 2041-2042, 1982.

9 N. Yamada, K. Maeda, Y. Usami, and T. Ohoyama, "Magnetic properties of intermetallic compound $Mn_{11}Ge_8$", J. Phys. Soc. Jpn. **55**, pp. 3721-3724, 1986.

10 N. Yamada, S. Funahashi, F. Izumi, M. Ikegame, and T. Ohoyama, "Magnetic Structure of intermetallic compounds κ-Mn_5Ge_2", J. Phys. Soc. Jpn. **56**, pp. 4107-4112, 1987.

11 N. Yamada, "Atomic magnetic moment and exchange interaction between Mn atoms in intermetallic compounds in Mn-Ge system", J. Phys. Soc. Jpn. **59**, pp. 273-288, 1990.

12 C. Bihler, C. Jaeger, T. Vallaitis, M. Gjukic, M. Brandt, E. Pippel, J. Woltersdorf, and U. Gösele, "Structural, and magnetic properties of Mn_5Ge_3 cluster in a dilute magnetic germanium matrix", Appl. Phys. Lett. **88**, pp. 112506, 2006.

13 A. P. Li, J. F. Wendelken, J. Shen, L.C. Feldman, J. R. Thompson, and H. H. Weitering, "Magnetism in Mn_xGe_{1-x} semiconductors mediated by impurity band carriers", Phys. Rev. B **72**, pp. 195205, 2005.

14 Shuangli Ye, "Magneto-transport in (Ga, Mn)As-based alloys and hybrids", Ph. D Thesis, Fachbereich Physik der philipps-Universtität Marburg, 2005.

15 C. Jarger, C. Bihler, T. Vallaitis, S. T. B. Goennenwein, M. Opel, R. Gross, and M. S. Brandt, "Spin glass-like behavior of Ge:Mn", Phys. Rev. B **74**, pp. 045330, 2006.

16 S. R. Shinde, S. B. Ogale, S. D. Sarma, J. R. Simpson, H. D. Drew, S. E. Lofland , C. Lanci, J. P. Buban, N. D. Browning, V. N. Kulkarni, J. Higgins, R. P. Sharma, R. L. Greene, and T. Venkatesan, "Ferromagnetism in laser deposited anatase $Ti_{1-x}Co_xO_{2-\delta}$ films", Phys. Rev. B **67**, pp. 115211, 2003.

17 J. H. Kim, H. Kim, D. Kim, Y. E. Ihm, and W. K. Choo, "Magnetoresistance in laser-deposited $Zn_{1-x}Co_xO$ thin films", Physica B **327**, pp. 304-306, 2003.

18 Z.-B Gu, C.-S. Yuan, M.-H. Lu, J. Wang, D. Wu, S.-T. Zhang, S.-N. Zhu, Y.-Y. Zhu, and Y.-F. Chen, "Magnetic and transport properties of (Mn, Co)-codoped ZnO films prepared by radio-frequency magnetron cosputtering", J. Appl. Phys. **98**, pp. 053908, 2005.

19 Y. D. Park, A. Wilson, A. T. Hanbicki, J. E. Mattson, T. Ambrose, G. Spanos, and B. T. Jonker, "Magnetoresistance of Mn:Ge ferromagnetic nanoclusters in a diluted semiconductors matrix", Appl. Phys. Lett. **69**, pp. 363-365, 1996.

20 N. Manyala, Y. Sidis, J. F. DiTusa, G. Aeppli, D. P. Young, and Z. Fisk, "Magnetoresistance from quantum interference effects in ferromagnets", Nature **404**, pp. 581-584, 2000.

21 H. Sun, C. B. Murray, D. Weller, L. Folks, and A. Moser, "Monodisperse FePt nanoparticles and ferromagnetic FePt nanocrystal superlattices", Science **287**, pp. 1989-1992, 2000.

22 P. Allia, M. Coisson, F. Spizzo, P. Tiberto, and F. Vinai, "Magnetic correlation states in cosputtered granular $Ag_{100-x}Fe_x$ films", Phys. Rev. B **73**, pp. 054409, 2006.

23 B. J. Hattink, M. García del Muro, Z. Konstantinović, X. Batlle, and A. Labarta, "Tunneling magnetoresistance in Co-ZrO_2 granular thin films", Phys. Rev. B **73**, pp. 045418, 2006.

24 L. M. Socolovsky, C. L. P. Oliveira, J. C. Denardin, M. Knobel, and I. L. Torriani, "Nanostructure of granular Co-SiO_2 thin films modified by thermal treatment and its relationship with the giant Hall effect", Phys. Rev. B **72**, pp. 184423, 2005.

25 H. Akinaga, "Magnetoresistive switch effect in metal/semiconductor hybrid granular films: extremely huge magnetoresistance effect at room temperature", Semicond. Sci. Technol. **17**, pp. 322-326, 2002.

26 Changgan Zeng, S. C. Erwin, L. C. Feldman, A. P. Li, R. Jin, Y. Song, J. R. Thompson and H. H. Weitering, "Epitaxial ferromagnetic Mn_5Ge_3 on Ge(111)", Appl. Phys. Lett. **83**, pp. 5002-5004, 2003.

27 E. L. Wolf, Principles of electron tunneling spectroscopy, Oxford University Press, New York, 1985.

28 J. S. Moodera, L. R. Kinder, T. M. Wong, and R. Meservey, "Large magnetoresistance at room temperature in ferromagnetic thin film tunnel junctions", Phys. Rev. Lett. **74,** pp. 3273-3276, 1995.

CHAPTER 5

MAGNEITC AND ELECTRICAL TRANSPORT PROPERTIES OF δ-DOPED AMORPHOUS $Ge_{1-x}Mn_x$ THIN FILMS

5.1 Introduction

The δ-doping (or digital doping) technique has been widely used in semiconductor research in order to separate the carriers from the dopants which in some circumstances lead to superior electrical properties. Aiming at controlling the spacing between the magnetic impurities, the same technique has also been used to fabricate diluted magnetic semiconductors. [1-6] In previous chapters, we have discussed the magnetic and electrical transport properties of amorphous $Ge_{1-x}Mn_x$ thin films and thin films with the coexistence of amorphous $Ge_{1-x}Mn_x$, Ge crystallites and high T_C secondary phases. In this chapter we will discuss the δ-doped amorphous $Ge_{1-x}Mn_x$ thin films. The main objective of studying the δ-doped samples is to investigate if and how the spacing between magnetic impurities will affect the magnetic properties in the amorphous $Ge_{1-x}Mn_x$ thin films and the possible origins of the ferromagnetism and characteristic temperature in $G_{1-x}Mn_x$. Figure 5.1 shows the schematic structure of the δ-doped thin films. The thickness of Ge layers ranges from 1 to 2 nm, and the thickness of Mn layers ranges from 0.125 to 0.5 nm in our δ-doped amorphous $Ge_{1-x}Mn_x$ samples.

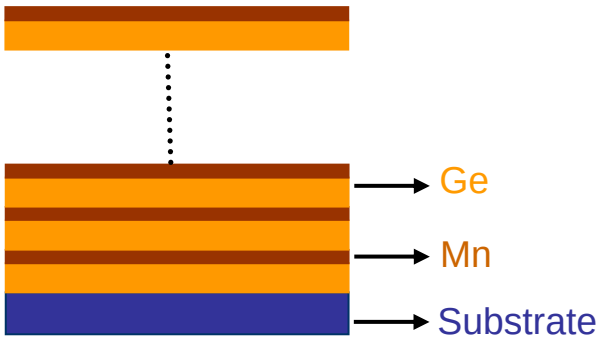

FIG. 5.1 Schematic illustration of the δ-doped thin film structure**.**

5.2 Experimental details

The samples have been prepared using MBE at a substrate temperature of 200 ^{o}C on GaAs (001) substrates. Prior to loading the samples into the chamber, the substrates were cleaned by acetone, alcohol iso-propylinque (iso-proponol) and deionized water, respectively. The Ge source material was heated by an electron beam at a current of 30 mA. The Mn was evaporated by a K-cell at a temperature of 800 ^{o}C. Three series of samples were fabricated by varying Ge and Mn layer thicknesses [see Table 5.1 for details]: (a) {Ge (1 nm)/Mn (0.125, 0.25 and 0.375 nm)}$_{50}$, (b) {Ge (1.5 nm)/Mn (0.125, 0.25, 0.375, 0.45, and 0.5 nm)}$_{40}$, and (c) {Ge (2 nm)/Mn (0.25, 0.375, and 0.5 nm)}$_{40}$. Here, the numbers outside the brackets are numbers of growth cycles. The structural properties of the samples were characterized by Raman spectroscopy and HRTEM. The magnetic and electrical transport properties of the samples were characterized using a commercial SQUID magnetometer and a four-probe technique, respectively.

5.3 Results and discussion

5.3.1 Structural properties

Figure 5.2(a) shows the Raman spectra of the samples in group B. Samples B1 to B4

Table 5.1 Growth conditions and parameters of the δ-doped amorphous Ge:Mn samples

Group	Sample name	Composition	No. of cycles	Conductivity 10^2 $(\Omega m)^{-1}$	T^*_C (K)
A	A1	Ge (1 nm)/Mn (0.125 nm)	50	2.93	30
A	A2	Ge (1 nm)/Mn (0.25 nm)	50	17.73	100
A	A3	Ge (1 nm)/Mn (0.375 nm)	50	14.52	135
B	B1	Ge (1.5 nm)/Mn (0.125 nm)	40	0.39	10
B	B2	Ge (1.5 nm)/Mn (0.25 nm)	40	1.89	70
B	B3	Ge (1.5 nm)/Mn (0.375 nm)	40	3.3	100
B	B4	Ge (1.5 nm)/Mn (0.45 nm)	40	13.3	130
B	B5	Ge (1.5 nm)/Mn (0.5 nm)	40	259.58	140
C	C1	Ge (2 nm)/Mn (0.25 nm)	40	1.55	45
C	C2	Ge (2 nm)/Mn (0.375 nm)	40	3.04	90
C	C3	Ge (2 nm)/Mn (0.5 nm)	40	4.17	115

exhibit a broad peak at 275 cm^{-1}, which is corresponding to the typical peak position of amorphous Ge. [7] The peak intensity decreases with increasing Mn concentration. The peaks at 292 cm^{-1} is due to the GaAs substrate. [12] Although the substrate also shows a peak at 267 cm^{-1}, it is very weak in comparison with the peak at 292 cm^{-1}. Although it is not well understood at the moment, a very sharp peak at 299 cm^{-1} appears when the Mn concentration is further increased (sample B5). The position of this peak is very close to the peak of nanocrystalline Ge. The same peak is also observed in sample C3, which is the sample with the highest Mn concentration in group C. This means that a higher Mn concentration actually improves the crystallinity of Ge. Figure 5.2(b) shows HRTEM

image of sample B1. We cannot see any crystalline phases in the figure, which is in good agreement with the Raman results. However, it is difficult for us to distinguish the Mn and Ge layers because the Mn layer is very thin.

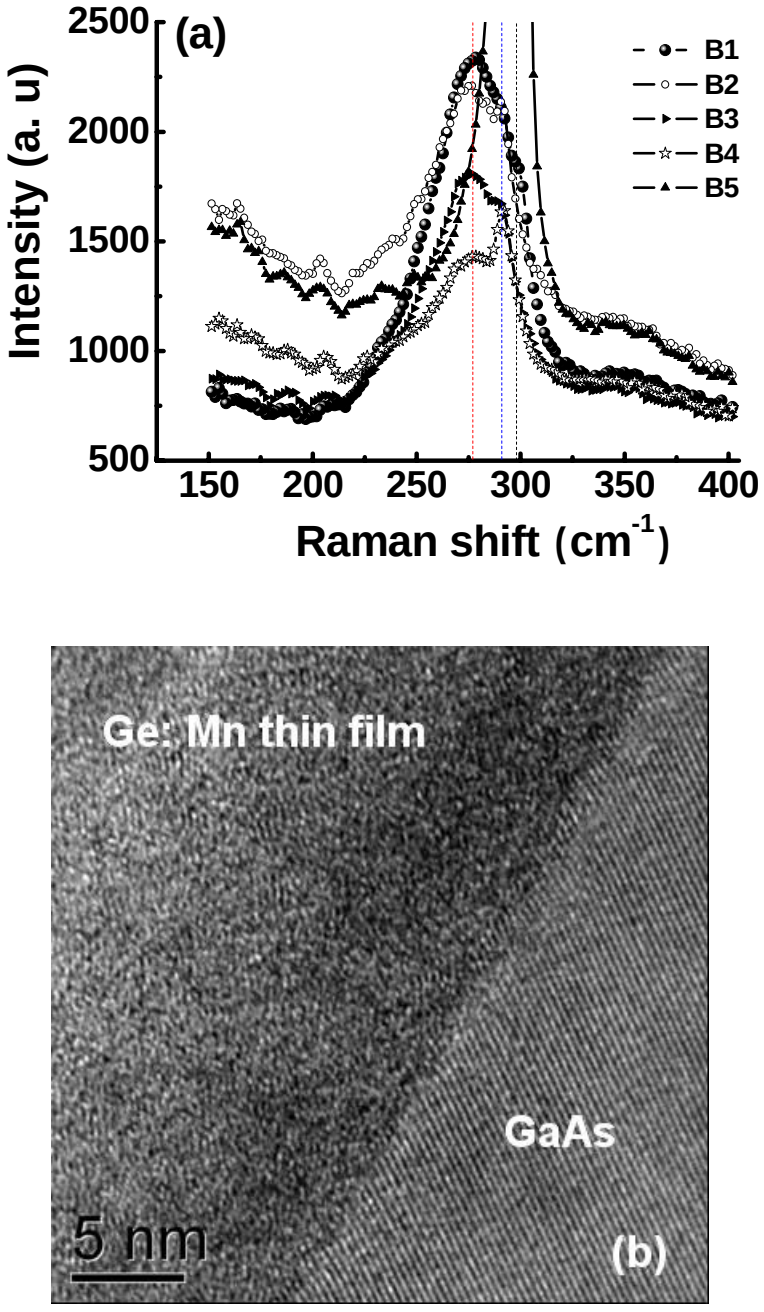

FIG. 5.2 (a) Raman spectra of group B samples. The dotted lines in the figure indicate the peak positions of amorphous Ge, GaAs substrate, and Ge crystalline phase at the positions of 275, 292 and 299 cm^{-1}, respectively. (b) HRTEM image for sample B1.

5.3.2 Electrical transport properties

The relationship between the Mn layer thickness and the electrical conductivity is shown in Fig. 5.3. In general, the conductivity increases with the thickness ratio between Mn and Ge layers when either one of them is fixed. This may be understood as being caused by either the increase of hole concentration due to Mn doping or formation of metallic phase. The former is more likely happening in the lightly doped samples while the latter may also become possible when the thickness of the Mn layer increases. The rapid increase of conductivity in sample B5 may indicate that the highly conductive regions are reaching the electrical percolation threshold.

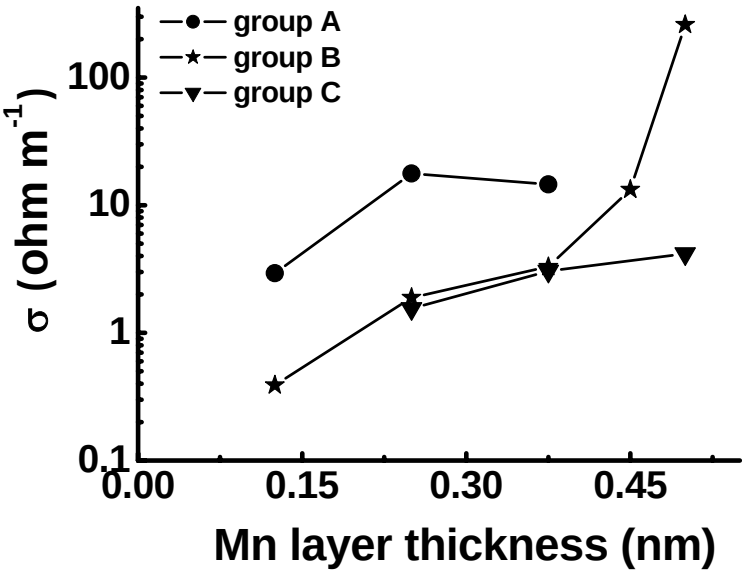

FIG. 5.3 The relationship between the Mn layer thickness and the electrical conductivity for different groups of samples studied in this chapter.

Figure 5.4 shows the normalized *R-T* curves over a temperature range from 5 to 300 K in group B. All samples exhibit a semiconducting-like behaviour, i.e., the resistance increases with the decrease of the temperature. In the sample B1 with the lowest Mn

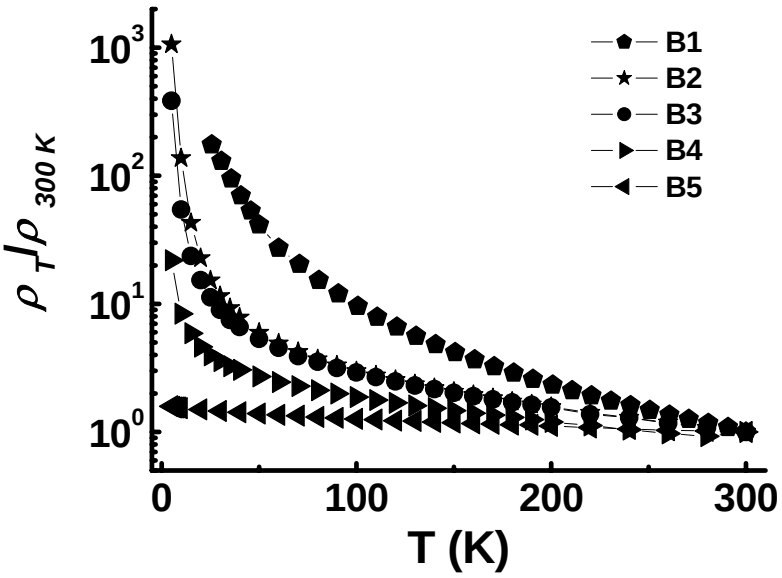

FIG. 5.4 Normalized log-scaled *R-T* curves for group B samples.

concentration, the resistance dramatically increases with decreasing temperature and is too high to be measured by the voltmeter below 20 K. When the Mn concentration increases further (samples B2 and B3), a sharp increase of the resistance at low temperatures is observed although the increase of the resistance is suppressed at the whole temperature range in comparison with sample B1. Samples of B2 and B3 exhibit similar temperature-dependent resistance behaviour. In sample B4, the increase of the resistance at low temperatures becomes less pronounced compared to sample B3. For sample B5 with the highest Mn concentration, the resistivity only slightly increases at low temperatures. Although the Mn layer in B5 is only a little thicker than that in B4, an obvious difference in the low-temperature conducting behaviour can be observed. The conduction behaviour in our δ-doped Ge:Mn thin films may be the competition result between Ge and Mn layers. At the lowest Mn concentration of sample B1, the conduction behaviour is dominated by Ge layers. Thus, an obvious semiconducting-like conducting behaviour can be observed. With increasing thickness of the Mn layer, the

semiconducting-like behaviour becomes less pronounced. Finally, the resistivity at low temperatures only slightly increases in sample B5, whose Mn concentration is highest.

5.3.3 Magnetic properties

Figure 5.5(a) shows both FC and ZFC curves of group B samples at the temperature range from 5 to 200 K with an applied magnetic field of 20 Oe. The magnetization for sample B1 is very weak and no hysteretic behaviour has been observed above 10 K. With increasing thickness of the Mn layer, the separation between ZFC and FC curves can be clearly observed in all the samples at low temperatures. The magnetization increases more rapidly in the higher Mn concentration samples, e.g., in samples B4 and B5. Figure 5.5(b) shows the normalized magnetization curves of samples B2 to B5. As can be seen clearly, the separation point between FC and ZFC curves increases with the increase of the Mn concentration. For the low Mn concentration samples (samples B2 and B3), the FC moment increases and eventually saturates with decreasing temperature below the separation point of the ZFC-FC curves. However, for moderate to highly doped samples (samples B4 and B5), the FC moment drops at low temperatures. The ZFC curve shows a cusp for low doped samples, i.e., B2 and B3. However, the cusp evolves into a hump with increasing thickness of the Mn layers. The cusp or hump temperatures are 15, 20, 40, and 75 K for samples B2, B3, B4, and B5, respectively.

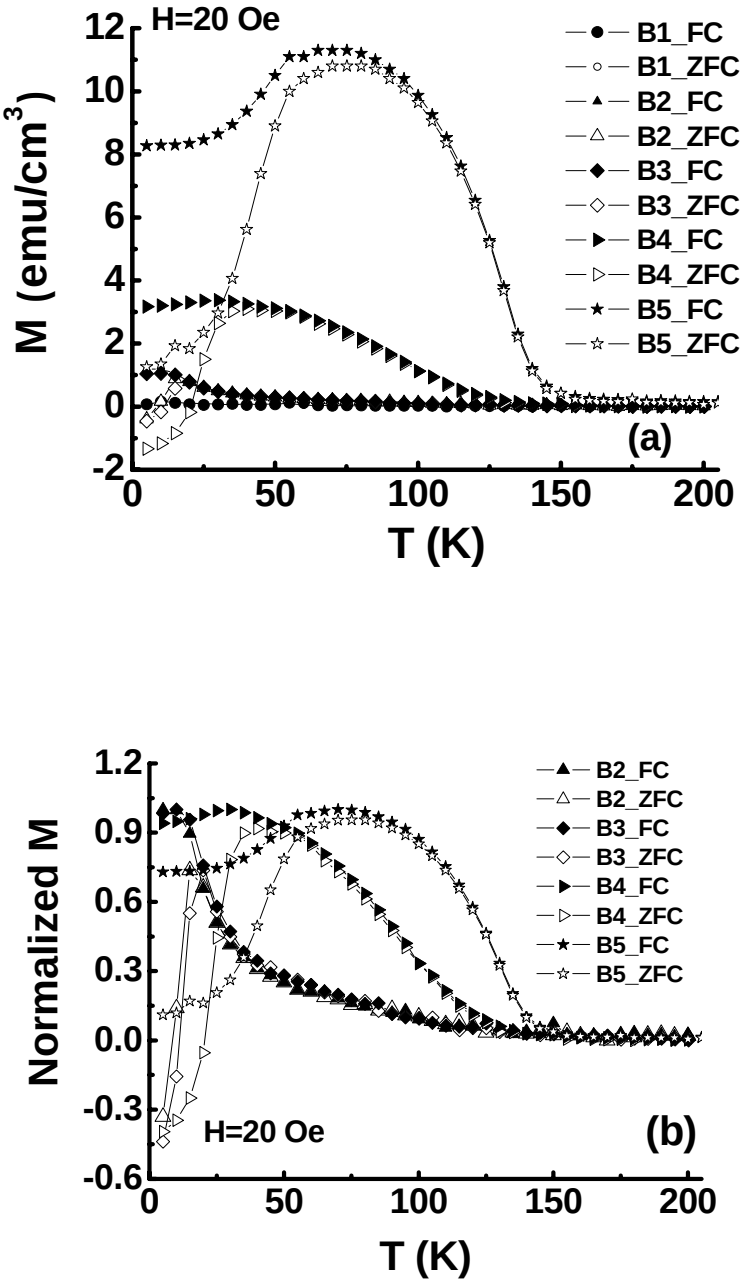

FIG. 5.5 (a) ZFC and FC curves for samples B1 to B5 at an applied magnetic field of 20 Oe at the temperature range from 5 to 200 K. (b) Normalized ZFC and FC curves for samples B2 to B5.

Figure 5.6(a) shows ZFC and FC curves for group A samples at the temperature range from 5 to 200 K with a magnetic field of 20 Oe. We can observe that there is also a rapid increase in the magnetization for sample A3 in comparison with those in sample

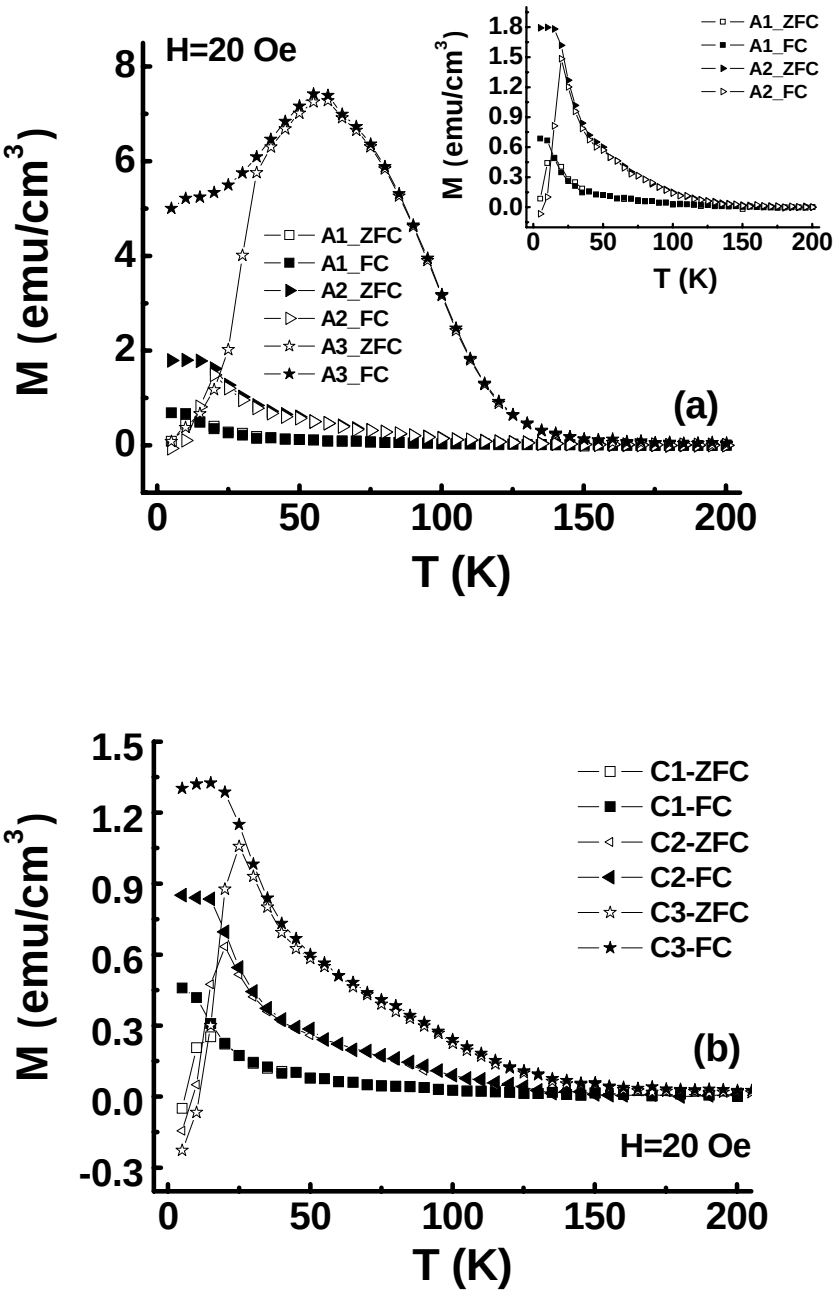

FIG. 5.6 (a) ZFC and FC curves for group A samples at the temperature range from 5 to 200 K at a magnetic field of 20 Oe. Inset: ZFC and FC curves for samples A1 and A2; (b) ZFC and FC curves for group C samples at the temperature range from 5 to 200 K at a magnetic field of 20 Oe.

A1 and A2. In order to see the *M-T* curves of samples A1 and A2 more clearly, the ZFC and FC curves of samples A1 and A2 are replotted and shown in the inset of Fig. 5.6(a). The separation between ZFC and FC curves can also be observed in all three samples.

With the increase of the Mn concentrations, the separation points shift to higher temperatures. The separation temperatures are 15, 20, and 40 K for A1, A2, and A3, respectively. The ZFC curves for samples A1 and A2 exhibit a cusp and the cusps evolve into a hump in sample A3 with increasing Mn layer thickness.

In Fig. 5.6 (b), we show ZFC and FC curves of group C samples at the temperature range from 5 to 200 K with a magnetic field of 20 Oe. The ZFC curves for all three samples exhibit a cusp at low temperatures and no hump is observed even in sample C3 with the highest Mn concentration, which is different from the samples in groups B and C. As discussed in Chapter 3, the hump in the ZFC curve is an indication of the formation of FM phase. Although the thickness of the Mn layer in sample C3 is higher than that of sample A3, the thickness of Ge layer is twice as that of sample A3. With the increase of the distance between the Mn layers, the long-range ordering may become weaker. Thus, the humps in samples A3, B4, and B5 cannot be observed in sample C3. The separation (cusp) temperatures of ZFC and FC curves increase with increasing Mn concentrations and are 15, 20, and 25 K for samples C1, C2, and C3, respectively.

Now, we will briefly discuss the *M*-*T* behaviours observed in three group samples. Majority of the *M*-*T* graphs observed show the paramagnetic-like behaviour above the temperatures of 40 K, whereas only those samples of A3, B4 and B5 exhibit a hump above 40 K. The former shows a sharp peak in the ZFC curves, otherwise known as cusp, where ZFC and FC curves diverge. Below the cusp temperature, the magnetic spins may experience random interactions with other magnetic spins, producing a highly irreversible and metastable state. Both the cusp and the separation between ZFC and FC curves are typical spin-glass behaviours. [8-10] The lack of long-range order in the amorphous structure may result in the randomness of magnetic spins in these samples, creating spin-glass-like structures in the process. The separation temperatures

between ZFC and FC curves in the latter are higher and do not coincide with the hump temperatures. The negative TRM and a noticeable broad peak in their ZFC curves with the separation temperature ranging from 70 to 105 K are observed in the latter. As discussed in Chapter 3, the hump and the negative TRM are the indication of the formation of the high-temperature FM phase, which suggests that the long-range order or Mn-rich nanoclusters may begin to form when the Mn layer thickness increases.

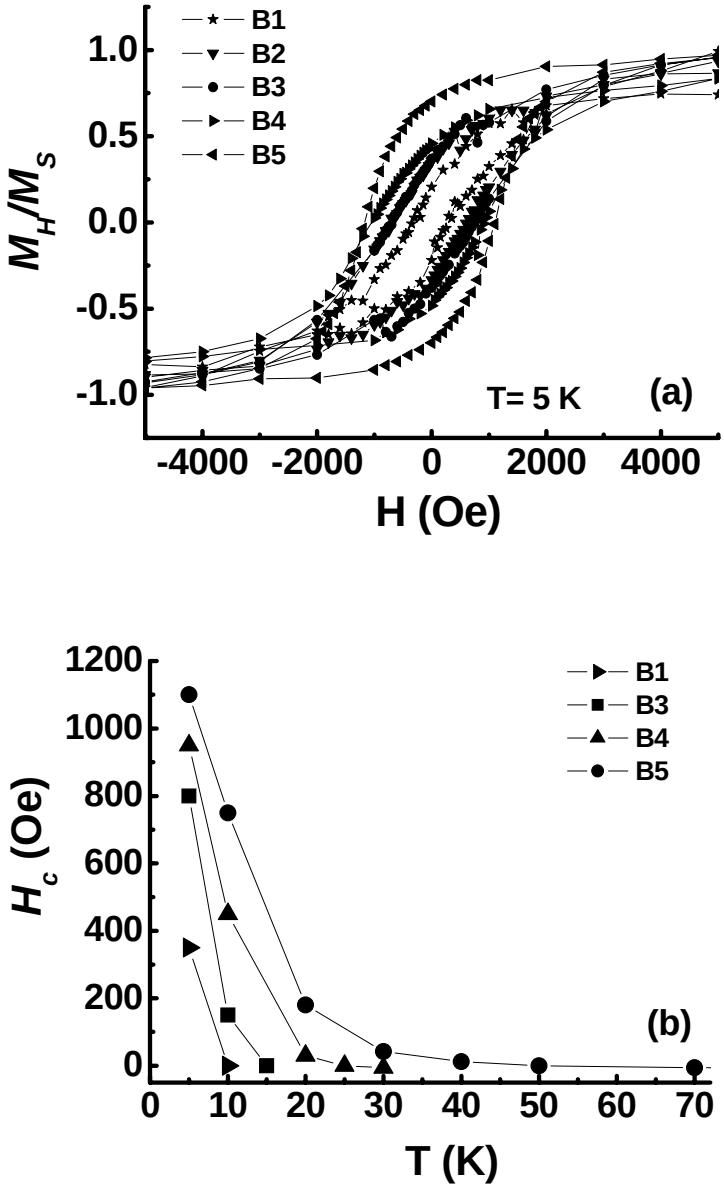

FIG. 5.7 (a) *M-H* curves for group B samples at 5 K with a maximum magnetic field of 5000 Oe. (b) Coercivity as a function of temperature for group B samples.

Figure 5.7(a) shows the normalized hysteresis curves at 5 K for group B samples. All samples exhibit a significant remanence, and the coercivity increases with the Mn concentration, which is around 350 Oe for sample B1 and 1100 Oe for sample B5. As can be seen from the figure, along with coercivity, the squareness also increases with the increase of the Mn concentration. In Fig. 5.7(b), the temperature-dependent coercivity as a function of temperature is exhibited. The coercivity decreases with decreasing Mn concentration at the same temperature and dramatically decreases with the increase of the temperature. The variation of the coercive field H_c with temperature is quite similar to the codoped $Ge_{1-x}Mn_x$ samples discussed in Chapter 3.

AC susceptibility measurements have also been done for sample B5. The real part (χ') of ac susceptibility for sample B5 at the temperature range from 5 to 200 K is presented in Fig. 5.8. In comparison with the dc ZFC magnetization, χ' has an onset around 145 K and exhibits a maximum around 113 K, which is close to the temperature point of the irreversible temperature in the ZFC-FC measurements. The peak position is frequency-dependent and shifts to the lower temperatures with the increase of the frequency. Also shown in the figure is the imaginary part (χ'') at the frequency of 10 Hz. The shape of the imaginary part is similar to that of the real part. A peak around 100 K is observed. Although ZFC and FC curves for sample B5 are quite similar to codoped amorphous samples A4 and A6 discussed in Chapter 3, the ac susceptibility is obviously different from them.

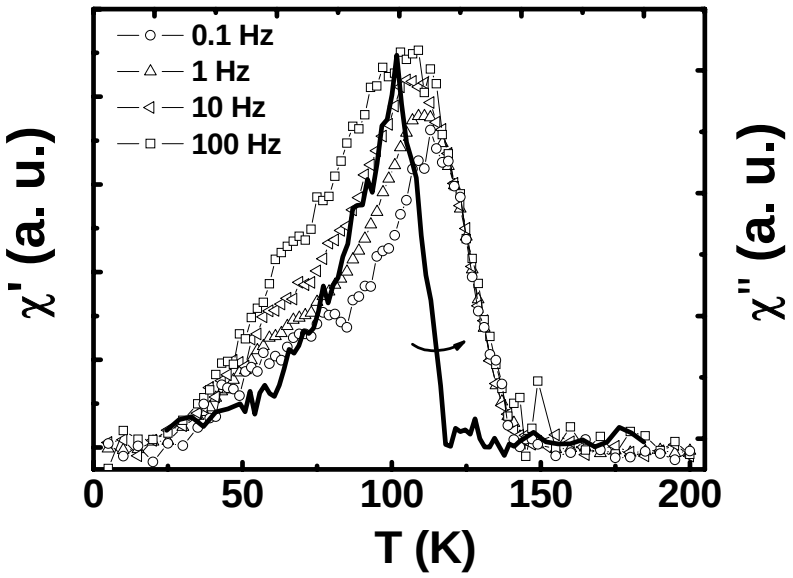

FIG. 5.8 Real and imaginary parts of the ac susceptibility for sample B5.

Figure 5.9 shows TRM curves with an applied magnetic field of 200 Oe for samples B1 to B5. It can be observed that the remanent magnetization turns to negative values above a certain temperature and the Mn concentration, which is similar to the codoped amorphous $Ge_{1-x}Mn_x$ samples discussed in Chapter 3. In samples B1 and B2 with the lowest Mn concentration, TRM was always positive before becoming zero. The TRM curves overlap with those of M_{FC}-M_{ZFC}. With increasing Mn concentration, TRM becomes negative at the temperature of 20, 30, and 45 K for samples B3, B4, and B5, respectively. The temperatures of turning to the negative values increase with the increase of the Mn concentration. These temperature values correlate well with the temperatures at which the ZFC moment starts to drop rapidly. The TRM curves do not coincide with that of M_{FC}-M_{ZFC} in these samples. Just as discussed in Chapter 3, the negative TRM results from the antiferromagnetic coupling between the low-temperature spin-glass-like phase and high-temperature clustered dopant phase. In the low Mn concentration, only spin-glass-like phase forms and no negative TRM is observed. With

the increasing of Mn concentration, the Mn-rich Ge:Mn nanocluster phase may form at the interfaces of Ge and Mn layers. The antiferromagnetic coupling between the high-temperature and low-temperature phases leads to the appearance of the negative TRM.

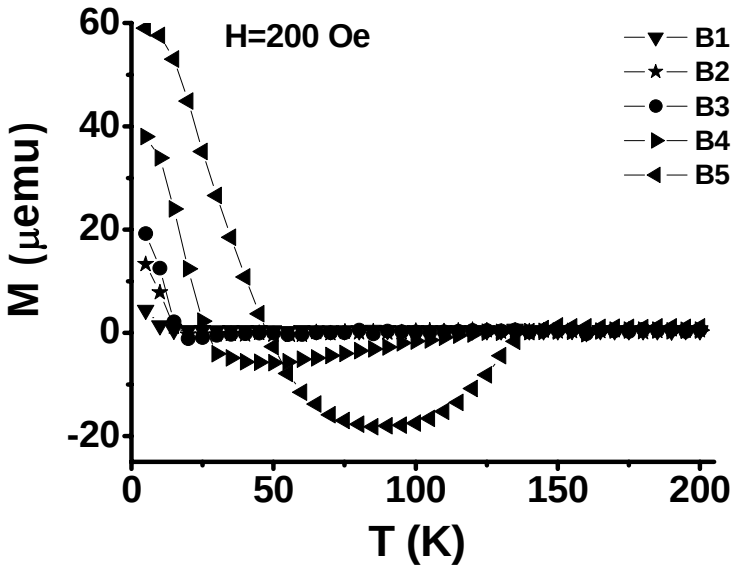

FIG. 5.9 TRM curves with a cooling magnetic field of 200 Oe for group B samples

5.3.4 Ordering temperature (T^*_C)

Based on these results, we would like to comment on the so-called Curie temperature reported for $Ge_{1-x}Mn_x$ diluted magnetic semiconductors. Since the magnetization curves differ from the classic Brillouin behaviour for ferromagnets, we obtain the ordering temperatures (T^*_C) by fitting the curves with the Curie-Weiss law at the high-temperature range. It can be observed from Fig. 5.10 that two factors will affect the ordering temperatures:

(1) The greater the Mn concentration, the higher ordering temperatures;

(2) The higher Mn to Ge ratio, the higher the ordering temperatures.

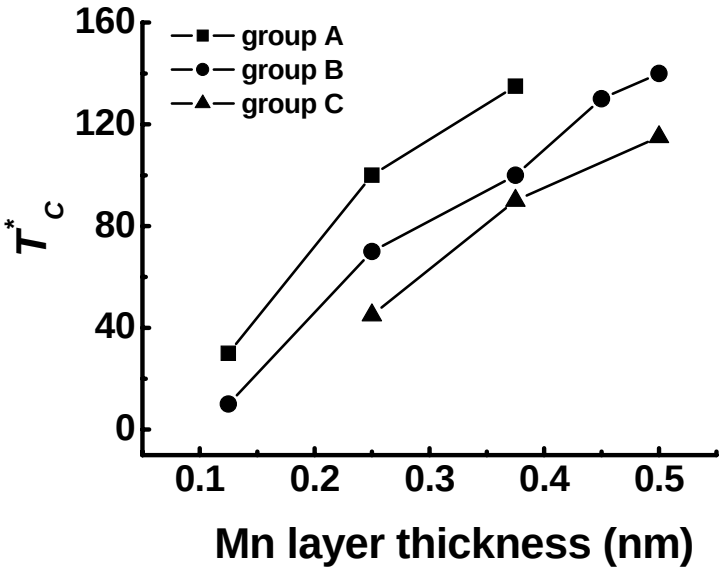

FIG. 5.10 Ordering temperatures (T^*_C) versus Mn layer thickness for different groups of samples.

This suggests that the thickness of the Mn layer and the distance between the Mn layers have a strong influence on the interactions between the Mn atoms within and between the layers. This is significantly different from the near linear T_C − Mn concentration relationship for the epitaxially grown $Ge_{1-x}Mn_x$ thin film samples with low Mn concentrations as reported by Park *et al*. [11]. A possible reason for the observation might be that at a low Mn-layer thickness or a higher Ge-layer separation the interaction of Mn atoms within or between the Mn layers is weak. However, as the Mn layers increase in thickness or as the distance separating the Mn layers decreases, the interactions of Mn atoms within or between the Mn layers becomes stronger. These two factors could contribute to a higher T^*_C. It is surprising that the T^*_C values of the *δ*-doped amorphous Ge:Mn samples are very close to those obtained from both the epitaxial [11-13] and amorphous $Ge_{1-x}Mn_x$ thin films [14]. This further suggests that the so-called Curie temperature reported in Ref. 11 may be not an indicator of the global

ordering of Ge:Mn DMSs, but rather the ordering temperature of magnetic clusters in the $Ge_{1-x}Mn_x$ system.

5.4 Summary

In summary, we have carried out a systematic study about structural, magnetic and electrical transport properties of the δ-doped amorphous $Ge_{1-x}Mn_x$ samples. Semiconducting-like conduction behaviour and low-temperature hysteresis loops were observed in all the samples. For the heavily doped samples, we have also observed the inverted hysteresis and negative TRM curves which were caused by the antiferromagnetic coupling between the high-temperature and low-temperature phases in this inhomogeneous system. T^*_C values of the δ-doped amorphous $Ge_{1-x}Mn_x$ samples were very close to those obtained from both the epitaxial and codoped amorphous $Ge_{1-x}Mn_x$ thin films, which suggested that the so-called Curie temperature reported in literature was not an indicator of the global ordering, but rather the ordering temperature of magnetic clusters in the $Ge_{1-x}Mn_x$ system.

References:

1 R. K. Kawakami, E. Johnston-Halperin, L F. Chen, M. Hanson, N. Guébels, J. S. Speck, A. C. Gossard, and D. D. Awschalom, "(Ga,Mn)As as a digital ferromagnetic heterostructure", Appl. Phys. Lett. **77**, pp. 2379-2381, 2000.

2 E. Johnston-Halperin, J. A. Schuller, C. S. Gallinat, T. C. Kreutz, R. C. Myers, R. K. Kawakami, H. Knotz, A. C. Gossard, and D. D. Awschalom, "Independent electronic

and magnetic doping in (Ga,Mn)As based digital ferromagnetic heterostructures", Phys. Rev. B **68**, pp. 165328, 2003.

3 T. C. Kreutz, W. D. Allen, E. G. Gwinn, D. D. Awschalom, and A. C. Gossard, "Structure-controlled magnetic anisotropy in ferromagnetic semiconductor superlattices", Phys. Rev. B **69**, pp. 081302(R), 2004.

4 T. C. Kreutz, G. Zanelatto, E. G. Gwinn, and A. C. Gossard, "Spacer-dependent transport and magnetic properties of digital ferromagnetic heterostructures", Appl. Phys. Lett. **81**, pp. 4766-4768, 2002.

5 X. Chen, M. Na, M. Cheon, S. Wang, H. Luo, B. D. McCombe, X. Liu, Y. Sasaki, T. Wojtowicz, J. K. Furdyna, S. J. Potashnik, and P. Schiffer, "Above-room-temperature ferromagnetism in GaSb/Mn digital alloys", Appl. Phys. Lett. **81**, pp. 511-513, 2002.

6 K. C. Ku, S. J. Potashnik, R. F. Wang, S. H. Chun, P. Schiffer, N. Samarth, M. J. Seong, A. Mascarenhas, E. Johnston-Halperin, R. C. Myers, A. C. Gossard, and D. D. Awschalom, "Highly enhanced Curie temperature in low-temperature annealed [Ga,Mn]As epilayers", Appl. Phys. Lett. **82**, pp. 2302-2304, 2003.

7 G. Patriarche, E. Le Bourhis. M. M. O. Khayyat and M. M. Chaudhri, "Indentation-induced crystallization and phase transformation of amorphous germanium", J. Appl. Phys. **96**, pp. 1464-1468, 2004.

8 M. Sahana, A. Venimadhav, M. S. Hegde, K. Nenkov, U. K. Röβler, K. Dörr, K.-H. Müller, "Magnetic properties and specific heat of $LaMn_{1-x}Ti_xO_{3+\delta}$", J. Magn. Magn. Mater. **260**, pp. 361-370, 2003.

9 A. Ray and R. Ranganathan, "Giant magnetoresistance in the disordered magnetic alloy $(FeNi)_{25}Au_{75}$", Phys. Rev. B **56**, pp. 6073-6078, 1997.

10 J. Dho, W. S. Kim, and N. H. Hur, "Reentrant spin glass behavior in Cr-doped perovskite manganites", Phys. Rev. Lett. **89**, pp. 027202, 2002.

11 Y. D. Park, A. T. Hanbicki, S. C. Erwin, C. S. Hellberg, J. M. Sullivan, J. E. Mattson, T. F. Ambrose, A. Wilson, G. Spanos, and B. T. Jonker, "A group-IV ferromagnetic semiconductors: Mn_xGe_{1-x}", Science **295**, pp. 651-654, 2002.

12 A. P. Li, J. Shen, J. R. Thompson, and H. H Weitering, "Ferromagnetic percolation in Mn_xGe_{1-x} dilute magnetic semiconductor", Appl. Phys. Lett. **86**, pp. 152507-152509, 2005;

13 A. P. Li, J. F. Wendelken, J. Shen, L. C. Feldman, J. R. Thompson, and H. H. Weitering, "Magnetism in Mn_xGe_{1-x} semiconductors mediated by impurity band carrier", Phys. Rev. B **72**, pp. 195205, 2005.

14 S. Yu, T. L. Anh, Y. E. Ihm, D. Kim, H. Kim, S. Oh, C. S. Kim, and H. Ryu, "Ferromagnetism in amorphous $Ge_{1-x}Mn_x$ grown by low temperature vapor deposition", Solid State Commun. **134**, pp. 641-645, 2005.

CHAPTER 6

A SPIN VALVE WITH AMORPHOUS $Ge_{0.67}Mn_{0.33}$ THIN FILM AS ONE OF ELECTRODES

6.1 Introduction

The ultimate aim of research on half-metals and DMSs is to apply them to spintronic devices, such as spin-valves and MTJs. The fabrication of all-semiconductor spintronic devices has already been realized by Ohno and Tanaka groups. [1-3] In this chapter, we will discuss some preliminary results that we have obtained on a spin valve using the amorphous $Ge_{0.67}Mn_{0.33}$ thin film as one of the ferromagnetic electrodes.

Since the invention of spin valves by Parkin *et al.* in 1991, [4] great efforts have been made to achieve a higher MR ratio at room temperature both experimentally and theoretically. [5-13] Figure 6.1 shows the schematic of a typical spin-valve structure which consists of primarily two ferromagnetic layers separated by a non-magnetic layer. [14] One of the FM layers is pinned by an antiferromagnetic layer such that its magnetization is relatively insensitive to the presence of moderate external fields. On the other hand, the magnetization in the other FM layer is free to rotate so as to respond to an external field. The former is called “pinned layer”, while the latter “free layer”. When a relatively small magnetic field is applied, the direction of magnetization of the free layer changes accordingly, leading to the change of resistance.

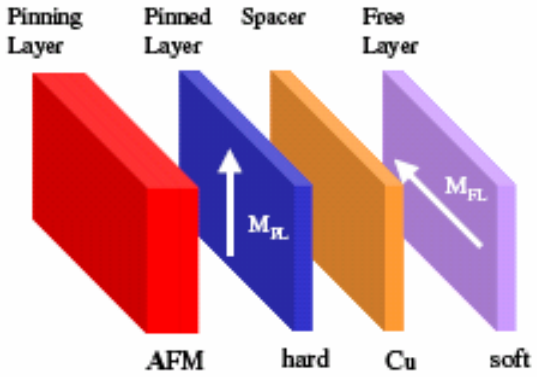

FIG. 6.1 Schematic illustration for a spin-valve structure. The arrows in the "pinned layer" and "free layer" point to the magnetization direction [After Y. H. Wu, Ref. 14].

Figures 6.2(a) and 6.2(b) show the schematic illustration of *M-H* and MR curves for a typical spin-valve structure. The red and blue arrows shown in the figures represent the magnetic orientations of the pinned and free layers. *M-H* and MR curves can be divided into three regions. In regions (I), the magnetizations of two magnetic layers are at the state of parallel alignment, where the resistance is at the minimum value. When sweeping the applied magnetic field to region (II), the magnetization of the free layer changes its orientation firstly due to its low coercivity field, leading to the antiparallel alignment of the magnetization between the two magnetic layers. The resistance reaches the maximum value. When the magnetic field is further increased to region (III), the magnetization of the pinned layer also changes its orientation. The magnetizations of two magnetic layers are at the state of parallel alignment again. The resistance is back to the minimum value.

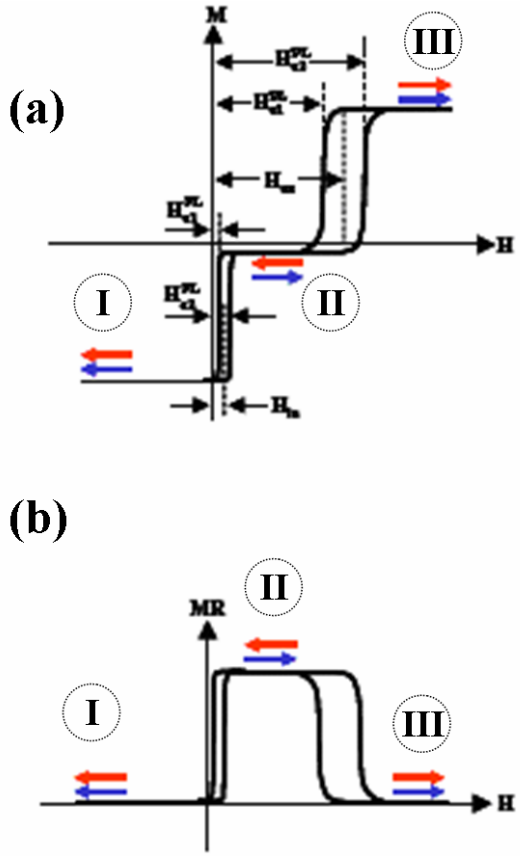

FIG. 6.2 Schematic illustration of (a) *M-H* and (b) MR curves for a typical spin-valve structure. H_{ex}: exchange-bias field; H_{in}: interlayer coupling field between the pinned and free layers; $(H_{c1}^{FL} - H_{c2}^{FL})$: coercivity of free layer; $(H_{c1}^{PL} - H_{c2}^{PL})$: coercivity of pinned layer. The red and blue arrows points to the magnetization orientation of the pinned layer and free layer, respectively. [After Y. H. Wu, Ref. 14].

6.2 Experimental details

A spin valve with the structure of $Ge_{0.67}Mn_{0.33}$ (30 nm)/Cu (2.4 nm)/NiFe (3 nm)/IrMn (8 nm) was fabricated, where the numbers in the bracket denoted the layer thickness. The schematic structure of the fabricated spin valve was shown in Fig. 6.3. The amorphous $Ge_{0.67}Mn_{0.33}$ layer was deposited first by MBE, followed immediately by the growth of other layers in a UHV sputter system (ULVAC MB98-4801). Prior to the deposition of other layers, the $Ge_{0.67}Mn_{0.33}$ layer was pre-cleaned in the pre-clean chamber so as to remove the oxides at the surface. The magnetic and electrical transport

properties were measured using a commercial SQUID at the temperature range from 15 to 300 K.

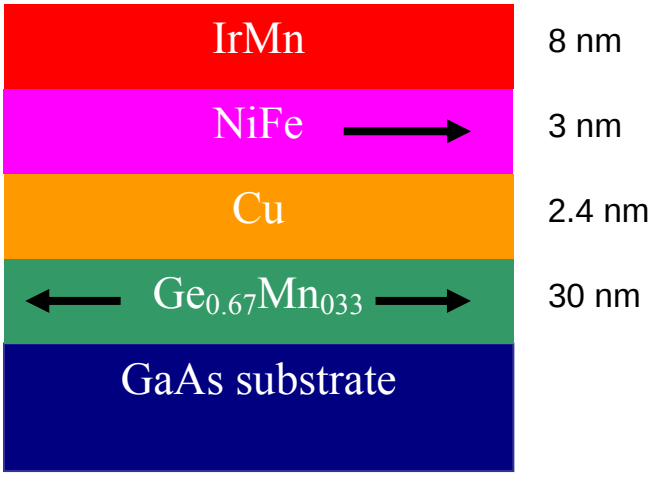

FIG. 6.3 Schematic illustration of the fabricated spin-valve structure discussed in this chapter. The arrows point to the magnetization orientation.

6.3 Results and discussion

6.3.1 *M-H* curves

Figure 6.4 shows *M-H* curves for the spin valve of $Ge_{0.67}Mn_{0.33}$ (30 nm)/Cu (2.4 nm)/NiFe (3 nm)/IrMn (8 nm) at 20, 50, and 100 K, respectively. The solid and dashed lines in the figure represent the magnetization orientation of NiFe and $Ge_{0.67}Mn_{0.33}$ layers, respectively. It can be observed that *M-H* curves are the combination of two magnetic subsystems, i.e., $Ge_{0.67}Mn_{0.33}$ and NiFe. The shape of *M-H* curves is similar to that shown in Fig. 6.2(a) for a standard spin-valve system. At region (I), the magnetizations of $Ge_{0.67}Mn_{0.33}$ and NiFe layers are parallel. At region (II), the magnetization of the $Ge_{0.67}Mn_{0.33}$ layer changes its orientation first, leading to antiparallel alignment between the two magnetic layers. When the magnetic field increases further, the magnetization of NiFe layer also changes its orientation, leading

to the parallel alignment of the magnetizations between two magnetic layers at region (III).

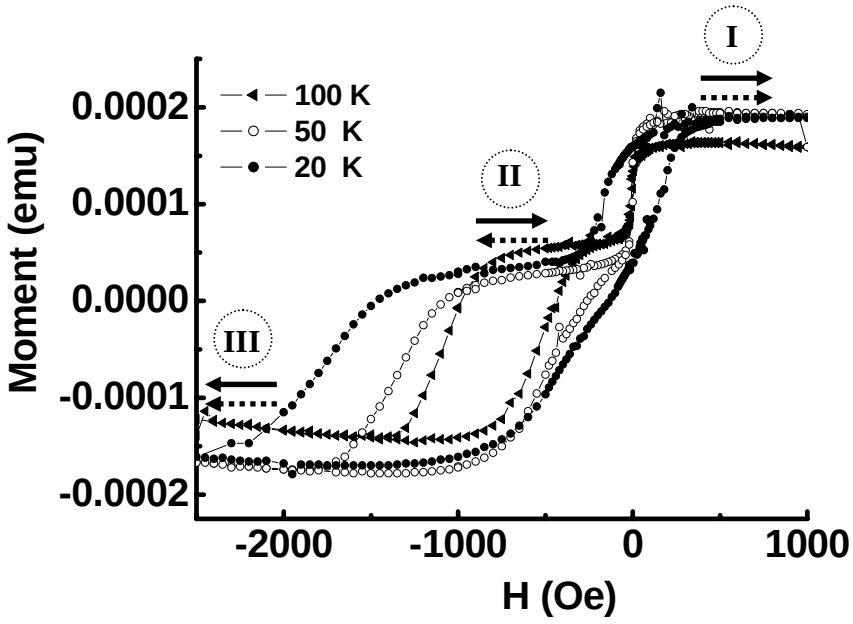

FIG. 6.4 *M-H* curves at 20, 50, and 100 K for the spin valve with the structure of $Ge_{0.67}Mn_{0.33}$ (30 nm)/Cu (2.4 nm)/NiFe (3 nm)/IrMn (8 nm). The solid and dashed lines present the magnetization orientations of NiFe and $Ge_{0.67}Mn_{0.33}$ layers, respectively.

6.3.2 Electrical transport properties

After discussing the magnetic properties, we now turn to the discussion about the electrical transport properties. Although we tried to measure MR curves at different temperatures, typical spin-valve MR curves as that shown in Fig. 6.2(b) cannot be obtained in our spin-valve structure. In the following section, we will briefly discuss the possible reason by simple calculations.

The carrier density, density of states at Fermi level, and conductivity [14] can be expressed as in equations 6.1, 6.2, and 6.3:

$$n = \frac{1}{3\pi^2}\left(\frac{2m_e E_F}{\hbar^2}\right)^{3/2}, \tag{6.1}$$

$$N(E_F) = \frac{1}{2\pi^2}\left(\frac{2m_e}{\hbar^2}\right)^{3/2}\sqrt{E_F}\ , \tag{6.2}$$

$$\sigma = \frac{e^2}{3}\Lambda_F \nu_F N(E_F), \tag{6.3}$$

where n is the carrier density, m_e is the electron effective mass, $\hbar$ is the reduced Plank constant, E_F is the Fermi energy, $N(E_F)$ is the density of state at the Fermi level, σ is the conductivity, Λ_F is mean free path, ν_F is Fermi velocity, and e is the electron charge. After substituting equations 6.1 and 6.2 into equation 6.3, we get equation 6.4.

$$\Lambda_F = \frac{3\sigma\hbar}{e^2}\left(\frac{\pi}{3n}\right)^{2/3}\ . \tag{6.4}$$

It can be found that the mean free path only relates to the conductivity and carrier density. The conductivity and carrier density of $Ge_{0.67}Mn_{0.33}$ thin film are around 1.7 $\Omega\ cm$ and $1.3\times10^{21}\ cm^{-3}$, respectively. After substituting these values into equation 6.4, we obtain the mean free path value of only 10^{-10} nm, which is too small to be considered. This may explain why the MR ratio is too small for this kind of spin-valve structure.

Instead of measuring the MR curves at different temperatures, we tried to obtain the temperature-dependent resistance curves at different applied magnetic fields. Figure 6.5 shows the temperature-dependent resistance curves measured at applied magnetic fields of -100 (upper curve) and 100 Oe (lower curve) at the temperature range from 20 to 100 K. Because the coercivity field of $Ge_{0.67}Mn_{0.33}$ layer is less than 100 Oe, we can obtain the resistance values at the states of the parallel and antiparallel alignments of the magnetizations between $Ge_{0.67}Mn_{0.33}$ and NiFe layers after applying the magnetic fields of 100 and -100 Oe, respectively. An obvious resistance difference below 200 K can be observed in Fig. 6.5. Then, the ratio of resistance change (ΔR%) in the states of

antiparallel and parallel alignments of the magnetizations between NiFe and $Ge_{0.67}Mn_{0.33}$ layers can be obtained after the definition in equation 6.5:

$$\Delta R\% = \frac{R_{AP} - R_P}{R_P} \times 100\%, \tag{6.5}$$

where R_{AP} and R_P are the resistances at the states of antiparallel and parallel alignments, respectively.

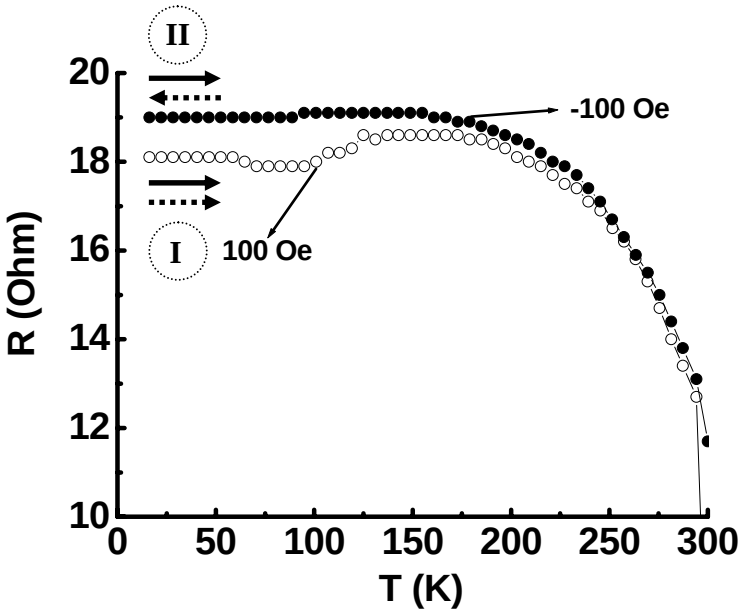

FIG. 6.5 *R-T* curves for the spin-valve structure of $Ge_{0.67}Mn_{0.33}$ (30 nm)/Cu (2.4 nm/NiFe (3 nm)/IrMn (8 nm) at the applied magnetic fields of 100 Oe (solid circles) and -100 Oe (open circles). The solid and dashed lines present the magnetization orientations of NiFe and $Ge_{0.67}Mn_{0.33}$ layers, respectively.

In Fig. 6.6, we plot the curve of $\Delta R\%$ as a function of temperature. Below 60 K, $\Delta R\%$ is almost constant and keeps the value of ~ 4.9%. Then, $\Delta R\%$ increases with the increase of the temperature and reaches the maximum of 6.7% around 100 K. Above 100 K, $\Delta R\%$ decreases with the decrease of the temperature. In comparison with the FC curve of amorphous $Ge_{0.67}Mn_{0.33}$ thin film at an applied magnetic field of 100 Oe shown in the inset of Fig. 6.6, a hump around 60 K is observed in both the temperature-

dependent ΔR% curve of the spin valve and the FC curve of amorphous $Ge_{0.67}Mn_{0.33}$ thin film. Fitting the FC curve of the amorphous $Ge_{0.67}Mn_{0.33}$ thin film with the Curie-Weiss law, we obtain a T^*_C around 110 K, which is very close to the temperature of the highest ΔR%. This suggests that the change of resistance in this spin-valve structure may originate from the amorphous $Ge_{0.67}Mn_{0.33}$ thin film, instead of the spin-valve structure.

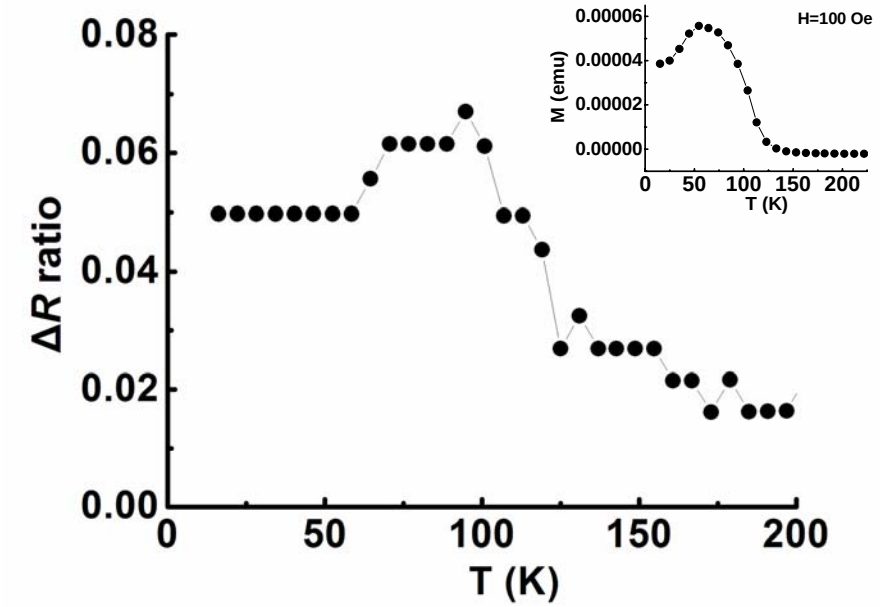

FIG. 6.6 ΔR ratio as a function of the temperature for the spin-valve structure of $Ge_{0.67}Mn_{0.33}$ (30 nm)/Cu (2.4 nm)/NiFe (3 nm)/IrMn (8 nm). The inset is the FC curve of the amorphous $Ge_{0.67}Mn_{0.33}$ thin film at an applied magnetic field of 100 Oe.

6.4 Summary

Some preliminary results on the application of the amorphous $Ge_{0.67}Mn_{0.33}$ thin film into the spin valve have been obtained. A spin valve with the structure of $Ge_{0.67}Mn_{0.33}$ (30 nm)/Cu (2.4 nm)/NiFe (3 nm)/IrMn (8 nm) was fabricated. Typical spin-valve *M-H* curves were obtained. The resistance change in this structure might originate from the amorphous $Ge_{0.67}Mn_{0.33}$ thin film, instead of the spin-valve structure.

References:

1 Y. Ohno, D. K. Young, B. Beschoten, F. Matsukura, H. Ohno, and D. D. Awschalom, "Electrical spin injection in a ferromagnetic semiconductor heterostructure", Nature **402**, pp. 790-792, 1999.

2 K. Takahashi and M. Tanaka, "Magnetotransport properties of MnAs/GaAs/MnAs ferromagnetic/semiconductor trilayer heterostructures", J. Appl. Phys. **87**, pp. 6695-6697, 2000.

3 R. Nakane, S. Sugahara, and M. Tanaka, "Growth and magnetoresistance of epitaxial metallic MnAs/NiAs/MnAs trilayers on GaAs (001) substrates", Physica E **21,** pp. 991-995, 2004.

4 B. Dieny, V. S. Speriosu, S. S. P. Parkin, B. A. Gurney, D. R. Wilhoit, and D. Mauri, "Giant magnetoresistive in soft ferromagnetic multilayers", Phys. Rev. B **43**, pp. 1297-1230, 1991.

5 S. Colis and A. Dinia, "Domain wall duplication in a hard-soft spin-valve structure using the CoFe/Ir/CoFe artificial antiferromagnetic subsystem", Phys. Rev. B **66**, pp. 174425, 2002.

6 L. Wang, J. J. Qiu, W. J. McMahon, K. B. Li, and Y. H. Wu, "Nano-oxide-layer insertion and specular effects in spin valves: Experiment and theory", Phys. Rev. B **69**, pp. 214402, 2004.

7 Z. C. Zhao, H. Wang, S. Q. Xiao, X. X. Zhong, Y. Z. Gu, Y. X. Xia, Q. Y. Jin, X. S. Wu, "Doping effects of a nano-nitride layer at the interfaces of a NiO/Co/Cu/Co/Cu structure", Phys. Status Solidi A **203**, pp.956 – 962, 2005.

8 Zhiya Zhao, P. Mani, G. J. Mankey, G. Gubbiotti, S. Tacchi, F. Spizzo, W.-T. Lee, C. T. Yu and M. J. Pechan, "Magnetic properties of uniaxial synthetic antiferromagnets for spin-valve applications", Phys. Rev. B **71**, pp. 104417, 2005.

9 R. L. Rodríguez-Suárez, S. M. Rezende, and A. Azevedo, "Ferromagnetic resonance investigation of the residual coupling in spin-valve systems", Phys. Rev. B **71**, pp. 224406, 2005.

10 M. Gmitra and J. Barnas´, "Current-driven destabilization of both collinear configurations in asymmetric spin valves", Phys. Rev. Lett. **96**, pp. 207205, 2006.

11 H. W. Joo, J. H. An, M. S. Lee, S. D. Choi, K. A. Lee, S. W. Kim, S. S. Lee, and D. G. Hwang , "Enhancement of magnetoresistance in [Pd/Co]N/Cu/Co/[Pd/Co]N/FeMn spin valves", J. Appl. Phys. **99**, pp. 08R504, 2006.

12 A. Deac, K. J. Lee, Y. Liu, O. Redon, M. Li, P. Wang, J. P. Nozières, and B. Dieny, "Current-induced magnetization switching in exchange-biased spin valves for current-perpendicular-to-plane giant magnetoresistance heads", Phys. Rev. B **73**, pp. 064414, 2006.

13 H. Fukuzawa, H. Yuasa, S. Hashimoto, H. Iwasaki, and Y. Tanaka, "Large magnetoresistance ratio of 10% by $Fe_{50}Co_{50}$ layers for current-confined-path current-perpendicular-to-plane giant magnetoresistance spin-valve films", Appl. Phys. Lett. **87**, pp. 082507, 2005.

14 A/Prof. Wu Yihong, Lecture notes for Spinelectronics.

CHAPTER 7

CONCLUSIONS AND RECOMMENDATION FOR FUTURE WORK

7.1 Conclusions

The research conducted in this thesis focused on fabrication and characterization of two kinds of spintronic materials: Fe_3O_4 and $Ge_{1-x}Mn_x$. Structure, magnetic, and electrical transport properties were investigated in detail to explore the possible application of these materials in spintronic devices. The important findings and conclusions were summarized as follows.

(1) In epitaxially-grown Fe_3O_4 nanostructures, detailed studies of bias-dependent and field-dependent dynamic conductance for both thin films and nanowires revealed that tunnelling was the dominant transport mechanism across antiphase boundaries near and above the Verwey transition temperature. Antiferromagnetic coupling across antiphase boundaries was responsible for the universal MR curve shape in Fe_3O_4. The antiferromagnetically coupled regions might be responsible for the low MR ratios obtained from Fe_3O_4-based spin valves and MTJs.

(2) In amorphous $Ge_{1-x}Mn_x$ thin films, we found that the amorphous $Ge_{1-x}Mn_x$ samples consisted of a low-temperature highly ordered spin-glass-like phase and a high-temperature “cluster dopants” phase. The magnetization

of the two phases was found to be coupled antiferromagnetically with each other at low temperatures. The good agreement between the values of T_C and T^*_C for amorphous samples and those of the two characteristic temperatures reported in literature for epitaxially-grown samples suggested that the ferromagnetic phase of the latter observed in the temperature range of 110-120 K was of extrinsic origin. The high-temperature phase was of characteristic nature of the Ge:Mn system, independent of crystalline structure and Mn concentrations unless secondary phases were formed uniformly in the samples. Carrier localization only occurred at low temperatures, which has been observed in the dynamic conductance and Hall effect studies. The dynamic conductance technique might be applied to the study of other types of inhomogeneous diluted magnetic semiconductor systems.

(3) In amorphous $Ge_{1-x}Mn_x$ thin films embedded with Ge crystallites and different types of secondary phases, we found that the magnetic properties were dominant by the high T_C secondary phases. Dynamic conductance studies revealed that the carrier localization only happened at low temperatures. A sharp increase of the magnetization was observed below 25 K. The critical temperature (T_C') was independent of the Mn composition and secondary phases and was very close to T_C or T_f reported in literature. Spin-dependent transport across the interface between the high T_C secondary phases and the host semiconductor matrix were studied in $Ge_{0.88}Mn_{0.12}$ nanowires with different diameters. Existence of a Schottky barrier at the nanoparticles / host semiconductor matrix interface and the

carrier localization at low temperatures were observed in granular $Ge_{0.74}Mn_{0.26}$ systems.

(4) In δ-doped amorphous $Ge_{1-x}Mn_x$ samples, we found that magnetic and electrical transport properties were dependent on both the Mn concentration and the ratio of Ge and Mn layer thicknesses. For heavily doped samples, we also observed the negative TRM and inverted hysteresis loops, which were caused by the antiferromagnetic coupling between the low-temperature spin-glass-like phase and the high-temperature nanoparticle phase in the inhomogeneous samples. It was surprising that the T^*_C values were very similar to both the epitaxial and amorphous $Ge_{1-x}Mn_x$ thin films, which suggested that the so-called Curie temperature reported in literature was not an indicator of global ordering, but rather the ordering temperature of magnetic clusters in Ge:Mn system.

(5) Some preliminary results about a spin valve with the structure of GeMn (30 nm)/Cu (2.4 nm)/NiFe (3 nm)/IrMn (8 nm) were reported. Typical spin-valve-like *M-H* curves were obtained in this structure.

7.2 Recommendation for future work

Recommendations for future work are as follows:

(1) To fabricate Fe_3O_4 thin films and nanowires with different thicknesses and change the widths between two voltage electrodes. The sizes of antiphase boundaries are dependent on the thickness of the thin films. Thus, the size effect of antiphase boundaries on the electrical transport properties can be obtained by fabricating samples with different thicknesses. By altering the

widths between two voltage probes, we can further study the size effect on the electrical transport properties across antiphase boundaries.

(2) To study magnetic and electrical transport properties of ion-implanted $Ge_{1-x}Mn_x$ thin films with low Mn concentrations. Although some preliminary results have been published by other groups, detailed studies of magnetic and electrical transport properties have not been done yet.

(3) To further fabricate spin valves and MTJs with the amorphous $Ge_{1-x}Mn_x$ thin films with different Mn concentrations and film thicknesses as one of ferromagnetic electrodes.

(4) To fabricate amorphous $Ge_{1-x}Mn_x$ nanowires with different Mn concentrations to study the dimension effect on the electrical transport properties. So far, most of the research work about DMSs has focused on thin film samples. The studies of one-dimension DMS nanowires may help one to have a better understanding of the origin of ferromagnetism in Ge-based DMSs.